INFORMATION TO USERS

This manuscript has been reproduced from the microfilm master. UMI films the text directly from the original or copy submitted. Thus, some thesis and dissertation copies are in typewriter face, while others may be from any type of computer printer.

The quality of this reproduction is dependent upon the quality of the copy submitted. Broken or indistinct print, colored or poor quality illustrations and photographs, print bleedthrough, substandard margins, and improper alignment can adversely affect reproduction.

In the unlikely event that the author did not send UMI a complete manuscript and there are missing pages, these will be noted. Also, if unauthorized copyright material had to be removed, a note will indicate the deletion.

Oversize materials (e.g., maps, drawings, charts) are reproduced by sectioning the original, beginning at the upper left-hand corner and continuing from left to right in equal sections with small overlaps. Each original is also photographed in one exposure and is included in reduced form at the back of the book.

Photographs included in the original manuscript have been reproduced xerographically in this copy. Higher quality 6" x 9" black and white photographic prints are available for any photographs or illustrations appearing in this copy for an additional charge. Contact UMI directly to order.

U·M·I

University Microfilms International
A Bell & Howell Information Company
300 North Zeeb Road, Ann Arbor, MI 48106-1346 USA
313/761-4700 800/521-0600

Order Number 9303405

The formation and characteristics of E-region thin ionization layers at high latitudes

Bristow, William Albert, Ph.D.

University of Alaska Fairbanks, 1992

U·M·I

300 N. Zeeb Rd.
Ann Arbor, MI 48106

THE FORMATION AND CHARACTERISTICS OF E-REGION THIN IONIZATION LAYERS AT HIGH LATITUDES

A

THESIS

Presented to the Faculty of the University of Alaska
in Partial Fulfillment of the Requirements
for the Degree of

DOCTOR OF PHILOSOPHY

By
William A. Bristow, B.S.E.E., B.S.Phys.

Fairbanks, Alaska
May, 1992

THE FORMATION AND CHARACTERISTICS OF E-REGION THIN IONIZATION LAYERS AT HIGH LATITUDES

By

William A. Bristow

RECOMMENDED:

Advisory Committee Chair

Department Head

APPROVED:

Dean, College of Natural Sciences

Dean of the Graduate School

5/1/92

Date

ABSTRACT

The formation and characteristics of E-region thin ionization layers at high latitudes is studied. Thin ionization layers at mid-latitudes are formed by the action of neutral wind shears redistributing the background ionization. At high-latitudes wind-shears are not as effective at the redistribution of ionization, and it is found that the high-latitude electric fields may cause layer formation. The mechanism for high-latitude layer formation is studied through numerical simulation and incoherent-scatter radar observations. A one-dimensional simulation examined high-latitude layer formation in detail. It examined the effects of the direction of the electric field. It was found that thin ionization layers formed for electric fields directed in the north-west and south-west quadrants. The layers formed by electric fields in the south-west quadrant form at altitudes which are consistent with observations, while fields in the north-west quadrant resulted in layer altitudes which were higher than usually observed. It was also found that the neutral wind acting in concert with the electric field may affect the altitude and thinness of layers. The one-dimensional simulation was extended to a three-dimensional model of the polar cap ionosphere. The three dimensional simulation showed that large areas of thin ionization layers may form for widely varying geophysical conditions. Incoherent-scatter radar observations showed the presence of thin ionization layers on 12 out of 16 nights of observation. High-resolution spectral data showed that the average ion mass within the layers was higher than that in the background ionization, demonstrating the presence of heavy metallic ions. Concurrent observation of thin layers and electric fields showed layers present for field directions between 40° and 140° west of magnetic north, which agrees with the simulation. However, the range of angles is more limited than was predicted. Antenna scanning observations examined the latitudinal extent of the layers, and found the layers were of a limited extent; the largest extent observed was about 200km.

TABLE OF CONTENTS

LIST OF FIGURES

Acknowledgments

As is nearly always the case, this work was accomplished with the help and support of many friends and acquaintances. I would like to thank all of those who have helped me along the way here at the Geophysical Institute. There are a few who I would like to thank in particular.

First I would like to thank the members of my advisory committee: Drs. Brenton Watkins, Roger Smith, Robert Piacenza, John Olson, and Robert Hunsucker. Each committee member had helpful suggestions which made the thesis a better document. John Olson and Brenton Watkins were especially helpful with a careful reading of the first draft and found many errors. A special thanks to John Olson and Roger Smith, who were both responsible in part for my interest in a graduate degree in physics. Both Roger and John taught undergraduate courses that were interesting enough to draw me away from electrical engineering and into physics. I would also like thank Bob Hunsucker for his help in contacting prospective employers.

Brenton Watkins has been my major advisor and friend from the start of my graduate education. Brent hired me as an undergraduate to do some electronics work, and was responsible for my entrance in the Geophysical Institute graduate program. Over the years, he has given me guidance enough to get me started on projects and freedom to pursue my interests where they lead. He was always ready with advice when it was needed to keep me on track. Brent has supplied the best computing resources available, as well as resources for travel and other research needs. There were also numerous Chinese lunches supplied along the way.

The site crew at the Sondrestrom radar facility also played an essential role in obtaining the data for the last section of the thesis. Craig Heinselman and John Jorgenson deserve special thanks for their work in developing special modes of operation.

I would also like to give a special thanks to my officemate, Don Rice. Don and I have shared an office for the last three years. No one could ask for a better officemate than Don. He has a nearly inexhaustible knowledge of computers among

other things, and was always willing to help. Don also has a great dry sense of humor, which made it fun to share an office.

I would also like to thank all of my friends and fellow graduate students. We have a closely knit group, which has always made living here fun. I would like to give special thanks to Don Hampton and Anne Ruggles for their friendship to me and my family.

I must also acknowledge the love and support of my wife, Martha and daughter, Sarah. Martha and I have been married ten years, seven of which have been spent with me in school. It has been a big sacrifice for both Martha and Sarah to put life on hold while I get done. Martha certainly does deserve the degree of PHT, that is Pushed Him Through. Although it has been hard it has also been a lot of fun. I am sure that when we are old and gray that we will look back on these as some of the best times of our lives.

In conclusion a poem or quotation is often used, I have chosen to use a short essay written by Albert Einstein, his self portrait:

> Of what is significant in one's own existence one is hardly aware, and it certainly should not bother the other fellow. What does a fish know about the water in which he swims all his life?
>
> The bitter and the sweet come from the outside, the hard from within, from one's own efforts. For the most part I do the thing which my own nature drives me to do. It is embarassing to earn so much respect and love for it. Arrows of hate have been shot at me too; but they never hit me, because somehow they belonged to another world, with which I have no connection whatsoever.
>
> I live in solitude which is painful in youth, but delicious in the years of maturity.

This short piece tells us a lot about Einstein and something about ourselves. Although it is not likely that any of our works will be as monumental as those of Einstein, let us hope that we can remain as humble about our small accomplishments.

CHAPTER 1
INTRODUCTION AND HISTORICAL DEVELOPMENT

1.1 Introduction

Thin layers of ionization are often observed in the E-region ionosphere. These layers are of high density, often higher than $10^5 cm^{-3}$, and persist for long periods, as much as an hour or more. Layer thickness is on the order of 1 to 3 km. Thin layers are most often observed in the altitude range of 100 to 120 km and remain at a nearly constant altitude though they may drift. The layers are one cause of the ionosonde signature of sporadic-E, where the trace shows a high top frequency in the E-region. The trace is flat or slanted, and may show lower frequency echos at higher altitudes. Sporadic-E has been observed and discussed by many authors (eg. Dungey, 1959; Whitehead, 1960; Axford 1963; Hunsucker and Owren, 1962.)

Ionospheric HF backscatter has been observed since 1926 (Bates, 1965), and sporadic-E has been observed since that time. Sporadic-E is a generic name for a group of different characteristic ionosonde traces. It has been defined as (Thomas and Smith, 1959): "Any abnormal E-region reflection which is characterized by one or more of the following:

1. Random time of occurrence;
2. Partial transparency;
3. Variation of penetration frequency with transmitter power as deduced from F-region reflections;
4. Uniform apparent reflection height, regardless of frequency."

During the International Geophysical Year (IGY) the various sporadic-E signatures (E_s) were classified according appearance on the ionogram. Nine standard types were identified: h (high), c (cusp), l (low), f (flat, when no regular E-layer is present), a (auroral), r (retardation), s (slant), q (equatorial), and n (not classified as any of the above). Thin ionization layers at high latitudes are primarily associated with the f type trace. However it is not possible to determine the ionospheric conditions which produce the trace from the trace type. Particle precipitation, for example, can produce any one of the characteristic traces, not just auroral.

Research on sporadic-E has followed two tracks; first a phenomenological study of the properties and incidence, and later a study of the physical mechanisms which

produce it. Sporadic-E ionization plays an important role in the propagation of HF radio waves. Much of the phenomenological study has been carried out with this practical application in mind.

Thin layers are formed by the redistribution of existing background plasma. In 1956 Dungey suggested that neutral wind shears pushing ions against the magnetic field could form a thin layer, Whitehead, Axford and others developed this further as an explanation for sporadic-E. Wind shears have been observed to produce thin ionization layers (eg. Constantinides and Bedinger, 1970), and are the broadly accepted mechanism for mid-latitude sporadic-E formation. At high latitudes, due to the large dip angle, the wind shear mechanism is not as effective as at mid latitudes. The action of high latitude electric fields has been proposed as another mechanism for layer formation (Nygren *et al.*,1984; Bristow and Watkins, 1991; Kirkwood and von Zahn, 1991).

Since the layers are of high density and persist for long periods, it was shown that they could not be composed of normal molecular ions since their recombination time is too short to allow for accumulation (Axford and Cunnold, 1965). Therefore it was concluded that the layers must be composed of long lived metallic ions. This was confirmed by experiment; metallic ions have been observed in mass spectrometer (eg. Narcisi et al., 1968) and incoherent-scatter radar measurements at mid-latitudes (Behnke and Vickrey, 1975) and high latitudes (Turunen *et al.*, 1988).

Thin ionization layers may be related to other ionospheric phenomenon. Recent observations at Arecibo have demonstrated a connection between thin ionization layers and "sudden" neutral sodium layers (Beatty et al.,1989). The Arecibo incoherent-scatter radar was used to observe a descending thin ionization layer while a lidar was used to observe the neutral sodium. As the ionization layer descended into the normal sodium layer, a thin sodium layer was observed to form. Sudden sodium layers have been observed at high latitudes as well, and some work has been done comparing ionosonde records and lidar which has shown some connection between sporadic-E and the sodium layers (von Zahn and Hansen, 1988). Some similar work was done observing neutral iron and sporadic-E (Bills and Gardner, 1990).

Another phenomenon which may be related to thin ionization layers is "enhanced aurora". Often the aurora exhibits one or more thin layers of enhanced brightness (Hallinan et al. 1985). The characteristics of these layers are in many ways similar to those of thin ionization layers: they are stable in altitude, thin, and persist for long periods. At present there is no satisfactory explanation for the brightness enhancements. Neither enhanced aurora nor sudden sodium layers is discussed further in this work.

1.2 Historical Development

The following is a compilation of some of the papers which played and important part in the development of the theory of sporadic-E. First papers concerning the wind shear theory at mid-latitudes are presented, then some discussion of the work that has been done at high latitudes. There are of course additional papers in the journals, however these are the main developments:

The first paper which led to the accepted theory for formation of mid-latitude thin ionization layers was presented by Dungey (1959). In the paper Dungey examined the equations governing the density and motion of a plasma in a magnetic field interacting with a neutral gas. He applied these equations to show that a shear in the neutral wind could lead to irregularities in the electron density. The approach is rather complicated in that he retained the time dependence of the momentum equation and the induced electric field. The results he obtained are essentially correct and served as the basis for all later work on the wind shear mechanism.

Dungey's wind shear theory was first applied to the formation of layers at mid-latitude by Whitehead and Axford. Whitehead (1960) discussed the observations of neutral wind in the 80-100 km range as measured by meteor trail motions. The observations showed: (1)The vertical component of the neutral wind is always small. (2)The horizontal wind is constant over large horizontal distances. (3)The horizontal velocity often reverses in direction over a height range of about 6km. Whitehead proceeded to derive a complicated, and probably incorrect, expression for the ion vertical velocity due to wind shears and applied it in an idealized way to obtain maximum electron density increases for different values of peak ion vertical velocity. He showed that large enhancements of the density are possible.

Later Axford (1963) also examined Dungey's wind shear mechanism. He solved the momentum and continuity equations in an approximate way and showed some numerical results for wind shears leading to enhanced layers. Although the treatment was more thorough than that of Whitehead there were still many shortcomings. For example, the collision frequency was assumed constant in altitude, also the ions were assumed to be O^+, however recombination was ignored so this assumption of ions was not significant. Axford discussed the possibility of wind shears due to gravity waves producing multiple layers. Further he suggested that layers would follow the movement of the nodal points of the waves, propagating downward.

In response to observations which were not in complete agreement with the wind shear theory, Whitehead (1965) derived the expected densities for mixtures of ions acted upon by wind shears. He contended that by considering mixtures of ions the discrepancies would disappear. He also mentioned that the electric fields would have to be considered when analyzing the observations, that simply knowing the neutral winds was not sufficient. Finally he discussed night time sporadic-E and concluded that without some source of ionization, recombination would not allow layers to form. From this he wrongly concluded that some local source of ionization was present.

The first mention of meteoric ions in connection with sporadic-E came from Axford and Cunnold (1965). In a paper, similar in content to that of Whitehead (1965), they discussed the problem of night time recombination. They discuss the possibility of the layers being composed of long lived constituents such as Fe^+, Mg^+, or Si^+.

Data from mass spectrometer measurements were presented by Narcisi et.al. (1968). The data demonstrated the presence of metallic ions in a sporadic-E layer. The mass spectrometer was carried on a rocket launched from Eglin AFB in Florida, on November 17, 1965. Thin ionization layers were detected at 89 and 93 km which were found to be composed of Fe^+, Mg^+, Ca^+, and Ni^+, listed in order of decreasing abundance. This was the first reported observation of metallic ions in sporadic-E layers.

Substantial confirmation of the wind shear theory was obtained in observation of mid-latitude sporadic-E layers in simultaneous observations of electron densities

and neutral winds. (Constantinides and Bedinger, 1970). The observations were made with a series of five rockets launched at one and one half hour intervals over a period of six hours. each rocket carried a Langmuir probe and a canister which released a vapor trail. Winds were derived from triangulation photography. Substantial agreement was found between the observations and the wind-shear theory.

The first incoherent-scatter radar observations of a thin metallic ion layer were presented in 1975 (Behnke and Vickery, 1975). High resolution data from Arecibo incoherent-scatter radar were presented demonstrating the presence of metallic ions in a sporadic-E layer. A Barker-coded double-pulse technique was used to obtain spectral information with 600 m resolution throughout the E region. A thin ionization layer was detected at roughly 100 km altitude. The layer was determined to be composed of 70% Fe^+. The authors mentioned that the first radar evidence of Fe^+ in a sporadic-E layer came from Zamlutti (1973) in his thesis research.

Also in 1975 a one-dimensional computer simulation of the ionosphere was developed and applied to the study of a mid-latitude sporadic-E layer observed by the Aladdin 1 experiment launched from Eglin AFB, on 20 November 1970 (MacLeod *et al.*, 1975). Parameters derived from the rocket data were used in the simulation and a detailed comparison was made between simulation results and the observations. The calculations supported the theory that mid-latitude sporadic-E layers are caused by wind shears redistributing metallic ions.

This was the last major development of the theory of mid-latitude sporadic-E. Later papers are mainly composed of further confirmations, or discussions of fine points. One point that should be noted is that all of the early theoretical papers discuss a steady state situation. Therefore they were examining the end state of the system. This leads to the conclusion that thin layers will only form at nodes of the ion vertical velocity profile.

At high latitudes the base of papers discussing sporadic-E is much more sparse. As mentioned above many of the papers are mainly concerned with the propagation of HF radio waves. There were some early observations connecting aurora and sporadic-E. Much later there were high resolution radar studies at EISCAT, and some theoretical discussion.

Some of the earliest high-latitude observations were simultaneous observations of all-sky camera and ionosonde from College Alaska (Hunsucker and Owren, 1962). A definite relationship was shown between the presence of aurora in the zenith and the ionosonde showing a sporadic-E trace. The ionosonde data showed several of the characteristic trace types, including auroral, retarted, slant, and flat, all in the presence of aurora. One example was presented where there was a sporadic-E layer without the presence of aurora.

Auroral E region ionization may cause ionosonde signatures which are very similar to those produced by thin ionization layers, however the altitude profile of the density is quite different. Density profiles produced by aurora typically show a large enhancement, ten to a few tens of kilometers thick (eg. Hunsucker, 1975), where as thin ionization layers are typically one to three kilometers thick. Since an ionosonde cannot give any information above a peak of a density profile, it can not yield any information about the thickness of a layer.

There were several papers produced from the Chatanika incoherent-scatter radar however thin ionization layers were not investigated. The basic altitude resolution of the system was 6km, which would smear out any thin layer. With the construction of the EISCAT system high resolution radar studies became possible at high latitudes.

The role of the electric field in the formation of thin ionization layers at high latitudes was discussed by Nygren *et al.*(1984 a.). The authors calculated the ion vertical velocity profiles generated by the perpendicular electric field. It was found that an uniform electric field directed in the N-W quadrant is capable of producing a velocity profile with a convergent null. It was also shown that a homogeneous neutral wind directed in the N-E quadrant will have the same effect. In an extension of the earlier paper, the authors discussed the formation of layers consisting of two different metallic ion species (Nygren *et al.*, 1984 b.). They demonstrated that under certain conditions the ions will form two separate layers with separation of a few km.

The first incoherent-scatter radar observations of high latitude thin ionization layers were presented by Turunen *et al.* (1985). A thin layer was observed for period of a few minutes immediately prior to an auroral arc entering the beam. The altitude resolution was 450 m. The layer was at 105 km altitude, and was

roughly 2 km thick. Simultaneous STARE radar data was presented which gave electric fields in the region. From this data they suggested that the observed layer was created by the action of the electric field.

This is the extent of the work that has been done towards an understanding of the formation and characteristics of thin ionization layers at high latitudes. There have been some additional observations of thin layers from EISCAT, but no firm conclusions may be drawn as to the formation mechanism. The motivation for the present work is to further develop our understanding of thin layers at high latitudes and to investigate the formation mechanism.

This work is organized in four main sections. First Incoherent-Scatter Radar (ISR) is discussed. ISR is the single most powerful tool available for observation of processes in the ionosphere. Many ionospheric parameters may be derived from the measurements. The discussion presents the theory behind ISR and the basic techniques. Also since the thin ionization layers are thin, specialized high resolution observation techniques are required. These techniques are also discussed. Next the theories of layer formation are discussed. Since the layers are formed by redistribution of the ambient plasma, the transport equations are discussed in detail. Both the wind shear and electric field mechanisms are examined. Next the source and morphology of metallic ions are discussed. The high latitude electric field is then examined, discussing measurement techniques and the average convection patterns. Finally two phenomena are discussed which are related to the thin layers; polarization electric field, and enhancements of conductivity. The third section presents a numerical computer simulation of the formation of thin layers. The details of the simulation are discussed then results are presented from a one dimensional study and a three dimensional model of the polar cap ionosphere. The electric field mechanism of layer formation is examined in detail. Finally the fourth section presents ISR data from observations at three different periods within a year. Thin layers were observed on the majority of nights of observations. The observations determined the electron density profiles, the ion mass within the layers, the electric fields, and the latitudinal distributions of the layers near Sondrestrom, Greenland.

CHAPTER 2
INCOHERENT-SCATTER RADAR

2.1 Introduction

Incoherent-Scatter Radar (ISR) is an experimental technique for determining various parameters of the ionospheric plasma. High power pulses of radio frequency energy are transmitted and the reflections from the ionosphere are received. The information obtained directly is the return power as a function of range and the power spectrum at each range. From this information several parameters of the ionosphere may be obtained. Some of these are: electron density profile, electron and ion temperatures, ion-neutral collision frequency, and ion drift velocity. These parameters are derived from the return signals and the theory of incoherent-scatter from the ionospheric plasma coupled with some assumptions about the scattering medium.

This chapter discusses the radar techniques for obtaining the information, discussing basic radar concepts, incoherent-scatter theory, techniques for gaining range resolution, and finally specific experiments.

2.2 Radar Equation

In a pulsed radar system, a pulse of duration τ_p and peak power P_t is transmitted and a portion scattered from the ionosphere is received by the antenna. The scattered power at the terminals of the receiver is given by the radar equation (Evans, 1969):

$$P_s = \frac{P_t A(0) L c \tau_p}{16\pi} \frac{N\sigma}{R^2} \tag{2.1}$$

Where $A(0)$ is the antenna's effective on-axis aperture, L is a loss factor which allows for items such as ohmic losses in transmission lines, and taper to antenna illumination etc., N is the electron density, σ is the scattering cross section of an electron, and R is the range to the scattering volume. The cross section is described by incoherent-scatter theory and is a function of the plasma parameters. For a given radar system several of these variables remain fixed and it is convenient to combine

those fixed parameters in to a single parameter C_s called the system constant. The radar equation then becomes:

$$P_s = \frac{C_s P_t \tau_p}{R^2} N\sigma \tag{2.2}$$

This simple relationship may be used to determine the electron density as a function of range from measurements of the scattered power. However use of this expression, where σ is the Thomson cross-section of the electron, is only valid when the radar wavelength is much shorter than the plasma Debye length, and scattering is from free electrons. By contrast for typical ionospheric conditions the radar wavelengths used are longer than the Debye length. For this latter situation collective effects must be considered and a modified form of the cross-section must be used; the form is discussed later in the section on incoherent-scatter theory.

2.3 Scattering

As the radar signal propagates through the ionosphere the wave fields exert a force on the ions and electrons there by accelerating them. The accelerated charges reradiate at the frequency of the wave field doppler shifted by the particle velocity. The acceleration is given by:

$$\frac{dv}{dt} = \frac{eE}{m} e^{i\omega t} \tag{2.3}$$

Since the ion mass is greater than that of the electron the electrons are accelerated more, and thus the scattering is mainly from the electrons. In the early incoherent-scatter experiments it was found that the return signal spectrum was much narrower than would be obtained if the scattering was from free electrons and it was concluded that electron-ion collective effects must be included in the analysis. One approach to finding the correct theory is to consider the ionosphere to be a continuous medium with a dielectric constant ϵ_0 with fluctuations $\delta\epsilon$, and to consider the scattering to arise from the fluctuations (Dougherty and Farley, 1960). If the volume filled by the antenna beam is much larger than the radar wavelength cubed, and the scattering is very small, then we may use a perturbative method, the Born approximation, to describe the scattering (eg. Jackson, 1975 pg.421). In

a region away from the scattering region the electric displacement may be written as:

$$\vec{D} = \vec{D}_0 + \vec{A}_{sc}\frac{e^{ikr}}{r} \tag{2.4}$$

where $\vec{D}_0$ is incident wave displacement and $\vec{A}_{sc}$ is the scattering amplitude:

$$\vec{A}_{sc} = \frac{1}{4\pi}\int e^{i\vec{k}\cdot\vec{x}}(\vec{k}\times(\vec{D}-\epsilon_0\vec{E})\times\vec{k} - \frac{\epsilon\omega}{c}\vec{k}\times(\vec{B}-\mu_0\vec{H}))d^3x \tag{2.5}$$

where the integration is over the scattering volume. Note that $\vec{D} \neq \epsilon_0\vec{E}$ and $\vec{B} \neq \mu_0\vec{H}$ within the scattering volume. We assume that ϵ and μ may be written as background quantities (ϵ_0, μ_0) with small spatially dependent fluctuations $(\delta\epsilon(x), \delta\mu(x))$. We have an integral relation for $\vec{D}$; to solve this we use the *first Born approximation*:

$$\vec{D} = [\epsilon_0 + \delta\epsilon(x)]\vec{E} \tag{2.6}$$

$$\vec{B} = [\mu_0 + \delta\mu(x)]\vec{H} \tag{2.7}$$

where $\delta\epsilon << \epsilon_0$ and $\delta\mu << \mu_0$, then to lowest order:

$$\vec{D} - \epsilon_0\vec{E} \approx \frac{\delta\epsilon}{\epsilon_0}\vec{D}_0 \tag{2.8}$$

$$\vec{B} - \mu_0\vec{H} \approx \frac{\delta\mu}{\mu_0}\vec{B}_0 \tag{2.9}$$

It can be shown that the contribution of the magnetic term is much smaller than that of the electric term (Budden, 1985) so we may write the scattering amplitude as:

$$\vec{A}_{sc} \approx \frac{1}{4\pi}\int e^{i\vec{k}\cdot\vec{x}}(\vec{k}\times\frac{\delta\epsilon(x)}{\epsilon_0}\vec{D}_0\times\vec{k})d^3x \tag{2.10}$$

$$\vec{A}_{sc} \approx \frac{1}{4\pi}(\vec{k}\times\vec{D}_0\times\vec{k})\int\frac{\delta\epsilon(x)}{\epsilon_0}e^{i\vec{k}\cdot\vec{x}}d^3x \tag{2.11}$$

or

$$\vec{A}_{sc} \propto \int\frac{\delta\epsilon(x)}{\epsilon_0}e^{i\vec{k}\cdot\vec{x}}d^3x \tag{2.12}$$

So we see that the scattering amplitude has a simple relation to the fluctuations of the dielectric constant. Now the wave vector $(\vec{k})$ here is given by the difference of the incident and reflected wave vectors:

$$\vec{k} = \vec{k}_i - \vec{k}_r \tag{2.13}$$

For back scatter the reflected wave vector is simply the negative of the incident vector so $\vec{k} = 2\vec{k}_i$, and if we express the fluctuations as the Fourier transform of the fluctuations in k-space we get the following:

$$\frac{\delta\epsilon(x)}{\epsilon_0} = \frac{1}{\sqrt{2\pi}} \int_{-\infty}^{+\infty} \frac{\delta\epsilon(k)}{\epsilon_0} e^{-i\vec{k}\cdot\vec{x}} dk \tag{2.14}$$

$$\vec{A}_{sc} \propto \int \left[\int_{-\infty}^{+\infty} \frac{\delta\epsilon(k)}{\epsilon_0} e^{i\vec{k}\cdot\vec{x}} dk \right] e^{-i2\vec{k}_i\cdot\vec{x}} d^3x \tag{2.15}$$

Changing the order of integration we get:

$$\vec{A}_{sc} \propto \int_{-\infty}^{+\infty} \left[\int e^{i\vec{k}\cdot\vec{x}} e^{-i2\vec{k}_i\cdot\vec{x}} d^3x \right] \frac{\delta\epsilon(k)}{\epsilon_0} dk \tag{2.16}$$

The volume integral of two complex exponentials over all space yields a delta function. Here the volume is considered to be much larger than the cube of the radar wavelength so the space integral is approximately:

$$\delta(\vec{k} - 2\vec{k}_i) = \int e^{i\vec{k}\cdot\vec{x}} e^{-i2\vec{k}_i\cdot\vec{x}} d^3x, \tag{2.17}$$

and

$$\vec{A}_{sc} \propto \int_{-\infty}^{+\infty} \delta(\vec{k} - 2\vec{k}_i) \frac{\delta\epsilon(k)}{\epsilon_0} dk, \tag{2.18}$$

$$\vec{A}_{sc} \propto \frac{\delta\epsilon(2k_i)}{\epsilon_0}. \tag{2.19}$$

This shows that the scattering amplitude for back-scatter is simply proportional to fluctuations of the dielectric constant with a scale size twice the wavelength of the incident radar beam. In a plasma, at frequencies above the plasma frequency, a simple expression for the dielectric constant is (eg. Nicholson 1983, pg. 137):

$$\epsilon(\omega) \approx 1 - \frac{\omega_p^2}{\omega^2}, \tag{2.20}$$

where ω_p is the plasma frequency and ω is the frequency of the incident radar pulse. For sufficiently high ω we have $\epsilon_0 \approx 1$. To find the fluctuations we can write :

$$\begin{aligned}
\delta\epsilon &= \epsilon - \epsilon_0 \\
&= (1 - \frac{\omega_p^2}{\omega^2}) - (1 - \frac{\omega_{p0}^2}{\omega^2}) \\
&= \frac{\omega_p^2 - \omega_{p0}^2}{\omega^2} \\
&= \frac{4\pi e^2}{m\omega^2}(N - N_0) \\
&= \frac{4\pi e^2}{m\omega^2}\delta N
\end{aligned} \tag{2.21}$$

That is, the fluctuations in the dielectric constant are proportional to fluctuations in the electron density. For incoherent-scatter from the ionosphere the fluctuations are naturally occuring, thermally-induced fluctuations. Although other physical conditions, such as turbulence, may yield fluctuations of the dielectric constant, the returns are clearly distinguishable in both total power and spectrum. The same scattering described here may lead to coherent scattering if the density fluctuations have some spatial coherence, such as may arise from waves.

The radar equation presented in the previous section was stated in terms of the cross section rather than the scattering amplitude. The cross section is related to the amplitude by (eg. Jackson, 1975, pg 420):

$$\sigma = \frac{|\vec{\epsilon} \cdot \vec{A}_{sc}|^2}{|\vec{D}_0|^2}, \tag{2.22}$$

where $\vec{\epsilon}$ is the polarization vector of the scattered wave. Inserting the expression for $\vec{A}_{sc}$ we get:

$$\begin{aligned}
\sigma &= \left|\vec{\epsilon} \cdot \frac{(\vec{k} \times \vec{D}_0 \times \vec{k})}{4\pi} \frac{4\pi e^2}{m} \delta N(2\vec{k}_i)\right|^2 / |\vec{D}_0|^2 \\
&= \left|\frac{k^2 e^2}{m\omega^2} \delta N(2\vec{k}_i)\right|^2 \\
&= \left(\frac{e^2}{mc^2}\right)^2 |\delta N(2\vec{k}_i)|^2 \\
&= r_e^2 |\delta N(2\vec{k}_i)|^2
\end{aligned} \tag{2.23}$$

The quantity $r_e = \frac{e^2}{mc^2}$, is the classical electron radius. It should be noted that δN is a function of time as well as wave number, and thus so is σ; it is this time dependence that is reflected in the power spectrum of the received signal. Also δN is actually the average value of the density fluctuations over the volume filled by the radar beam.

As a side note we should consider the validity of the arguments presented in this section. It was assumed that the fluctuations of the dielectric constant were small so that the perturbative method could be used. By showing that the fluctuations are proportional to the fluctuations of the electron density we have shown the assumption is justified. Any fluctuation of the electron density is countered by the Coulomb force and therefore must be small.

2.4 Incoherent-Scatter Theory

The theory of incoherent-scatter describes the spectrum of plasma density fluctuations in terms of the various parameters: ion and electron temperatures, density, and collision frequency. The spectrum has two features which were not expected in the early development of incoherent-scatter. First, the spectrum is very much narrower than expected, reflecting the thermal velocity distribution of the ions rather than the electrons. Second, the spectrum has a characteristic shape; "double humped", peaking at a finite doppler shift rather than at zero shift.

There are two methods which have been used to develop incoherent-scatter theory: an elegant macroscopic theory based on the Nyquist fluctuation and dissipation theory, the work of Dougherty and Farley (1960, 1963); and a microscopic approach based on the direct application of plasma kinetic theory, "The dressed test particle theory" (Fejer, 1960, Hagfors, 1961, Rosenbluth and Rostoker, 1962, Salpeter 1961, etc). The two theories have been shown to yield equivalent results (Evans, 1969).The theory of Doughtery and Farley is referenced most often in the literature, and the work presented later is based upon this theory, so it will be discussed in detail. However, the dressed test particle theory will briefly be discussed qualitatively since it gives a simple physical picture of the scattering process.

As was shown in the previous section the majority of scattering is from electrons, however collective effects determine the shape of the power spectrum. In a plasma

the ions and electrons are randomly distributed however there is a tendency for the electrons to form clouds around the ions. If a positive test particle is placed at rest in a plasma of uniform density, the ions and electrons redistribute so that the charge is screened. At some distance away from the charge there will be no electric field. The ions are pushed away and the electrons are attracted; at equilibrium the ion density in the area of the test charge is decreased by half the value of the test charge and the electron density is increased by the same amount. This is Debye shielding as discussed in basic texts on plasma theory. If, however, the test charge is not at rest, then the ions, because of their high inertia, cannot redistribute fast enough to participate in the screening and a larger fraction of the charge neutralization comes from the redistribution of electrons. The higher the velocity of the test charge, the more the screening will be due to the increase of electron density, and thus the larger the scattering cross section. Now, if we view each ion as a test charge as it executes random thermal motion, it generates fluctuations in the electron density; the higher the velocity the larger the fluctuation. If the ions have a maxwellian distribution there are fewer ions at high velocities and thus the cross section must decrease at high velocities. However, the cross section may peak at some doppler shift away from zero. The electrons do not act as the test particles since their inertia is so low. Thus the power spectral width mainly depends on the ion thermal velocity distribution, and the peak of the spectrum is not at zero doppler shift.

In contrast to the above discussion the method of Dougherty and Farley makes use of a generalized version of the Nyquist theorem which describes the noise fluctuations in circuit elements. The generalized theorem states that for a linear system with the application of a generalized force $V(t)$ which produces a response $I(t)$ such that the power dissipated is $V(t)I(t)$, and $V(t)$ and $I(t)$ are the real parts of $V_0e^{i\omega t}$ and $I_0e^{i\omega t}$, with $I_0 = Y(\omega)V_0$, where $Y(\omega)$ is a generalized admittance, then when the system is in thermal equilibrium and disconnected from the disturbing force, the response $I(t)$, instead of falling to zero, becomes a stochastic function of time having a spectrum:

$$|I(\omega)|^2 d\omega = \frac{1}{\pi} G(\omega) KT d\omega, \tag{2.24}$$

where $G(\omega)$ is the real part of the generalized admittance.

To apply this to a plasma we must define the terms. The response we are interested in is the displacement of electrons. To find this displacement we must examine the electrons as part of a larger linear system consisting of the ions, electrons, and electromagnetic fields. Also, forces and displacements are vector quantities, and the admittance is a second order tensor quantity. We introduce a fictitious force $\vec{F}$ acting on the electrons. We must also consider the force due to the electric field, so we may write:

$$N_0\vec{u}_e = \mathbf{Y_e} \cdot (\vec{F} - e\vec{E}) \tag{2.25}$$

To get this in the form to which the theory may be applied, $\vec{E}$ must be eliminated from the expression. To do this we must examine the behavior of the ions and the field:

$$N_0\vec{u}_i = \mathbf{Y_i} \cdot e\vec{E} \tag{2.26}$$

$$\vec{j} = N_0 e(\vec{u}_i - \vec{u}_e) \tag{2.27}$$

and

$$\vec{j} = \mathbf{\Gamma} \cdot E \tag{2.28}$$

Here $\mathbf{Y_i}$ is the admittance tensor for the ions, and $\mathbf{\Gamma}$ is the conductivity tensor. With these expressions $\vec{E}$ may be eliminated and we get:

$$N_0\vec{u}_e = \mathbf{Y'} \cdot \vec{F} \tag{2.29}$$

where:

$$\mathbf{Y'} = (\mathbf{Y_i} - \mathbf{\Gamma}/e^2)(\mathbf{Y_i} + \mathbf{Y_e} - \mathbf{\Gamma}/e^2)^{-1}\mathbf{Y_e} \tag{2.30}$$

Now, we are interested in δN so note:

$$N = N_0 + \delta N \tag{2.31}$$

$$\frac{dN}{dt} = -\nabla \cdot (N\vec{u}). \tag{2.32}$$

For a specific fourier component this yields:

$$-i\omega\delta N = -i\vec{k} \cdot (N_o\vec{u}) \tag{2.33}$$

$$|\delta N(k,\omega)|^2 = \frac{k^2}{\omega^2}|N_0\vec{u}(k,\omega)|^2; \tag{2.34}$$

so we have for the fluctuations:

$$|\delta N(k,\omega)|^2 d\omega = \frac{KTk^2}{\pi\omega^2} R[\mathbf{Y}'(\omega)]d\omega. \tag{2.35}$$

The problem reduces to finding the generalized admittance tensor. The derivation is presented in the appendix of Doughtery and Farley (1960) for the simplest case, with no magnetic field, equal electron and ion temperatures, and neglecting collisions. The derivation examines the distribution functions by applying the fictitious force in the Vlasov equation. Here the results are quoted directly. $\mathbf{Y}$ may be normalized to:

$$\mathbf{Y_s} = \frac{N_0\omega}{KT_sk^2}\mathbf{y_s} \tag{2.36}$$

and, in a coordinate system chosen such that $\vec{k} = (0,0,k)$, $\mathbf{y_s}$ is diagonal and all that is needed is the $\{zz\}$ component which may be written as:

$$y_{zz} = \frac{i + (\theta - i\psi)J}{1 - \psi J}, \tag{2.37}$$

where J is the normalized Gordeyev integral:

$$J = \int_0^\infty exp[-i(\theta - i\psi)t' - \phi^{-2}sin^2(\alpha)sin^2(\tfrac{1}{2}\phi t') - \tfrac{1}{4}t'^2cos^2(\alpha)]dt' \tag{2.38}$$

$$\theta = \left(\frac{\omega}{k}\right)\left(\frac{m}{2KT}\right)^{1/2}, \tag{2.39}$$

$$\phi = \left(\frac{\Omega}{k}\right)\left(\frac{m}{2KT}\right)^{1/2}, \tag{2.40}$$

$$\psi = \left(\frac{\nu}{k}\right)\left(\frac{m}{2KT}\right)^{1/2}, \tag{2.41}$$

and α is the angle between the radar beam and the magnetic field. The $\{zz\}$ component of the conductivity tensor is simply $\Gamma_{zz} = \frac{i\omega}{4\pi}$, with this the cross-section may be written as:

$$\sigma(\omega)d\omega = \frac{r_e^2 N_0}{\pi\omega} Re[\mathbf{y}'_{zz}]d\omega \tag{2.42}$$

$$Re[y'_{zz}] = \frac{|y_{zze}|^2 Re[y_{zzi}] + |\mu y_{zzi} + ik^2\lambda_D^2|^2 Re[y_{zze}]}{|y_{zze} + \mu y_{zzi} + ik^2\lambda_D^2|^2} \tag{2.43}$$

where μ is the temperature ratio T_e/T_i, and λ_D is the electron Debye length.

The spectrum depends on several parameters: number density, electron and ion temperatures, ion mass, and the ion-neutral collision frequency. It is interesting to note that some of the parameters only appear in ratios, such as the ion temperature to mass ratio. Thus it is not possible to determine the two parameters independently. In order to determine one of these quantities the other must be known or assumed. Most often an average ion mass profile is assumed and the temperatures are then determined. In the upper ionosphere, above about 200km altitude, it is assumed that the ions are mainly O^+, while in the lower ionosphere a mixture of O_2^+ and NO^+ is assumed. Figure 2.1 is a plot of the cross section as a function of frequency and altitude for typical ionospheric parameters. The figure shows the spectrum is, in general, narrower at lower altitudes and broadens at higher altitudes. The width of the spectrum is mainly influenced by the ion temperature and the ion-neutral collision frequency, a low temperature gives a narrower velocity distribution, as does a high collision frequency.

The total scattering cross section for a single electron is the integral of the differential cross section over all frequencies, Dougherty and Farley give this as:

$$\sigma_{tot} = r_e^2 \left[\frac{k^2\lambda_D^2}{1 + k^2\lambda_D^2} + \frac{1}{(1 + k^2\lambda_d^2)(1 + T_e/T_i + k^2\lambda_D^2)} \right] \tag{2.44}$$

When the radar wavelength is much greater than the Debye length ($k^2\lambda_d^2 << 1$) and the ion and electron temperatures are equal, the quantity in the brackets reduces to $\frac{1}{2}$. Thus the scattering is half that predicted by the Thomson scatter from free electrons with radius r_e. In most applications the wavelength is much greater than the Debye length but the two temperatures are not equal so the number densities derived from the simple theory must be corrected by the factor $(1 + T_e/T_i)$.

2.5 Parameter Estimation

As discussed in the previous section the spectrum of the radar return contains information about the plasma parameters, viz. ion and electron temperatures, and electron density. The Doppler shift of the spectrum is a measure of the mean ion motion along the line of sight of the radar. To extract this information an estimate of the power spectrum is obtained and a theoretical spectrum is fitted to the estimated spectrum. Often the auto-correlation function (ACF), which is

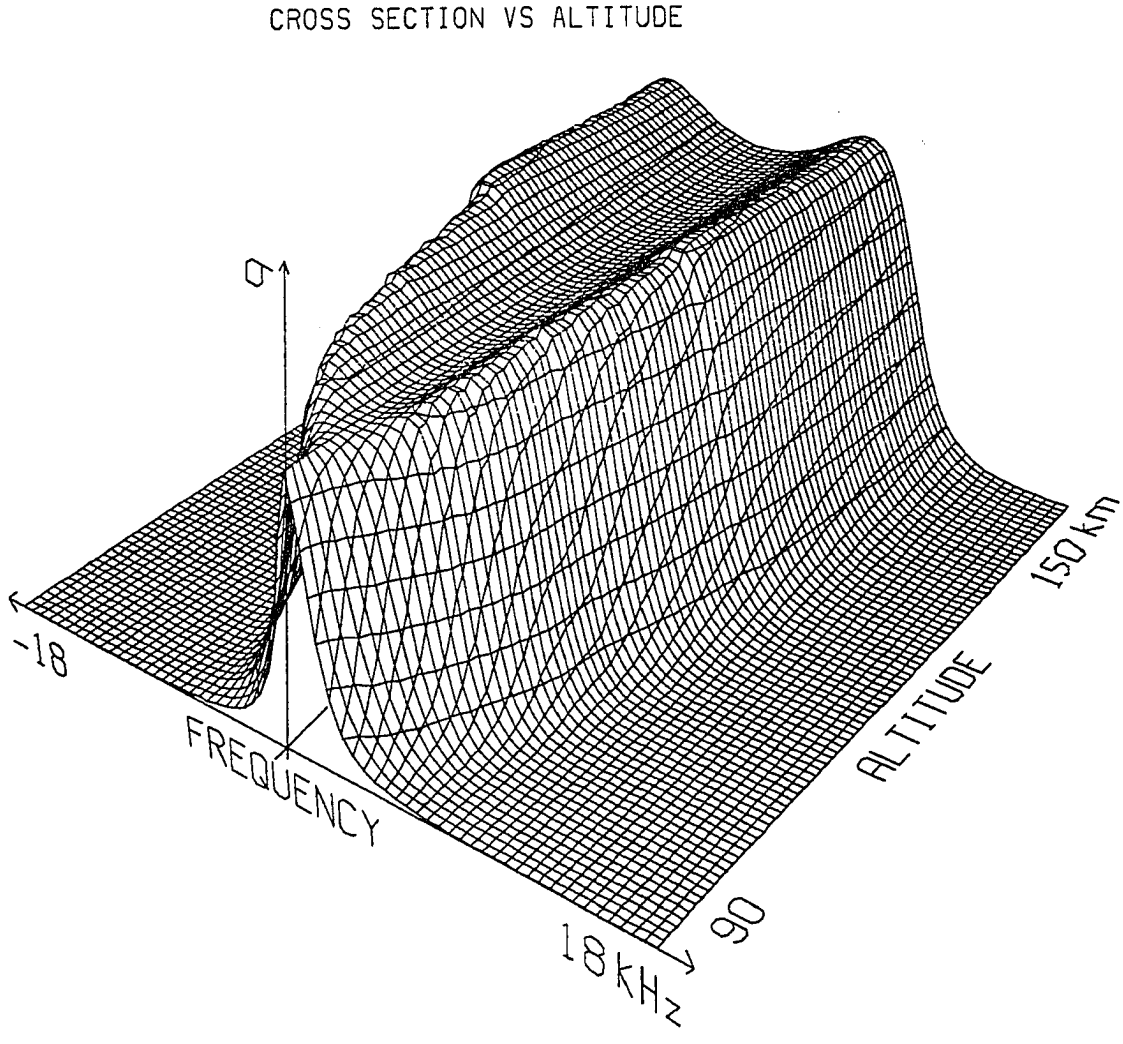

Fig. 2.1. Incoherent-Scatter cross section as a function of frequency and range for the altitude region 90 to 150 km.

the Fourier transform of the power spectrum, is measured instead of the spectrum. Assuming the density fluctuations are random, the returns may be represented by a Gaussian random variable. In addition, there is measurement noise, which also may be represented as a Gaussian random variable. Using the theory of incoherent-scatter, one fits a set of parameters to the measured spectrum or ACF by a nonlinear least squares procedure. An estimate of the values of the various parameters is obtained, however there is some uncertainty in the estimates. Although the actual values of the parameters are not random variables, the estimates of them are, and as such, have associated probability distributions and variances. From a knowledge of the variances of the data an estimate of the variances of the parameters may be obtained. In a recent paper Vallinkoski (Vallinkoski, 1988) demonstrated the application of standard statistical techniques to estimate the errors in incoherent-scatter measurements. In this section some of those results will be discussed.

The measurement is described by a random variable, the vector $\vec{m}$ where the elements of $\vec{m}$ are the data points, either the ACF at certain lags or the spectrum at various frequencies. It may be expressed as:

$$\vec{m} = \vec{f}(\vec{x}) + \vec{\epsilon} \tag{2.45}$$

where $\vec{f}(x)$ is the theoretical spectrum or ACF, $\vec{x}$ is the parameter vector, and $\vec{\epsilon}$ represents the error. The probability density function for the measurements is assumed to be the multivariate normal distribution:

$$D(m|x) = \frac{1}{(2\pi)^{M/2}|\Sigma|^{1/2}} \exp\{-\frac{1}{2}[\vec{m} - \vec{f}(x)]^T \Sigma^{-1} [\vec{m} - \vec{f}(x)]\}, \tag{2.46}$$

where M is the number of data points, and $\Sigma = E(\epsilon\epsilon^T)$ is the error covariance matrix. To obtain an estimate of the parameters we choose to maximize $D(m|x)$. The problem may be expressed as minimizing the following:

$$S(x) = [\vec{m} - \vec{f}(x)]^T \Sigma^{-1} [\vec{m} - \vec{f}(x)]. \tag{2.47}$$

Minimizing $S(x)$ gives the "maximum likelihood estimate" of the parameters x. If the errors in the various lags are not correlated, Σ is diagonal and the problem reduces to the standard least squares problem.

To estimate the errors the function $f(x)$ is expanded about the maximum likelihood point, x_0, and $S(x)$ is linearized:

$$\vec{m} = \vec{f}(x_0) + \mathbf{A} \cdot (\vec{x} - \vec{x}_0) + \vec{\epsilon} \tag{2.48}$$

where the columns A_i of $\mathbf{A}$ are :

$$A_i = \frac{\partial f}{\partial x_i}. \tag{2.49}$$

With this a matrix $\mathbf{Q}$ is defined as:

$$\mathbf{Q} = \mathbf{A}^T \mathbf{\Sigma}^{-1} \mathbf{A} \tag{2.50}$$

And the measurement errors are given by the diagonal of the inverse of $\mathbf{Q}$; $\sigma_k^2 = (\mathbf{Q}^{-1})_{kk}$.

The results presented here give some guidelines for experiment design. For a certain degree of accuracy in the measurement of the parameters, this theory gives allowable levels of measurement error. In a later section measurement error will be discussed in more detail; the error will be shown to depend on the signal strength, the noise power and the integration time. With the theory presented here the required integration time may be determined for a certain accuracy in the parameter estimates.

2.6 Radar Techniques

In the previous discussion the radar equation and description of the scattering process were presented without mention of the radar signal or system. This discussion was idealized and made no mention of such topics as range and frequency resolution. This section presents these topics, and discusses how they affect incoherent-scatter experiments.

To discuss radar techniques first we must examine the radar signal in more detail. The typical pulsed radar transmit signal is a pulse of finite duration at the carrier frequency which may be modulated. We can describe the signal as $s(t) = b(t)e^{i\omega_0 t}$ where ω_0 is the carrier frequency, and $b(t)$ describes the shape of the pulse envelope, including any phase information. A typical form for $b(t)$ is a square pulse with periodic 180° phase changes. The signal at the terminals of

the receiver (that is, the signal before it has passed through any filters, mixers, gain, etc.) is the scatter from the ionosphere, the scattering cross section of which was described earlier. The signal scattered from a discrete target moving with a finite velocity is a replica of the transmit signal with its amplitude multiplied by the target's scattering cross section and its frequency doppler shifted in correspondence with the target velocity. In the previous sections the cross section was described as a function of frequency. If we describe the cross section of the medium as a function of doppler velocity ($\sigma = \sigma(v)$) then, at the terminals of the receiver, the signal scattered from a single scattering volume is the sum of the scattering from each velocity component:

$$s(t) = \int_{-\infty}^{+\infty} b(t-t')e^{i\omega(t-t')}\sigma(v)dv \tag{2.51}$$

where t' is the time delay from transmission to reception and is given by:

$$\begin{aligned} t' &= \frac{2R(t)}{c} \\ &= \frac{2(R+vt)}{c} \end{aligned} \tag{2.52}$$

R is the nominal range to the scattering volume, so:

$$s(t) = \int_{-\infty}^{+\infty} b(t-\frac{2(R+vt)}{c})e^{i\omega_0(t-\frac{2(R+vt)}{c})}\sigma(v)dv \tag{2.53}$$

This is the received signal from a single scattering volume, ie. a single range gate of the ionosphere. To get the actual signal we must integrate over range as well:

$$s(t) = \int_0^{\infty}\int_{-\infty}^{+\infty} b(t-\frac{2(R+vt)}{c})e^{i\omega_0(t-\frac{2(R_0+vt)}{c})}\sigma(v)dvdR \tag{2.54}$$

Now since we have an expression for the cross section in terms of frequency note that the doppler shifted frequency for a given velocity is:

$$\omega = (1-\frac{2v}{c})\omega_0 \tag{2.55}$$

or

$$\frac{2v}{c} = \frac{\omega_0-\omega}{\omega_0} \tag{2.56}$$

where ω_0 is the radar carrier frequency, therefore:

$$s(t) = \int_0^{\infty} \int_{-\infty}^{+\infty} b((1-2v/c)t - 2R/c) e^{i(\omega t - 2\omega_0 R/c)} \sigma(\omega_0 - \omega, R) d\omega dR \qquad (2.57)$$

If $2v/c << 1$ then the envelope ($b(t)$) is not affected by the scattering and:

$$s(t) = \int_0^{\infty} \int_{-\infty}^{+\infty} b(t - 2R/c) e^{i(\omega t - 2\omega_0 R/c)} \sigma(\omega_0 - \omega, R) d\omega dR \qquad (2.58)$$

The return signal is thus the convolution in both range and frequency of the transmitted signal with the cross section of the medium. To find the spectrum of $s(t)$ one takes the fourier transform:

$$\begin{aligned} s(\Omega) &= \int_0^{\infty} \int_{-\infty}^{+\infty} \left[\int_{-\infty}^{+\infty} b(t - 2R/c) e^{i(\omega t - 2\omega_0 R/c)} e^{-i\Omega t} dt \right] \sigma(\omega_0 - \omega, R) d\omega dR \\ &= \int_0^{\infty} \int_{-\infty}^{+\infty} b(\Omega - \omega) e^{i(\Omega - \omega - \omega_0) 2R/c} \sigma(\omega_0 - \omega, R) d\omega dR \end{aligned} \qquad (2.59)$$

Again we see the that the spectrum of the return signal is the convoultion in range and frequency of the transmitted signal and the cross section of the medium.

To take this further we must examine the signal after it has passed through the receiver. It can be shown that to obtain the highest possible signal to noise ratio the receiver system response should be that of a filter matched to the return. In cases where short or coded pulses are used the filter is matched to the transmitted pulse. The impulse response of a matched filter is given by the complex conjugate of the transmitted signal. A filter with these characteristics has the same bandwidth as the transmitted pulse and thus allows all of the signal to pass while blocking noise from outside the band. Thus the signal becomes:

$$\begin{aligned} g(t) &= \int s(t') b^*(t - t') e^{-i\omega_0 t'} dt' \\ &= \int_0^{\infty} \int_{-\infty}^{+\infty} \int_{-\infty}^{+\infty} b(t' - 2R/c) b^*(t - t') e^{i((\omega - \omega_0)t' - 2\omega_0 R/c)} \sigma(\omega_0 - \omega, R) d\omega dR dt' \\ &= \int_0^{\infty} \int_{-\infty}^{+\infty} \sigma(\omega_0 - \omega, R) e^{-i2\omega_0 R/c} \chi(\omega, R) d\omega dR \end{aligned} \qquad (2.60)$$

where

$$\chi(R,\omega) = \int_{-\infty}^{+\infty} b(t' - 2R/c)b^*(t - t')e^{i(\omega-\omega_0)t'}dt' \tag{2.61}$$

is the *Ambiguity Function* of the radar system. The final signal is the two dimensional convolution of the range and spectral distribution of the medium with the system ambiguity function. Figure 2.2 is a plot of the ambiguity function for an uncoded square pulse.

This convolution behavior leads to two important results which limit the performance of a radar system. First, since there is convolution in range the range resolution (δh), ie. the distance over which the return can be considered to be from an independent layer of the ionosphere, is limited, and is equal to $c\tau_p/2$. Second, a similar result holds for the frequency resolution, and trying to improve either resolution tends to degrade the other. To obtain accurate information about the medium the ambiguity function must be much more strongly peaked than the properties of the medium. That is to say that parameter changes must occur over distances large compared to the range resolution, and the spectrum of the medium must be broad compared to that of the ambiguity function. Methods for improving range resolution are called pulse compression and will be discussed in the next section.

The ambiguity function just derived is actually the single pulse ambiguity function. In some experiments pulse trains or multiple pulses groups are used to make a single measurement. In this case b(t) is replaced by a function which for a pulse train takes the form:

$$b'(t) = \prod(t/T)b(t - np) \tag{2.62}$$

Where $\prod(t/T)$ represents a window function of length T, and $b(t - np)$ is a periodic function of period p, with the individual pulses described by $b(t)$. The range resolution is that of the short pulse. In frequency the ambiguity function now takes the form of the convolution of the spectrum of the window with that of the periodic function, $b(t - np)$, and consists of lines separated in frequency by the Pulse Repetition Frequency (PRF) divided by the number of pulses. Each line is not truly a line but rather the Fourier transform of the sample window weighted by transform of the individual pulse spectrum. The spectral resolution is thus given by the PRF and the length of time sampling. One restriction in using this method

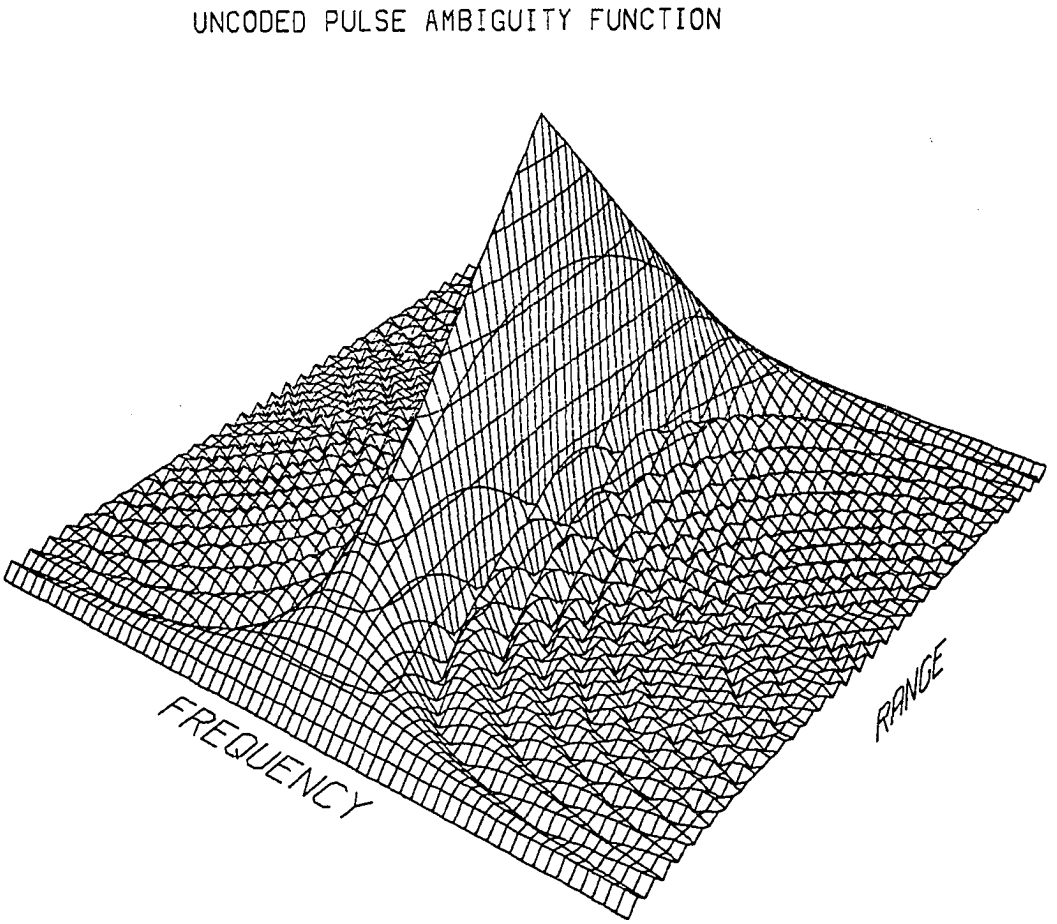

Fig. 2.2. Ambiguity function for an uncoded pulse. The range axis runs plus and minus the pulse length, and the frequency axis runs plus and minus half the number of samples times the reciprocal of the pulse length.

is that the PRF must be low enough so that the returns from one pulse subside before transmitting the next. Also it is assumed the properties of the medium remain essentially constant over the sampling period.

Another restriction on obtaining arbitrarily good range resolution is the signal to noise ratio (SNR). The signal at the terminals of the receiver consists of the scattered pulse along with noise. The noise is additive and the signal voltage may be described as:

$$v(t) = v_s(t) + v_n(t) \tag{2.63}$$

The noise is considered to be stationary and white across the bandwidth for the receiver; stationary meaning the statistical characteristics do not change with time, white meaning that the power is a constant function of frequency. The received noise power is given by:

$$P_n = kTB \tag{2.64}$$

Where k is Boltzmann's constant, T is the system temperature, and B is the bandwidth. Increasing range resolution in general means increasing the bandwidth, and thus increasing the noise power. In addition from the radar equation the received signal power is proportional to the pulse duration:

$$\delta h = \frac{c\tau_p}{2} \tag{2.65}$$

$$P_s \propto \delta h \tag{2.66}$$

$$P_n \propto B \propto 1/\delta h \tag{2.67}$$

$$P_s/Pn \propto \delta h^2 \tag{2.68}$$

The signal to noise ratio is proportional to the square of the range resolution. Thus improving range resolution, ie. decreasing δh, results in a quadratic decrease in the signal to noise ratio.

To see how the SNR affects the results of a radar experiment we must examine the statistical uncertainties. The voltage at the terminals of the receiver is the sum of two independent gaussian random variables: the component due to the scattering $v_s(t)$, and the component due to the noise $v_n(t)$. The signal is sampled

and an estimate of the power is formed for the various ranges and for a time when the signal is entirely noise.

$$\begin{aligned} < P_r > &=< (v_s + v_n)^2/R > \\ &=< \frac{v_s^2}{R} > + < \frac{v_n^2}{R} > + < \frac{v_s v_n}{R} >, \end{aligned} \tag{2.69}$$

where <> represents time averaging. Since the signal and noise are uncorrelated, the last term equals zero and we may write:

$$< P_r >=< P_s > + < P_n > \tag{2.70}$$

To find the power due to the scattering the average noise power is subtracted from the signal plus noise power.

$$< P_s >=< P_r > - < P_n > \tag{2.71}$$

To find the uncertainty in the scattered power we assume the mean of the noise is very well known, and so all of the uncertainty is that of the signal plus noise. The variance is given by:

$$\delta P_r^2 = \frac{1}{N}\sum (P_r - < P_r >)^2 \tag{2.72}$$

P_r may be written as $P_r =< P_r > (1 + \epsilon)$ where ϵ is a random variable. Then:

$$\begin{aligned} \delta P_r^2 &= \frac{1}{N} < P_r >^2 \sum \epsilon^2 \\ &=< P_r >^2 \epsilon_{rms}^2 \\ &= (< P_s > + < P_n >)^2 \epsilon_{rms}^2 \\ &=< P_s >^2 (1 + \frac{1}{SNR})^2 \epsilon_{rms}^2 \end{aligned} \tag{2.73}$$

Farley (1969) evaluated ϵ and found that for various methods of forming the estimate (ie. synchronous detection, asynchronously pumped parametric amplifier, etc.) $\epsilon = cN^{-1/2}$, where the constant is nearly equal to one and thus:

$$\delta P_s \approx \frac{< P_s >}{N^{1/2}}(1 + \frac{1}{SNR}) \tag{2.74}$$

This shows that the uncertainty in the electron density measurements is inversely proportional to the SNR, and the square root of the number of radar pulses. Thus any decrease in the SNR leads to a significant increase in the integration time required for a certain degree of accuracy. The expression also shows that for SNR greater than one there is little improvement in integration time for improvement in SNR.

2.7 Description of Basic Experiments

Long pulse– Figure 2.3 illustrates the long pulse experiment. The figure is a range-time diagram which illustrates the altitude range sampled by a pulse transmitted at time $t = 0$ and received at time $t = \tau_d + n\tau_s$ (τ_s is the sample spacing). A single long pulse of duration τ_p is transmitted, such that $1/\tau$ is much less than the spectral width of the medium. The return is sampled after some delay time (τ_d). Each sample contains information from a range of altitudes, $\frac{c\tau}{2}$. All samples from the period τ_p contain information about the common range, h_0. These samples are Fourier transformed to obtain the power spectrum from the range h_0. The return may be continually sampled, and the samples grouped according to range. For the groupings to be considered independent, the groups will be separated by τ_p seconds. That is, the first sample of one group will occur τ seconds later than the first sample of the previous group. This yields a basic altitude resolution of $\delta h = \frac{c\tau}{2}$.

Multi-pulse– Figure 2.4 illustrates the multi-pulse technique. The figure is a range time diagram for two short pulses of duration τ_p separated by six τ_l (τ_l is the lag time). As stated above the length of the pulse in the long-pulse experiment must be long enough so that the spectral width is much wider than reciprocal pulse width. This is equivalent to saying that the correlation time, defined as the first zero crossing of the auto-correlation function, must be much shorter than the pulse width. In the lower ionosphere the correlation time is long and the range resolution requirements force the use of shorter pulses. In this case the long pulse method is not adequate and other methods are required, such as multi-pulse. A series of short pulses are transmitted at various multiples of the lag time (τ_l), and the return sampled at the lag spacing. In the figure two pulses are shown spaced by six τ_l. The product of the first and sixth samples give an estimate of the auto correlation function at six τ_l at the range h_0. The second and seventh sample give an estimate of the ACF at lag six τ_l at the altitude $h_0 + \frac{c\tau_l}{2}$, etc. Note that the lag spacing determines the range resolution. Also note that the first sample contains returns from the first pulse at range h_0 and from the second pulse at a lower range. The sixth sample contains return from the second pulse at range h_0 and from the

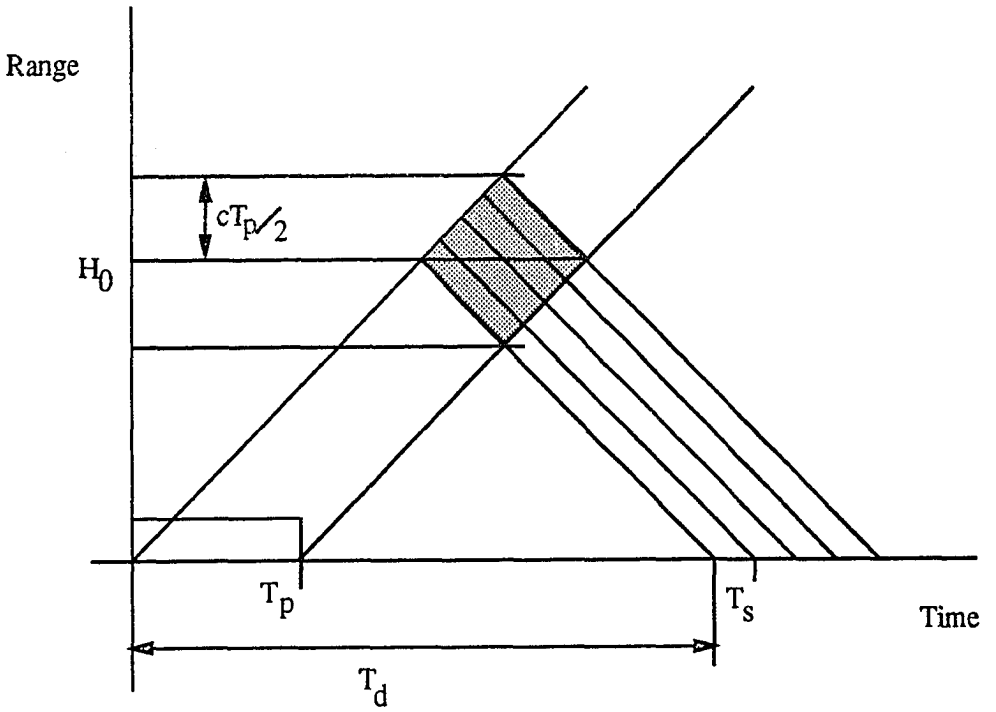

Fig. 2.3. Range-Time diagram for a single long pulse. Diagram illustrates the ranges from which signal returns are included in each sample.

first pulse at a higher range. It is assumed that the returns not from a common altitude are uncorrelated, and will average to zero over several interpulse periods. In multi-pulse experiments which have more than two pulses care must be taken so that the pulse spacings insure that no two sample pairs have contributions from a common range except for the desired range.

Velocity Vector Determination– As stated above, the Doppler shift of the power spectrum gives an estimate of the line of sight bulk plasma velocity. A typical experiment to determine the plasma velocity vector, using a monostatic radar, measures the line of sight velocity along three directions. The three velocity components are then combined to form a velocity vector. Figure 2.5 illustrates the geometry. The line of sight velocity in any direction is the projection of the velocity vector along the direction. The measured velocity may be expressed as:

$$V_1 = \vec{V} \cdot \hat{d}_1$$

where d_1 is a unit vector in direction 1. The complete measured vector is:

$$\begin{pmatrix} V_1 \\ V_2 \\ V_3 \end{pmatrix} = \begin{pmatrix} d_{1x} & d_{1y} & d_{1z} \\ d_{2x} & d_{2y} & d_{2z} \\ d_{3x} & d_{3y} & d_{3z} \end{pmatrix} \begin{pmatrix} V_x \\ V_y \\ V_z \end{pmatrix} \tag{2.75}$$

To recover the velocity vector we multiply the measured vector by the inverse of the direction matrix. This gives the velocity vector projected on the orthogonal coordinate system. This velocity vector may then be used to determine the electric field or neutral wind, depending on the altitude range.

2.8 Experimental Constraints Resulting from the Medium

Figure 2.6 shows a typical plot of the electron density profile, the spectra at various altitudes are shown in figure 2.1. The density profile shows what range resolution is required for different altitude ranges. In the lower region, 60–130 kilometers, the density changes rapidly, with significant changes taking place within a few kilometers. It is also within this region that thin layers of ionization may appear having a vertical extent of a kilometer or less. At higher altitudes the changes

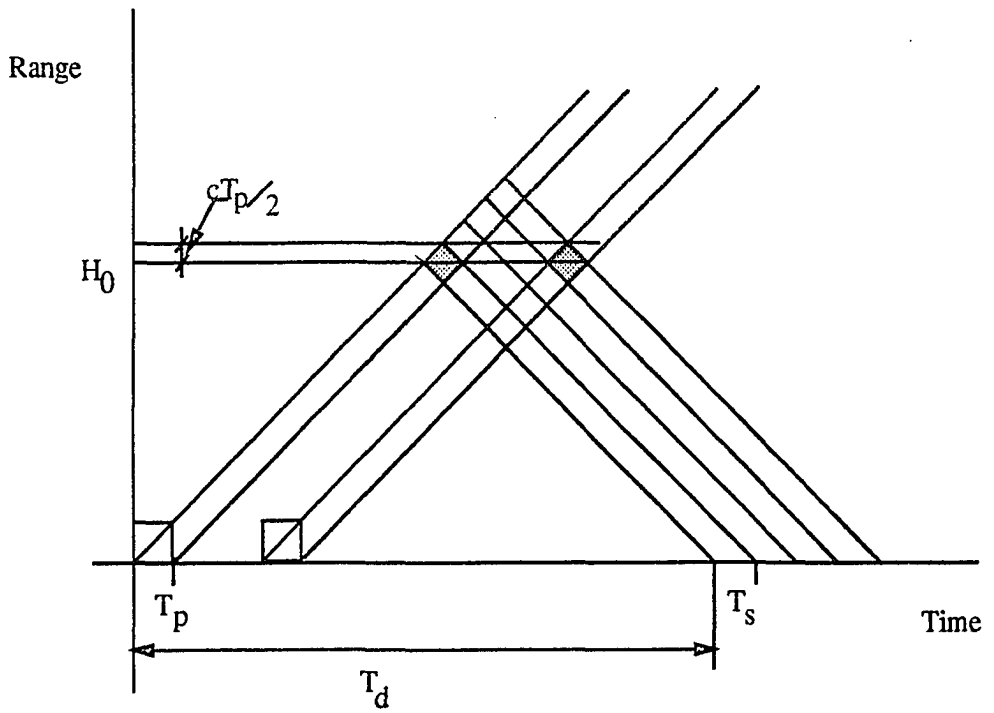

Fig. 2.4. Range-Time diagram for double-pulse experiments. Diagram illustrates the ranges from which signal returns are included in each sample.

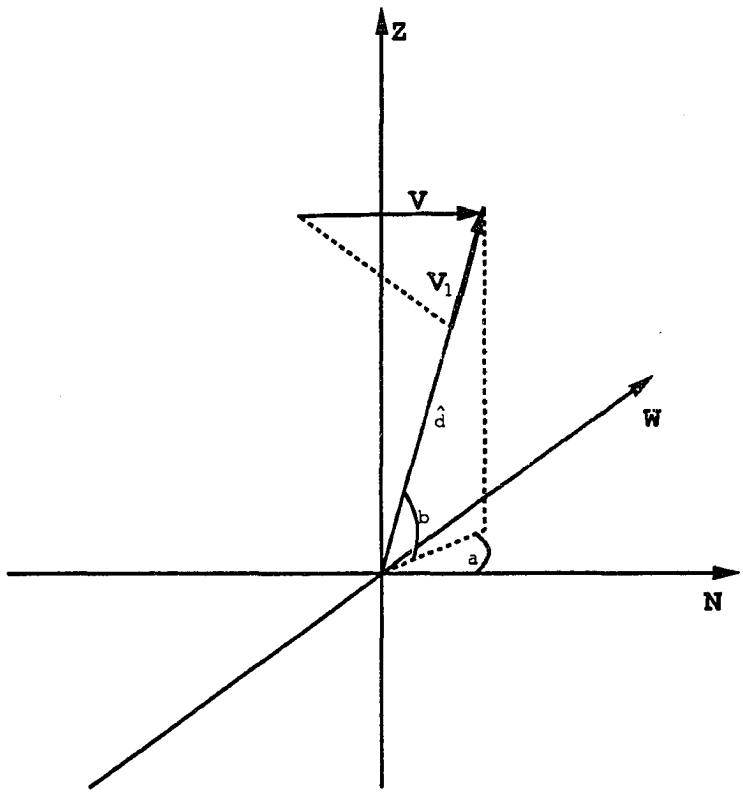

Fig. 2.5. Projection of a velocity vector along a line-of-sight. $\mathbf{V}$ represents the plasma velocity, and $\mathbf{V}_1$ is the projection along the radar look direction.

become less rapid. Above 150 kilometers range resolution of a few kilometers is sufficient; above 300 km resolution of as much as 50 km is often acceptable.

The spectra plot shows the spectral resolution requirements. In general, the spectral width is narrow in the lower ionosphere, increasing with altitude. In the lower ionosphere the spectrum is collision dominated and very narrow; below about 90 km the spectrum will typically be less than 500 Hz wide. Here the spectrum may be obtained with pulse-to-pulse methods and a Pulse Repetition Frequency (PRF) of about 1000 Hz is typically used. This PRF is quite high and leads to a difficulty in that the scatter from above 150 km will not return before the start of the new pulse, and the spectrum becomes contaminated with returns from the higher ranges. However the spectral width increases rapidly with altitude and, as such, the portion of the return from the higher ranges will have a broad spectrum; the result will appear as a raising of the noise level in the narrow spectrum of the low ranges. Above 90 km the spectrum increases in width and is generally too wide for pulse-to-pulse methods. Near 100 km the spectra are typically a few kilohertz wide and range up to more than 20 kHz wide at ranges above 250 km. A common technique for obtaining spectral measurements in the lower altitudes is the use of the multi-pulse auto-correlation method (Farley 1972). In this technique a group short pulses are transmitted within one inter-pulse period. The short pulses, of length τ are separated at integral multiples of τ. The separation of a pair of pulses in a group must be different from the separation of all other pairs in the group. The return is sampled at the lag time and the various cross products are formed. Thus an estimate of the autocorrelation function is obtained, and the power spectrum is simply the Fourier transform of the autocorrelation function. Above roughly 200 km, spectral measurements are made directly from long pulse measurements. A single long pulse is transmitted and the return is sampled at a rate high enough so that the Nyquist frequency is higher than the spectral width of the medium. At Sondrestrom a typical experiment is a 320 μsec pulse sampled at 14μsec, this gives a Nyquist of approximately 35 kHz; F-region spectra are usually less than 30 kHz wide.

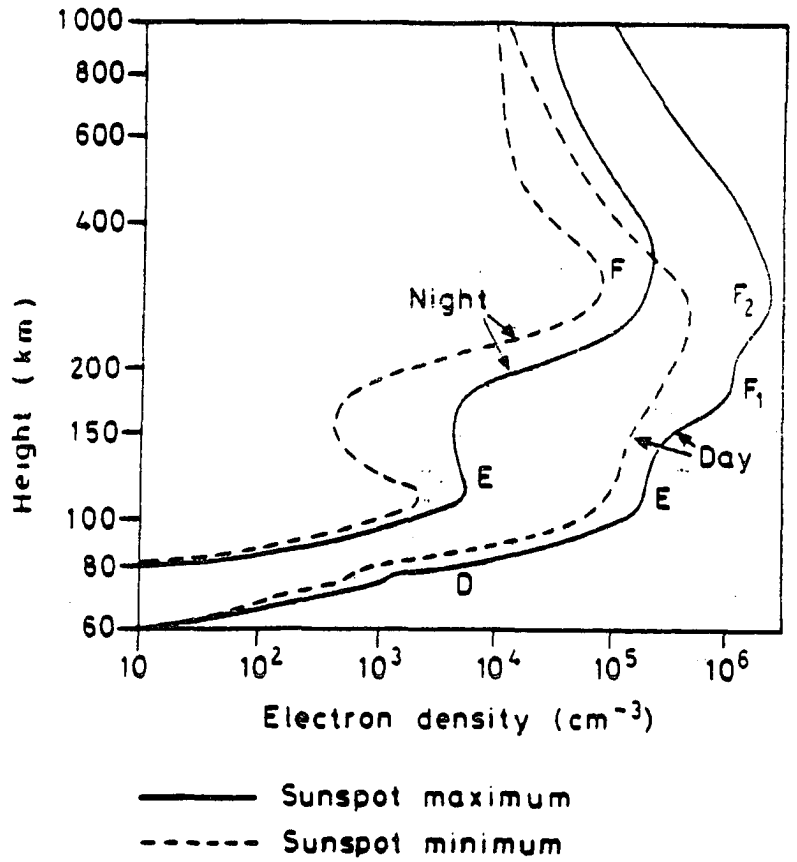

Fig. 2.6. Typical electron density profiles for mid-latitude ionosphere. Profiles are shown for day and night for both solar maximum and solar minimum conditions. Figure is from "The Upper Atmosphere and Solar Terrestrial Relations", J.K. Hargraves, Van Nostrand Reinhold, 1979.

2.9 Pulse Compression

As discussed above, after passing through the receiver system the return signal can be expressed as the convolution in range and frequency of the cross section of the medium, with the system's ambiguity function. Since the object of the experiments is to find the properties of the medium it is desirable that the cross section is easily extracted from the signal. The operation is convolution, and the signal would be an exact replica of the cross section if the ambiguity function were a two dimensional delta function. This is of course not realizable, in fact, for ordinary single pulses the width in frequency is inversely proportional to the width in range. Also, as discussed above, improving range resolution by decreasing pulse width, ie. making the pulse appear more like delta function in range, decreases the signal to noise ratio quadraticly. Pulse compression is a technique for improving the signal to noise ratio for a given range resolution. The frequency properties of compressed pulses are not in general an improvement over those of uncompressed pulses. However when used with the pulse to pulse or multi-pulse methods good range and frequency resolution may be obtained. In addition, when spectral information is not needed, density profiles may be obtained with good range resolution.

The idea behind pulse compression is to make a long pulse have the range resolution of a shorter pulse. The energy transmitted will be that of the long pulse and thus the return power is higher. The bandwidth required is that of the short pulse, and so the noise power is the same as that of the short pulse. Thus by increasing the pulse length the signal to noise ratio can be improved while maintaining good range resolution. A restriction on pulse length is that the medium must remain correlated over the pulse length; that is, the spectrum of the medium must be narrow.

Pulse compression is achieved by modulating the transmitted signal within the length of the pulse. This may be in the form of binary phase changes, step phase changes, step frequency changes, or linear frequency or phase changes. The modulation most commonly used in incoherent-scatter radar applications is binary phase changes. In such, the phase of the transmitted signal is changed at intervals equal to the pulse length of the desired range resolution. This time or "baud length" becomes the range resolution.

To find desirable forms of signals, $b(t)$, examine the single pulse ambiguity function:

$$\chi(\omega,t) = \int_{-\infty}^{+\infty} b(t'-2R/c)b^*(t-t')e^{i(\omega-\omega_0)t'}dt' \tag{2.76}$$

If the spectrum of the medium is very narrow, ie. the medium remains correlated, then an integral only has contribution for zero doppler shift and we get a function of time only:

$$\chi(t) = \int_{-\infty}^{+\infty} b(t'-2R/c)b^*(t-t')dt' \tag{2.77}$$

This is the autocorrelation function (ACF) of b(t). Thus good range resolution is obtained from signals with a strongly peaked ACF. A special class of functions that have strongly peaked ACFs are the Barker codes. Barker codes are unique in that the ACF of a code of length N has a normalized central peak and uniform sidelobes of height $1/N$. The sum of the area in the side lobes is the lowest of any code of the same length, ie. Barker codes are optimal. The longest known Barker code is 13 bauds, which has side lobes down by a little over 20 dB from the peak. Figure 2.7 shows the thirteen baud Barker code and it's autocorrelation function.

2.10 The Coded Long-pulse Technique

The pulse compression technique discussed in the previous section may lead to significant improvement in signal to noise ratio for a given range resolution requirement, and thus shortens the integration time required to make a measurement. In making spectral measurements further improvement is possible. The multipulse technique discussed earlier involves transmitting a group of short pulses, or a group of coded pulses. The spacing between the pulses is in general very short and the radar beam must remain on between the pulses, wasting power and duty cycle. The "Coded Long Pulse" (Sulzer, 1986) is a technique for making spectral measurements with good range resolution and makes full use of the available duty cycle for typical transmitters that have been used. This is a single pulse method, which uses coded pulses and temporal averaging to gain range resolution. The pulse is modulated with a pseudo random binary sequence which changes periodicly, as

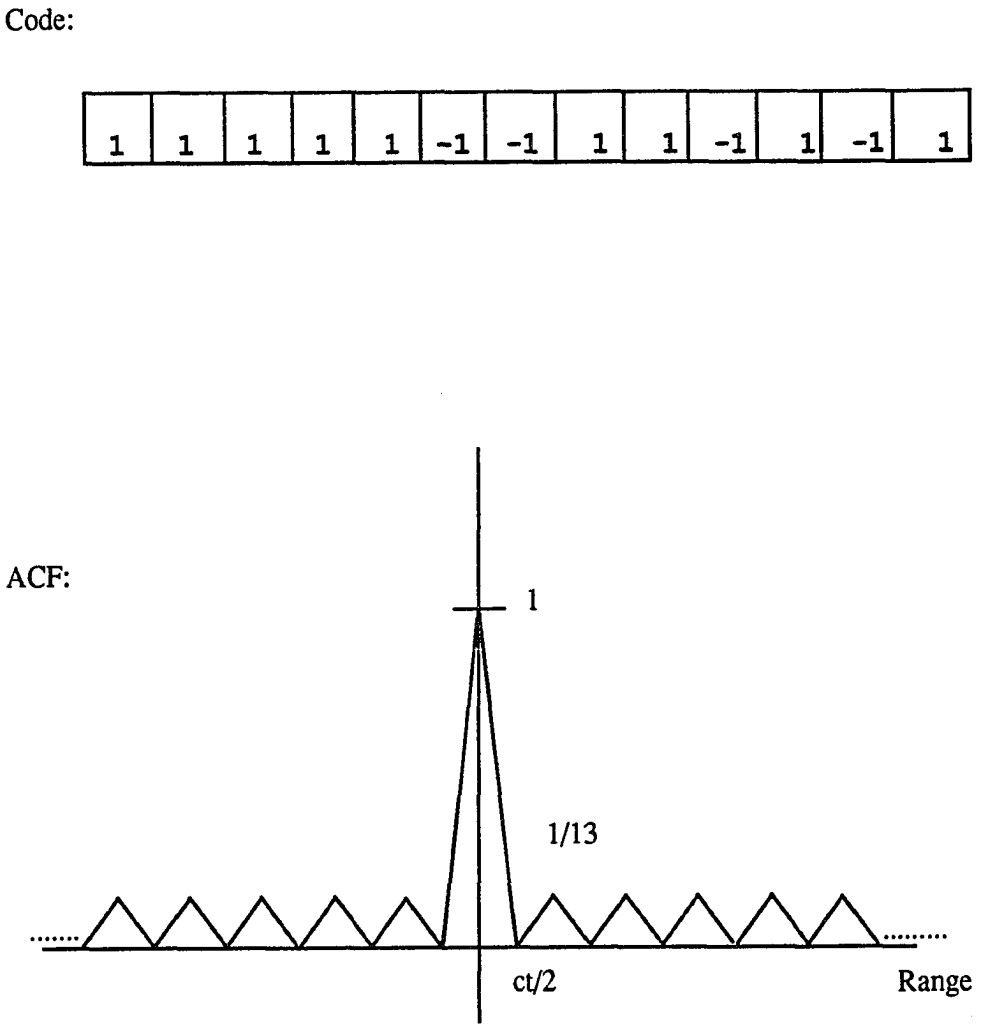

Fig. 2.7. 13 element Barker code and its auto correlation function.

often as on each pulse. The return signal is mixed down to base band and filtered to obtain:

$$s(t) = \int_0^{\infty} \int_{-\infty}^{+\infty} b(t - 2R/c) e^{i(\omega t - 2\omega_0 R/c)} \sigma(\omega_0 - \omega, R) d\omega dR \tag{2.78}$$

The base band signal is sampled at the baud rate and then multiplied by a replica of the transmitted signal shifted to align the first baud of the code with each range. An array of signals is now obtained:

$$\begin{aligned} g_k(t) &= s(t) b(t - t_k) \\ &= \left[\int_0^{\infty} \int_{-\infty}^{+\infty} b(t - 2R/c) e^{i(\omega t - 2\omega_0 R/c)} \sigma(\omega_0 - \omega, R) d\omega dR \right] b(t - t_k) \end{aligned} \tag{2.79}$$

This is Fourier transformed to obtain:

$$G_k(\Omega) = \int_0^{\infty} \int_{-\infty}^{+\infty} \left[\int_{-\infty}^{+\infty} b(t - 2R/c) b(t - t_k) e^{-i(\Omega - \omega)t} dt \right] e^{-i2\omega_0 R/c} \sigma(\omega_0 - \omega, R) d\omega dR \tag{2.80}$$

The integral over the code is once again an ambiguity function. The code is changed on each pulse and $G_k(\Omega)$ is integrated over time. The integration time is short enough that the properties of the medium remain constant so the integration only affects the ambiguity function. Although the ambiguity function of a single pulse may have no resemblance to a two dimensional delta function, the integral over several different codes will. Figure 2.8 shows ambiguity functions for a single 128 baud code and the integral over 50 different codes. As the plot shows, the integrated ambiguity function is strongly peaked; however there is a noise floor generated by the code. For a suitable code length, such as 128 baud, the central peak is significantly higher than the noise floor. This technique represents a significant improvement over multipulse techniques in spectral measurements.

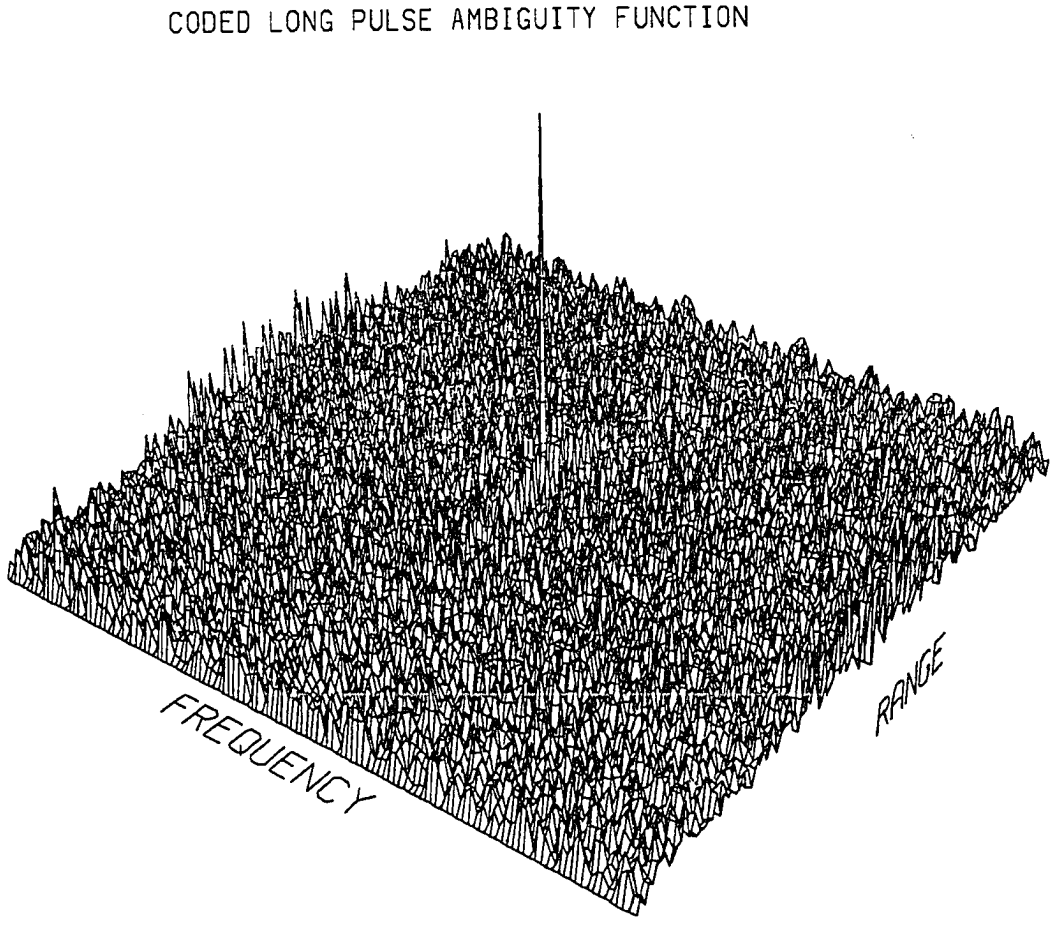

Fig. 2.8a. Ambiguity function for a single 128 baud coded-long-pulse. The range axis runs plus and minus the pulse length, and the frequency axis runs plus and minus half the number of bauds times the reciprocal of the pulse length.

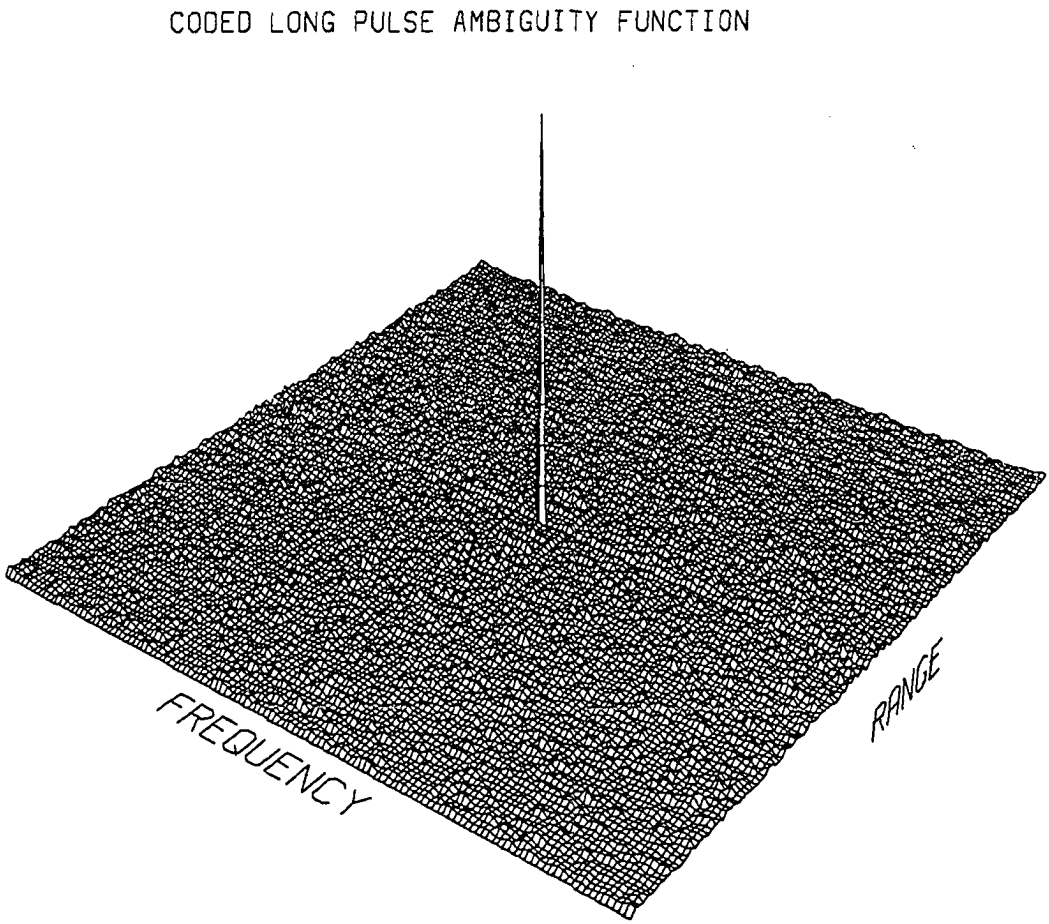

Fig. 2.8b. Ambiguity function for integration over 50, 128 baud, coded-long-pulses. The range axis runs plus and minus the pulse length, and the frequency axis runs plus and minus half the number of bauds times the reciprocal of the pulse length.

2.11 Effects of Coding Techniques on Parameter Estimation

The objective of radar experiments is to determine ionospheric parameters, with a certain height resolution, within a certain time, while maintaining a reasonable uncertainty. As discussed earlier, the uncertainty of parameter determination depends on the uncertainty of the measurements, which was shown to depend mainly on the signal to noise ratio. Each of the experimental techniques have different resolution and noise characteristics. In this section the method for determining the uncertainty will be presented, and specific high resolution experiments will be discussed.

The expression given earlier for the uncertainty in the scattered power measurements is of the same form as the expression for measuring the ACF (Farley, 1969):

$$\sigma_\rho^2 = \frac{c}{N}(1 + \frac{1}{SNR})^2 \tag{2.81}$$

where now the constant, c, may not be unity, and may depend on the lag. The SNR now may have some additional "noise" due to clutter, that is, returns from ranges other than the one of interest. The clutter may have a significant effect on the integration time required. With this expression and the results presented earlier on the estimation of the parameters, the various experiments may be examined and we may predict the integration time required to achieve a desired degree of accuracy.

Consider a multi-pulse group consisting of five pulses. At any given time the return will be composed of the return from all five pulses at various altitudes along with noise. The return may now be expressed as:

$$< P_r >=< P_s > +4* < P_0 > + < P_n > \tag{2.82}$$

where P_0 represents the return from the unwanted ranges and $< P_0 > \approx < P_s >$. In this case the uncertainty is given by:

$$\sigma_\rho^2 = \frac{c}{N}(n_p + \frac{1}{SNR})^2 \tag{2.83}$$

where n_p is the number of pulses in the multi pulse group, and SNR is the single pulse signal to noise ratio. In cases where the signal to noise ratio is small the

clutter has little effect on the integration time, however will have an effect when this is not the case.

Now consider compressed pulses using a Barker code. It can be shown that after convolution with the code the signal consists of:

$$< P_r >= n_b^2 < P_s > +(n_b - 1)* < P_0 > + < P_n > \tag{2.84}$$

where n_b is the number of bauds in the code and the uncertainty is given by

$$\sigma_\rho^2 = \frac{c}{N}(1 + \frac{1}{n_b} + \frac{1}{n_b^2} + \frac{1}{n_b SNR})^2 \tag{2.85}$$

The advantage of pulse compression now becomes obvious; there is an effective increase of the SNR by a factor of the code length.

When the coded long pulse is used, the return power is similar to the multi-pulse, however the unwanted returns are multiplied by the code:

$$< P_r >=< P_s > +(n_b - 1) < b_i b_k P_0 > + < P_n > \tag{2.86}$$

$b_i b_k$ is the product of different bauds of the code, randomly plus or minus one, which will average to zero over time. The actual value of the clutter depends on the integration time. The uncertainty is given by:

$$\begin{aligned} \sigma_\rho^2 &= \frac{c}{N}(1 + (n_b - 1)\frac{< b_i b_k P_0 >}{< P_s >} + \frac{1}{SNR})^2 \\ &\approx \frac{c}{N}(1 + (n_b - 1) < b_i b_k > + \frac{1}{SNR})^2 \end{aligned} \tag{2.87}$$

In general, the clutter can be expected to be no worse than the multi pulse measurements, in addition in the coded long pulse there are multiple estimates of each lag on every pulse, while the multi-pulse experiment gives only one estimate per inter pulse period.

Another method which is very useful is to combine pulse compression with multipulse, for example Barker coded multipulse. In this case the return power is given by:

$$< P_r >= n_b^2 < P_s > +(n_b - 1)* < P_0 > +n_b(n_p - 1) < P_0 > +n_b < P_n > \tag{2.88}$$

and the uncertainty is given by:

$$\sigma_\rho^2 = \frac{c}{N}\left(1 + \frac{n_p}{n_b} + \frac{1}{n_b^2} + \frac{1}{n_b SNR}\right)^2 \tag{2.89}$$

Thus the pulse compression not only improves the noise performance but also decreases the clutter. In cases when the SNR is very poor this technique will lead to the shortest integration times of those presented here.

For high resolution measurements the SNR is usually very poor. Figure 2.9 shows the SNR vs. electron density for 300 meter resolution with the parameters of the Sondrestrom ISR ($T_{sys} = 100$). Figure 2.10 shows the number of interpulse periods (NIPP) for a Barker coded multi-pulse to attain 50% accuracy in each lag. For electron density of 10^5, NIPP is fairly small under 2000, thus the accuracy could be attained in a few tens of seconds. As the density drops off to 10^4 the time increases greatly is NIPP is roughly 2.1×10^5. When the duty cycle is 3% this corresponds to a minimum time of 34 minutes.

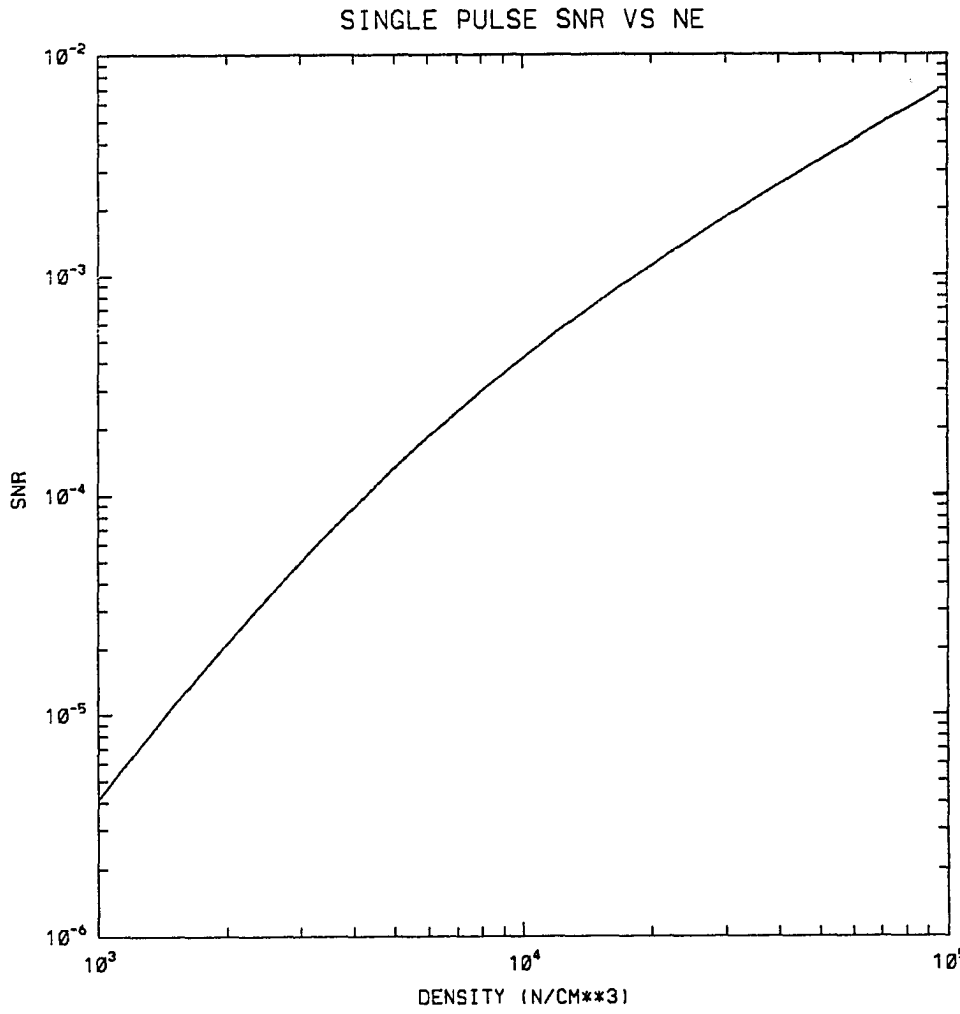

Fig. 2.9. Signal to noise ratio as a function of electron density for a single pulse. The parameters are 300m resolution, 120km range, and the system constant is for Sondrestrom.

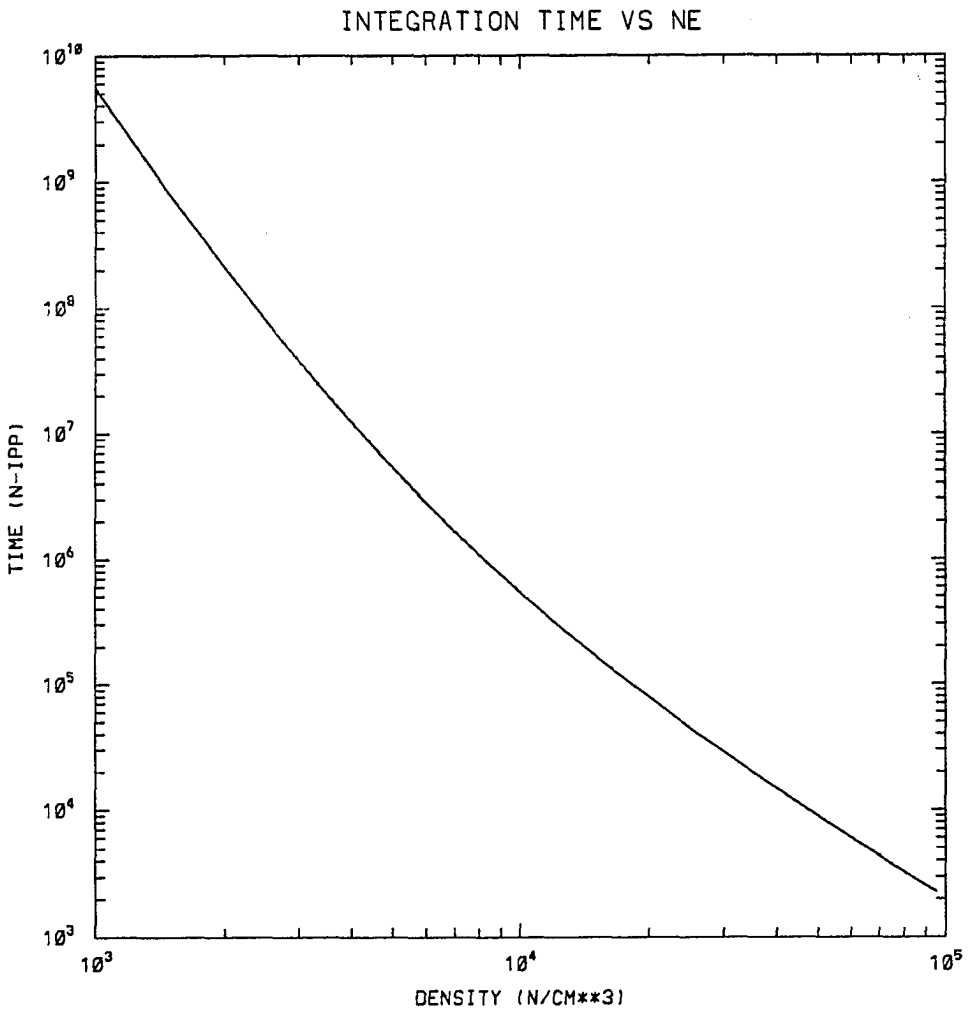

Fig. 2.10. Integration time required to obtain 50% accuracy as a function of electron density for a 13 baud, 5 pulse, Barker coded multi-pulse. The parameters are the same as for the previous figure.

CHAPTER 3
THEORY OF THIN LAYER FORMATION

3.1 Transport Equations

As discussed in the introduction thin ionization layers can be formed by the redistribution of ionization under the action of neutral winds and electric fields. To understand this mechanism we must examine the equations which govern the motion of the plasma in the ionosphere. The ionosphere is part of a complex system composed of the ionization, the earth's magnetic field and the neutral atmosphere. The plasma consists of several chemical species with densities which change with both space and time. The degree of interaction between the plasma and the neutral gas also changes with altitude. The ionized and neutral constituents interact through collisions, exchanging momentum, energy and charge. The altitude region of interest in this work, 90 to 150 km, is among the most complex because this is a transition region between the lowest part of the ionosphere, where the plasma motion is collision dominated and thus entirely controlled by the neutral gas motions, and the upper ionosphere where the motion is collisionless and thus primarily controlled by electric and magnetic fields. The densities of the various ion species in this region are governed to a large extent by chemistry. At the highest altitudes, where the plasma is mainly composed of O^+ ions, densities are controlled mainly by vertical transport, and chemistry may often be ignored. At lower altitudes other ions become dominant and the complex chemical reactions must be considered. Finally the temperatures of the ions, electrons, and neutrals all play a role in both the motions and chemistry. In this altitude region the equations for the temperatures have their most complex form. The equations which govern the density, motions, and temperatures of the ionospheric plasma are derived from the various velocity moments of the Boltzmann equation (eg. Schunk 1974), and are:

Continuity:

$$\frac{\partial n_s}{\partial t} + \nabla \cdot (n_s \vec{v}_s) = \frac{\delta n_s}{\delta t} \tag{3.1}$$

Momentum:

$$m_s\frac{D\vec{v}_s}{Dt} + \frac{1}{n_s}\nabla\cdot\mathbf{P} - m_s\vec{G} - e_s(\vec{E} + \frac{1}{c}\vec{v}_s\times\vec{B}) = \frac{\delta M_s}{\delta t} \tag{3.2}$$

Energy:

$$\frac{D_s}{Dt}(\tfrac{3}{2}P_s) + \tfrac{3}{2}P_s(\nabla\cdot\vec{v}_s) + \nabla\cdot\vec{q}_s + \mathbf{P_s}:\nabla\vec{v}_s = \frac{\delta E_s}{\delta t} \tag{3.3}$$

With the following quantities defined for species s: n_s density, T_s temperature, $\vec{v}_s$ velocity, $\mathbf{P_s}$ pressure tensor, P_s scalar pressure, and $\vec{q}$ heat flow vector. This is an open set of equations with several quantities left undefined. The method of taking moments of the Boltzmann equation will always lead to an open set, requiring some higher moment. A more complete set of equations would include two higher order equations, for the pressure tensor and heat flow. In the region of interest for this study some approximations are made which replace these higher order equations. To completely describe processes in the ionosphere these equations must be solved for each ion species, for electrons, and for the neutrals. In the following, the above equations will be examined in detail and the approximations will be discussed.

The Continuity Equation:

The continuity equation states that the rate of change of the density of species at any point is equal to the negative of the divergence of the flow plus any local production or loss. Production is mainly due to three sources: photo ionization, solar ultra violet radiation ionizing neutral particles; chemical production ie., charge exchange reactions where an ion of one species reacts with a neutral of the species being examined; and collisional ionization by energetic particle precipitation. Two additional minor sources of ionization are X-rays and Gamma rays, these short wavelength photons are mainly absorbed below 100 km.

Photoionization is the major source of ionization in the day side ionosphere. The ionization energies of the three major species are all below 16 eV. Molecular oxygen has an ionization energy of 12.08 eV which translates to a wavelength of 1026 angstroms. The solar flux is significant at these wavelengths, and so can produce ionization. The photoionization rate for a given species j at altitude z is:

$$P_z^j = n_j(z)\int_{\lambda_{th}}^{0} I_z(\lambda)\sigma_j^i(\lambda)d\lambda \tag{3.4}$$

The ionization cross sections (σ_j^i) for the major neutral species may be found in Rees (1989). The intensity of the solar radiation ($I_z(\lambda)$) at altitude z is given by the Lambert-Beer exponential absorption law:

$$I_z(\lambda) = I_\infty \exp[-\tau(\lambda)] \tag{3.5}$$

Where $\tau(\lambda)$ is the optical depth at wavelength λ. The expression for $\tau(\lambda)$ is given in Rees, it is a function of both solar zenith angle and altitude. In addition, for solar zenith angles larger than 90°, the limb of the earth blocks any solar radiation from reaching the ionosphere below a certain altitude: the shadow height.

Chemical production and loss do not change the overall level of ionization, rather they change the plasma composition. There are five major ionic species: NO^+, O_2^+ ,O^+ ,N_2^+, and N^+. The ions constantly undergo collisions with the neutral atmosphere and will often react in a charge exchange reaction. For example an N_2^+ ion may collide with an O_2 molecule yielding O_2^+ and N_2 and releasing 3.53 eV of energy. This reaction occurs at a rate given by the product of the concentrations of the reactants and a rate coefficient. Many of the rate coefficients in the ionosphere are temperature dependent.

Collisional ionization by precipitating particles is an important source of ionization on the night side at high latitudes. Energetic particles are accelerated in the magnetosphere to energies as high as 100 keV or higher and thus may penetrate to the lower ionosphere. As they pass through the atmosphere they collide with the neutrals producing ion-electron pairs, the ejected electrons may have enough energy to produce further ionization. In the work presented here this source of ionization is neglected. Although this is the major source of ionization on the night side, it is mainly concentrated in the auroral oval; it is not a constant source, occurring only intermittently in an unpredictable manner in association with geomagnetic storms and substorms. In addition it is not likely that collisional ionization plays any direct role in the formation of thin layers. The thickness of the thin ionization layers is much less than is possible from collisional ionization.

Loss of ionization takes place mainly by radiative recombination, ie. an electron and ion combine to form a neutral and release a photon. The release of the photon is required to conserve both momentum and energy. Another loss mechanism is

three body recombination, where an electron and ion collide with a third body, no photon is released and momentum and energy are conserved by the third body carrying away momentum and energy.

In solving both the continuity and momentum equations it is necessary to examine each ion species and some minor neutral species, but not the electrons or the major neutral species. Charge neutrality is a very good assumption in the ionosphere. Thus by solving for the total ion density the electron density is determined. The electrons and ions may have different velocities, yielding currents. It is not necessary to find the electron velocity to determine the currents; they may be determined from the electric field and the conductivity tensor. Since the neutral atmosphere is in hydrostatic equilibrium, momentum transfer from ions to the neutrals can have only a small effect on the neutral density profile. Also the ratio of the neutrals to ions in the E-region is on the order of 10^7, and so the chemistry does not affect the densities of the major neutral species. This is not true for some minor neutral species, such as NO. These minor neutral constituents play a major role in both the ion chemistry and the neutral energy equation.

The Momentum Equation

The momentum equation is a vector equation and must be examined component by component. The coordinate system used is a Cartesian system with $\hat{x}$ and $\hat{y}$ in the plane parallel to the earth's surface, and $\hat{z}$ upward. Although the terms of the equation have variations in the x-y plane the changes in the $\hat{z}$ direction are much more rapid. To study the momentum equation we will only consider the $\hat{z}$ variation of the terms.

First, examine the electro-magnetic term, $e_s(\vec{E}+\frac{1}{c}\vec{v}_s \times \vec{B})$. The magnetic field is the earth's magnetic field which does not exhibit significant change in the altitude range of interest. Any perturbations to the field due to ionospheric currents are small and may be ignored. The electric field is the convection electric field which maps down along the magnetic field lines from the magnetosphere. Maxwell's equations give:

$$\nabla \cdot \vec{E} = \rho \tag{3.6}$$

$$\nabla \times \vec{E} = 0 \tag{3.7}$$

By assuming plane symmetry, the curl equation shows that the $\hat{x}$ and $\hat{y}$ components of the field do not change with altitude. Thus only the $\hat{z}$ component may vary with altitude. The variations are determined by Poisson's equation. To a good approximation the ionospheric plasma is charge neutral and, although some small polarization charge may exist, the convection electric field is essentially unchanged over the altitude region of interest.

The velocity vector does change significantly over the altitude range. In the upper regions, above roughly 150 km, the velocity vector is in the $\vec{E} \times \vec{B}$ direction, while in the lowest region the velocity vector may follow the neutral wind. Figure 3.1 shows the altitude variation of the magnitude of this term for typical high latitude ionospheric parameters ($\vec{E} = 30mV/m$ directed to magnetic south, $\vec{B} = 45\mu T$, Dip = 75°).

The term $\nabla \cdot \mathbf{P}$, the divergence of the pressure, tensor may be written out as:

$$\nabla \cdot \mathbf{P} = \nabla \cdot \tau + \nabla P \tag{3.8}$$

Where τ is the stress tensor and P is the scalar pressure. The elements of the stress tensor are of the form $\tau_{ij} = c_{ij} n_s m_s (v_s - v_n)^2$. Figure 3.2 shows the magnitude of the $\hat{z}$ derivative for $c_{ij} = 1$, along with the pressure gradient. The figure shows that derivative of the scalar pressure is always the larger term and thus $\nabla \cdot \mathbf{P}$ is replaced by ∇P. This allows us to eliminate the first of the higher order equations discussed above. The pressure is assumed to be isotropic and we use the equation of state for an ideal gas: $P = nkT$. The magnitude of the pressure gradient is in general much less than that of the $\vec{E} + \vec{v} \times \vec{B}$ term however in the presence of thin layers of ionization large pressure gradients do exist and this term may be important in limiting layer thinness.

The term $\delta M/\delta t$, the momentum source term, is given by collisions with the neutral gas:

$$\frac{\delta M}{\delta t} = m_s \nu_{sn} (\vec{v}_n - \vec{v}_s) \tag{3.9}$$

where ν_{sn} is the species-neutral collision frequency. As can be seen, this is a source of momentum when the neutral velocity is greater than the species velocity, or a sink of momentum when the neutral velocity is less than the species velocity. Since the collision frequency is proportional to the neutral density, this term becomes less

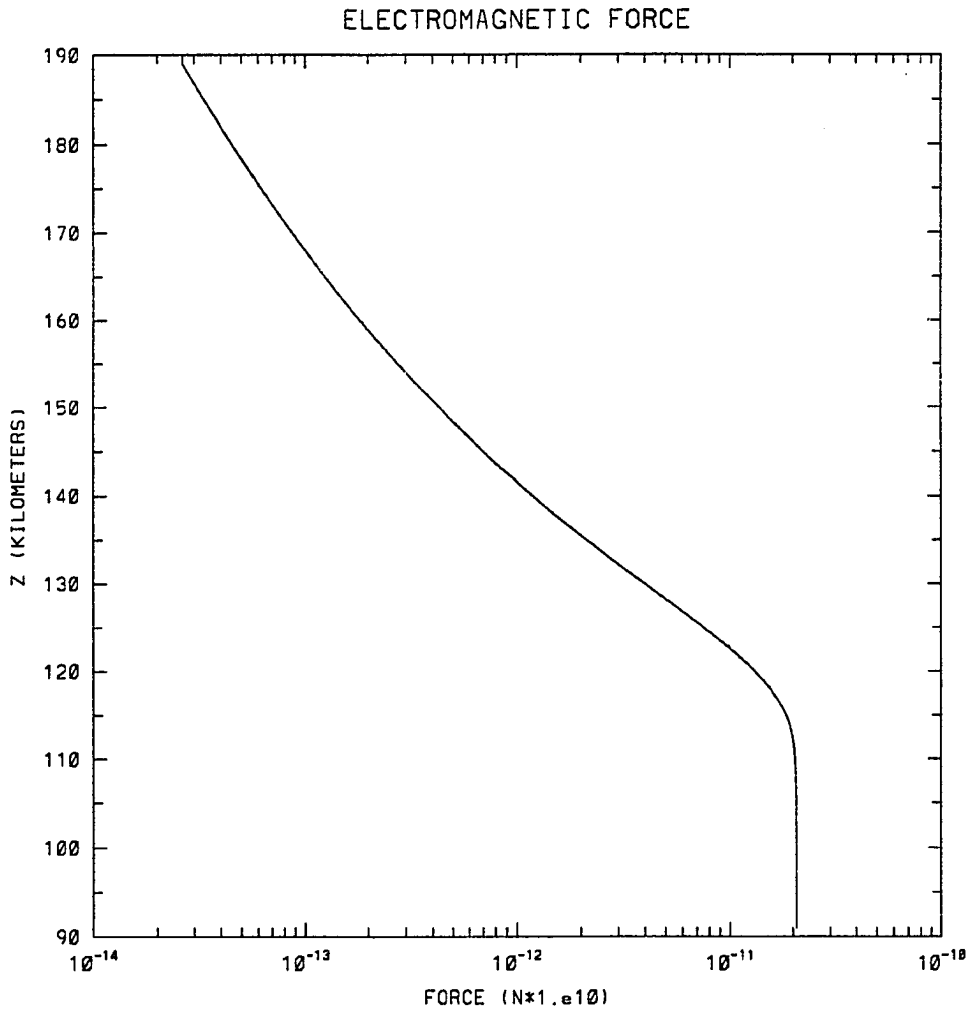

Fig. 3.1. Altitude profile of the electromagnetic source term of the momentum equation.

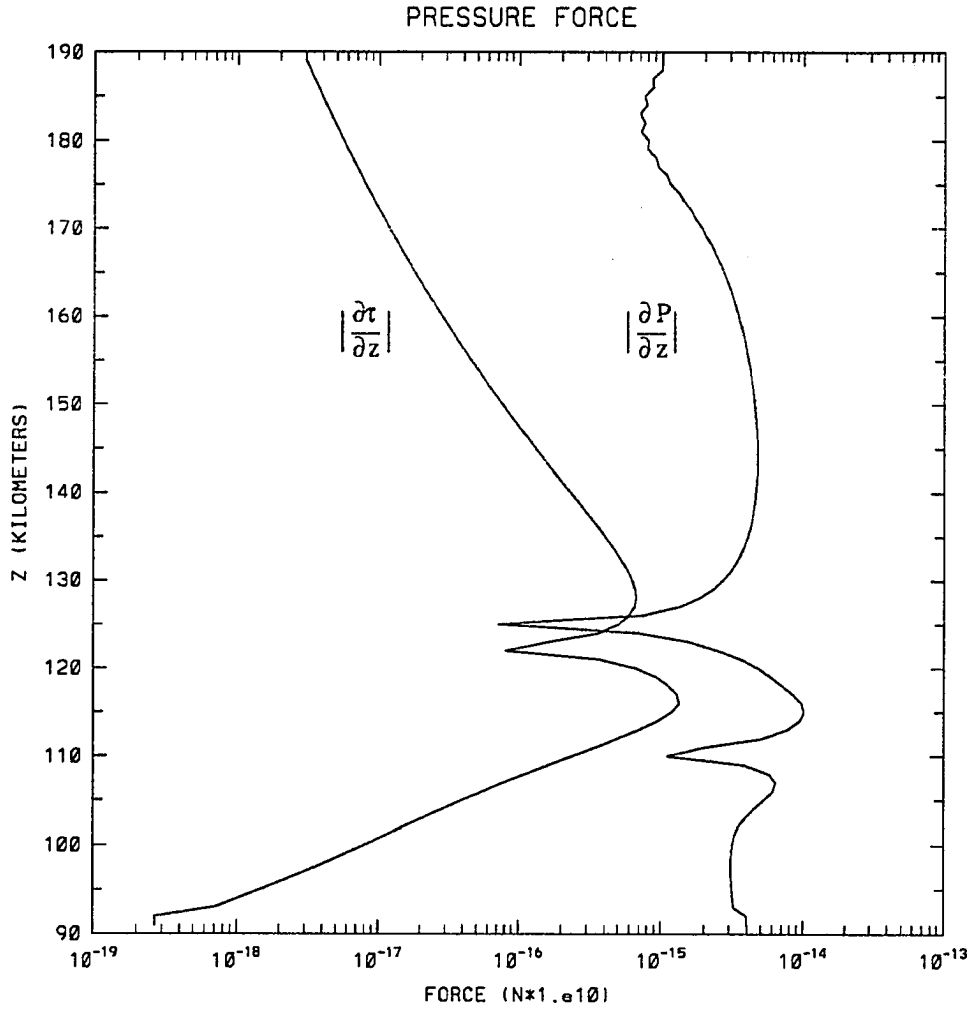

Fig. 3.2. Altitude profile of the gradient of the scalar pressure and the gradient of the first element of the stress tensor.

important with increasing altitude; figure 3.3 shows the altitude variation for typical conditions. The magnitude of this term is nearly identical to the electromagnetic force and in the absence of a pressure gradient this term precisely balances the electromagnetic term.

The magnitude of the gravitational term is about 5.0×10^{-25} newtons. This is always much less than the the other terms and will be ignored.

Finally examine the inertia term, $m_s D\vec{v}_s/Dt$. Since the time variations of the velocity vector are small (except for wave activity) this term is also small and is ignored. This leaves the following for the momentum equation:

$$0 = e_s(\vec{E} + \vec{v}_s \times \vec{B}) - m_s\nu_{sn}(\vec{v}_s - \vec{v}_n) - \tfrac{1}{n}\nabla P \tag{3.10}$$

With this we can get a formal solution for the species velocity vector:

$$\vec{v}_s = \beta^{-1}\left[e_s\vec{E} + m_s\nu_{sn}\vec{v}_n - \tfrac{1}{n}\nabla P\right] \tag{3.11}$$

where β is a matrix defined as follows:

$$\beta = \begin{pmatrix} m_s\nu_{sn} & e_sB_z & -e_sB_y \\ -e_sB_z & m_s\nu_{sn} & e_sB_x \\ e_sB_y & -e_sB_x & m_s\nu_{sn} \end{pmatrix} \tag{3.12}$$

The Energy Equation:

The reason for solving the energy equation is to obtain the species temperatures, so it is convenient to rewrite it as a differential equation for temperature. To do this, some of the terms of the equation must be better defined. As shown in the discussion of momentum, the pressure tensor may be replaced by the scalar pressure so $\mathbf{P} : \nabla\vec{v}$ is replaced by $P\nabla\cdot\vec{v}$. The heat flow vector is given by $\vec{q} = -\lambda\nabla T - \alpha\vec{J}$. In taking the divergence we get $\nabla\cdot\vec{q} = -\nabla\cdot(\lambda\nabla T) - \nabla\cdot(\alpha\vec{J})$. The second term is the divergence of the current, and since we cannot have any significant charge accumulation this term is zero and we are left with $\nabla\cdot\vec{q} = -(\nabla\lambda\cdot\nabla T + \lambda\nabla^2 T)$ where λ is the coefficient of thermal conductivity.

The energy source term is given by Schunk (Schunk, 1975)as:

$$\frac{\delta E}{\delta t} = -\frac{n_s m_s \nu_{sn}}{m_s + m_n}[3k(T_s - T_n) - m_n(\vec{v}_s - \vec{v}_n)^2]. \tag{3.13}$$

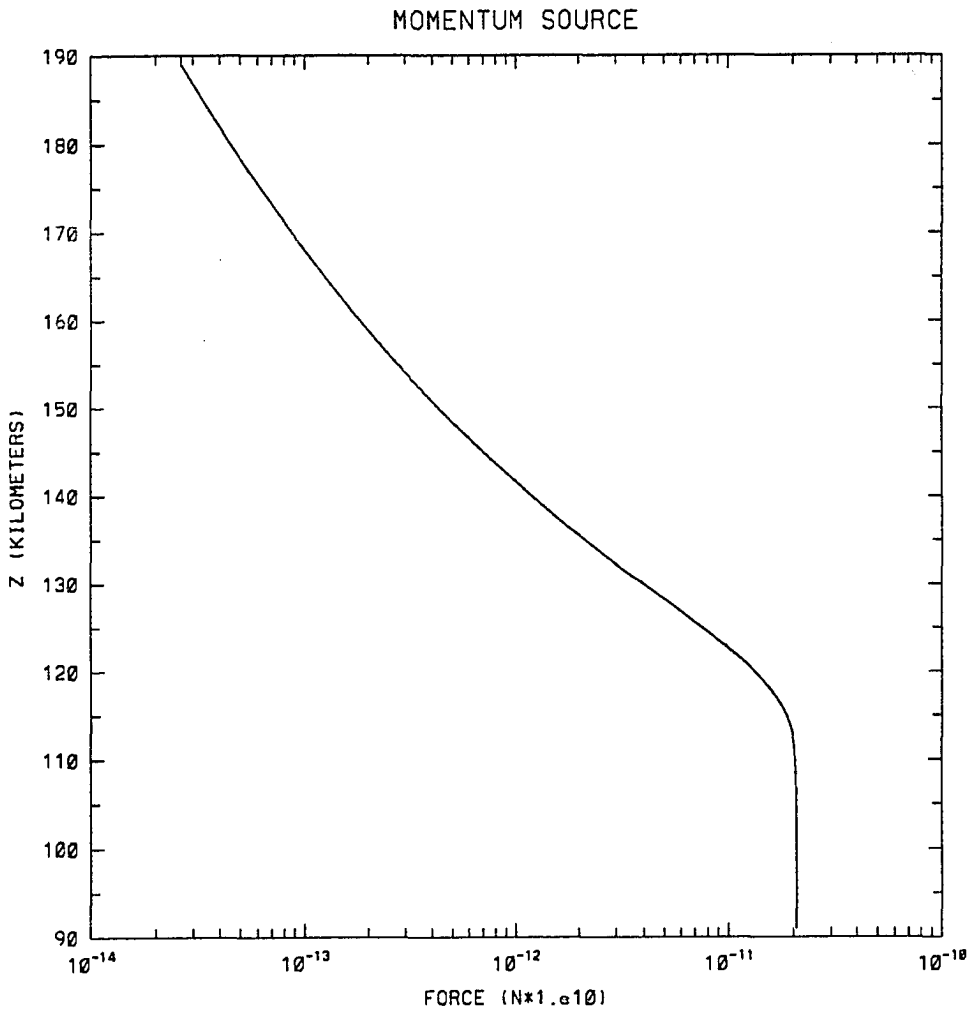

Fig. 3.3. Altitude profile of the momentum transfer source term of the momentum equation.

With these definitions the energy equation may be written as:

$$\frac{\partial T_s}{\partial t} = \frac{2\lambda}{3nk}\frac{\partial^2 T_s}{\partial z^2} + \left[\frac{2}{3nk}\frac{\partial \lambda}{\partial z} - v_z\right]\frac{\partial T_s}{\partial z} - \left[\frac{v_z}{n}\frac{\partial n}{\partial z} + \frac{1}{n}\frac{\partial n}{\partial t} + \frac{5}{3}\frac{\partial v_z}{\partial z}\right]T_s - \frac{\nu_{sn}}{3k}\left[3k(T_s - T_n) - m_n(\vec{v}_s - \vec{v}_n)^2\right] \tag{3.14}$$

In some past studies this equation has been simplified further, however all of the terms of this equation are significant so it is not simplified here.

3.2 Thin Layer Formation Theories

The first studies of thin ionization layers were undertaken to explain midlatitude sporadic-E layers. The only reasonable mechanism postulated for the formation of the thin layers was the redistribution of background ionization. In 1959 Dungey discussed the effects of a magnetic field on turbulence in an ionized gas. He illustrated that an appropriately directed shear flow in the neutral gas could lead to the formation of irregularities in the electron density. Figure 3.4 illustrates this. In the figure the dashed diagonal lines represent magnetic field lines, the curve represents the horizontal neutral wind profile. The neutral wind forces the plasma to move along the magnetic field lines and may lead to convergent flow. This convergence leads to the accumulation of ions in a thin layer. The figure shows that in the northern hemisphere, a north-directed wind at high altitudes and a south-directed wind at low altitude would be required for convergent flow. The figure is a simplification of the actual process, a shear in the east west wind may also lead to convergent flow. Accumulation of ionization at a certain altitude depends on the gradient of the ion vertical velocity. The thinness of the layer and the time for formation will depend on the steepness of the gradient. In the literature it is often assumed that to obtain layers of enhanced density the ion vertical velocity profile must have a convergent null, which is an altitude where the velocity is zero with flow up from below and down from above. It has been shown that a steep, appropriately directed, vertical gradient in the ion velocity may also lead to thin ionization layers. (Bristow and Watkins, 1991).

To examine the wind-shear mechanism that was first proposed by Dungey (1959) and others (eg Whitehead, 1961, Axford, 1961) we must use momentum equation and impose the condition that there is an electric field established to make the

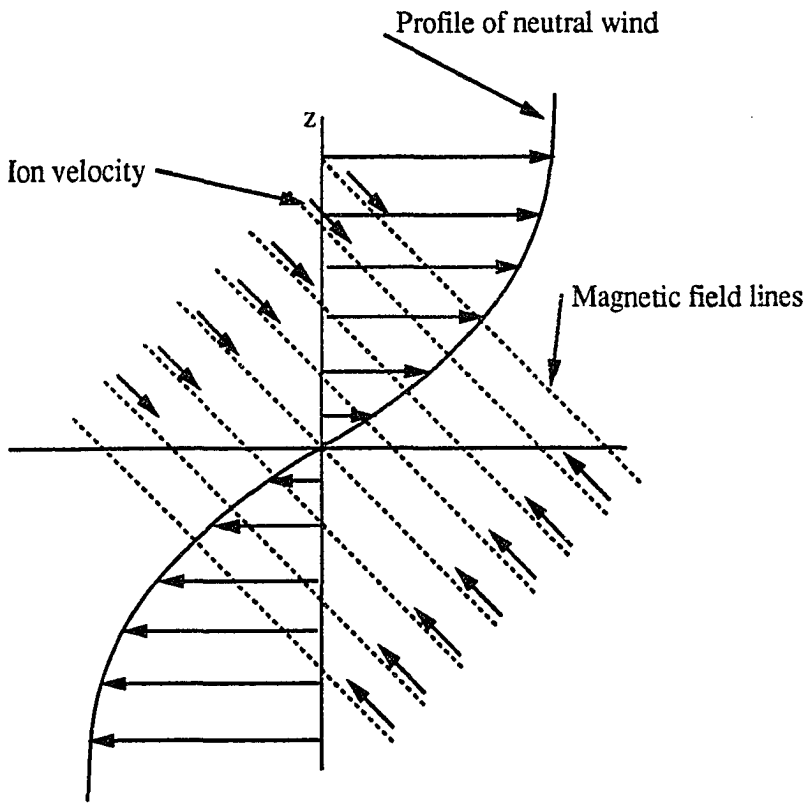

Fig. 3.4. The simplest form of Dungey's wind shear mechanism. The diagonal dashed lines represent magnetic field lines, and the curve represents the altitude profile of the neutral wind horizontal velocity. The ions are confined to move along the field lines, and move up the field from below the null and down from above. Figure is after Axford, 1961.

vertical velocity of the ions and electrons equal. The electric field is the polarization electric field which will be discussed in detail, and a complete expression will be given, in a later section. The velocity vector is determined from equation 3.12. Ignoring the pressure gradient term, and assuming there is no externally applied electric field, or vertical neutral winds, equation 3.12 becomes:

$$\vec{v} = C \begin{pmatrix} \frac{(m_i\nu_{in})^2+(eB_x)^2}{m_i\nu_{in}} & -eB_z & \frac{e^2B_xB_z}{m_i\nu_{in}} \\ eB_z & m_i\nu_{in} & -eB_x \\ \frac{e^2B_xB_z}{m_i\nu_in} & eB_x & \frac{(m_i\nu_{in})^2+(eB_z)^2}{m_i\nu_{in}} \end{pmatrix} \begin{pmatrix} m_i\nu_{in}U_x \\ m_i\nu_{in}U_y \\ eE_z \end{pmatrix}, \tag{3.15}$$

where the leading constant is:

$$C = \frac{1}{(eB_x)^2 + (m_i\nu_{in})^2 + (eB_z)^2}.$$

This yields, for the $\hat{z}$ component of the velocity:

$$v_z = C\Big[e^2B_xB_zU_x + m_i\nu_{in}eB_xU_y + \frac{(m_i\nu_{in})^2 + (eB_z)^2}{m_i\nu_{in}}eE_z\Big]. \tag{3.16}$$

The value of E_z is obtained by setting the $\hat{z}$ component of the ion and electron velocities equal; it is found to be:

$$E_z = -B_xU_y\frac{(m_e\nu_{en} + m_i\nu_{in})m_e\nu_{en}m_i\nu_{in}}{m_i\nu_{in}[(m_e\nu_{en})^2 + (eB_z)^2] + m_e\nu_{en}[(m_i\nu_{in})^2 + (eB_z)^2]} \tag{3.17}$$

This expression leads to the interesting conclusion that at the magnetic equator $E_z = -B_xU_y$, the electric force precisely balances the force due to the neutral wind and therefore the windshear mechanism fails. Also note that as B_x becomes smaller, ie. increasing dip angle, the vertical velocity decreases, and so the wind shear mechanism also becomes less effective at high latitudes. Figure 3.5 shows the ion vertical velocity profile for a dip angle of 45° generated by a north-south neutral wind with velocity of 200 m/s which reverses over a 6 km range with the velocity null at 110 km. Figure 3.6 shows the same velocity for a shear in the east-west neutral wind at the same latitude. Both figures illustrate steep gradients which could lead to the formation of thin layers. The magnitude of the gradient also depends on the altitude and magnitude of the wind shear. Figure 3.7 and 3.8 show the value of the maximum gradient of the ion vertical velocity as a function of dip angle for the

two wind directions. As can be seen in the figures the gradient maximizes at a dip angle of 45 degrees for the north-south neutral wind, falling off at both high and low latitudes, the figure for the east-west wind is essentially the same, the peak is at a slightly lower latitude, about 40 deg. It is therefore concluded that the wind shear mechanism for formation of thin layers is most effective at mid-latitudes.

Another mechanism for layer formation is the action of the convection electric field. At high latitudes the strong electric fields that are often present can generate ion velocity profiles with large gradients. In a recent paper Nygren *et al.*(1984) solved the stationary state equation of ion motion for various field directions and demonstrated that the electric field direction is an important factor in determining the ion vertical velocity profile. It was shown that an electric field alone, in the absence of any neutral wind shears, can cause a velocity profile with a convergent null. A field directed in the N-W quadrant produces a profile with a convergent null at an altitude dependent on angle. No other field direction produces profiles with convergent nulls; S-W quadrant produces downward flow, S-E produces divergent flow, and N-E produces upward flow. The conclusion drawn by Nygren *et al.* (1984) is that an electric field directed in the N-W quadrant would be capable of producing a sporadic E-layer. Their results however predict that the convergent nulls will occur at altitudes varying from 120 km for an electric field directed 60° west of north, to 130 km for a field at 30° west of north. The majority of sporadic E-layer observations have been much lower; generally between 100 and 120 km. As discussed above a convergent null is not necessary for layer formation, and the velocity profiles obtained for various field directions have gradients of sufficient magnitude for the formation of thin layers at altitudes in agreement with observations. In addition the electric field does not act alone in the absence of a neutral wind. There is always some neutral wind present, which may aid or thwart the formation of thin layers. The electric field mechanism will be discussed later in chapter 4 which discusses computer simulation of layer formation.

Another key factor in layer formation is the presence of long-lived metallic ions. Normal molecular ions have recombination rates which, in the absence of any local source, do not allow accumulation to very high densities. The continuity equation

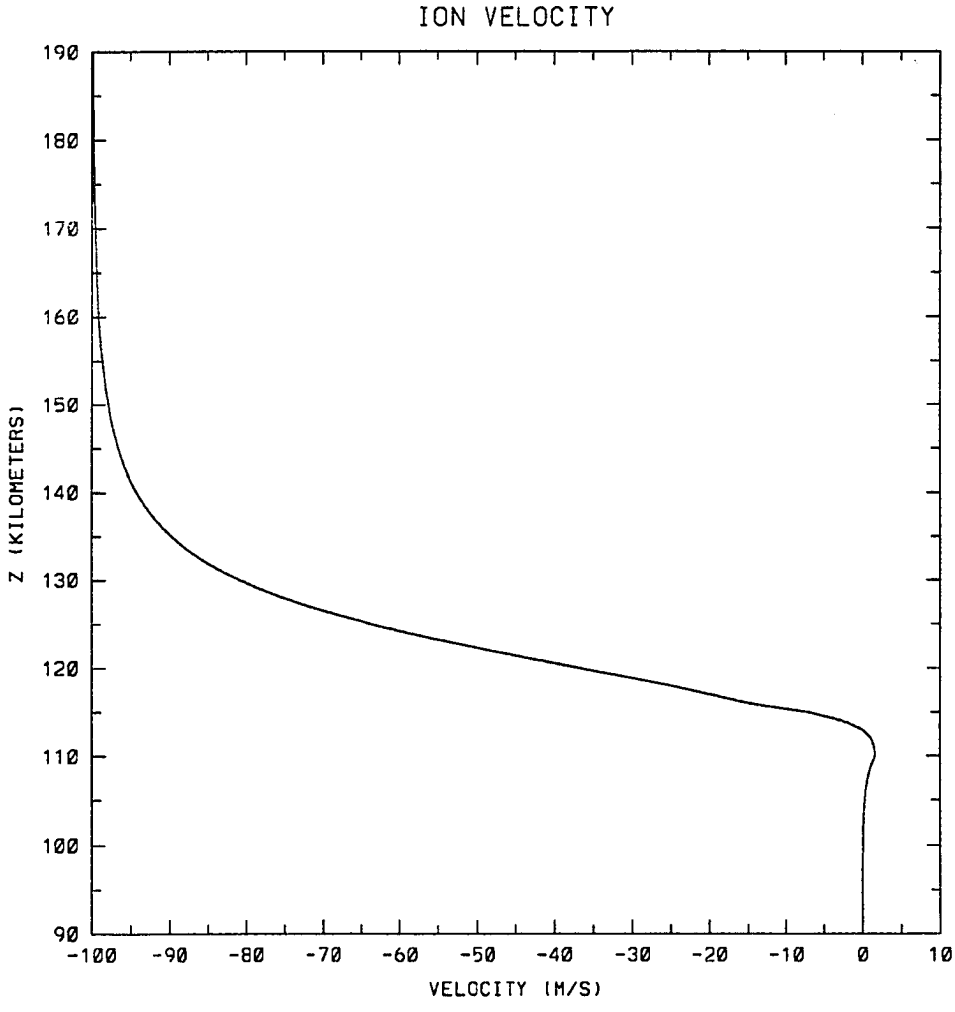

Fig. 3.5. Ion vertical velocity altitude profile due to a shear in the meridional wind.

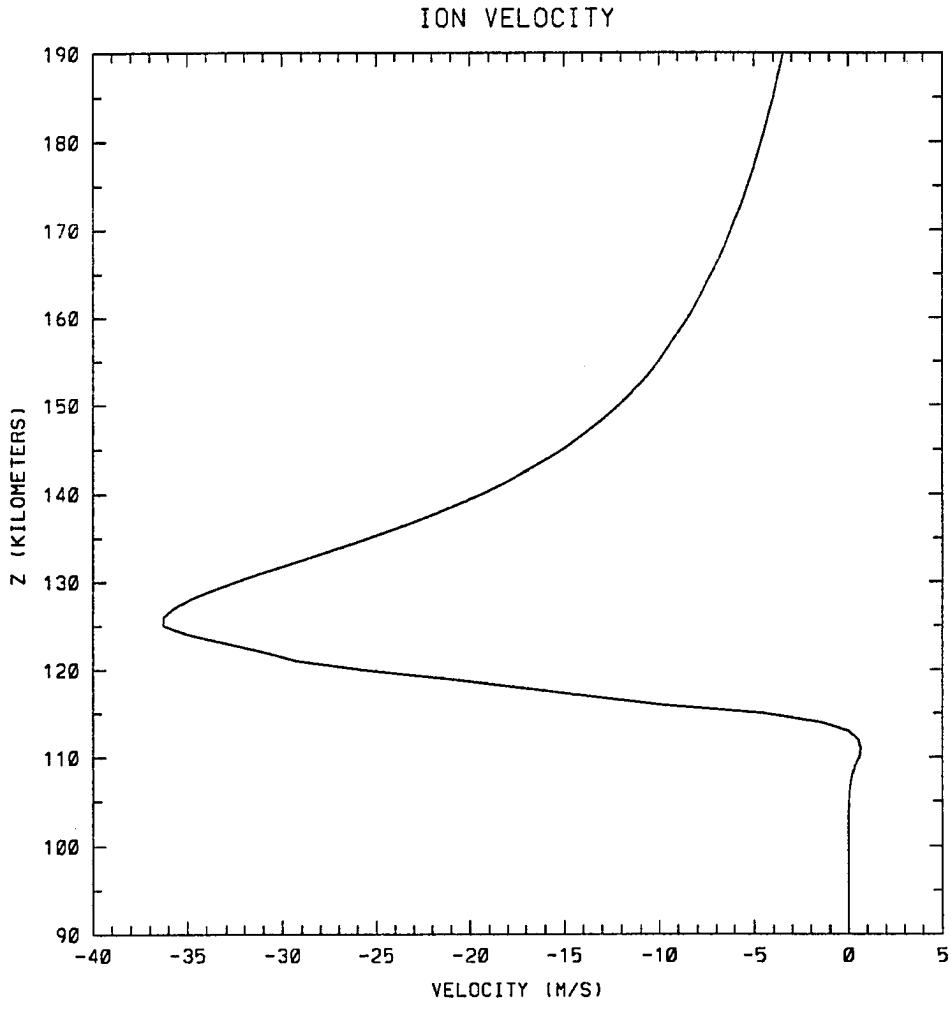

Fig. 3.6. Ion vertical velocity altitude profile due to a shear in the zonal wind.

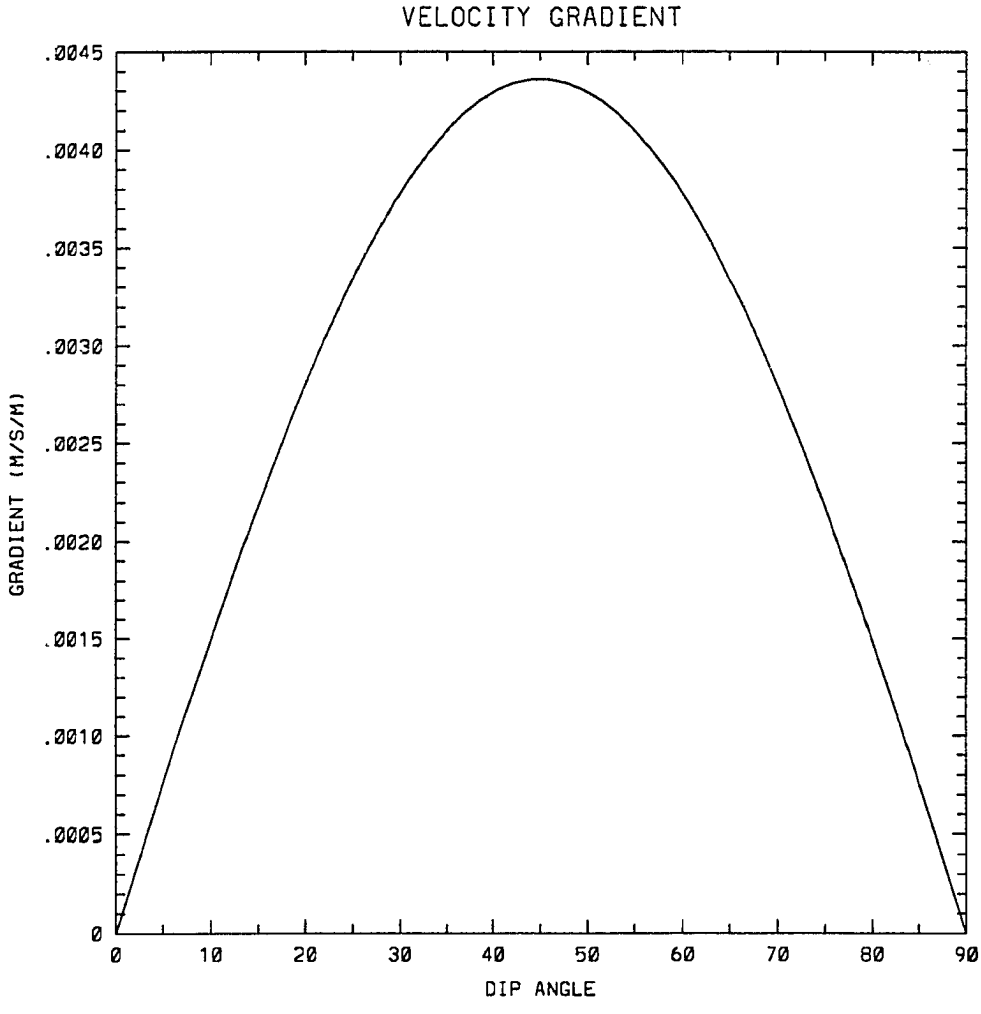

Fig. 3.7. Maximum gradient in the ion vertical velocity altitude profile, due to a shear in the meridional wind, as a function of dip angle.

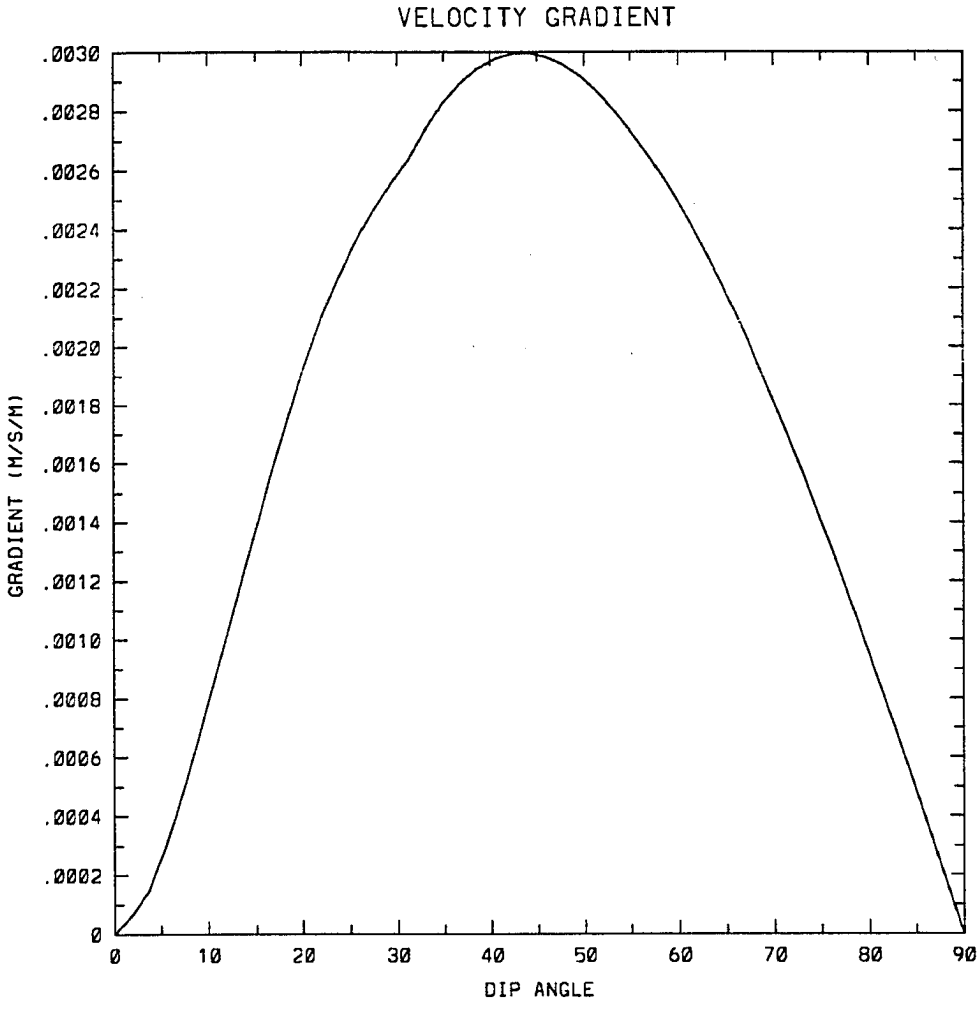

Fig. 3.8. Maximum gradient in the ion vertical velocity altitude profile, due to a shear in the zonal wind, as a function of dip angle.

in the E-region, including transport and recombination for a single species ionosphere, is: $\partial n/\partial t = -\partial/\partial z(nv_z) - n^2\alpha$; where α is a recombination coefficient. For a positive time derivative, transport must be greater than loss, this gives the approximate condition: $-\partial v_z/\partial z > n\alpha$. From figure 3.7 we see the maximum velocity gradient is on the order of $4 \times 10^{-3} m/s/m$, the recombination rate coefficient for nitric oxide, the most common and longest lived ion in the lower ionosphere, is about $4 \times 10^{-7} cm^{-3})/s$ which give a rough maximum density of $10^4 cm^{-3}$. This is much lower than observation; layers often have density in excess of $10^5 cm^{-3}$. Metallic ions were detected in the thin layers in rocket experiments (eg. Narcisi, 1968) and are routinely detected in incoherent-scatter observations (eg. Behnke and Vickrey, 1975). The recombination rates for metallic ions are much smaller than those of the molecular ions and there is no other effective loss mechanism in the E-region. Thus the metallic ions can accumulate to very high densities, limited only by the pressure gradient and the total column metallic ion content.

3.3 Meteor Ablation

The main source of metallic ions is the ablation of meteoroids in the upper atmosphere. Meteor ablation is an interesting problem which has been examined by many authors (eg. Bronshten, 1983). Meteors are objects in space, in heliocentric orbits, which are captured by the earth, and burn up as they enter the atmosphere. Meteorites are simply chunks of meteors which fall all the way to the earth. As a meteor approaches the earth it is acted on by frictional drag from the atmosphere, the motion is described by the equation:

$$M\frac{dv}{dt} = -\Gamma S \rho v^2 \tag{3.18}$$

Where Γ is a drag coefficient, S is the crossectional area, and ρ is the atmospheric density. As the frictional drag increases the meteor heats up, the surface liquifies, and eventually material starts to evaporate. The evaporated atoms collide with the ambient atoms and molecules, resulting in ionization. The meteor leaves a trail of ionization which may be detected by radar and causes optical emissions which may be observed. This discussion is an over simplification of the process, the actual interaction between the meteor and atmosphere may not be described by a simple

drag coefficient. At the highest altitudes the interaction is single particle collisions, while at lower altitudes the atmosphere acts more like a fluid and a shock forms in front of the meteor. In addition, the meteor may fragment in flight changing the interaction significantly. The result is that the meteor ablation process is not understood well enough to make accurate determination of the altitude deposition profile from theoretical considerations. Although accurate deposition profiles can only be inferred from observations, it is useful to examine the theoretical ionization production rate due to meteors as shown in figure 3.9. The figure shows a peak between 100 and 110 km of about 10^{-1} /cm^{3}s, with a rapid drop off in the number ablating above the peak.

Meteors range in size from approximately 10^{-6}g on up. Smaller particles enter the atmosphere but radiate enough heat away so they do not ablate. Spectroscopic observations of meteors show the presence of the neutral species: Fe, Mg, Na, Ca, Mn, Cr, Al, Ni, H, O, N, and ionic species: Ca^+, Mg^+, Si^+, Fe^+, N^+, and O^+. Figure 3.10 shows the mass flux of meteors as a function of size. As the figure shows there is some discrepancy between the meteor count observed with radio techniques and those observed by satellites and optical techniques. This discrepancy leads to an uncertainty in the total annual mass flux which is in the range of 4,200 to 16,100 tons per year. Some recent work in the meteor radar studies (Olsson-Steel and Elford, 1987) give some support to the larger number. The explanation for the under-estimation of the mass flux by radio techniques is the inability of typical meteor radar to detect underdense meteor trails above a height of 105-110 km. Olsson-Steel and Elford present observations using 2MHz radar which is a longer wavelength than the typical meteor radar, and thus able to detect meteor trails of lower density. Their observations suggest that many of the small meteors may have higher entry velocities, than previously expected, and are burning up at higher altitudes. Their results showed the altitude of the peak of meteor echos to be between 100 and 110 km, with significant numbers of meteors ablating up to 140 km, the limit of their measurements. This suggests two important conclusions, first that the actual amount of meteoric material entering the atmosphere is higher than measured previously, second the material is being dumped at higher altitudes than previously assumed. In the past it has been difficult to explain the presence of

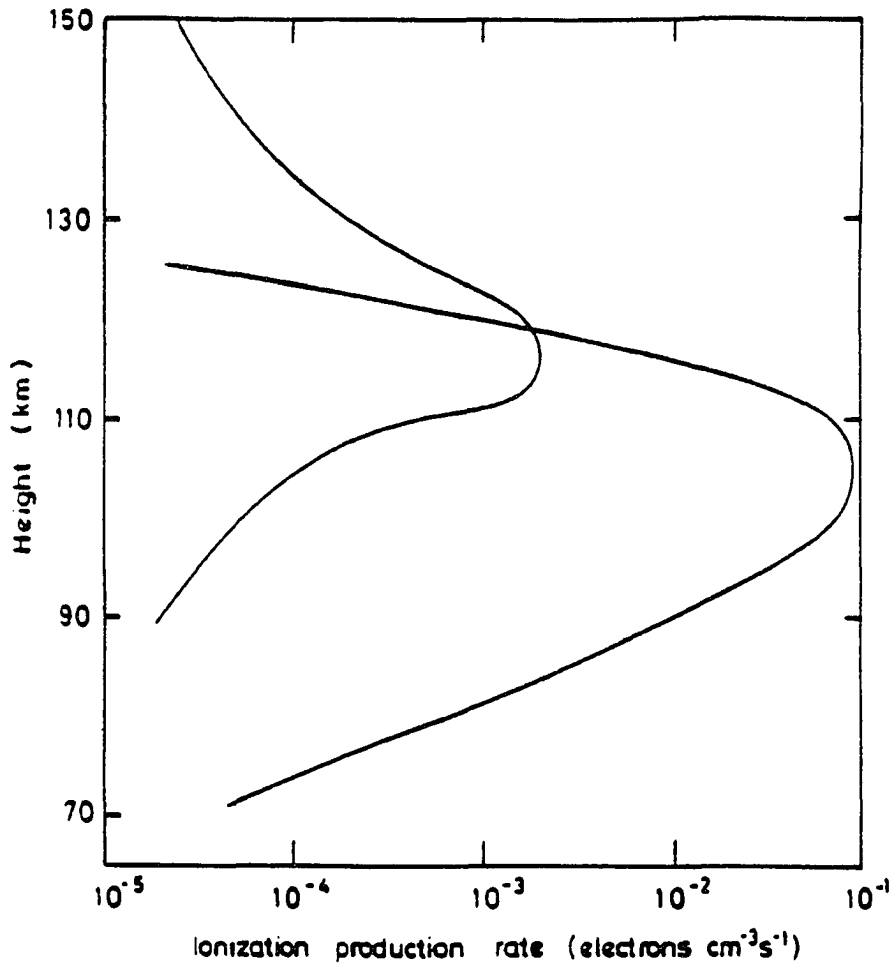

Fig. 3.9. The total theoretical ionization rate profile due to meteors (lower curve) and micrometeors in the terrestrial ionosphere. Figure is taken from "Cosmic Dust", D.W. Hughes, John Wiley & Sons, 1978.

metallic ions in the altitude region where they are observed (Grebowsky and Pharo, 1984). It was not understood how ions which were deposited below 100 km altitude could be transported upward to above 100 km where a transport mechanism exists to move the ions to higher altitudes. If there is a significant amount of meteors ablating above 100 km the presence of the metallic ions would be explained.

3.4 Meteor Statistics

The meteor influx can be divided into two parts: the sporadic background, and the meteor showers. A Meteor shower occurs when the earth passes through debris produced by the decay of a comet. This was discovered in the 1860 when it was noticed that the Perseids were moving in the same orbit as the comet Swift-Tuttle. Dust blown off the comet nucleus and pieces broken off in low velocity collisions will remain in approximately the same orbit as the comet forming an annulus of debris in space. Meteor showers occur where the orbit of the earth cross this annulus. The main process for formation of the sporadic background is collisions. Objects in helio-centric orbits have collisions, often fragmenting, and change to orbits which intersect the earth's orbit. The orbits of small dust particles are also affected by radiation pressure from the sun, which causes them to lose angular momentum and spiral in towards the sun. A final source for sporadic meteors is the interaction of Jupiter with objects in the asteroid belt. Since Jupiter is so massive its gravitational attraction perturbs orbits of other objects and may accelerate asteroids out of the asteroid belt and in to orbits which intersect the earth's orbit.

Figure 3.11 shows the annual variation in meteoric activity and figure 3.12 the hourly visual meteor rate. As 3.11 shows, the optical and radio meteors both show similar behavior, having a peak in the months August to December and a minimum from February to June, with roughly a 30% difference between the peak and minimum. Figure 3.12 shows that the meteor showers represent a significant increase in the flux over a short duration. The total mass flux is greatly elevated during the showers. One observation during the Geminid shower showed the density of neutral sodium at 92 km to increase from $1.5 \times 10^3 cm^{-3}$ to $5. \times 10^3 cm^{-3}$ (Zbindin *et al.*1975).

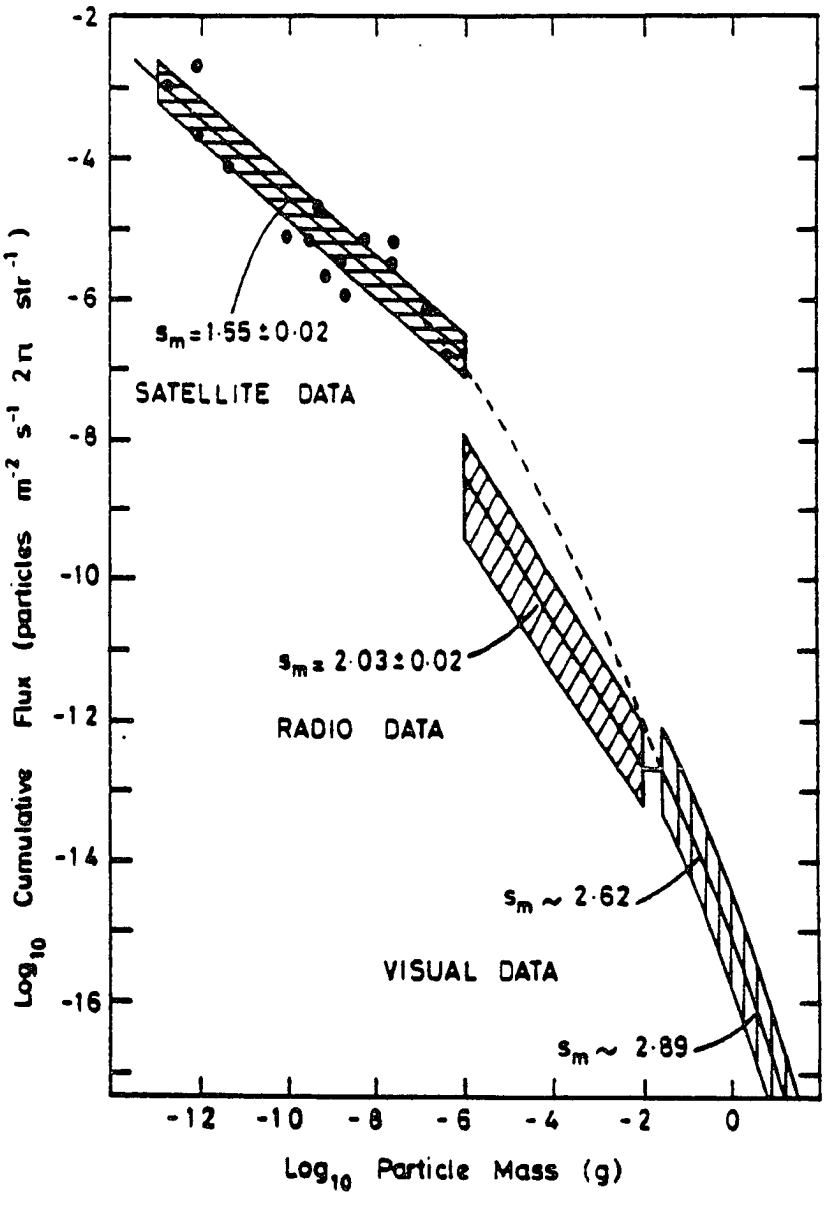

Fig. 3.10. The cumulative flux of particles in to the earth's atmosphere as a function of mass. The dashed line is an interpolation between satellite and visual data. Figure is taken from "Cosmic Dust", D.W. Hughes, John Wiley & Sons, 1978.

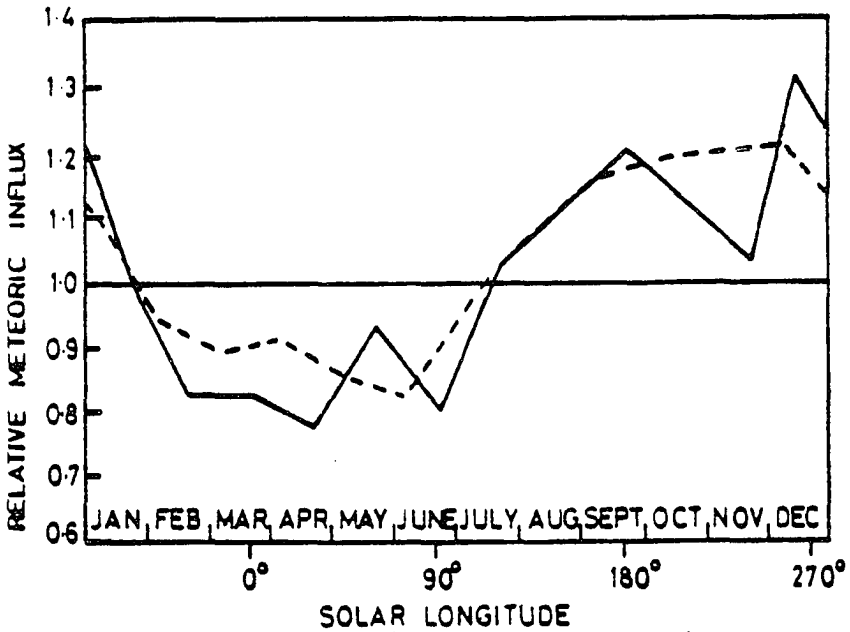

The annual variation in meteoric activity, corrected for the apex effect. — Radio meteors, Southern Hemisphere (Weiss, 1957) ---- Telescopic meteors, Northern Hemisphere (Kresákova and Kresák 1955)

Fig. 3.11. The annual variation in meteoric activity. Figure Taken from "Cosmic Dust", D.W. Hughes, John Wiley & Sons, 1978.

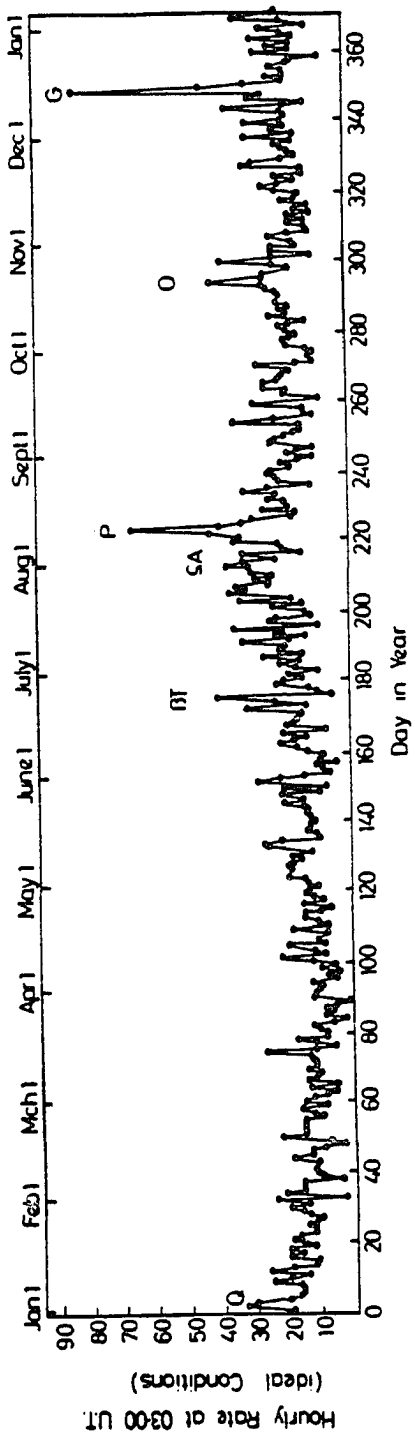

Fig. 3.12. The hourly visual meteor rate (magnitude brighter than 2.0) at 0300 UT as a function of day of the year. Figure is taken from "Cosmic Dust", D.W. Hughes, John Wiley & Sons, 1978.

3.5 Metallic Ion Morphology

It is difficult to determine the behavior of the distribution of metallic ions after deposition in the atmosphere. As discussed above, meteor ablation takes place mainly between 70 and 120 km, with the peak expected near 100 km. Metallic ions are observed by satellites in a range of altitudes as high as 1000 km. Satellites are useful for the determination of the presence of metallic ions but can not give a full altitude profile. Rocket borne mass spectrometors have been used to obtain profiles (eg. Zbinden it et al..1975) but only give a snapshot of the profile at a single time and location. Optical techniques are also unable to yield much information about metallic ions. Of the metallic ion species only Ca^+ has an emission which is observable, and lidars have been used in only a few observations (Granier *et al.*,1989).

Figure 3.13, taken from Zbindin *et al.*, shows the results from a rocket borne mass spectrometer. The data were obtained at a mid-latitude site, at a time close to the maximum of the Perseids meteor shower. The metallic ions show two peaks one at about 95 km, with density about $2 \times 10^4 cm^{-3}$, the other at 120 km, and density $3 \times 10^3 cm^{-3}$. The presence of two peaks possibly indicates the action waves in the neutral atmosphere. This profile shows that although the peak of the meteor deposition profile is near 100 km, there are significant amounts of metallic ions above this altitude.

Figure 3.14 (Grebowsky and Pharo, 1984) shows a compilation of observations of Fe^+ by the AE-C satellite in the latitude range 30° to 90° north. The observations are from a nearly circular orbit near 250 km altitude. As the figure shows metallic ions are often found in this altitude region, particularly in the day side high latitude region. This localized concentration of observations is understandable since the large electric fields in this region are oriented to give an upward drift velocity, the ions are transported from the meteor deposition region. A significant amount of ions must be deposited above 100 km or be transported from below 100 km. Once above 100 km an electric field with an eastward component will give an upward drift velocity.

Lidar observations of Ca^+ ions, figure 3.15 (Granier *et al.*, 1989), show three typical profiles: A diffuse low density layer between 85 and 105 km, a very dense

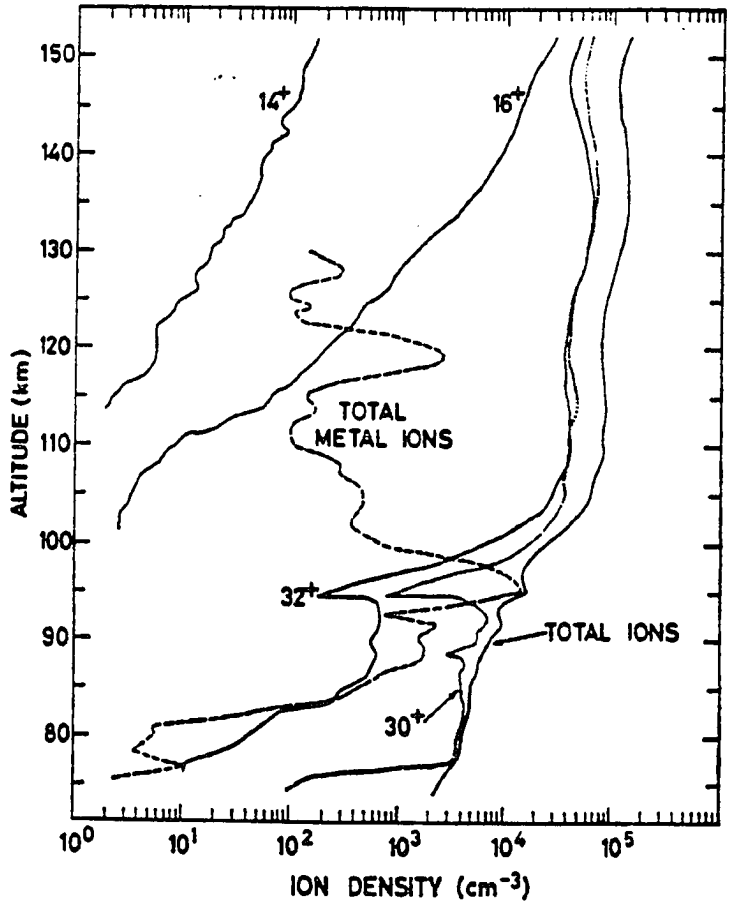

Fig. 3.13. Density profiles showing total metallic ions and N^+, O^+, O_2^+, and NO^+. The profiles are derived from a rocket borne mass spectrometer. Figure is from Zbindin *et al.*, 1985.

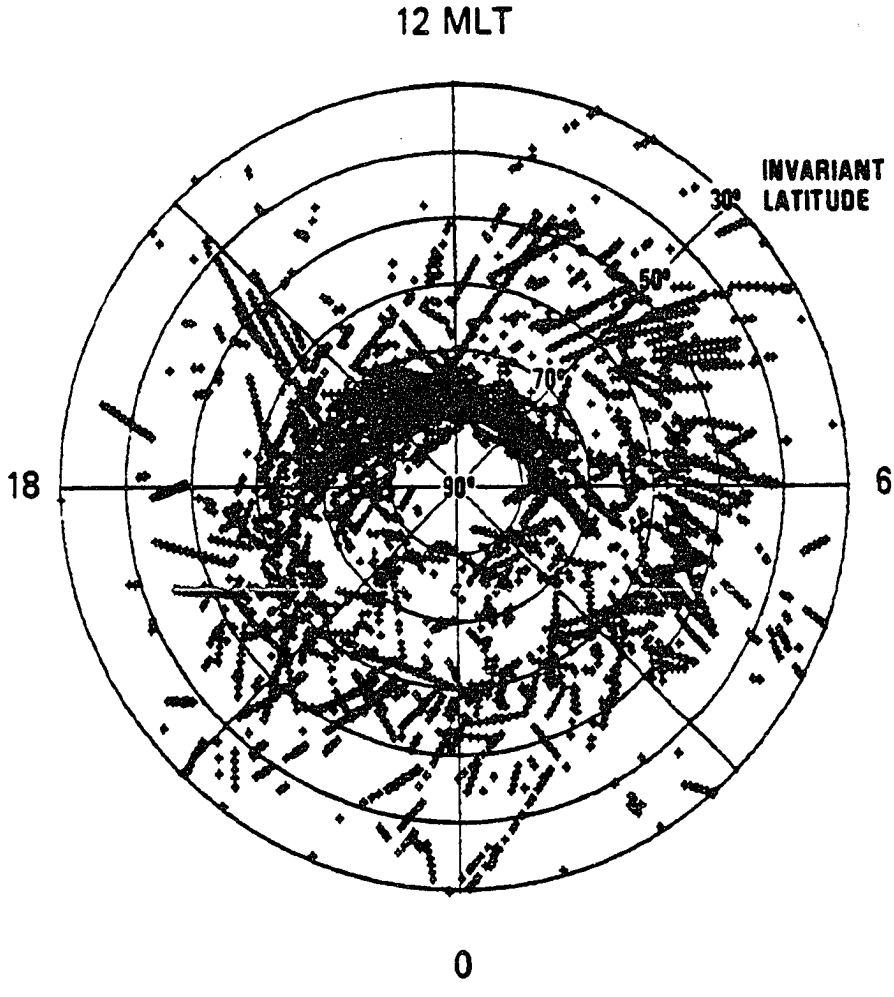

Fig. 3.14. The F-region Fe^+ from AE-C satellite observations in the region from 30° north invariant latitude. Figure is taken from Grebowski and Pharo, 1985.

thin layer above 95 km, or a combination of the two. Thin layers were observed in 80% of the nights of observation. The observations are again for a mid-latitude site and are for night time. The observations show very large variations in the total column abundance from night to night, with a range of 2×10^7 to 6×10^8. The total column density is highest when the layers are present. Since the profiles do not show any ions present above the layers it would indicate that the layers are formed with flow up from below. This is possible if the layers are formed by wind shears, however wind shears would not explain a higher column density.

The observations discussed here indicate that it is difficult to make any general statment about the morphology of metallic ions. Meteor deposition is in the range of 70 to 120 km. What happens after deposition is dependent on several factors, including latitude, neutral wind direction and magnitude, and electric field direction and magnitude. In the high latitude region it can be assumed that there is sufficient transport of ions from the meteor deposition region to altitudes where the thin layers are formed.

3.6 Convection Electric Field

The effects of processes in the magnetosphere are manifested in the high latitude ionosphere in two main ways: current systems and particle precipitation associated with the aurora, and large scale plasma convection. By observing ionospheric convection we observe the signature of convection in the magnetosphere. The large scale convection electric field plays a major role in determining the characteristics of the high latitude ionosphere: Joule heating from the electric field is a major heat source; antisunward motion of the F-region ionosphere over the polar cap brings high density day side plasma into the polar cap, sunward convection of low density plasma from the night side is associated with ionization troughs at dusk and dawn.

The convection pattern for southward IMF B_z conditions is a two-celled pattern with antisunward convection over the pole, and sunward convection equatorward of the polar cap. For northward B_z conditions the pattern is not clearly understood, it may be either four-celled or a distorted two-cell pattern; the data is inconclusive at this time.

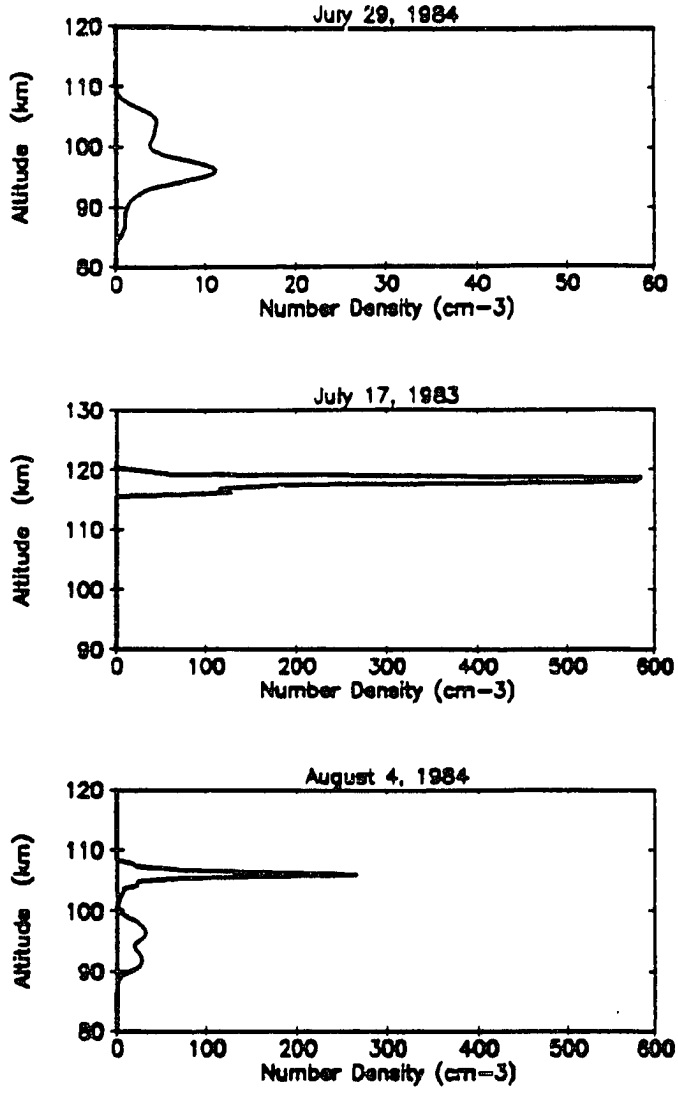

Fig. 3.15. Examples of Ca^+ as derived from lidar measurements. The plots show the three typical profiles. Figure is taken from Granier *et al.*, 1989.

In the F-region ionosphere, where the plasma is nearly collisionless, the motion of the ionization is, on the large scale, determined by the generalized Ohms Law ($\vec{E} + \vec{v} \times \vec{B} = 0$). This relation tells us that when a plasma moves across a magnetic field, an electric field will be generated, or that an imposed electric field will cause the plasma to drift across the magnetic field. This, together with the assumption that the conductivity parallel to the magnetic field is infinite, yields that for finite currents no field aligned electric field may exist and magnetic field lines will be equipotentials. Thus any electric field generated in the magnetosphere, or in the solar wind on open field lines, will map down into the ionosphere. The electric field drives ionospheric convection, and, since the ionosphere is a conducting medium, the field causes currents to flow. These are the large scale effects that magnetospheric convection causes in the ionosphere, in addition to the currents and horizontal convection, the electric field will cause vertical redistribution of the ionization.

3.7 Electric Field Measurement Techniques: Radar and Satellite

Radar Measurements:

Electric fields can be measured with an Incoherent-Scatter Radar (ISR) by measuring the plasma bulk velocity ($\vec{v}$) in an altitude region where collisions with the neutral atmosphere may be neglected; usually in the F-region. When collisions are negligible the motion is purely $\vec{E} \times \vec{B}$ and the electric field is determined from:

$$\vec{E} = \frac{-\vec{v} \times \vec{B}}{B^2}. \tag{3.19}$$

To find the vector velocity the line of sight velocity for three different directions are required. There are two basic ways of achieving this: one tristatic measurement, or three monostatic measurements. Monostatic simply means having one transmitter and one receiver looking along the same line. To make vector velocity measurements the radar must look in three different directions, each for a period long enough to give adequate signal to noise ratio. The time required is usually on the order of two to five minutes; this yields independent vectors every six to fifteen minutes, a running average may be used yielding new vectors at each antenna position. Tristatic measurements means having three receivers looking at the same

volume at the same time. This has the advantages of being faster, making the three measurements simultaneously, as well as having the measurement spatially localized. The main disadvantage of tristatic radar systems is significantly higher cost, as well as placing some restrictions on the experiments that may be performed.

Another experiment to measure ion velocity vectors with a monostatic system is the"multi-position" experiment, where 6 to 14 antenna positions are used, deriving velocity vectors from various triplet combinations. This experiment gives velocity vectors over a range of latitudes. This technique is described in Horwitz *et al.* 1978, where they measured the electric field in the latitude range 63°-68°, for a 60 hour period.

There are two main sources of uncertainty in the electric field measurements. First there is the statistical uncertainty in the spectrum's first moment estimate due to noise. The uncertainty is generally on the order of 2-5 mV/m. This uncertainty may be decreased by maximizing the signal to noise ratio, which is accomplished by lengthening the time spent in each antenna position. The other source of uncertainty is the temporal and spatial variation of the field. Since the field is derived from three independent antenna directions there is some spatial separation of the observed volumes. If there is variation of the field over the separation distance there may be significant uncertainty in the measurement. For an elevation angle of 70° at 250 km range the separation is on the order of 120 km. As mentioned above the time required to obtain an independent velocity vector ranges from 6-15 minutes. To minimize uncertainty due to temporal variations, the shortest possible integration time should be used.

Satellite Measurements:

One method of satellite electric field measurement is the plasma double-probe method. Two probes extend from the satellite body a distance of some tens of meters. The probes are connected to a differential amplifier. The potential difference between the two probes drives the amplifier. The current source is the ambient plasma, as such the current levels are very low and a very high impedance amplifier is required. To make vector field measurements two or more sets of probes are

required; one extended axially, another radially. As the satellite spins the radial pair measures the two components of the field in the plane of rotation.

The double-probe method is very fast, obtaining a new vector with every rotation of the the satellite. Figure 3.16 (Maynard, 1974) shows some typical polar cap electric field data from three successive passes of the Ogo 6 satellite. As the UT scale shows the satellite traverses the polar cap in a time on the order of 10 min. thus in the same time it would take a radar to make one vector measurement, the satellite gives a complete picture of the field along its orbit. One problem with the satellite measurement is, again as indicated by the UT scale, passes of the satellite are separated by approximately one hundred minutes. Thus two successive passes can show significant temporal difference.

At present there is no way to get a complete picture of the convection pattern at a given time. The best that can be done is to paste together data from several satellite passes or to use data from two or more radars working in concert. This gives a average convection pattern which may or may not bear a good resemblance to the actual ionospheric convection at any one location.

3.8 Convection Pattern

Figure 3.17 is a typical convection pattern (for southward IMF Bz) taken from Heppner and Maynard, 1987, which presents an empirical model of the high latitude electric field based upon data from the Ogo 6 and DE 2 satellites. The pattern, convection electric field model A, shows antisunward convection over the pole, and the return flow at lower latitudes. There is some distortion both at the noon and midnight boundaries of the polar cap. On the night side there is the Harang discontinuity (indicated by the dashed line), with its characteristic flow reversal. On the day side there is a similar, and even more intense, flow reversal. This pattern is for negative IMF B_y conditions. Heppner and Maynard present three basic patterns to represent ionospheric convection for all IMF B_z negative conditions. That is, they contend that the pattern for any given set of conditions is a distortion of one of the basic patterns. Figure 3.18, field model DE, and 3.19, field model BC, are the two other patterns. All three are two cell patterns distorted different amounts and directions. The patterns for model A and model DE are for northern hemisphere

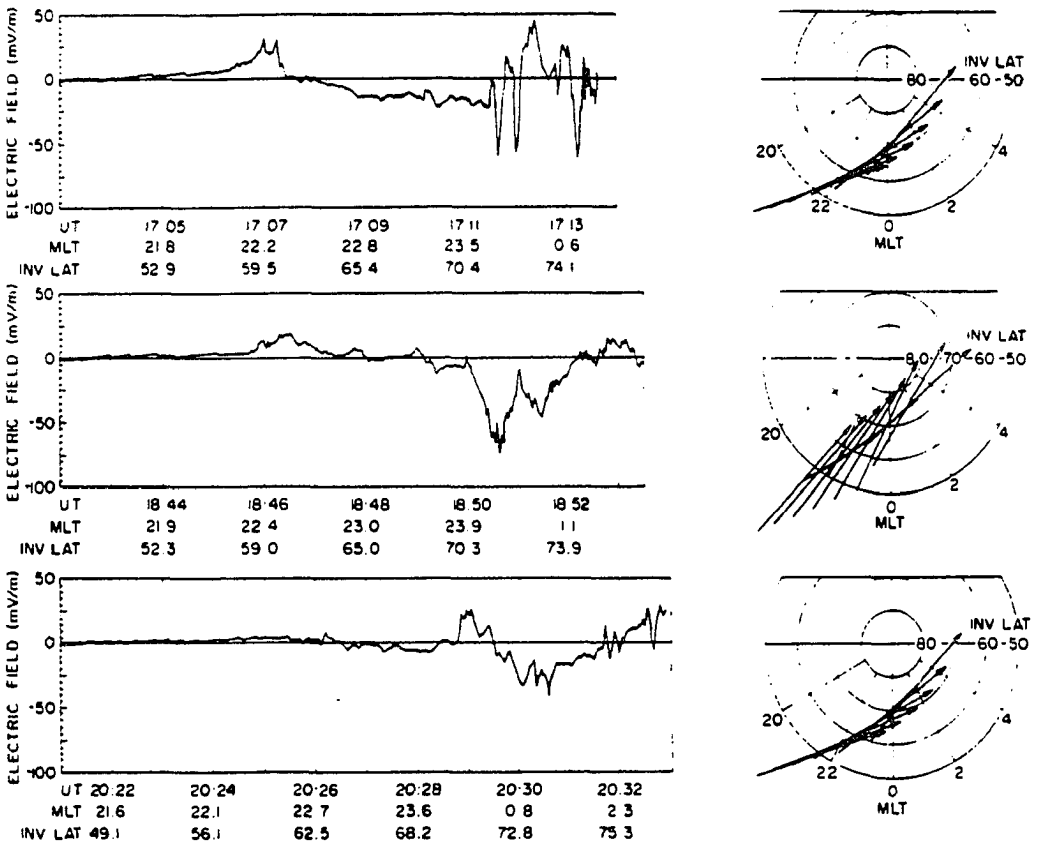

Fig. 3.16. Ogo 6 electric field data for three consecutive passes of the satellite during an active period on November 30, 1969. The UT time scales illustrate the time between passes. Figure is taken from Maynard, 1974.

under -B_y IMF conditions. In both cases the cross polar cap potential is the same, 76 kV, however the distribution of the potential differs between the two. The "A" pattern is fairly symmetric with the zero potential line passing directly over the pole. The "DE" pattern shows a much larger dawn cell. The two patterns represent the same IMF conditions and the same values of the Kp index. The third pattern, BC, is representative of the pattern for +B_y IMF conditions, here the evening cell is larger, and the flow over the pole directed slightly dawn to dusk.

Figure 3.20 shows the convection patterns for positive IMF B_z conditions. The patterns shown are simply distortions of the two patterns "BC" and "DE". The degree of distortion is determined by how strong the northward field is; when the field is very strongly northward the pattern becomes highly distorted, as shown in the right hand panels of the figure. The pattern becomes so highly distorted that there is sunward flow within the polar cap.

3.9 Polarization Electric Field

In examining the momentum equations for ions and electrons it is seen that, because of the mass difference, electron motion is not influenced by collisions as much as the ion motion is. The momentum source term is multiplied by the particle mass, and thus is much smaller for electrons. Because of the higher thermal velocity the electron-neutral collision frequency is higher than the ion-neutral collision frequency, however it is not high enough to make up the difference. This leads to a velocity difference between ions and electrons and thus to current flow. If there is a density gradient in some direction then any velocity difference in that direction would lead to charge separation. Since any significant charge separation can not exist, a polarization field is set up which stops the electrons from out-running the ions in the direction of the gradient. In the ionosphere the vertical density gradient is large, and in the presence of the thin layers the gradient may be very large. If the ionosphere is assumed to be homogeneous in the plane perpendicular to the vertical, then the polarization field is directed vertically. To find the polarization field a coordinate system is chosen with the $\hat{z}$ axis parallel to the magnetic field, and the density gradient in the x-z plane at an angle θ from the $\hat{x}$ axis. The momentum equations for both electrons and ions are solved and the condition is imposed that

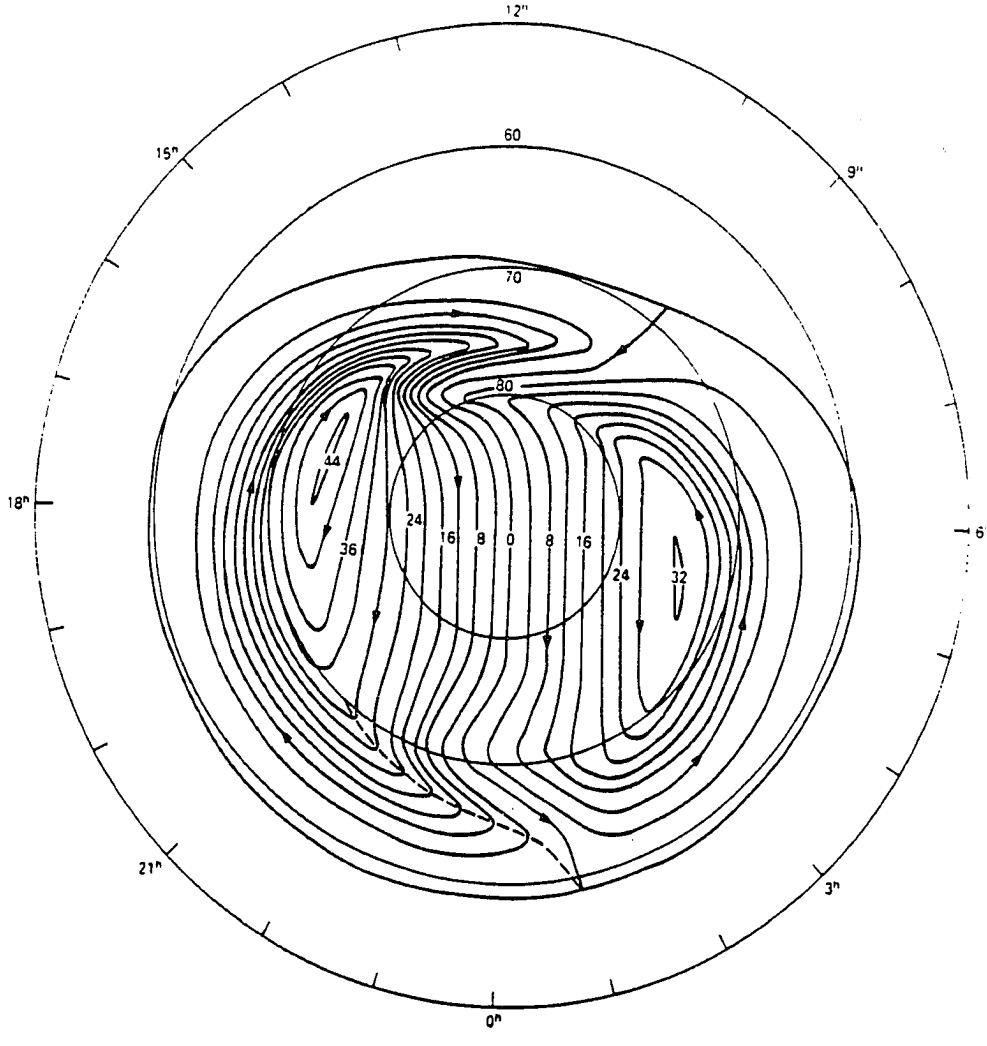

Fig. 3.17. Convection electric field model pattern "HM A", one of two models representing the convection pattern for southward B_z, negative B_y conditions in the northern hemisphere. Figure is taken from Hepner and Maynard, 1987.

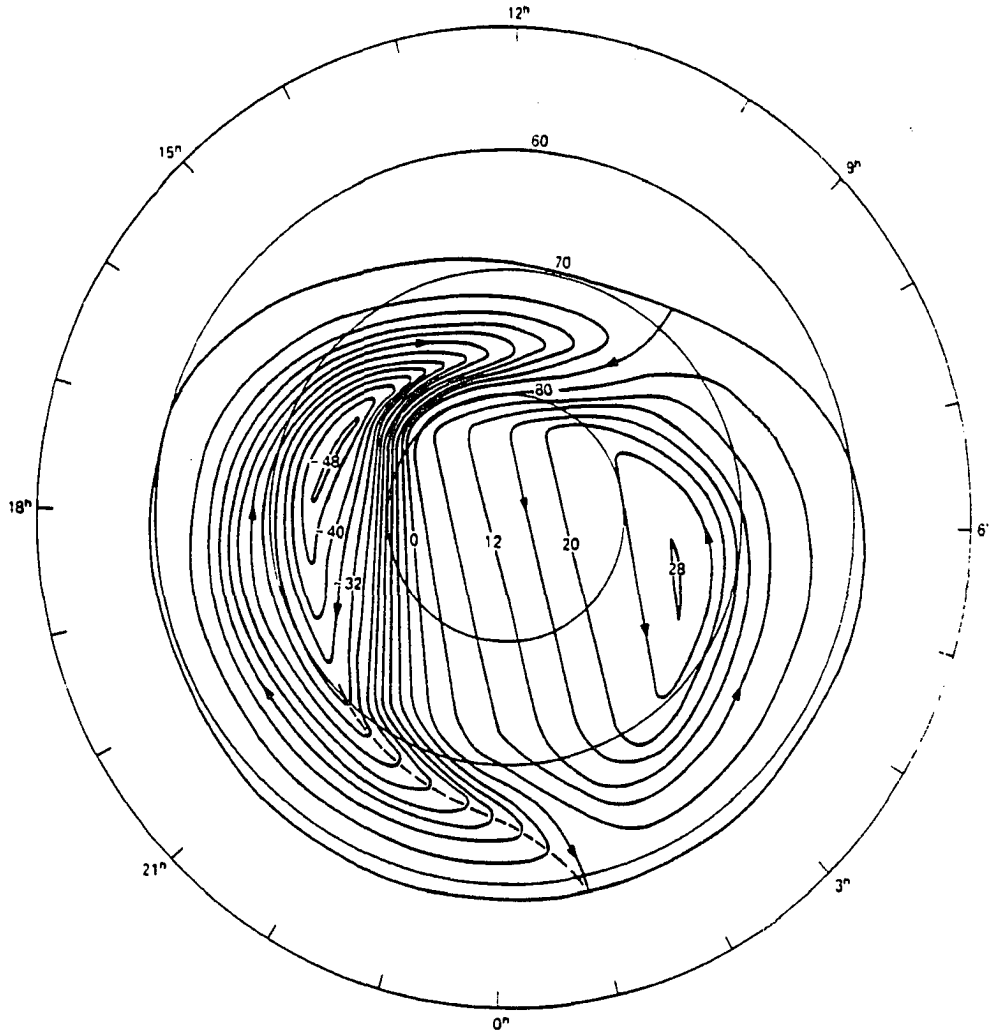

Fig. 3.18. Convection electric field model pattern "HM DE", the second of two models representing the convection pattern for southward B_z, negative B_y conditions in the northern hemisphere. Figure is taken from Hepner and Maynard, 1987.

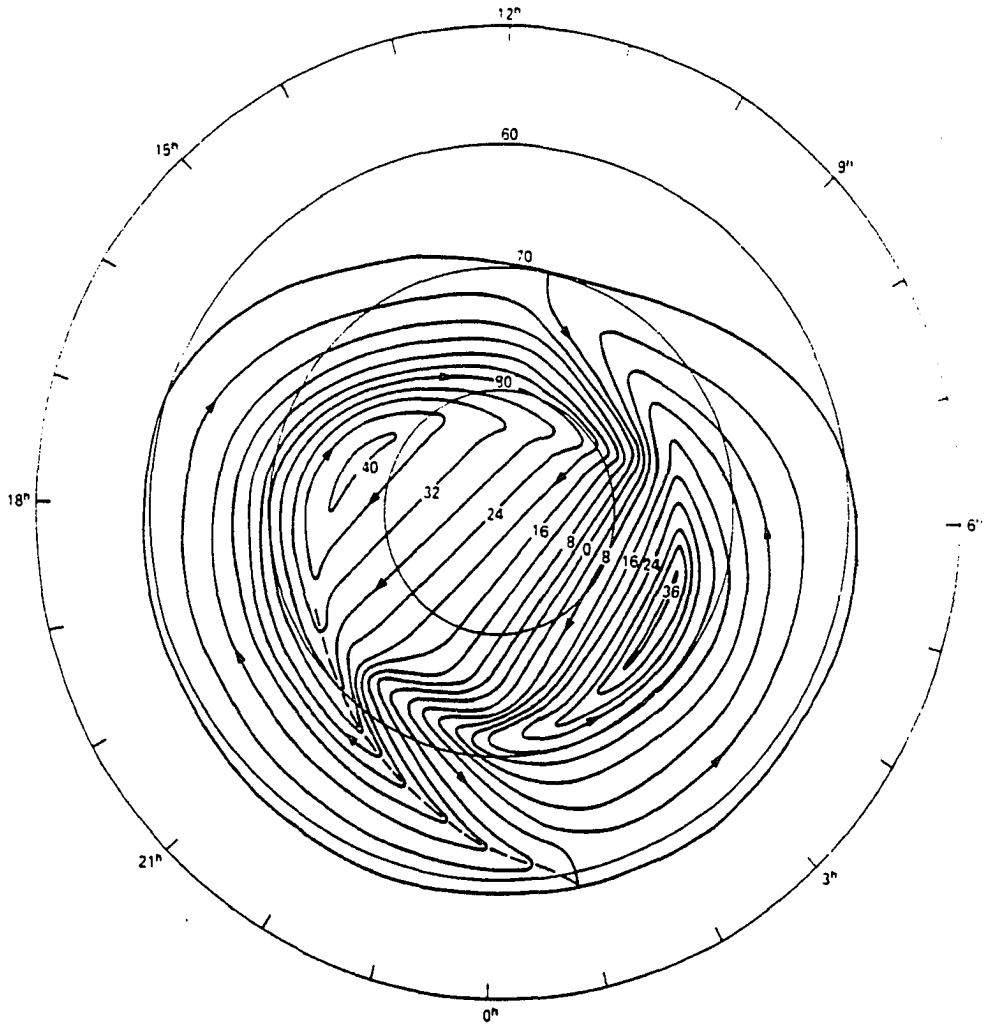

Fig. 3.19. Convection electric field model pattern "HM BC", model representing the convection pattern for southward B_z, positive B_y conditions in the northern hemisphere. Figure is taken from Hepner and Maynard, 1987.

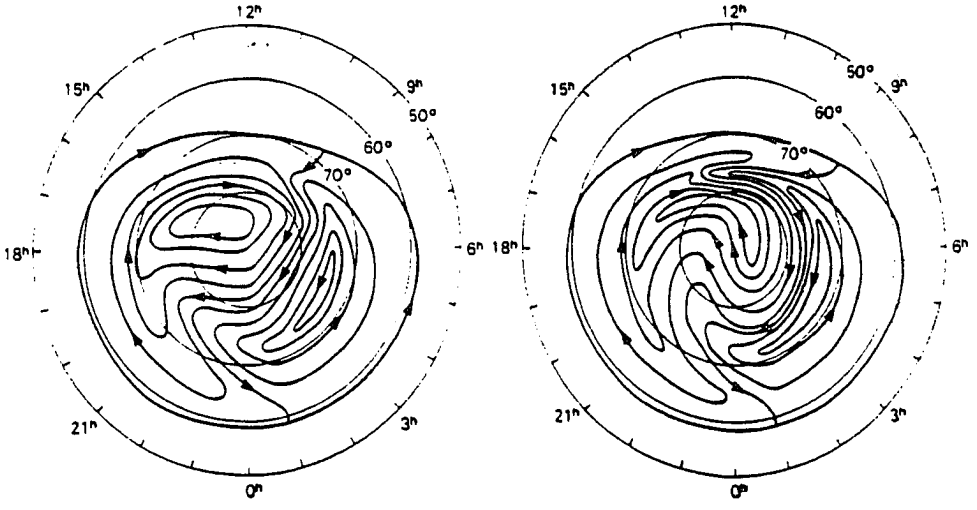

Rotationally twisted distortions of model BC, usually observed when the IMF B_z is weakly (left) and strongly (right) positive.

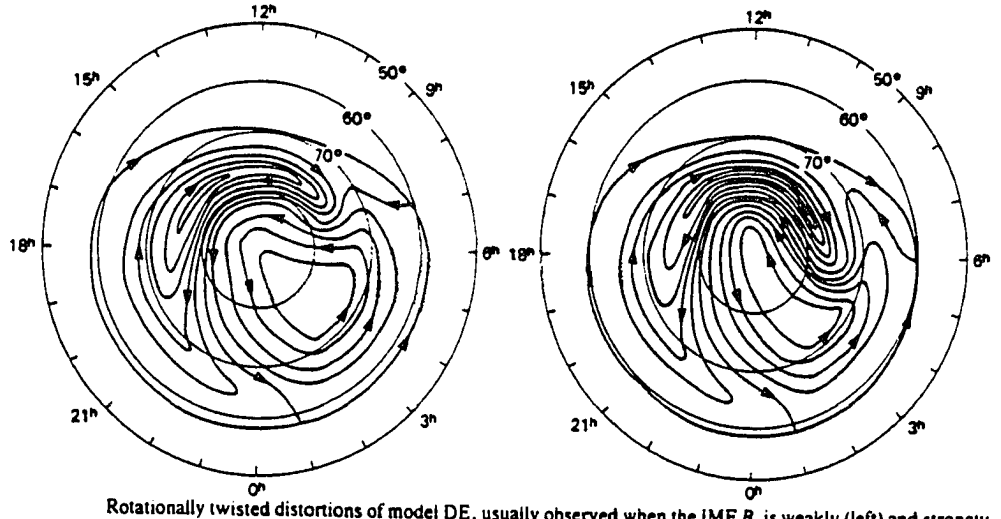

Rotationally twisted distortions of model DE, usually observed when the IMF B_z is weakly (left) and strongly (right) positive.

Fig. 3.20. Convection electric field model patterns for northward B_z conditions. The patterns are distortions of the patterns for southward B_z conditions. Figure is taken from Hepner and Maynard, 1987.

the velocity components parallel to the density gradient are equal. If the ion and electron densities and temperatures are assumed equal then the polarization field can be shown to be:

$$
\begin{aligned}
E_p = \Big[& \Big(\frac{\omega_i}{\nu_{in}} + \frac{\omega_e}{\nu_{en}}\Big)\frac{\sin^2\theta}{B} + \Big(\frac{\nu_{in}\omega_i}{\omega_i^2+\nu_{in}^2} + \frac{\nu_{en}\omega_e}{\omega_e^2+\nu_{en}^2}\Big)\frac{\cos^2\theta}{B}\Big]^{-1} \\
& * \Big[\frac{1}{n}\frac{dp}{dz}\sin\theta\Big(\frac{1}{m_i\nu_{in}} - \frac{1}{m_e\nu_{en}}\Big) \\
& + \frac{1}{n}\frac{dp}{dx}\cos\theta\Big(\frac{\nu_{in}}{m_i(\omega_i^2+\nu_{in}^2)} - \frac{\nu_{en}}{m_e(\omega_e^2+\nu_{en}^2)}\Big) \\
& - \Big(\frac{\nu_{in}\omega_i}{\omega_i^2+\nu_{in}^2} - \frac{\nu_{en}\omega_e}{\omega_e^2+\nu_{en}^2}\Big)\Big(\frac{E_{x0}}{B} - u_{ny}\Big)\cos\theta \\
& + \Big(\frac{\omega_i^2}{\omega_i^2+\nu_{in}^2} - \frac{\omega_e^2}{\omega_e^2+\nu_{en}^2}\Big)\frac{E_{y0}}{B}\cos\theta\Big]
\end{aligned}
\tag{3.20}
$$

Figure 3.21 is a plot of the field magnitude for high latitude conditions with a typical density profile with a thin layer. As the figure shows the field is small, on the order of a few tenths of a milivolt per meter at the lower altitudes, exponentially decreasing with altitude. At the layer altitude the density gradient is large and there is a significant jump of the field.

It should be noted that for certain configurations this field has a component parallel to the magnetic field. This is in part why the field magnitude is so small in the figure. The mobility of the electrons along the field is very large, and so it only takes a small field to restrain their motion. At the equator the density gradient is perpendicular to the magnetic field, and the polarization field may be quite large. As shown in the discussion of wind-shears, at the equator, $E_z = B_0 U_y$; for a wind of 200 m/s the field is 9 mV/m.

3.10 Conductivity

As discussed in the previous section the velocity difference between the ions and electrons leads to current flow. The currents may be found from the product of the electric field vector with the conductivity tensor:

$$\vec{J} = \sigma \cdot \vec{E} \tag{3.21}$$

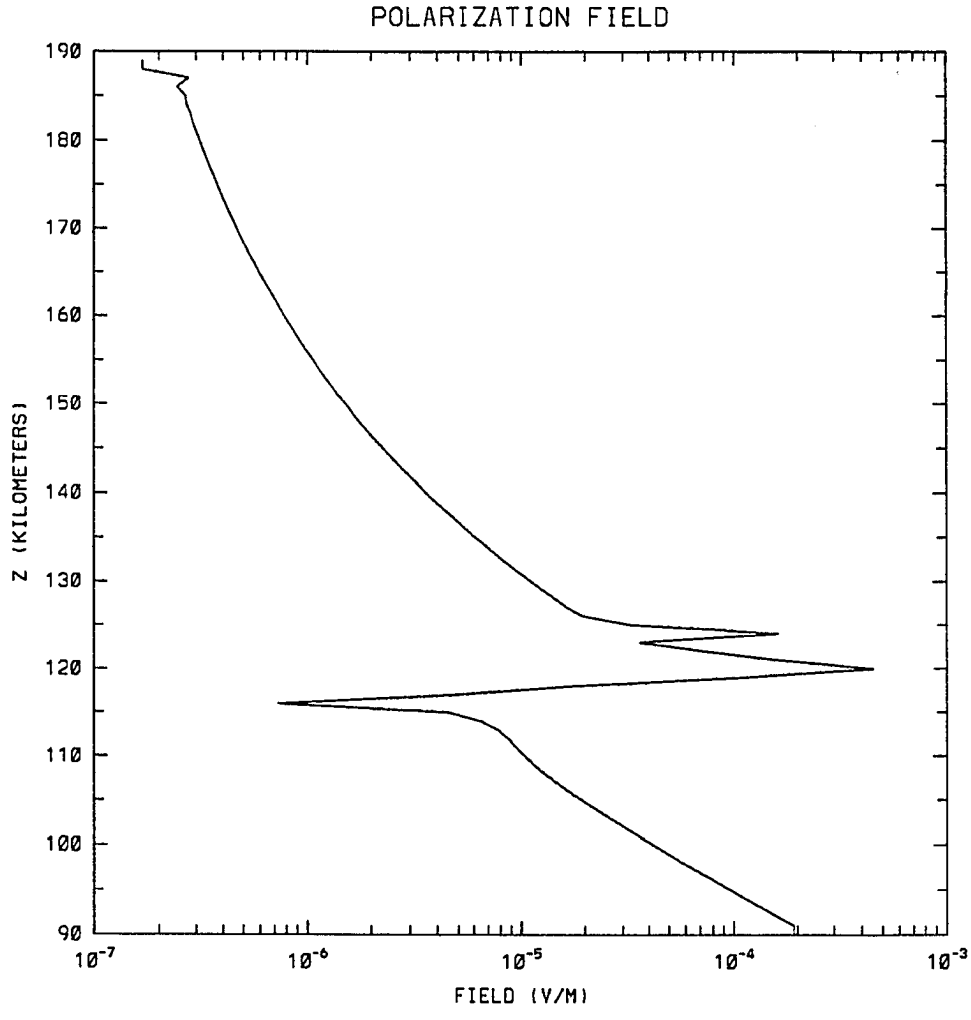

Fig. 3.21. Altitude profile of the magnitude of the polarization electric field due to vertical motion of ionization.

where the conductivity tensor is given by:

$$\sigma = \begin{pmatrix} \sigma_p & -\sigma_H & 0 \\ \sigma_H & \sigma_p & 0 \\ 0 & 0 & \sigma_0 \end{pmatrix} \tag{3.22}$$

where σ_p, σ_H and, σ_0 are the Pedersen, Hall and Parallel conductivities respectively. These terms are:

$$\sigma_0 = e^2 n\left(\frac{1}{m_e \nu_{en}} + \frac{1}{m_i \nu_{in}}\right) \tag{3.23}$$

$$\sigma_p = \frac{en}{B}\left(\frac{\nu_{en}\omega_e}{\omega_e^2 + \nu_{en}^2} + \frac{\nu_{in}\omega_i}{\omega_i^2 + \nu_{in}^2}\right) \tag{3.24}$$

$$\sigma_H = \frac{en}{B}\left(\frac{\omega_e^2}{\omega_e^2 + \nu_{en}^2} - \frac{\omega_i^2}{\omega_i^2 + \nu_{in}^2}\right) \tag{3.25}$$

The parallel conductivity is large and is often considered to be infinite which excludes the possibility of field aligned electric fields. The Hall and Pedersen conductivities are strongly dependent on the densities and collision frequencies. Because of the collision frequency dependence, density in the lower E-region leads to higher conductivity than equal density at a higher altitude. For this reason thin ionization layers may play a significant role in determining the conductivity of the ionosphere. Figure 3.22 shows the altitude profiles for conductivity under typical night time conditions, and for the presence of a thin ionization layer. As the figure shows the conductivities are significantly higher in the layer. An important parameter is the height integrated conductivity. This parameter gives a total conductance for the ionosphere. The height integrated conductivities from figure 3.22 are $\Sigma_p = 3.02$ mho, and $\Sigma_H = 6.75$ mho without the layer, and $\Sigma_p = 0.56$ mho, and $\Sigma_H = 11.63$ mho with the layer. In this example the Pedersen conductance decreases, while the Hall conductance is greatly enhanced, thus the layer not only effects the magnitude of the currents but also the direction.

In areas where the layers have an edge there will be a horizontal gradient in the conductivities. This leads to the possibility of field aligned currents. To see this recall $\vec{J} = \sigma \cdot \vec{E}$, and $\nabla \cdot \vec{J} = 0$. With the assumption of infinite parallel conductivity this leads to:

$$\vec{J}_{||} = \nabla_\perp \cdot (\Sigma_\perp \cdot \vec{E}_\perp) \tag{3.26}$$

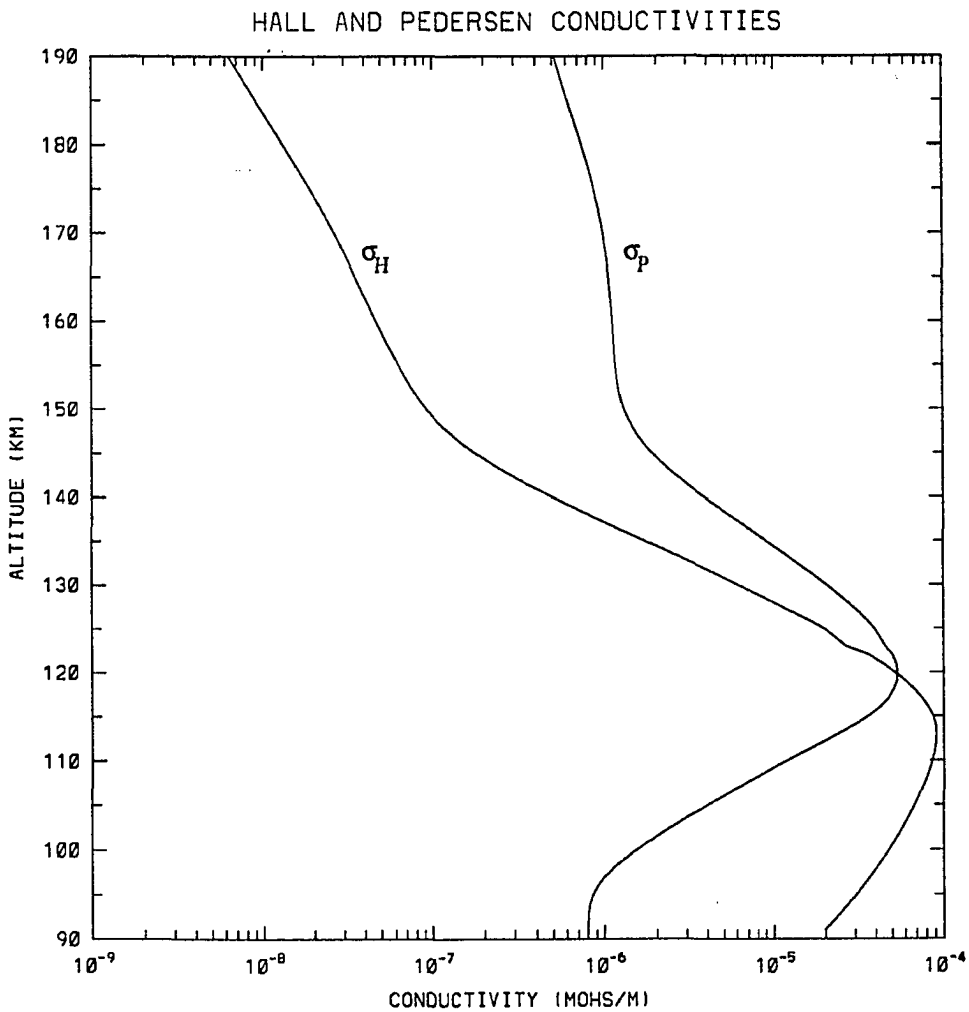

Fig. 3.22a. Altitude profile of the Hall and Pedersen conductivities without the presence of a thin ionization layer.

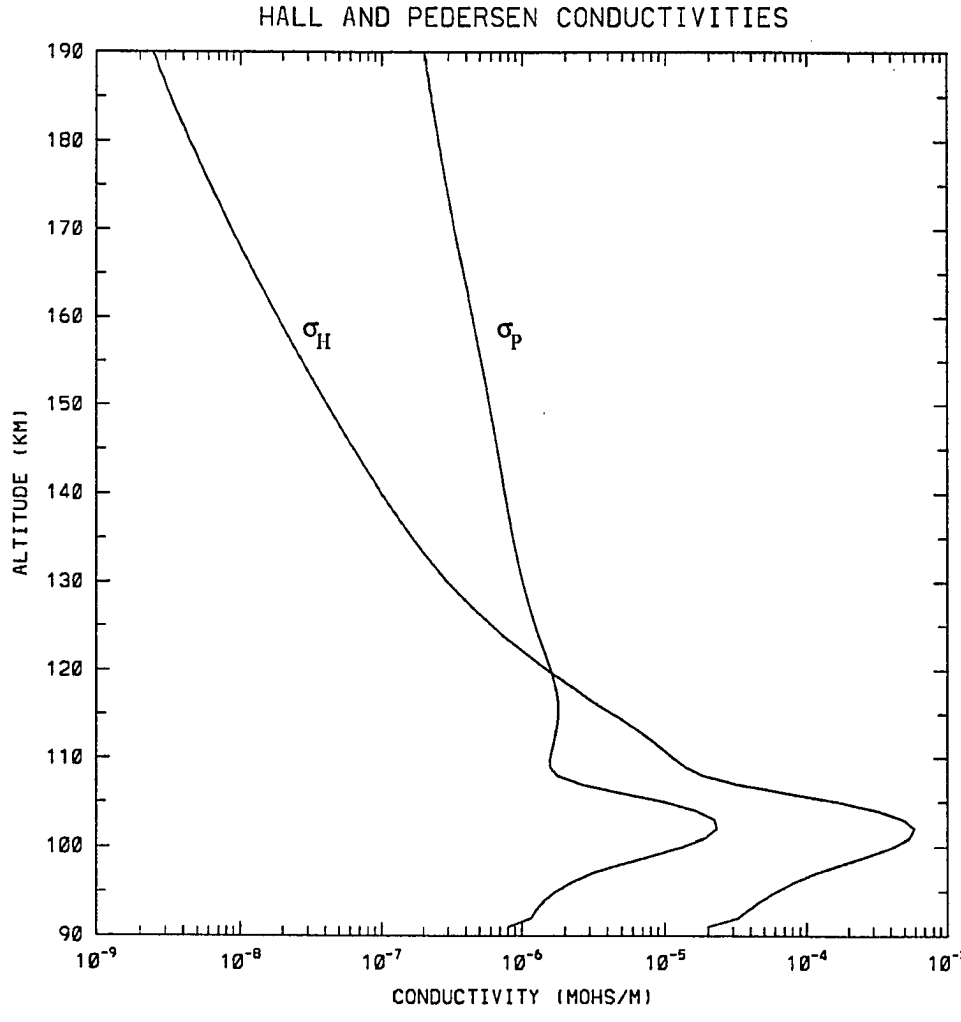

Fig. 3.22b. Altitude profile of the Hall and Pedersen conductivities with the presence of a thin ionization layer.

So even if the perpendicular electric field is continuous through an area the conductivity gradients will lead to field aligned currents. Thin ionization layers are observed to have definite edges, and may play an important role in the global current system.

CHAPTER 4
SIMULATION OF FORMATION OF THIN IONIZATION LAYERS

4.1 Introduction

The previous chapter presented the theories of thin ionization layer formation. The mechanisms for formation of thin ionization layers include wind shears and the action of the perpendicular electric field. In this chapter a numerical simulation of layer formation is discused. First a one dimensional simulation is discussed in which the altitude profiles for ion densities and the ion, electron and neutral temperatures are obtained in the altitude region between 90 and 190 km, with one km resolution. The simulation examines the role of the electric field in layer formation at high latitudes. Next a three dimensional model is examined which includes the effects of ionospheric convection and the neutral winds in the high latitude region. The simulation attempts to determine the geographic distribution of thin ionization layers.

In the simulations the stationary state ion momentum equation is solved and the continuity equation is integrated numerically. Next the energy equation is integrated numerically to obtain the temperature profiles. The neutral temperatures are fed into the equation of hydrostatic equilibrium to get the neutral density profile.

4.2 Computational Approach

In the one dimensional simulation the atmosphere is assumed to be infinite in horizontal extent and planar, with variations only in the vertical direction ($\hat{z}$). The ion velocity profile is obtained from the stationary equation of ion motion which was discussed in the previous chapter:

$$\vec{v}_s = \beta^{-1}\left[e_s\vec{E} + m_s\nu_{sn}\vec{v}_n - \tfrac{1}{n}\nabla P\right] \tag{4.1}$$

ν denotes the ion-neutral collision frequency, $\vec{u}$ denotes the neutral wind velocity, e is the electron charge, $\vec{v}$ is the ion velocity, n is the ion number density, m is the ion mass, P is the pressure, and β is a matrix obtained by decomposing the cross

product to a vector-matrix product. The electric field is, of course, taken to be perpendicular to $\vec{B}$ and the neutral wind is assumed to be horizontal.

To find density profiles the ion continuity equation is numerically integrated.

$$\frac{\partial n}{\partial t} + \frac{\partial}{\partial z}(nv_z) = Q - L \tag{4.2}$$

The Q (source) and L (loss) terms are chemical production or loss of an ion species from chemical reactions. A source term is of the form an ion species having a charge exchange reaction with a neutral species to produce the species being examined. Thus chemical production of one ion species is the loss of another. A loss reaction is the ion reacting with a neutral to produce another ion and neutral, or recombination with an electron to produce a neutral. The form of each term is the product of the density of the ion with the density of the neutral and the reaction rate coefficient. The continuity equation is written for each ion species as:

$$\frac{\partial n_k}{\partial t} = -\frac{\partial}{\partial z}(nv_z)_k + n_p n_q S_k^{pq} - n_k(n_s L^s + n_e L^e) \tag{4.3}$$

Where S_k^{pq} denotes the reaction rate coefficient for production of ion k from the reaction of ion p with neutral q, L^s is the reaction rate coefficient for loss of ion k from reaction with neutral s, and L^e is the reaction rate coefficient for radiative recombination. There is summation over repeated indices. For the major ions the reaction rate coefficients are taken from Rees [1989]. Metallic ions are lost through three body reactions and thus the rate coefficients for loss are very small and may be ignored in the altitude region of interest (Solomon *et al.*,1982). No photoionization (night-time conditions) or electron precipitation terms are included.

This must be solved for each ion species ($O^+, O_2^+, N^+, N_2^+, NO^+, Fe^+$) and for the minor neutral species nitric oxide (NO). The densities of the major neutral species are not affected. Thus we have a system of seven coupled differential equations. To integrate the system numerically an implicit integration scheme was chosen (eg. Potter, pg 36). In this scheme the density at time step n+1 is:

$$n_k^{n+1} = n_k^n - \frac{\partial}{\partial z}(n_k v_{kz})^n \Delta t + \left[(Q_k^n - L_k^n) + (Q_k^{n+1} - L_k^{n+1})\right]\frac{\Delta t}{2} \tag{4.4}$$

The use of the source and loss terms at time step $n+1$ implies that the densities of the ions are already known at the new time step. The implicit integration scheme

insures stability for any time step. The convective term is integrated explicitly i.e., is only included for time step n since the time scale for the chemistry is much faster than for convection. In this procedure the differential equations are transformed to a system of coupled algebraic equations. The boundary conditions chosen for continuity are that the ion flux is zero at the lower boundary, the derivative of the flux is constant at the top.

Many of the reactions used in the continuity equation are temperature dependent, the pressure is also temperature dependent. To find the temperatures the energy equation is integrated for the ions, neutrals and electrons. Rather than solve the equations for each individual ion species, the ions are approximated by a single generic ion with density equal to the total ion density, and having the average ion mass. The energy equation is rearranged to get a differential equation for temperature. We assume that the pressure tensor ($\mathbf{P}$) may be approximated by the scalar pressure, and that the heat flux is simply proportional to the temperature gradient ($\vec{q} = -\lambda \nabla T$ where λ is the thermal conductivity.) With these assumptions the equation is as follows:

$$\begin{aligned}\frac{\partial T}{\partial t} = \frac{2\lambda}{3nk}\nabla^2 T - (\vec{v} - \frac{2}{3nk}\nabla\lambda)\cdot\nabla T \\ - [\frac{1}{n}(\frac{\partial n}{\partial t} + \vec{v}\cdot\nabla n) + \frac{7}{3}\nabla\cdot\vec{v}]T + \frac{2}{3nk}[Q - L]\end{aligned} \tag{4.5}$$

The source (Q) and loss (L) terms for the ions and neutrals are Joule heating and energy exchange by elastic collisions. The Joule heating term is given by:

$$Q_s = n_s m_s \nu'_{sn}(\vec{v}_s - \vec{v}_n)^2 \tag{4.6}$$

Where the collision frequency (ν'_{sn}) is the energy transfer collision frequency which is related to the momentum transfer collision frequency by:

$$\nu'_{sn} = \frac{m_n}{m_n + m_s}\nu_{sn} \tag{4.7}$$

Thus for ions the energy transfer collision frequency is approximately one half that for momentum transfer (Rees, pg.109). This heating term is calculated for ion-neutral collisions as a heat source for both the ions and the neutrals and for electron neutral collisions as a heat source for electrons and neutrals. This is a major source

of heating for the ions and in regions of high velocity difference between the ions and neutrals the ion temperature becomes greatly elevated.

The loss terms are of the form:

$$L_{1,2} = 3n_1 \frac{m_1}{m_1 + m_2} n u_{12} k (T_2 - T_1) \tag{4.8}$$

Although this term is called a loss, it may be a source if the temperature T_2 is less than T_1.

An additional loss term for the neutrals is radiation from nitric oxide. Nitric oxide (NO) has an emission line at $5.3\mu m$ which is due to vibrational transitions. NO molecules are excited to elevated vibrational states through collisions, or are formed in an excited state. Since NO is a minor species, the atmosphere is optically thin to the $5.3\mu m$ radiation, and the energy escapes from the region. This is a major cooling mechanism for the neutral atmosphere (Kockarts, 1980).

The temperature equations form a system of three coupled second order non-linear differential equations, and are in fact coupled to the continuity equation as well. The coupling between the continuity and energy equations is simply ignored here and the densities in the energy equations and temperatures in the continuity equations are just updated at each time step. Again an implicit method is used to integrate these equations. The method used is Crank-Nicholson (Potter, pg.77) which is unconditionally stable and has second order accuracy in both time and space. This method leads to a tri-diagonal matrix which can be solved in a fast and efficient manner. The initial condition was that the ion and electron temperature profiles are equal to the initial neutral temperature profile which is taken from the MSIS-86 model atmosphere. The boundary conditions were that the temperatures are fixed at the lower boundary and the derivatives were fixed at the upper boundary.

Next, it was assumed that the neutral atmosphere was in hydrostatic equilibrium at all times but the equilibrium slowly changes as the temperature changes. To get the neutral density the equation of hydrostatic equilibrium was solved for the three major species, N_2, O_2, and O. The density and temperature values at the base altitude (z_0) were taken from the MSIS-86 model atmosphere for solar

maximum conditions. The force on the neutrals due to the ion drift was included to examine any effect it may have on the neutrals.

4.3 Results of One Dimensional Simulation

To illustrate the high latitude effects the parameters were chosen B = 45μT, Dip angle = 75°, E = 50mV/m, and u = 0. Using these parameters, the resultant initial vertical component of the ion velocity for several field directions is plotted in figure 4.1. The angles indicate the direction of the electric field measured counter clockwise from magnetic north. The profiles illustrate that at the highest altitudes the motion of the ions is purely $\vec{E} \times \vec{B}$, at lower altitudes the ion-neutral collisions become important and the total velocity vector changes magnitude and direction. As the total vector changes direction the vertical component changes, and may even reverse as in the cases where the profiles show nulls (recall that a null is an altitude where the vertical velocity goes to zero, a convergent null is where the flow is into the null from above and below, a divergent null is where flow is away from the null both above and below). Note the altitude of the convergent null for the 45° profile at approximately 123 km. As mentioned earlier, this altitude is well above 100km. Note also that all profiles have a null near or below the 100km level. These nulls are not convergent in the sense described earlier, with flow up from below and down from above, however the profiles where the flow is downward at all altitudes will result in ion accumulation at this altitude.

Figure 4.2 shows the initial ion density profiles. Initial density profiles for the major species are approximated from mass spectrometer measurements by Zbinden *et al.* [1975]. Since the metal ion densities presented in that paper already show definite layers their profiles cannot be used. As discussed in the previous chapter metallic ions are deposited by meteor ablation, which takes place mainly in the region from 70 to 120 km [MacLeod *et al.* 1975]. Actual density profiles for metallic ions are not well known, therefore an arbitrary initial profile with a peak at 120 km and magnitude $3 \times 10^3 cm^{-3}$ was chosen. Since the ion Fe^+ is often detected in sporadic E-layers an ion mass 56 amu was adopted.

The one dimensional simulation was run for several directions of the electric field. The first case used an electric field of magnitude 50 mV/m and its horizontal

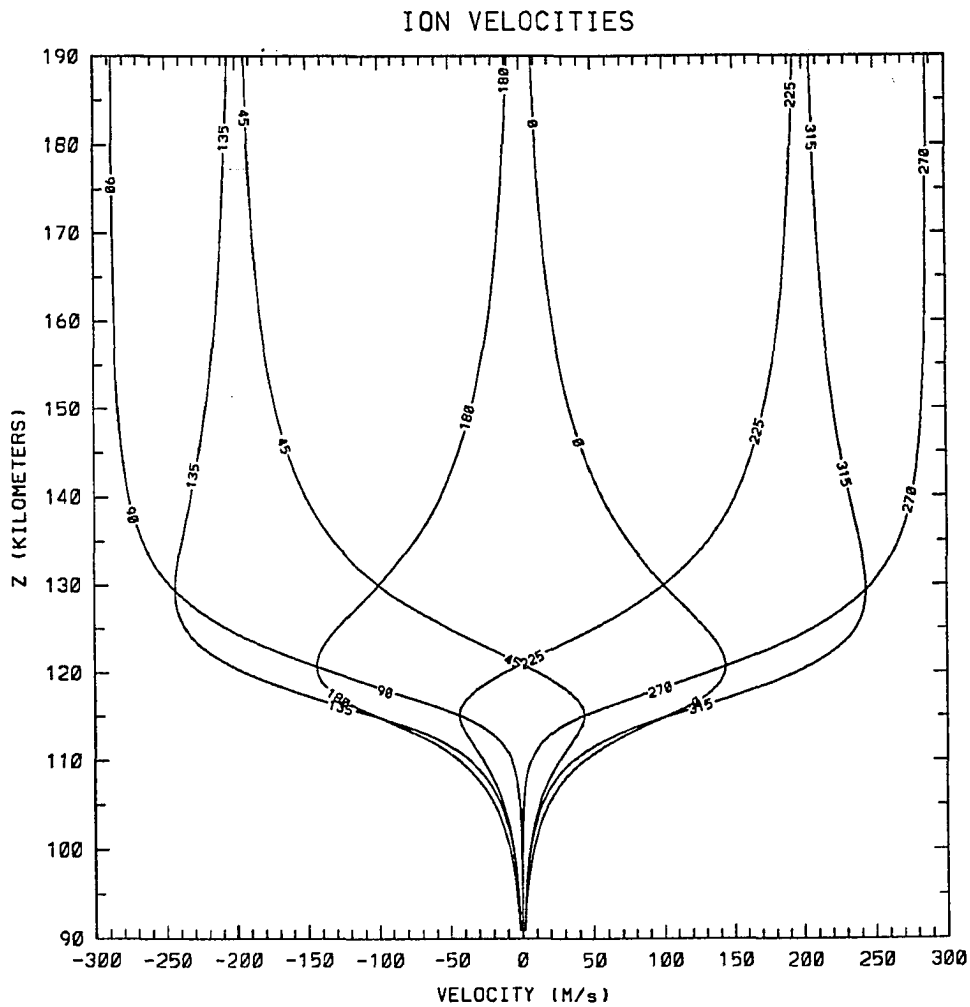

Fig. 4.1. Ion vertical velocity profiles generated for various field directions. The angles indicate the direction of the electric field vector west of north.

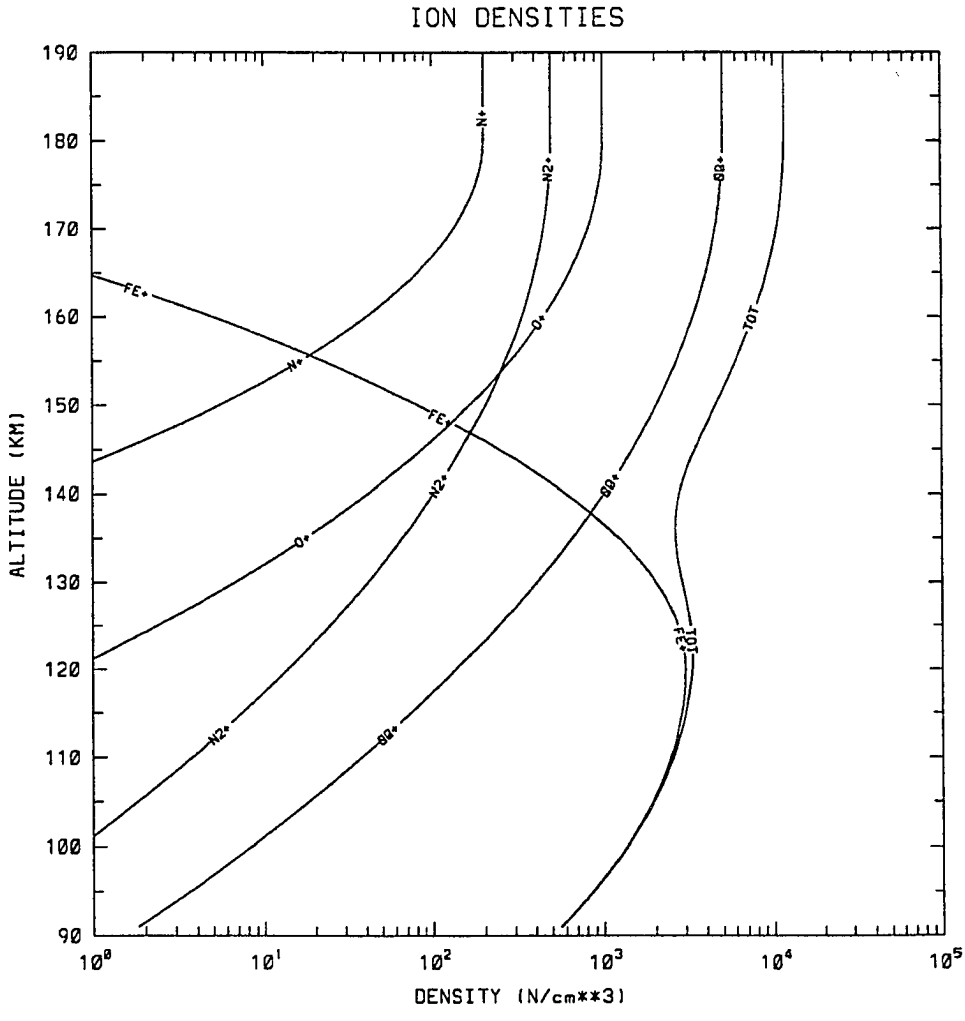

Fig. 4.2. Initial ion density altitude profiles.

component directed in the north west quadrant, 45° west of magnetic north. As discussed earlier, this field produces a velocity profile with a convergent null at approximately 123 km. Figure 4.3 shows the evolution of the density profiles at 250, 500, 750 and 1000 sec. after the application of the electric field. As would be expected, a thin layer forms at the altitude of the velocity null and the layer is composed almost entirely of the metallic ions. The layer forms quite quickly and is well established at 250 seconds. At this time the layer has a peak density of approximately 5.0×10^4 cm^{-3}, and a thickness at half maximum of a few kilometers. The layer is composed primarily of the metallic ions, although there is some enhancement of nitric oxide ions. All of the ions are driven to this altitude, however N^+,O^+, and O_2^+ all react quickly, and do not accumulate at the layer altitude. As time progresses the layer remains fixed in altitude, and reaches maximum density of nearly $1 \times 10^5 cm^{-3}$ within 1000 sec. As the metallic ion density becomes sufficiently enhanced, the nitric oxide ions begin to recombine more readily, and a dip in NO^+ density profile appears. This dip is expected due to the increased electron density, and has been observed in mass spectrometer data (Zbinden *et al.*); however the observations show a greater depletion of the molecular ions.

Next, a field directed to 90° is examined, i.e. magnetic west. This field direction produces no convergent null in the velocity profile, however the flow is downward for all altitudes, decreasing in magnitude with decreasing altitude. This flow leads to a negative divergence of the flux, and thus accumulation, at approximately 110-115 km. Figure 4.4 shows the evolution of the density profiles at 500, 1000, 1500 and 2000 sec. after the application of the electric field. Note that the accumulation is slightly broader than in the previous case on the order of 2–3 km, however the altitude is roughly 108 km, within the range where layers are normally observed. It is of interest to note that the layer is initially composed of nitric oxide ions, and that the metal ions are concentrated in a thinner layer along the bottom of the total layer. As time progresses the density of the NO^+ decreases, and the metallic ions begin to dominate the layer.

The next case examined used a field directed to 180° (magnetic south). The behavior for this field direction is similar to that of the 90° case. As shown in figure 4.5 a layer forms in the altitude region just above 100 km within 500 sec.; the layer

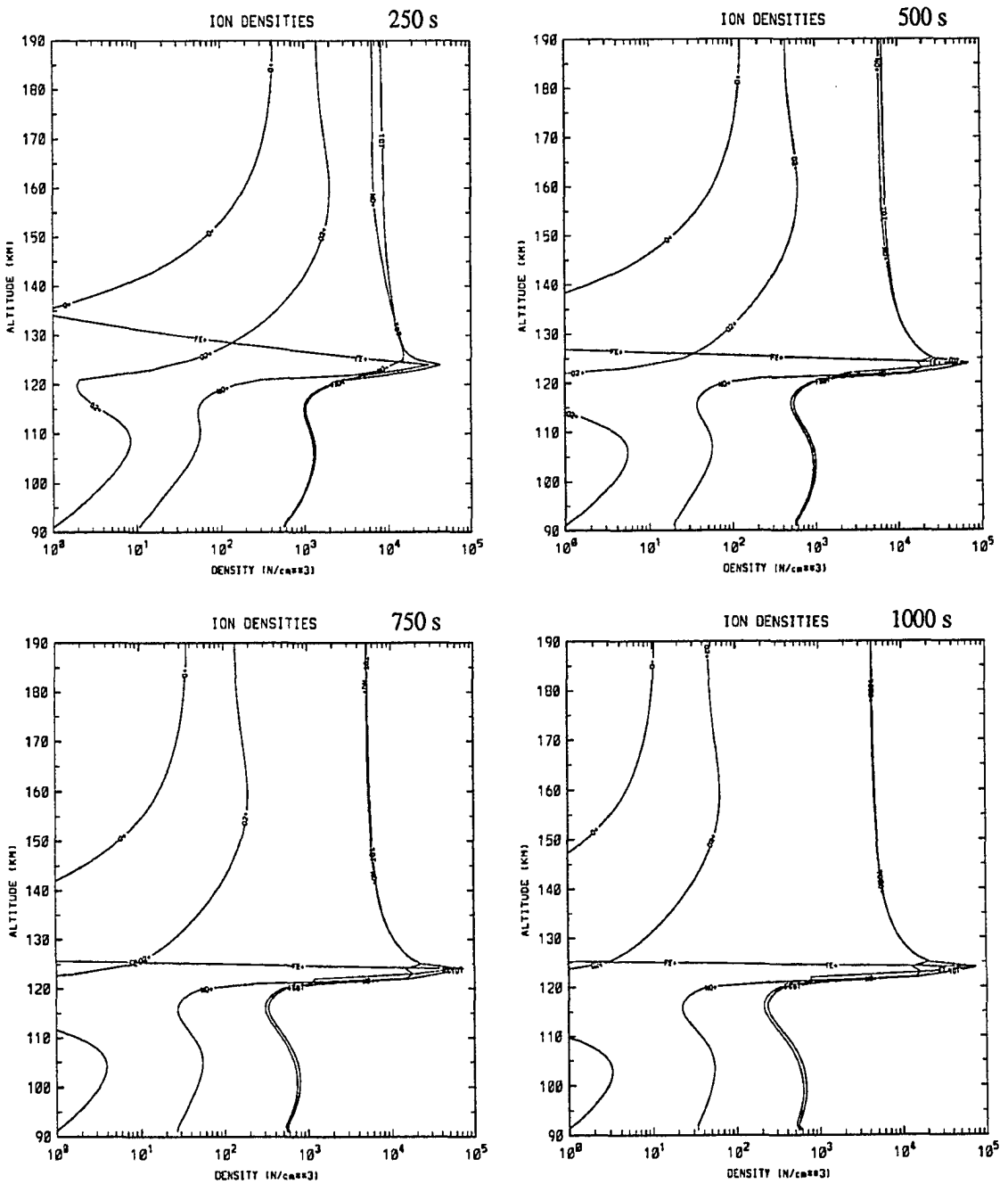

Fig. 4.3. Simulation results showing the time evolution of the density profiles produced by an electric field of 50 mV/m at 45° west of magnetic north.

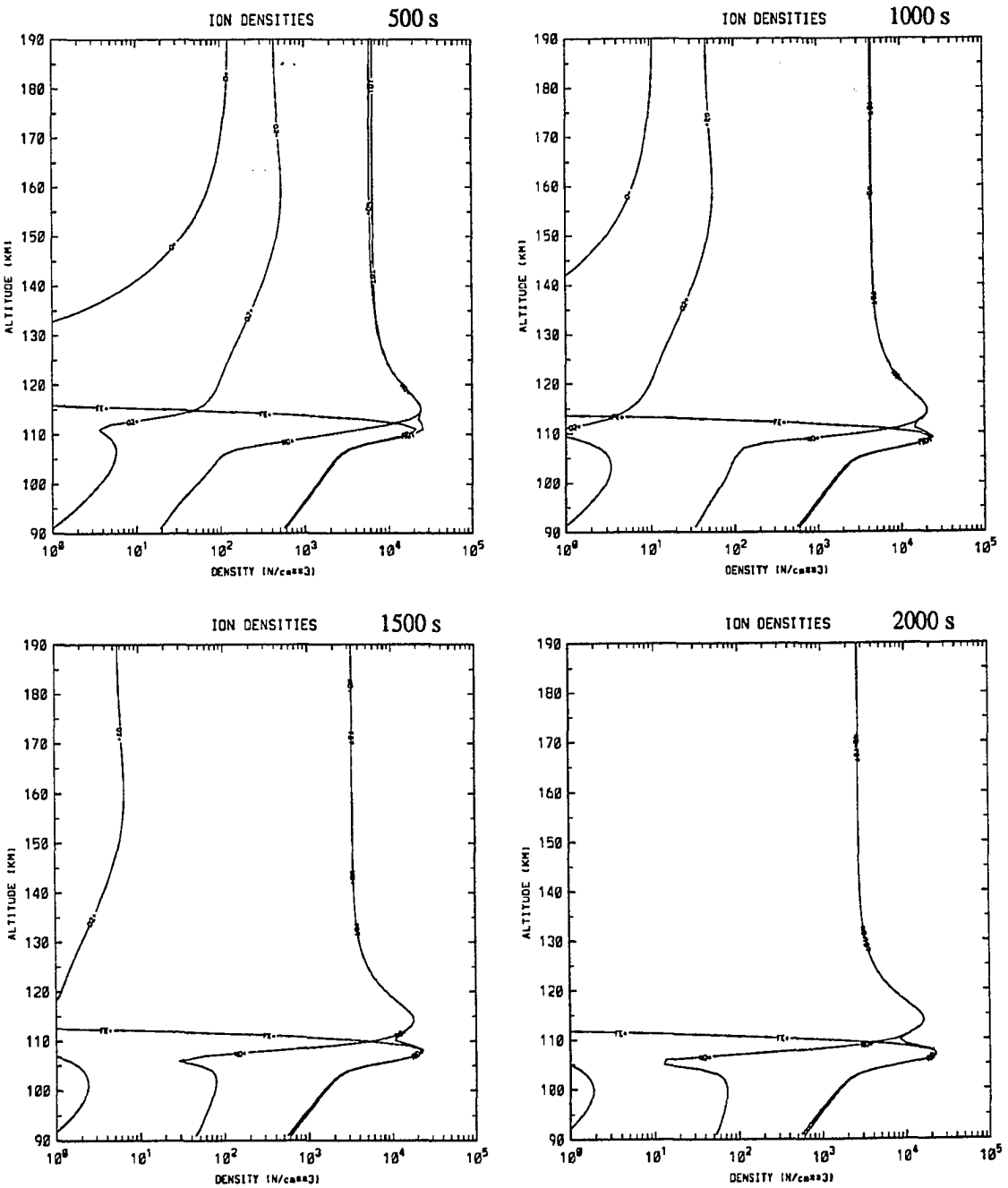

Fig. 4.4. Simulation results showing the time evolution of the density profiles produced by an electric field of 50 mV/m directed to magnetic west.

is broad, with a thickness on the order of 5 km. As time progresses the layer becomes thinner and moves down to below 100 km altitude. The layer remains thicker than the previous cases, and the peak density does not exceed 3×10^4.

The next case examined used a field directed to 270° (magnetic east). This field direction yields an ion vertical velocity profile with upward velocities over the entire altitude range. Figure 4.6 shows the ion density profile generated at 2000 sec after the application of the electric field . The ions are forced upwards and flow out of the upper boundary, leaving the lower altitude region depleted of all ionization.

The final field direction examined was 0°, magnetic north. Figure 4.7 shows the density profile obtained from this field direction at 2000 sec after the application of the field. Again the velocity profile shows upward velocities over the entire altitude region. Again the lower altitude regions become depleted of ionization.

The electric field used in the simulation is static, however the electric field in the ionosphere is usually changing in magnitude and direction, particularly near midnight in the auroral zone. In general in the auroral zone, for the afternoon and evening sector, the electric field points approximately towards the magnetic north, and in the morning sector points approximately to magnetic south. In the period a few hours to either side of magnetic midnight the field reverses and may change direction in an erratic manner rotating through west and to the south (eg. Horwitz *et al.*;1978). It is possible that thin layers may be formed at an altitude above 120 km by a field directed to the north-west, then as the field rotates to the south the layer may be transported to a lower altitude. To simulate this behavior the field was directed in the north west quadrant (45° west of magnetic north) for a period of 800 sec., a time sufficient for the formation of a very thin layer, and then switched to magnetic south for a period of 1200 sec., figure 4.8 shows the density profiles for this run. The figure shows that the layer is essentially the same as was obtained in the case in which the field was pointed to magnetic south for the entire time. The initial very thin layer did not transport in tact, but rather dispersed and reformed the layer for the south directed field.

The effects of the neutral wind were examined for various field directions and wind directions. The velocity profiles obtained for some of the field directions, although are very similar to those obtained in the absence of the wind, have some

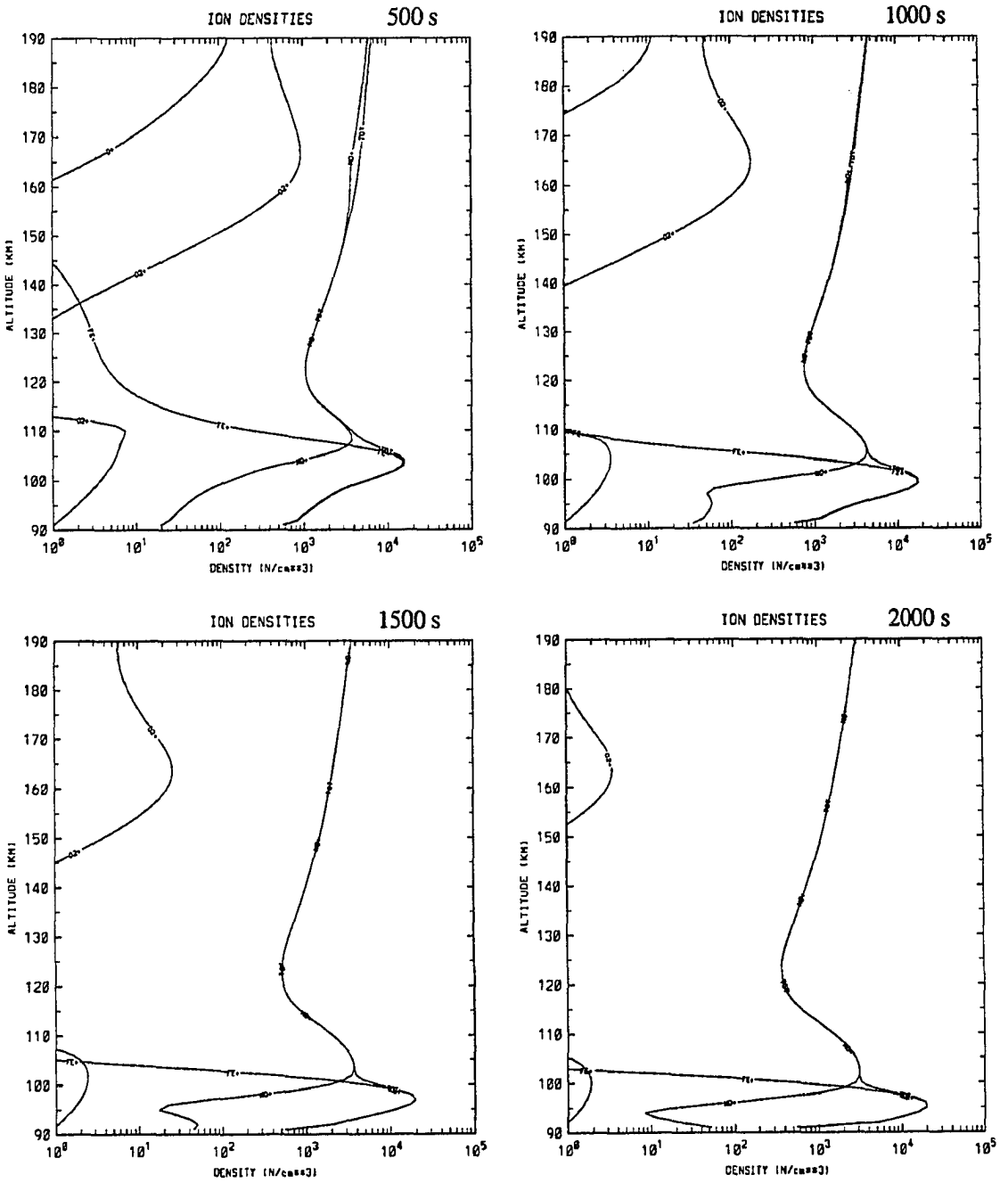

Fig. 4.5. Simulation results showing the time evolution of the density profile produced by an electric field of 50 mV/m directed to magnetic south.

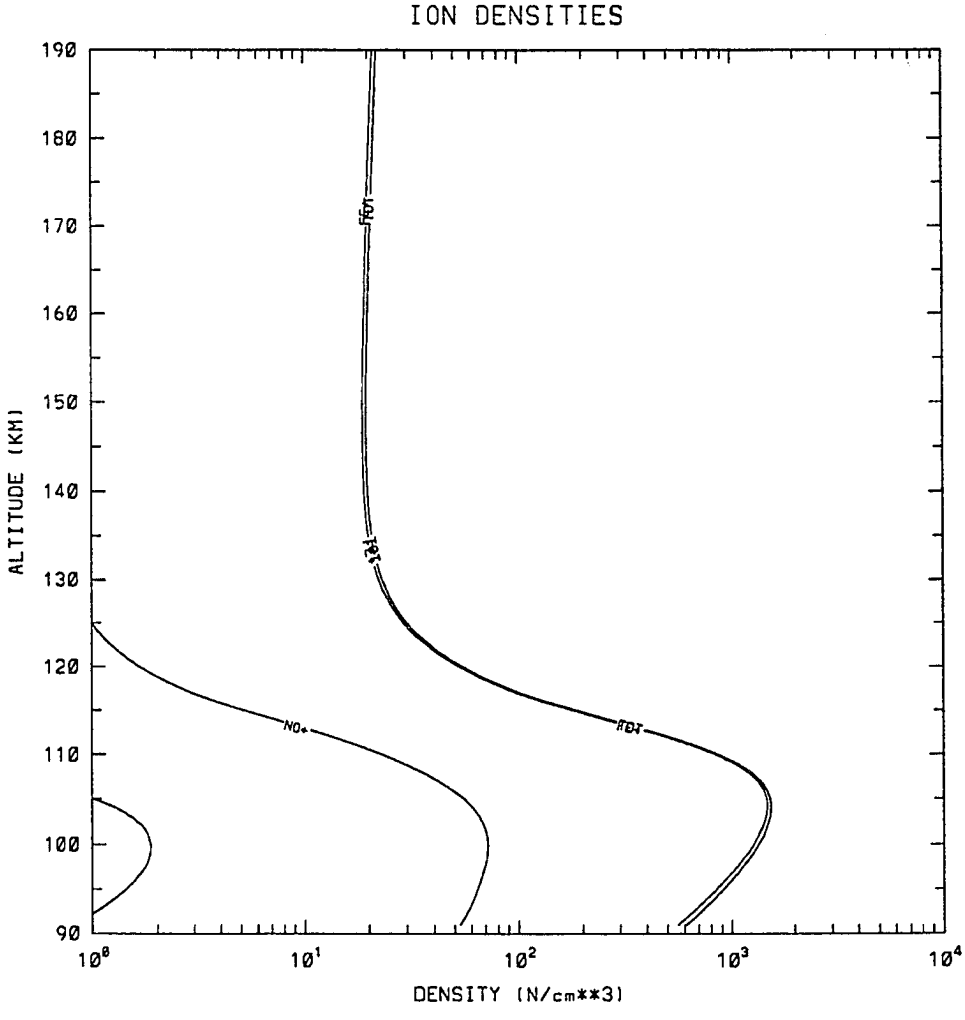

Fig. 4.6. Simulation results showing the density profile generated by an electric field of 50 mV/m directed to magnetic east.

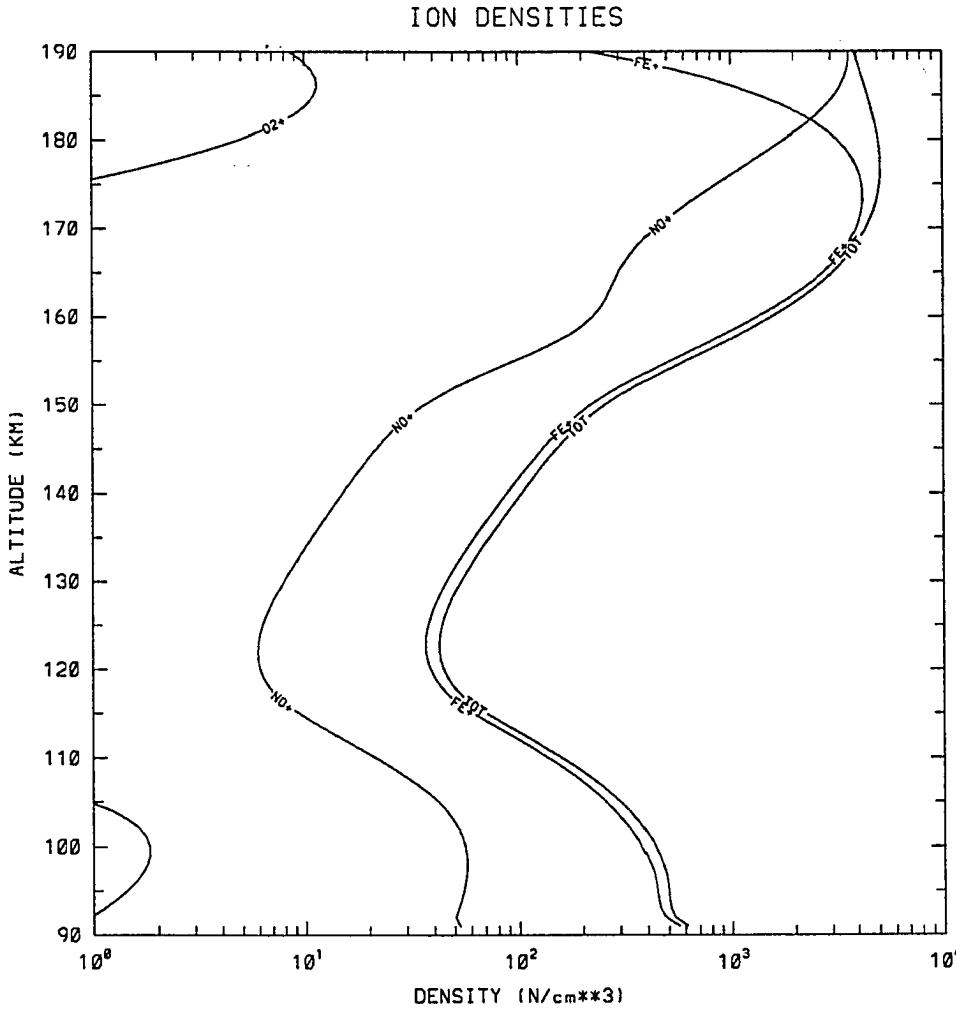

Fig. 4.7. Simulation results showing the density profile generated by an electric field of 50 mV/m directed to magnetic north.

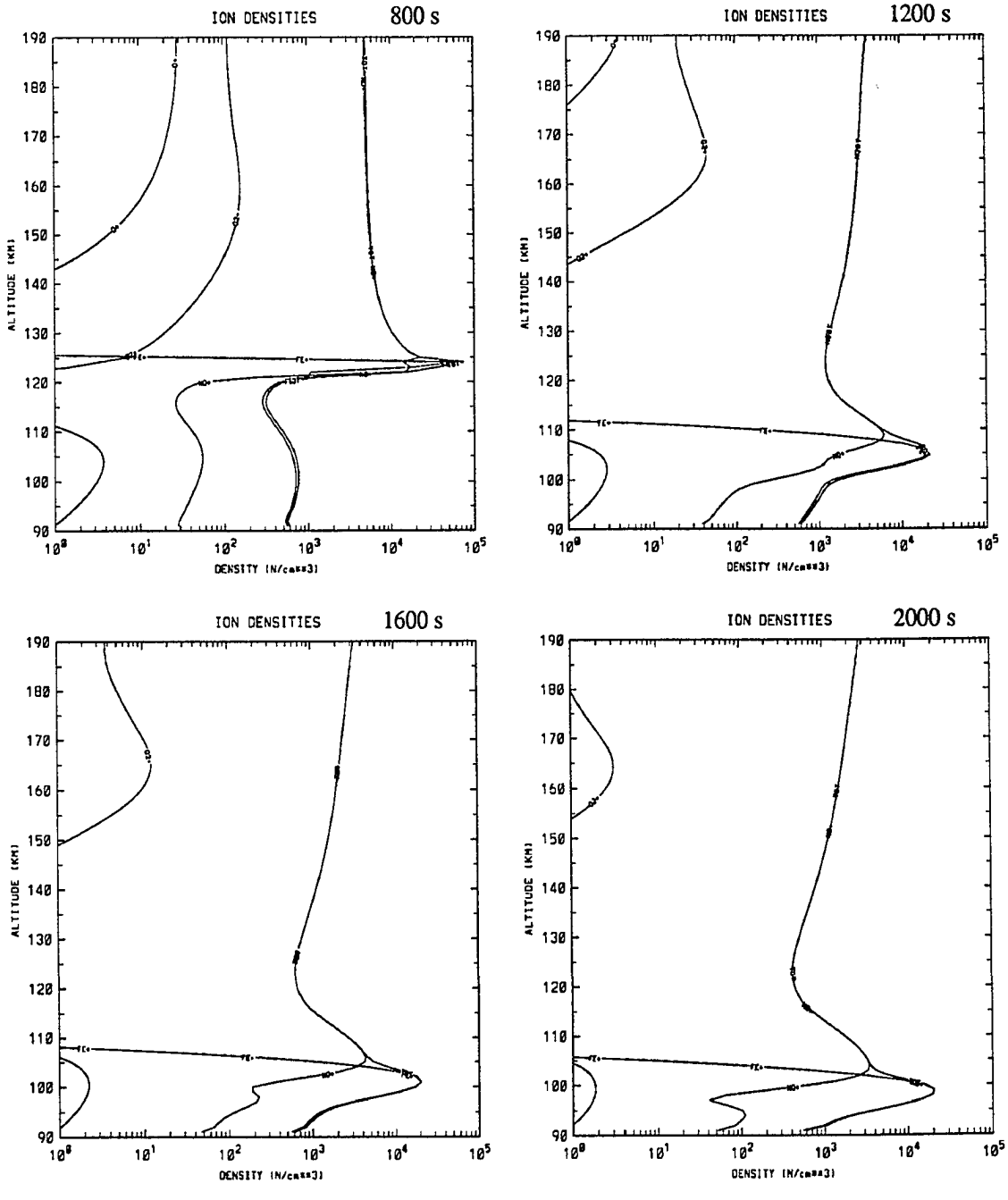

Fig. 4.8. Simulation results showing the time evolution of the density profile for changing conditions. Initially the field was 50 mV/m directed to 45° west of north for 800 sec, then changed to magnetic south for 1200 sec.

significant differences. Figure 4.9 shows the velocity profile obtained for an electric field of 50 mV/m at 90° west of north and a neutral wind of 200 m/s directed to magnetic east. Although the profile looks very similar to that obtained in the absence of the neutral wind, the profile has a convergent null at roughly 110 km. This leads to the production of a very thin layer of ionization at an altitude just above 110 km (figure 4.10). This behavior, ie. causing a thinner layer, is limited to a small range of field directions from magnetic west to about 100° west of north. A stronger neutral wind would expand this range.

The neutral wind may have a vertical component which, although much smaller than the horizontal component, has significant effect on the ion vertical velocity. An upward neutral velocity of about 0.5 m/s will lead to convergent nulls of the ion vertical velocity near 100 km altitude depending on electric field magnitude and direction, and the horizontal neutral wind magnitude and direction. The vertical neutral wind magnitude associated with tides is of this order of magnitude (Forbes, 1982), and short term localized winds of much greater magnitude may exist (Hoppe and Hansen, 1986). Figure 4.11 is a plot of the density profile obtained for a field 20 mv/m at 110°, and a vertical neutral wind of 0.5 m/s upward. As the figure shows this results in a thin layer forming at about 104 km altitude.

4.4 Temperature

The large electric field used here, with the assumption the neutrals are stationary, leads to significant Joule heating. The ion temperatures over the altitude range 110 - 190km are elevated to above 2000° K, well above the neutral and electron temperatures. The profiles are in fairly good agreement with previous work done by both Rees and Walker (1968) and Roble and Hastings (1977). The ion temperature profile for the 45° field, shown in figure 4.12, shows some additional enhancement in the ion temperature at the altitude where the metallic ion layer forms. This enhancement results from additional Joule heating due to the increased average ion mass within the thin layer.

In calculating the temperature profiles the neutral atmosphere is assumed to be stationary, while in truth it is in motion and the ion motion accelerates the neutrals in the direction of the ions. As the neutrals are accelerated by the ions

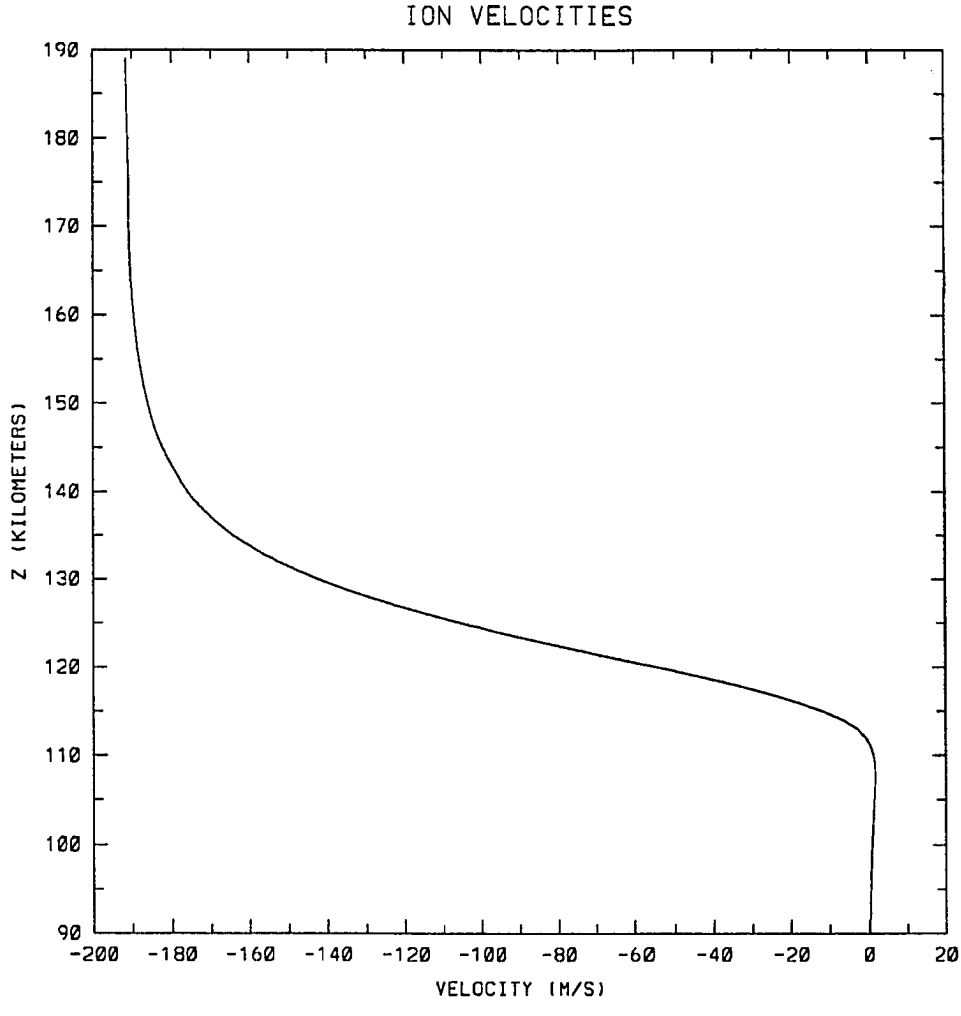

Fig. 4.9. Ion vertical velocity profile obtained for an electric field of 50 mV/m directed to magnetic west and a neutral wind of 200 m/s directed to magnetic east.

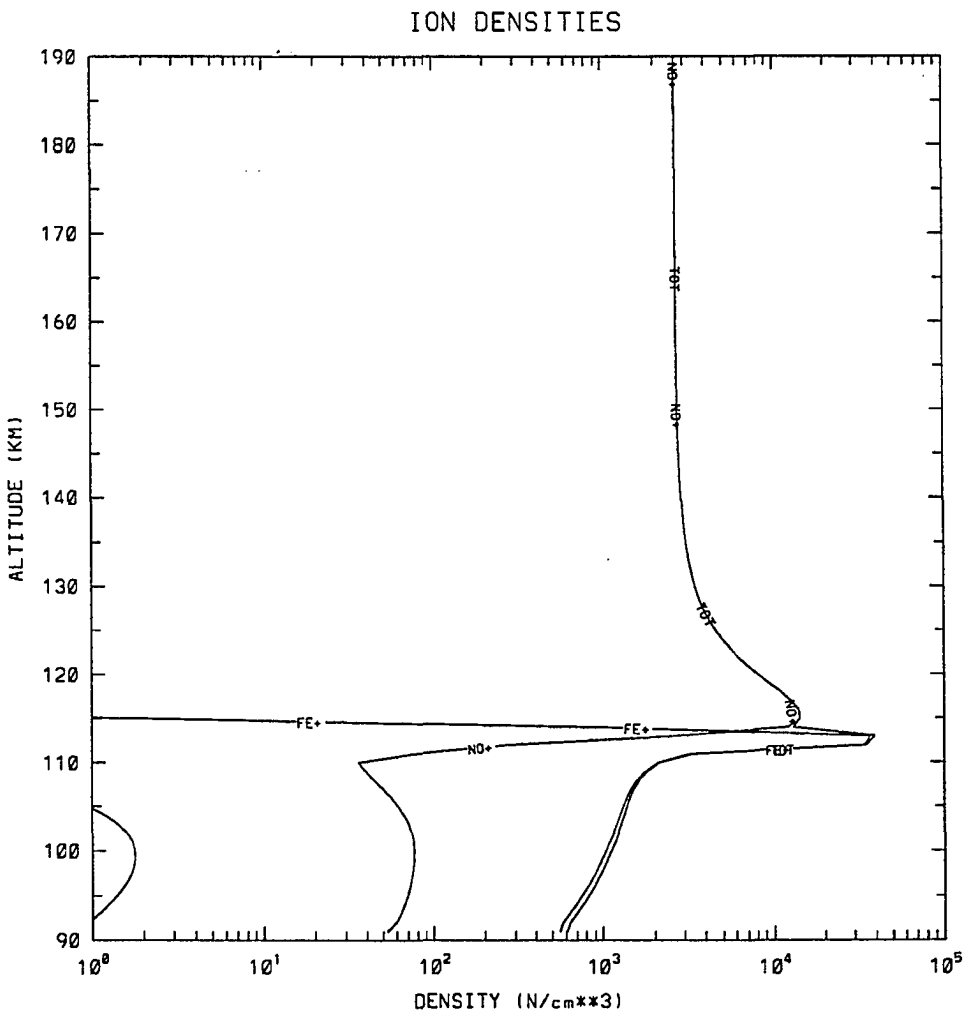

Fig. 4.10. Density profile obtained for electric field of 50 mV/m directed to magnetic west and a neutral wind of 200 m/s directed to magnetic east.

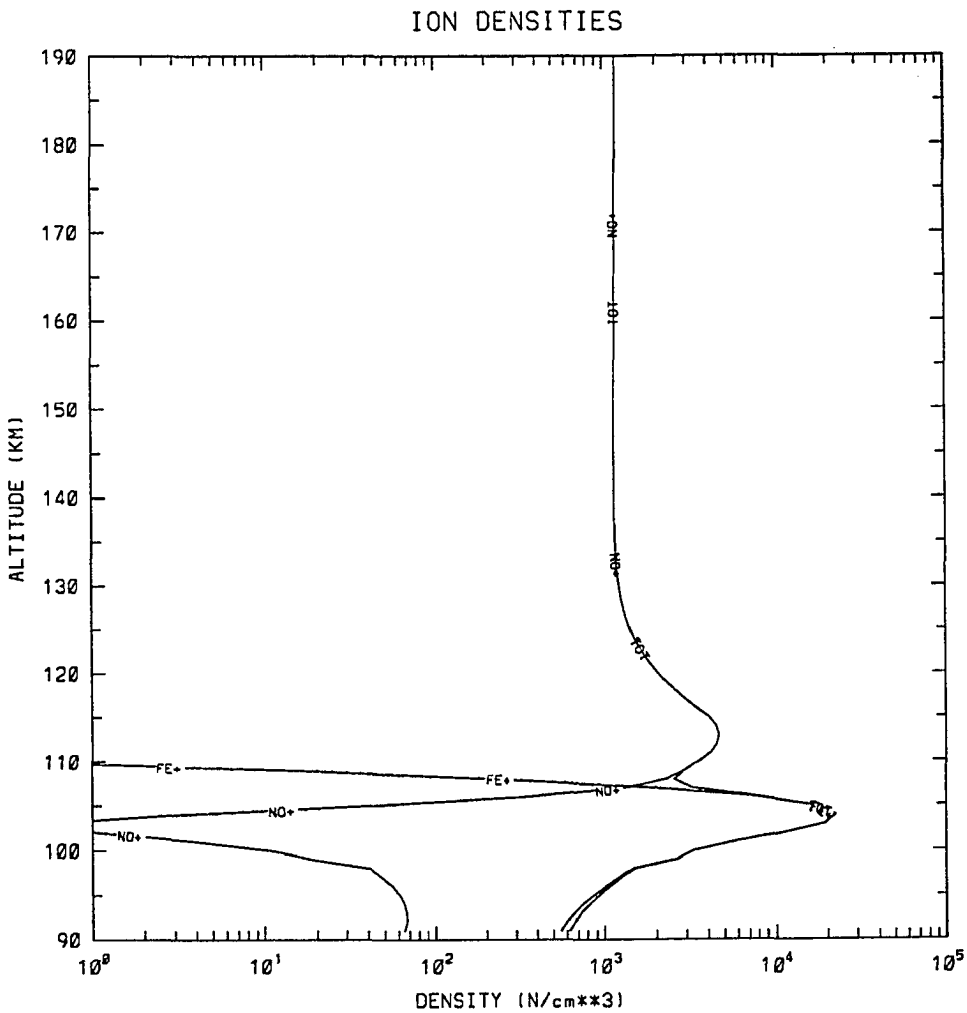

Fig. 4.11. Density profile obtained for a field of 20 mV/m directed to 110°, and a vertical neutral wind of 0.5 m/s upward.

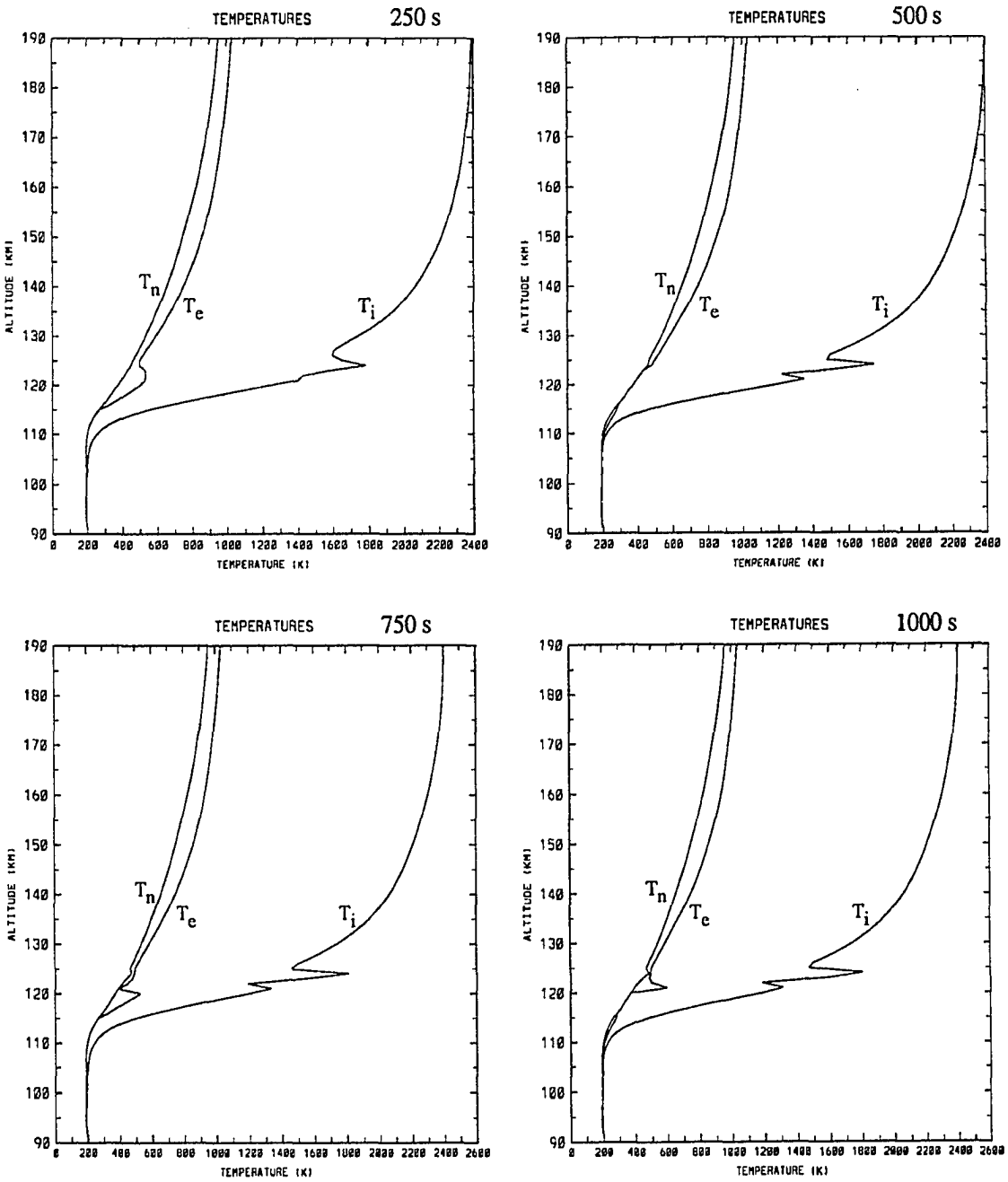

Fig. 4.12. Time evolution of the temperature profile obtained for an electric field of 50 mV/m directed to 45°.

the velocity difference between the ions and neutrals is decreased, thus decreasing the joule heating. The time constant for the neutral gas to respond to the ion motion, and for the temperature to equilibrate is on the order of two hours (eg. Fedder and Banks, 1972). Therefore the heating computed here is likely to be an upper limit. These conditions would only occur during the transient period after an initial increase in the electric field and before the neutral gas begins moving in the direction of the ions.

4.5 Discussion and Summary of One Dimensional Model Results

Electric fields directed to the north-west and south-west resulted in the formation of a layer of enhanced ion density. The field directions of 90° and 180° both produced layers that were initially broad but became thinner with time; the altitudes of these thin layers are similar to observations of sporadic-E layers. It may be concluded that a general downward plasma flow that decreases in magnitude with decreasing altitude can cause the formation of sporadic-E layers, and that electric fields directed between 0° and 180° west of magnetic north can cause this flow pattern. Examining the velocity profiles from other field directions shows that fields directed between 180° and 270° also have downward flow over some altitude region and thus could also lead to layer formation.

Electric fields directed to the north-east and south-east did not result in the formation of thin layers. For the most part these field directions lead to upward flow. This flow moves the metallic ions to higher altitudes, and indeed would explain why metallic ions are often found in the F-region, while the ablation region is in the lower E-region (Grebowsky and Pharo, 1985).

The profile for the changing field conditions showed that layer formation depends more on the current field direction than on the history of the field. Although a very thin layer was formed by the initial field, after the field changed the behavior was essentially the same as if the field had been pointed to the final direction the whole time.

The neutral wind also may play a role in layer formation at high latitudes. As was shown, a constant neutral wind in conjunction with the electric field may cause convergent nulls in the ion vertical velocity for a limited range of field directions,

even though the field alone would not produce a convergent null. This appears to be effective only for a limited range of electric field and wind directions, and only causes significant differences above 110 km. An upward neutral wind of small magnitude has a similar result but is effective for a broader range of field directions, and is effective at lower altitudes. In addition wind shears, although not as effective as at mid-latitudes, may play a role in the formation of thin layers at high latitudes.

The existence of very thin layers much below 110 km is not well explained by the model presented here. Although the layers formed by this mechanism for electric fields directed to the south-west quadrant would appear as sporadic-E layers in ionosonde data, they are not as thin as layers often observed by ISR or rockets. The layers generated by the south directed fields are on the order of 5 km in thickness, full width at half maximum. As discussed, changing field directions do not appear to be capable of forming the very thin layers, and the layers formed by the combined action of an eastward neutral wind and the electric field only appear to be very thin near 110 km or higher. Upward neutral motion of roughly a half meter per second will lead to convergent flow in the ions near to 100 km, however the layer formed in the simulation was still on the order of 2–3 km in thickness. Stronger upward neutral winds are possible but since the very thin layers are observed for long periods the conditions to maintain the layer must be persistent. Also since the observations are frequent, the conditions for formation must occur regularly.

The existence of a peak in the ion temperature profile may have implications for the analysis of incoherent scatter radar (ISR) data. Quite often ISR data will exhibit a decrease in ion temperature at the altitude of a sporadic-E layer. A common procedure for analysis of such data is to change the ion mass in the analysis routine until the temperature matches that outside of the layer. From this procedure the percentage of metal ions in the layer may be determined. The results here show it is possible that this may under estimate the metal ion content of the layer because of the ion temperature increase at the layer. It is likely that this will be a problem only if the layer is in the altitude region of significant joule heating.

4.6 Three Dimensional Model

Starting with the one dimensional model a three dimensional model of the high latitude region was constructed. The continuity and momentum equations were solved in three dimensions while the energy equation is simply solved in one dimension at each location. The thin layer model uses externally supplied model of the convection pattern, neutral wind pattern, and photoionization pattern.

A dipole magnetic field is assumed to be a sufficient description for the earth's field. The potential for a magnetic dipole is given by:

$$\Phi_m = \frac{\vec{m} \cdot \vec{x}}{r^3} \tag{4.9}$$

Where $\vec{m}$ is the earths dipole moment. The field is given by the negative of the gradient of the potential:

$$B_r = \frac{2m\cos\theta}{r^3} \tag{4.10}$$

$$B_\theta = \frac{-m\sin\theta}{r^3} \tag{4.11}$$

It is convenient to write the magnetic field in terms of the magnitude and the dip angle:

$$B_x = B_{mag}\sin(Dip) \tag{4.12}$$

$$B_z = B_{mag}\cos(Dip) \tag{4.13}$$

Where the magnitude and dip are given by:

$$B_{mag} = \frac{B_0}{2}\sqrt{1+3\cos^2\theta} \tag{4.14}$$

$$Dip = \pi - \tan^{-1}\left(\frac{\tan(\theta)}{2}\right) \tag{4.15}$$

The leading constant, B_0, is the magnitude of the field at the north pole at the altitude of interest. The angle θ is the colatitude.

The convection model used is that of Heppner and Maynard (1987). The model is based upon data from Ogo 6 and DE 2 satellites. Figure 4.13 shows a potential pattern for southward B_z conditions, pattern A from the model. The pattern shows antisunward flow over the pole, and the return flow at lower latitudes. There is

some distortion both at the noon and midnight boundaries of the polar cap. The model is discussed in more detail in the previous chapter.

The neutral wind model is the Vector Spherical Harmonic (VSH) model from the University of Michigan Space Physics Research Lab (Killeen *et al.*, 1987). The neutral wind patterns are produced from the output of the NCAR-TIGCM model. The model comes with coefficient libraries for TIGCM outputs for varying geophysical conditions. To use the model the parameters required are: Julian day, f10.7 solar flux, AP, UT, altitude, latitude, and longitude. Figure 4.14 shows the neutral wind field from the model for four different heights at 33 km intervals. The parameters used to generate this set of plots are: Jday=250, F10.7=250, AP=50, UT=0. As can be seen in the figure, at the high altitudes the neutrals are highly influenced by ionospheric convection showing the typical two cell pattern while not coinciding identically with the ionospheric convection pattern. At lower altitudes the winds do not show any influence of the ion drag. Ion drag is only one of the forces which influence the motion of the neutral atmosphere, others include advection, pressure force, Coriolis force, and viscous drag. At the low altitudes pressure and Coriolis forces dominate the motion.

In this simulation a rather simple minded approach is taken for the photoionization pattern in that the geographic and magnetic poles are taken to be coincident for the determination of the solar zenith angle, and location of the terminator. As the main interest here is to study the general behavior of the night side and not to make any prediction about specific geophysical conditions it will have little effect.

As was discussed above the ion velocity is mainly determined by the electric field and the neutral wind. At high altitudes the velocity is almost entirely $\vec{E} \times \vec{B}$ while at the lowest altitude the ions move with the neutral wind. Figure 4.15 shows the ion velocity field at 33 km intervals using the neutral wind and convection pattern discussed above. At 90 km the ion velocity field is nearly identical to the neutral wind. At the highest altitudes the flow lines are parallel to the contours of the potential pattern. This is of course as expected since at high altitudes the plasma is essentially collisionless. Coming down in altitude collisions begin to play a part, and the velocity vector rotates from the $\vec{E} \times \vec{B}$ direction to the parallel to $\vec{E}$ direction, finally at the lowest altitudes the collisions become so dominant that

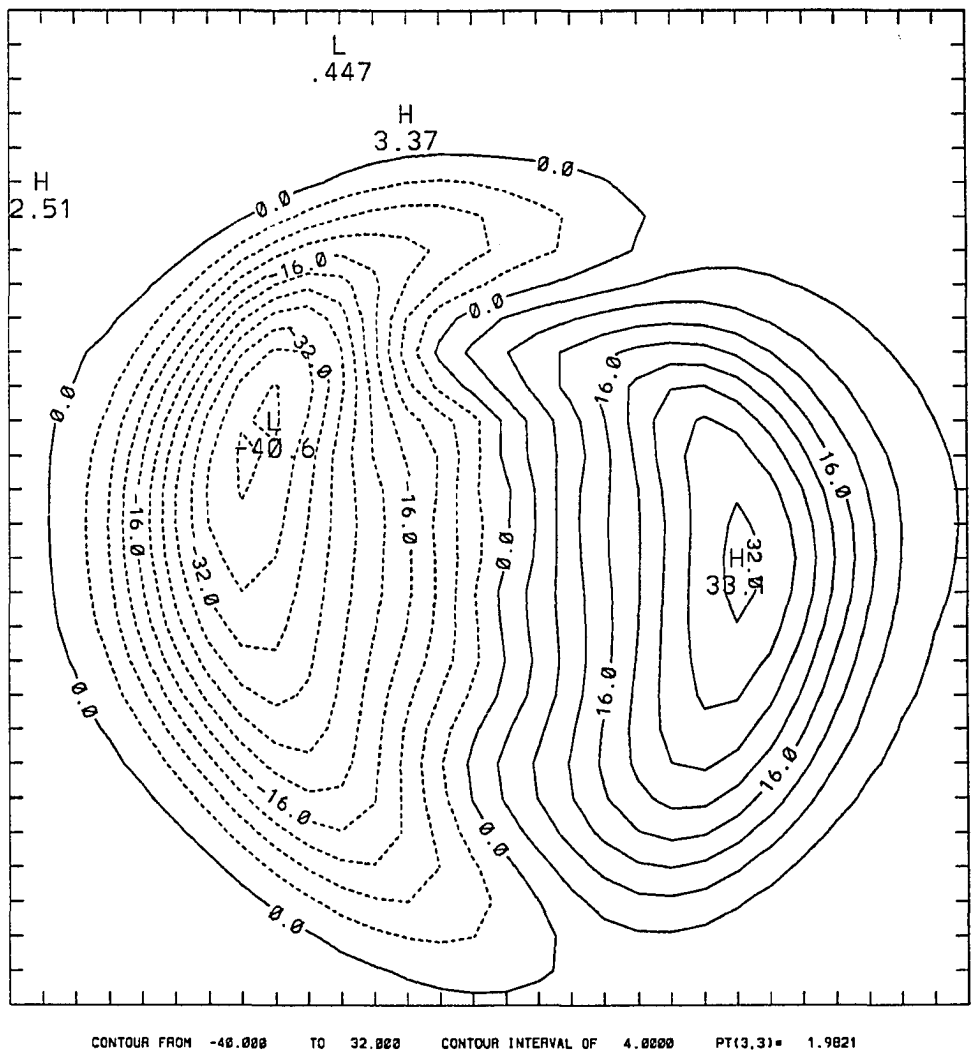

Fig. 4.13. Potential pattern 'A' from the Heppner-Maynard convection electric field model.

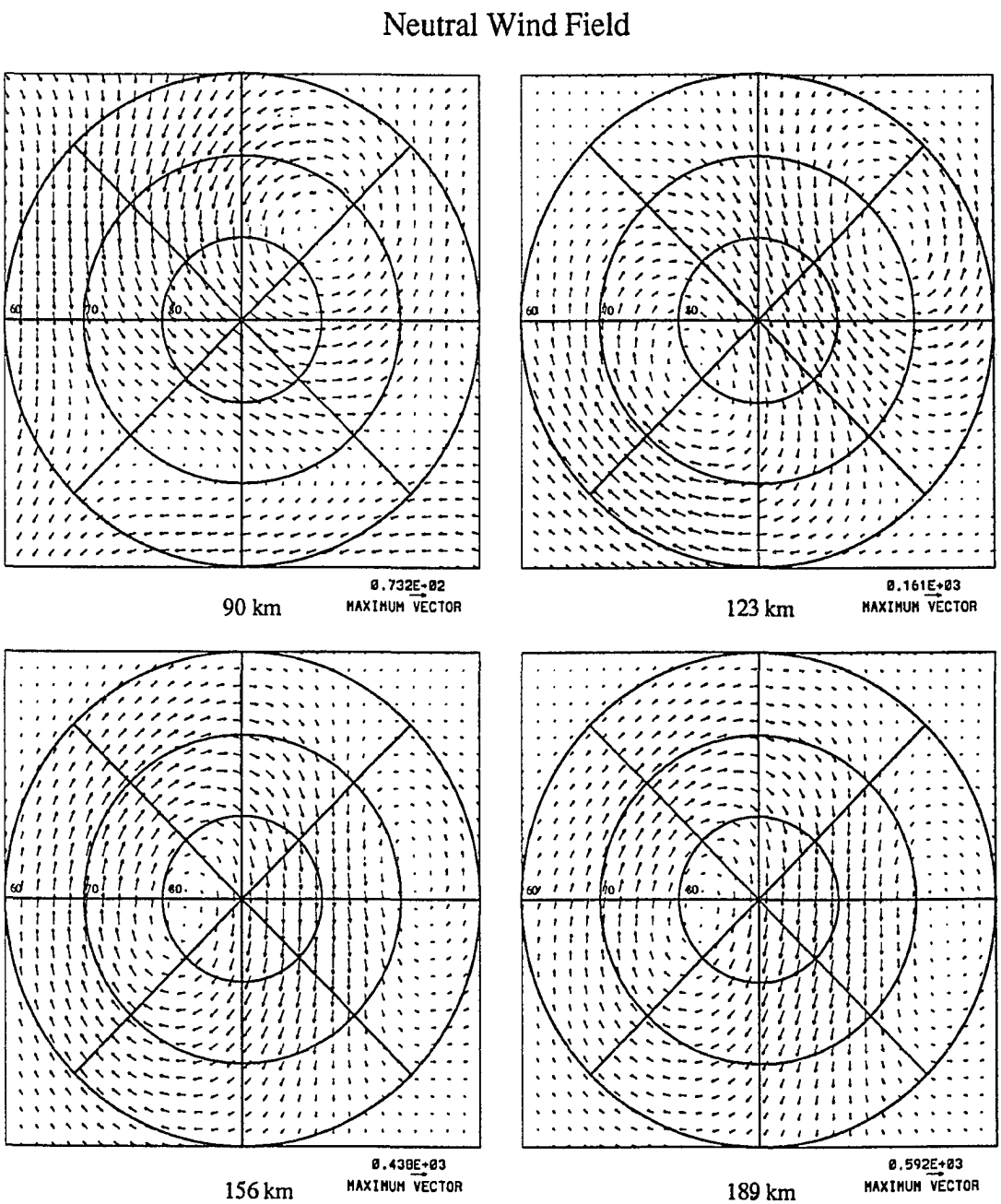

Fig. 4.14. The neutral wind field for the polar cap region at 90, 123, 167, and 189 km, generated by the VSH neutral wind model.

the ions become 'tied' to the neutrals and thus flow with the neutral wind. Note also the magnitudes of the velocities; over a kilometer per second at high altitudes, and less than a hundred meters per second at the low altitudes. This behavior makes the concept of flux tubes difficult to apply in the lower ionosphere. In the higher ionosphere the equations of continuity and energy may be solved in one dimension along a flux tube, and the trajectory of the flux tube traced in time, this is the Lagrangian approach. With the velocity differences between the high and low altitudes the flux tubes would become stretched and twisted with time. Because of this the Eulerian approach is required; a three dimensional grid is established and the equations are solved at each point.

4.7 Results of Three Dimensional Simulation

The simulation was run for the various convection patterns. Figure 4.16 is a contour plot of peak electron density below 140 km from the run using pattern 'A' from Heppner-Maynard. This pattern corresponds to southward B_z and negative B_y. The white circles on the plot indicate the latitudes of Sondrestrom and EISCAT. The day side shows typical high and fairly uniform densities produced by solar photo-ionization. There is some depletion of density at dusk where the low density night side plasma is convected into the day side, and vertical flow is upward. On the night side there is considerable spatial structure. An area of very low densities is found between dusk and midnight in the latitude region between 60° and 70°. In this area there is no photo ionization, and the ion vertical velocity is upward over the entire altitude range. Any E-region ionization is either lost through recombination or transported up to F-region altitudes. At the lowest latitudes the densities are generally low, but are higher than in the 60° to 70° latitude region. At the lower latitudes the electric field is small and there is little transport of ionization; the density changes are due solely to recombination. North of 70° in the pre-midnight sector and between 60° and 70° in the post-midnight sector there is an area of fairly high densities ($> 10^4$).

Figure 4.17 shows all areas where the densities are concentrated in a layer with thickness of less than 5 kilometers at half maximum. It is seen to coincide with the high density area of figure 4.16. Figure 4.18 shows electron density contours as a

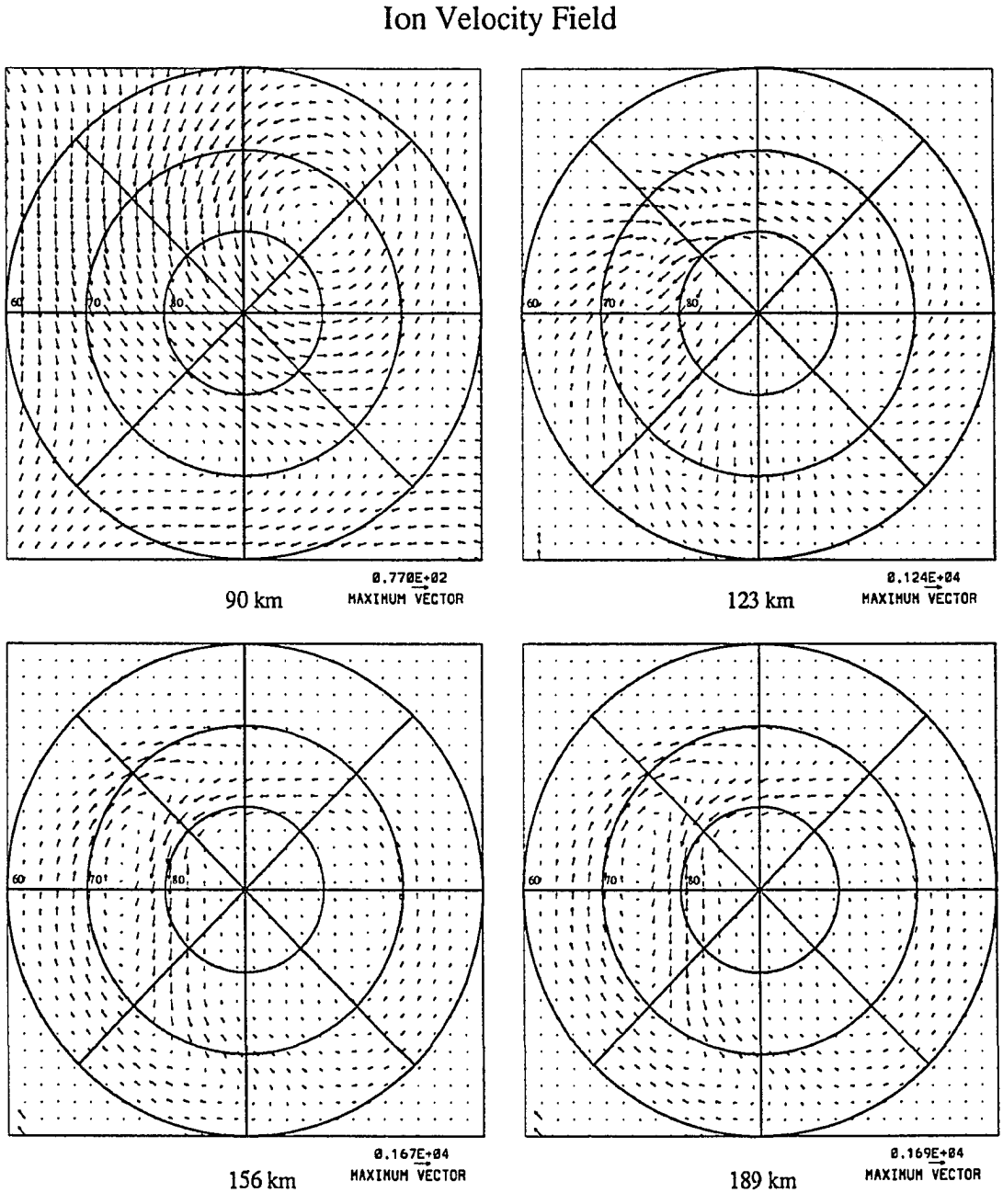

Fig. 4.15. Ion velocity field for the polar cap area at 90, 123, 156, 189 km, generated using Heppner-Maynard potential pattern 'A' and the neutral wind field shown in figure 4.14.

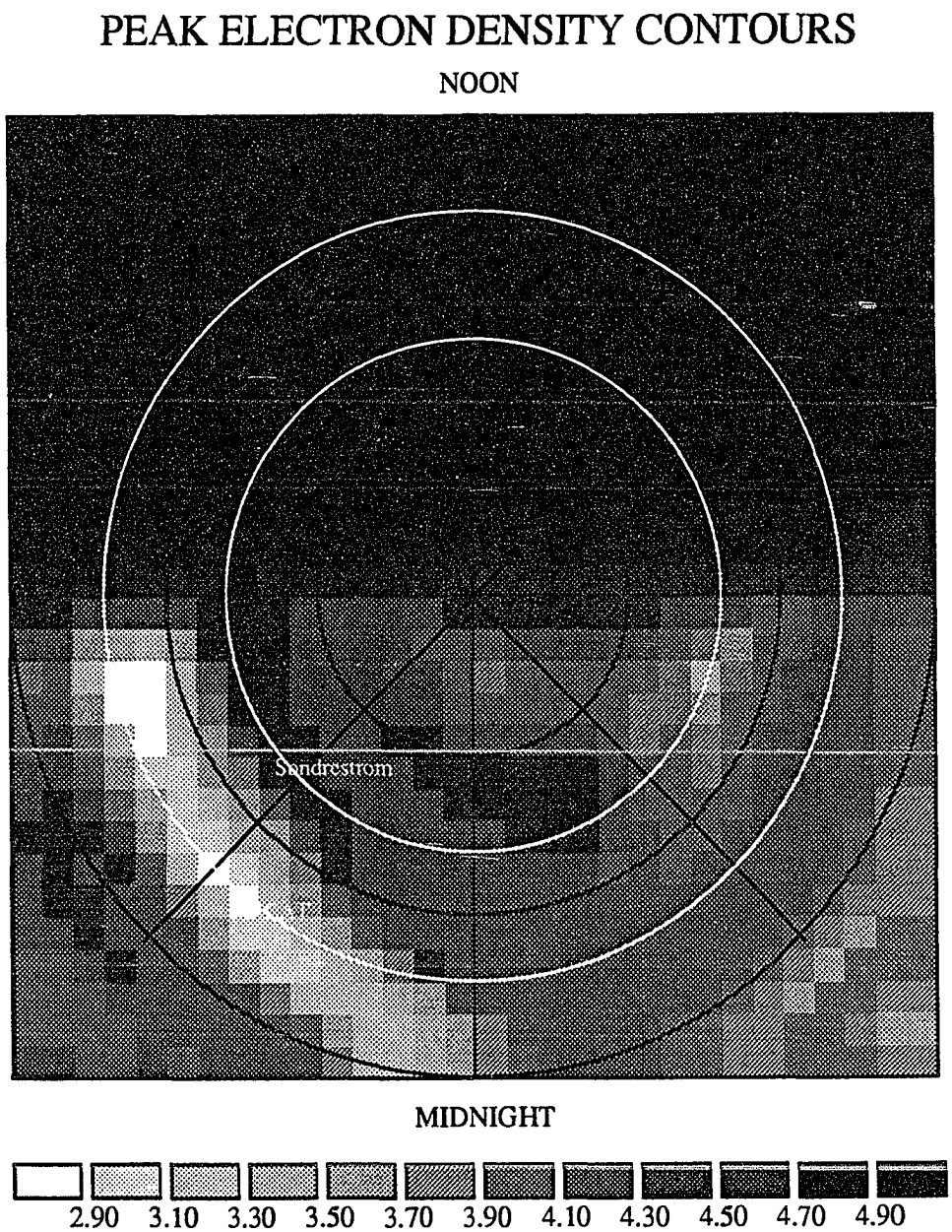

Fig. 4.16. Peak electron density contours below 130km using Heppner-Maynard potential pattern 'A'.

function of altitude and magnetic local time at the latitude of Sondrestrom, 4.19 shows the same for EISCAT latitude. In both plots there is a layer of ionization below 120 km. In figure 4.18 the layer forms in the period around 2100 MLT at an altitude of roughly 105 km remains low and then increases in altitude just before magnetic midnight. In figure 4.19 the layer forms just after magnetic midnight at roughly 108 km, then comes down in altitude to below 100 km and remains until morning.

The next run of the simulation is for Heppner-Maynard (H-M) pattern 'BC', which corresponds to southward B_z and positive B_y. It is similar to pattern 'A' except it is slightly rotated and the dusk cell is larger. Figure 4.20 shows the convection pattern, peak density contours, and the density profiles for Sondrestrom and EISCAT. The peak contours are very similar to those obtained in the previous case. There is a region of low densities on the evening side between 60° and 70°, the area is slightly larger in this case. There is an area of low densities on the dawn side north of 70°. This depletion is present in the previous case but is more pronounced here. The area of thin layers is again roughly north of 70° on the evening side, and between 60° and 70° on the morning side, although it extends to lower latitudes in this case. The density profile for Sondrestrom latitude shows the same general features of the previous run. A layer forms near 2100 MLT and persists until 2400. In this case however the layer appears and departs more suddenly. The EISCAT profile also shows the same general features as the previous run. A layer forms near 2400 MLT and persists until morning. In this case the layer forms earlier.

The results for H-M pattern 'DE' are shown in figure 4.21; this pattern is very similar to pattern 'A' but has a larger dawn cell. Again the results are very similar to the two previous cases. The peak density contours are in essentially the same area as the case for pattern 'A', however the area of depletion on the evening side is more pronounced, and the area of depletion on the dawn side north of 70° is a little larger. The density profile for Sondrestrom latitude shows the same general features, but appears more stable in altitude than in case 'A'. The EISCAT profile is essentially the same as in the previous cases.

The next run is for H-M pattern 'BCP', corresponding to a distortion of pattern 'BC' for B_z weakly northward. The resulting density contours are shown in figure

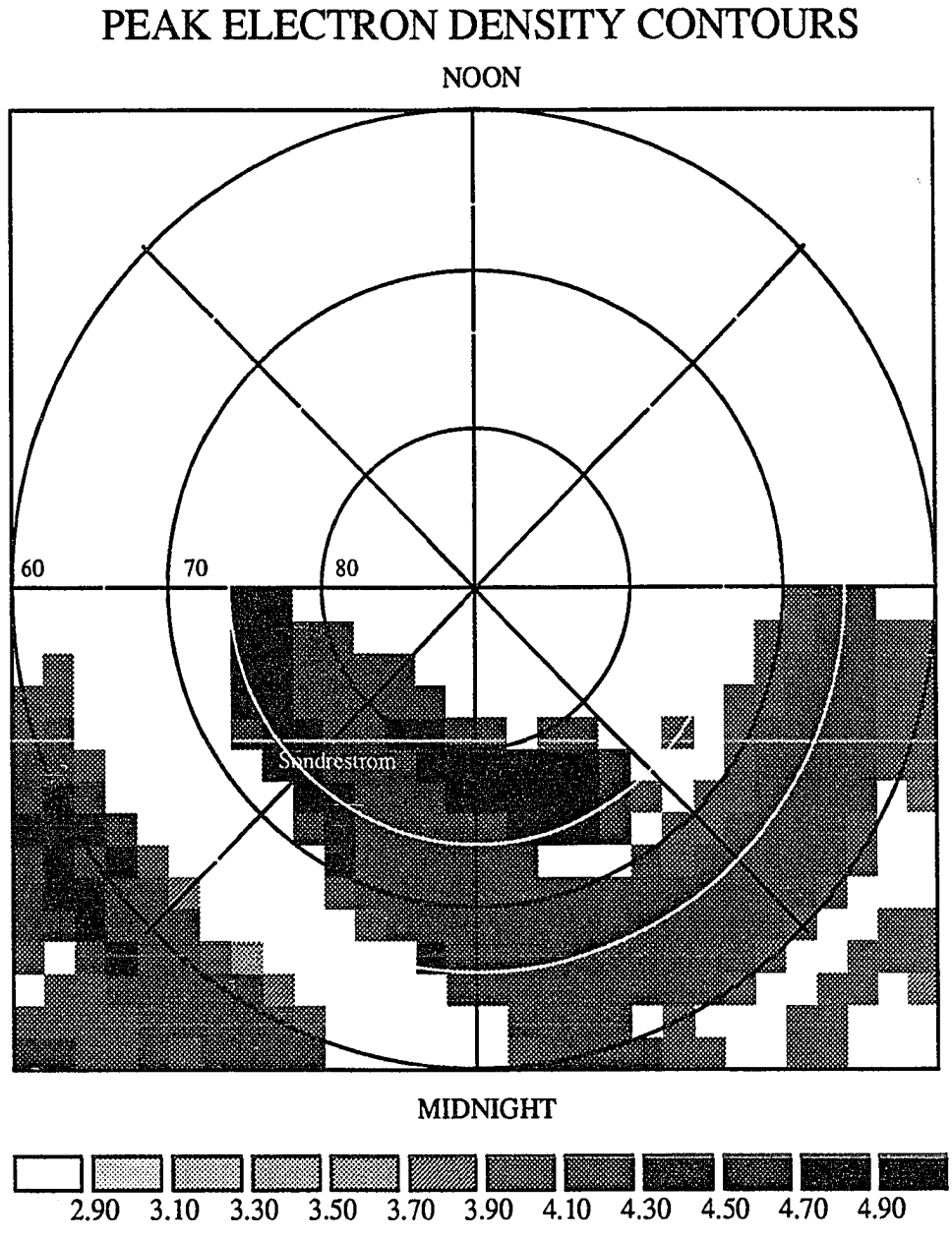

Fig. 4.17. Areas of peak electron density with altitude extent at half maximum less than 5 km.

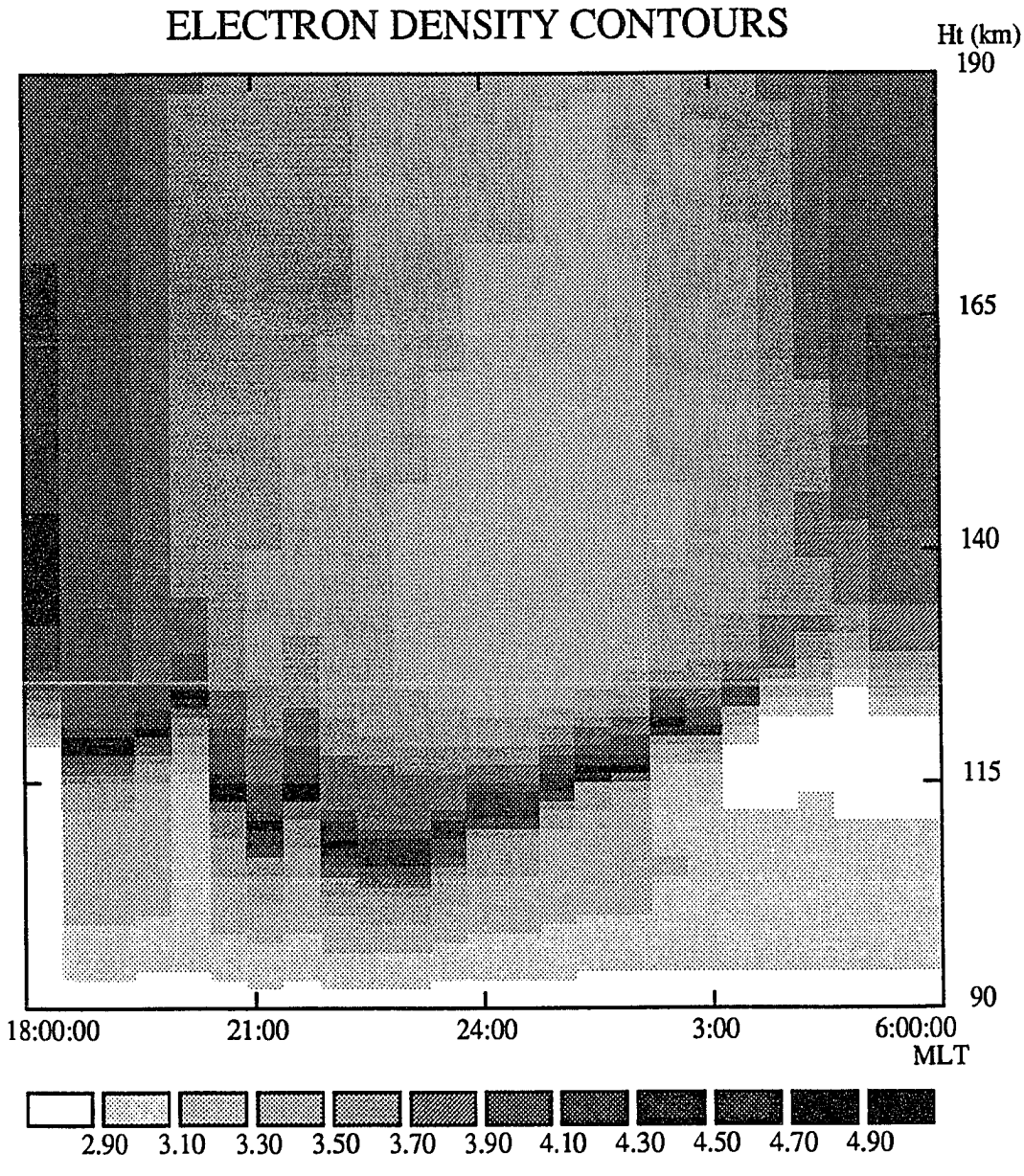

Fig. 4.18. Electron density contours plotted as a function of altitude and magnetic local time for the latitude of Sondrestrom, Greenland.

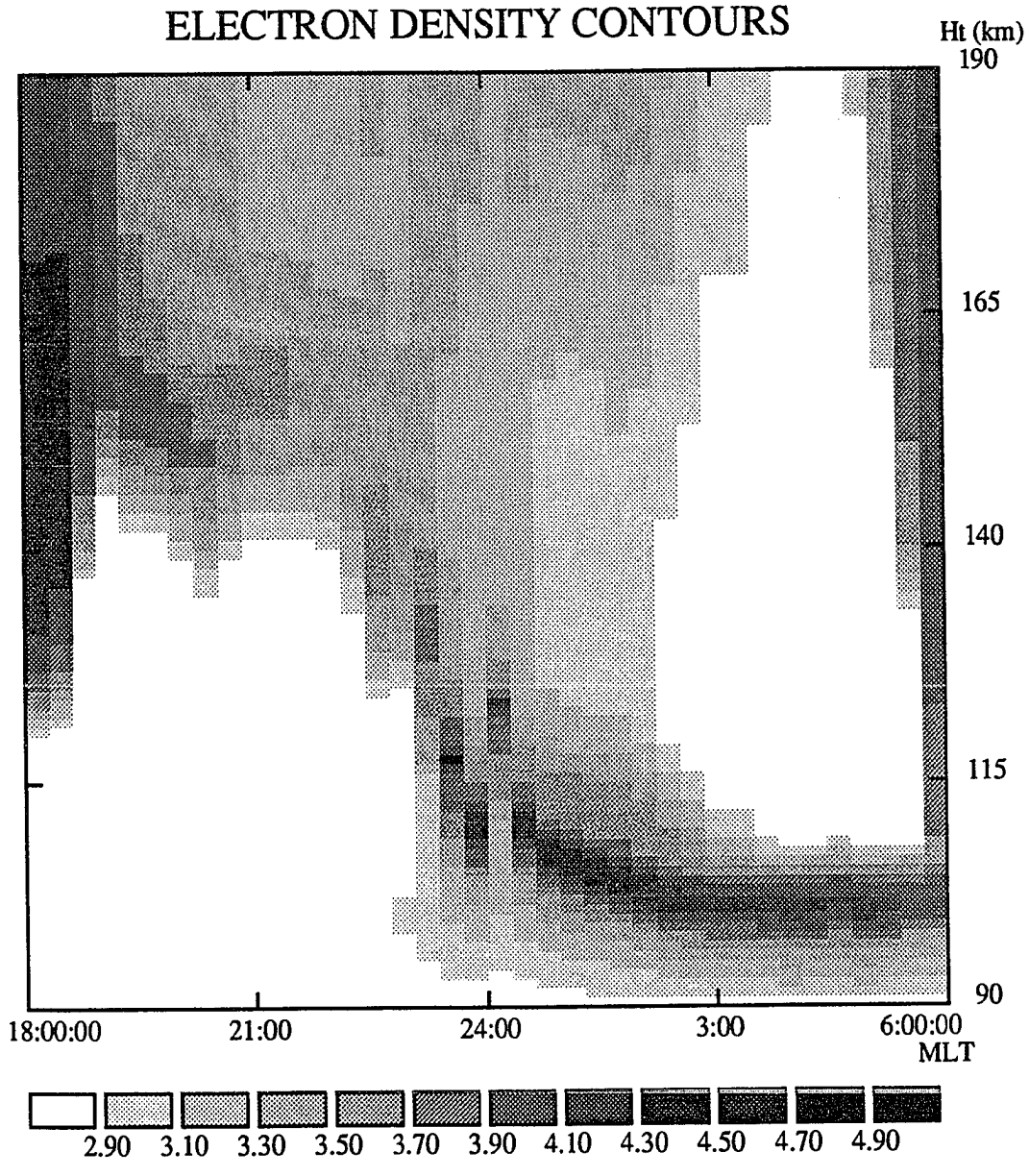

Fig. 4.19. Electron density contours plotted as a function of altitude and magnetic local time for the latitude of EISCAT.

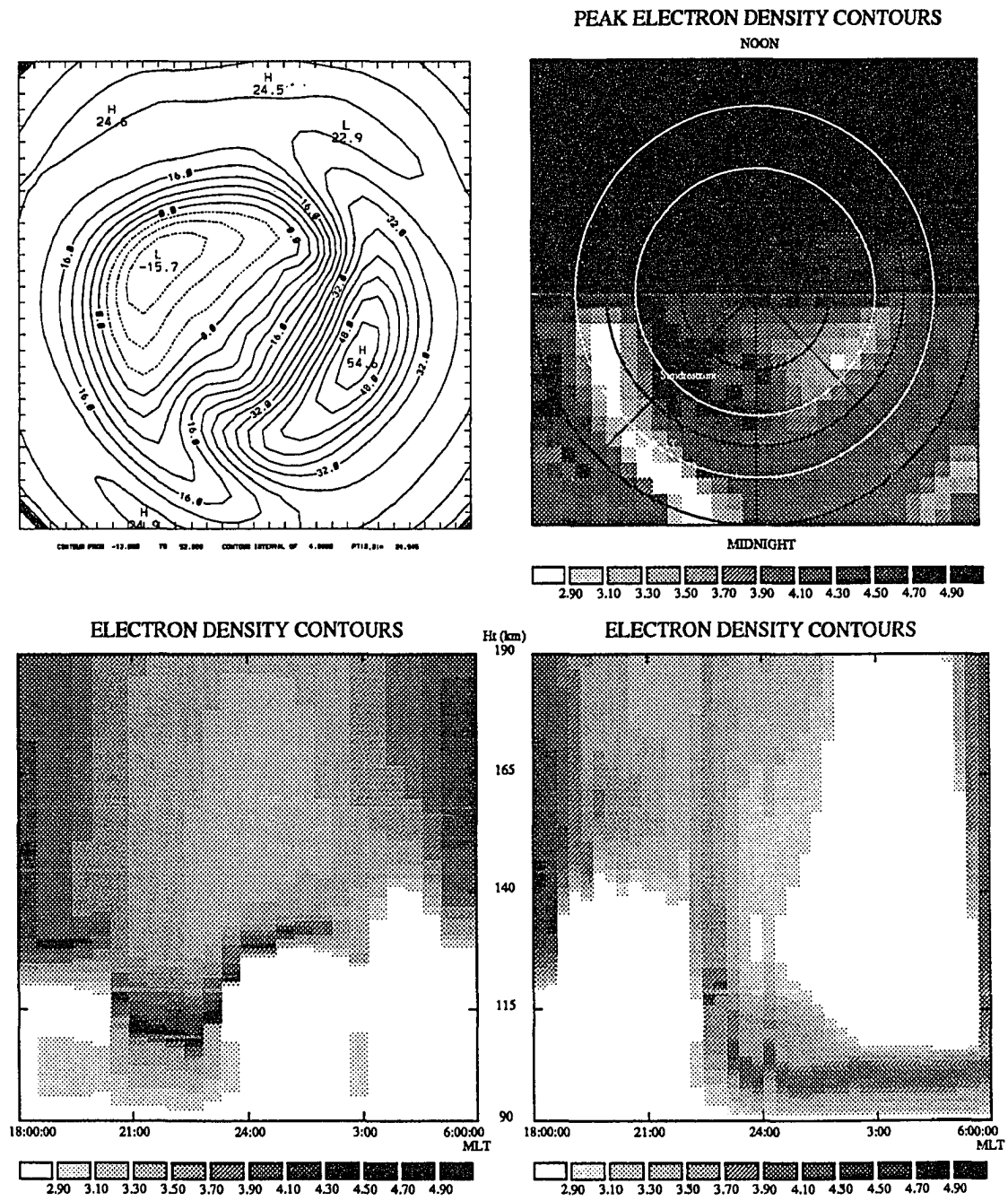

Fig. 4.20. Convection pattern, peak densities, and density contours for Sondrestrom and EISCAT, produced using Heppner-Maynard potential pattern 'BC'.

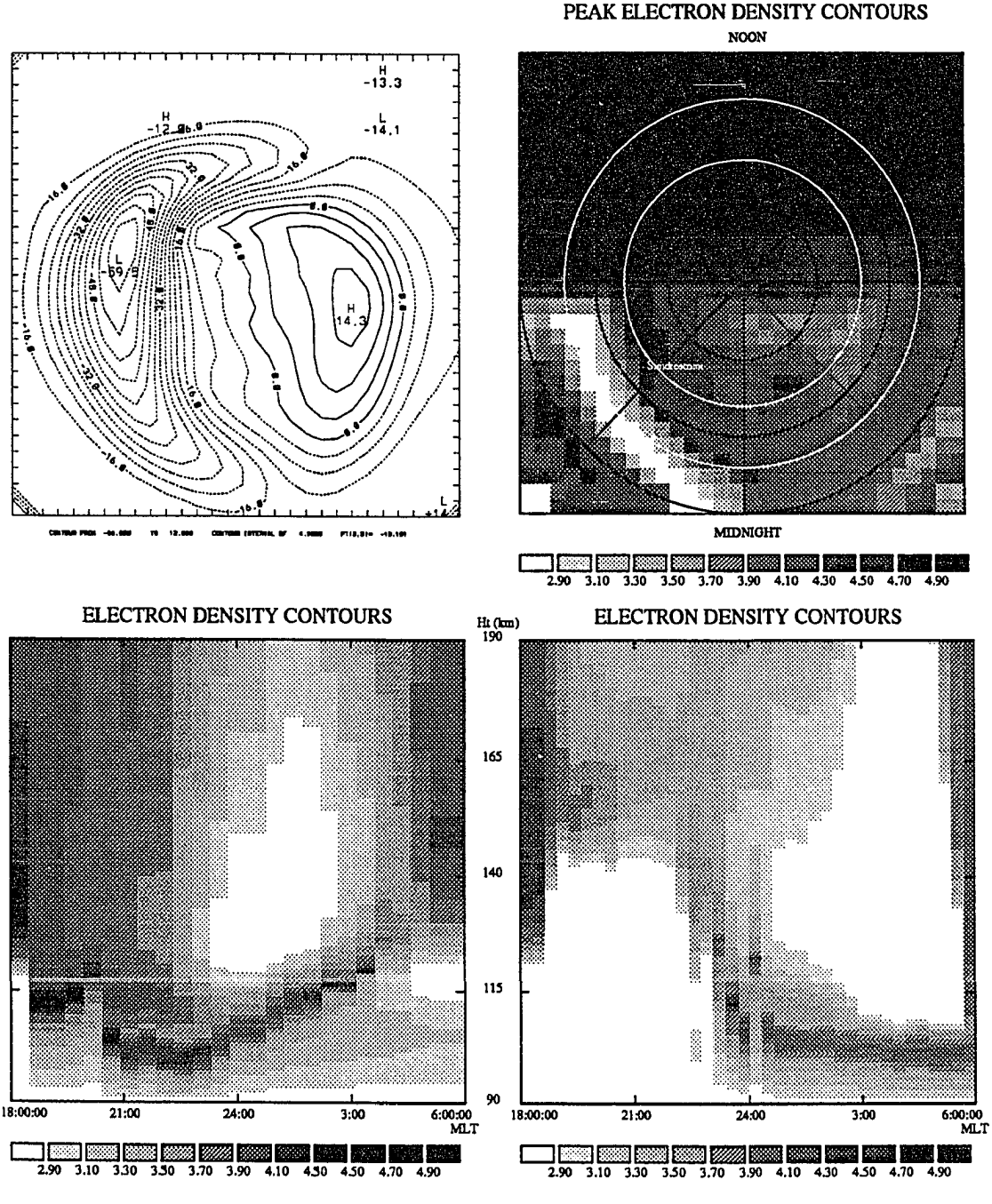

Fig. 4.21. Convection pattern, peak densities, and density contours for Sondrestrom and EISCAT, produced using Heppner-Maynard potential pattern 'DE'.

4.22. There are significant differences between the results for this case and for the patterns with southward B_z. The peak density contours show a layer to be present on the evening side from roughly 55° to 75° latitude, with a lower density layer present on the morning side. The density profile for Sondrestrom shows a layer forming just after 1800 and persisting until just before 2400, when it disperses. The layer moves downward slowly over whole time. The profile for EISCAT shows the layer forming early, just after 1800, and descending until just before 2400. After 2400 the layer persists however it is of lower density.

Figures 4.23 and 4.24 show the results for H-M patterns 'BCPP' and 'DEP', corresponding to patterns 'BC' for B_z strongly northward, and 'DE' for B_z weakly northward. The results are very similar to those obtained for 'BCP'. The high density layer area is concentrated on the evening side, however for 'DEP' it extends a little farther to the morning side. The Sondrestrom latitude plot shows a layer in each case forming early, roughly 1800, and persisting until roughly 2400. In 'BCPP' the layer disperses a little earlier, in 'DEP' a little later.

4.8 Discussion and Summary of Three Dimensional Simulation Results

The results of the three dimensional simulation showed an area of thin layers for each of the potential patterns. The southward B_z patterns all resulted in thin layers forming in the pre-midnight sector in the latitude range north of 70°, and after midnight south of 70°. The pre-midnight layers were in general higher in altitude and of a shorter duration. For northward B_z conditions the layers were mainly in the pre-midnight sector for all latitudes, and occurred at earlier times.

The result of the simulation suggest that thin layers should be present for some time on any night at all latitudes north of approximately 60°. Experiments have shown the presence of layers on the majority of nights, but often there are nights when no layers are observed. A possible explanation for the absence of layers is the lack of metallic ions. There may be times when there is insufficient transport to the altitude region where they may be concentrated in to a layer. Another explanation is that the convection patterns do not accurately represent the electric field in the high latitude ionosphere. On some nights the electric field may not be appropriately directed at any time.

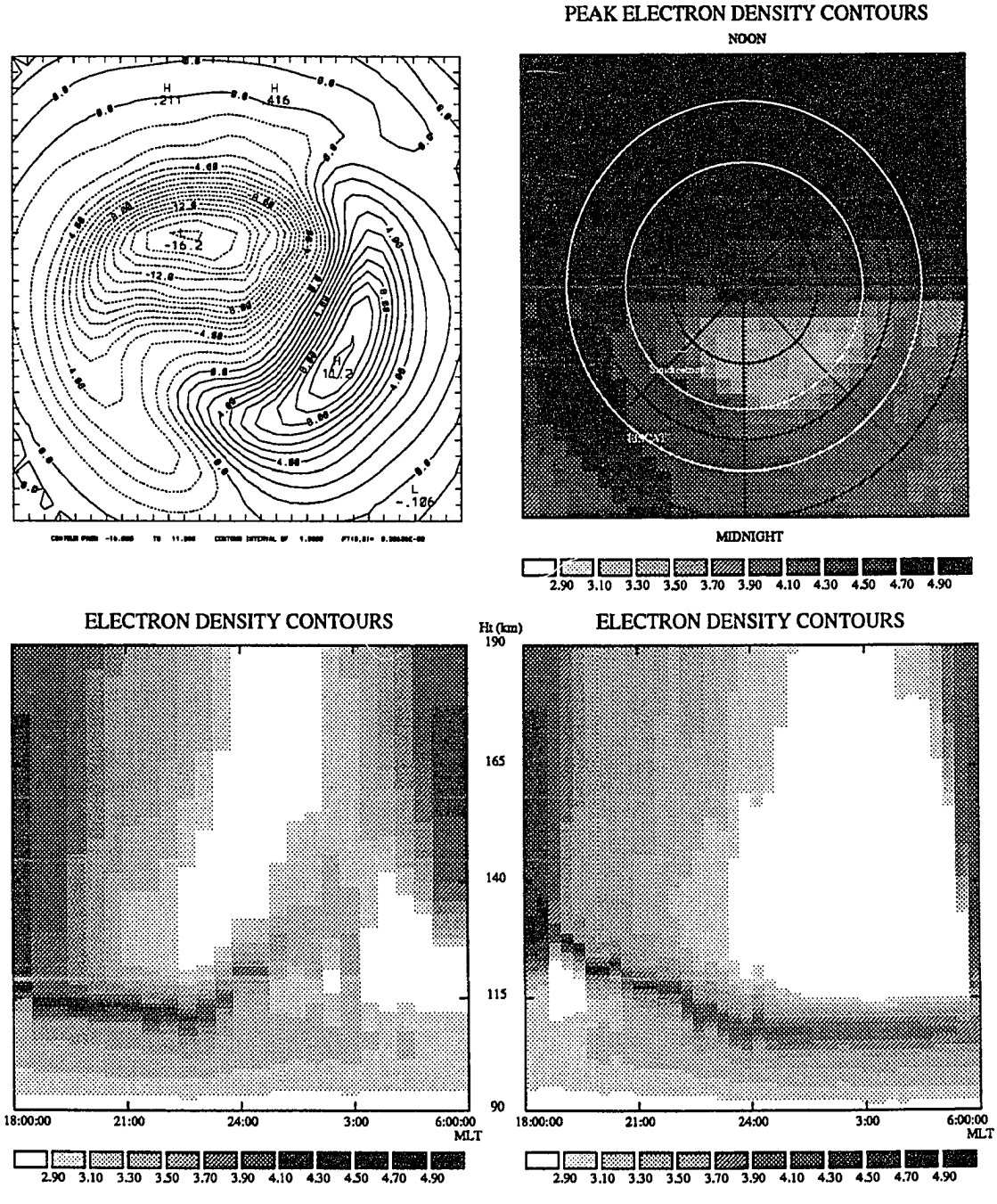

Fig. 4.22. Convection pattern, peak densities, and density contours for Sondrestrom and EISCAT, produced using Heppner-Maynard potential pattern 'BCP'.

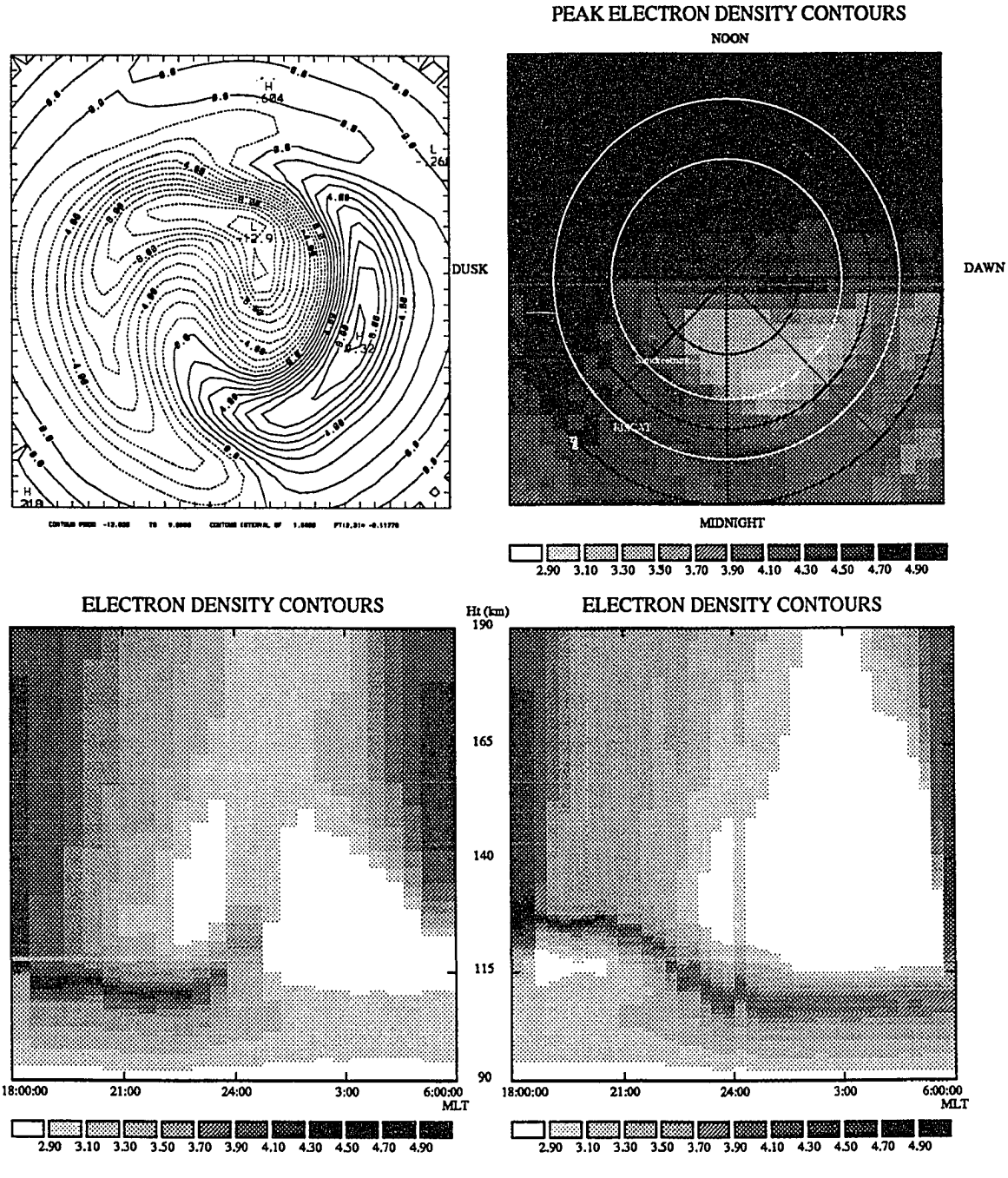

Fig. 4.23. Convection pattern, peak densities, and density contours for Sondrestrom and EISCAT, produced using Heppner-Maynard potential pattern 'BCPP'.

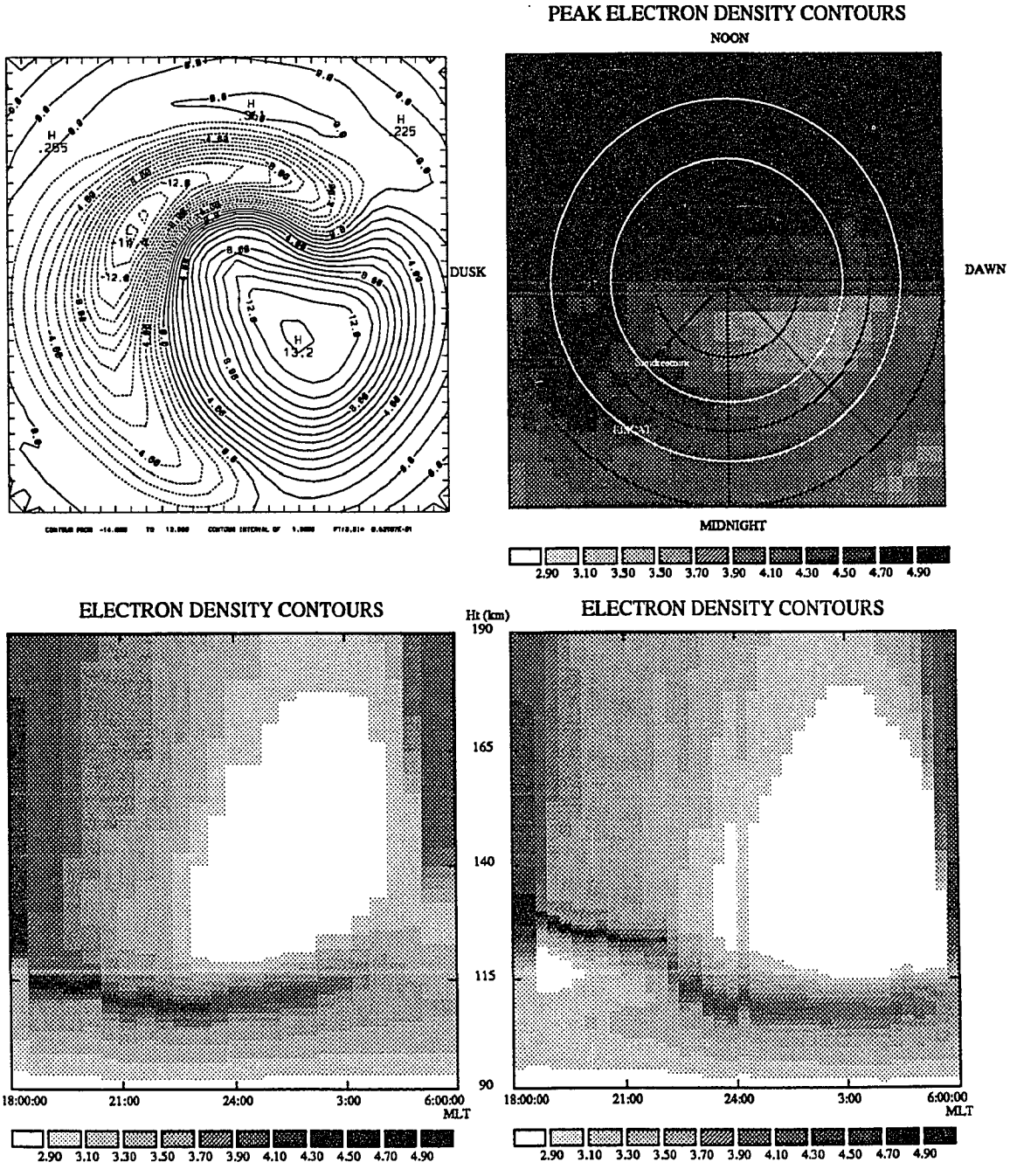

Fig. 4.24. Convection pattern, peak densities, and density contours for Sondrestrom and EISCAT, produced using Heppner-Maynard potential pattern 'DEP'.

CHAPTER 5
INCOHERENT-SCATTER OBSERVATIONS OF THIN IONIZATION LAYERS AT SONDRESTROM

5.1 Introduction

Observations of thin ionization layers were carried out for three periods over a year using the incoherent-scatter radar located at Sondrestrom, Greenland. In this chapter the observations are discused and compared with the predictions of the simulation presented in the previous chapter.

An incoherent-scatter radar is the best tool available to examine the formation and characteristics of thin ionization layers because the electron density profile can be observed over an extended period. At the same time other ionospheric parameters such as the electric field, plasma temperature, and the mean ion mass, may be determined. The main limitation of the radar technique is the time required to make measurements when the densities are low (eg. Hunsucker, 1991). As discussed in the chapter on radar techniques the uncertainties in the measurements are proportional to the signal to noise ratio which depends on the densities and the integration time. For low densities the integration time may become too long for the experiment to be useful. Another limitation is the requirement of three different pointing directions for the determination of the vector electric fields. With a monostatic system this requires the line of sight velocities to be measured at locations separated by as much 250 km, at times the field may have significant variations over this distance and the measurement may not accurately represent the field.

5.2 Description of Experiments

The experiments were carried out using the Sondrestrom incoherent-scatter radar located at Sondrestrom, Greenland, geographic latitude 66°59′, longitude 309°03′, magnetic latitude 73.9°, dip angle 80.35°. The radar operating frequency is approximately 1290 MHz, and normally operates at an output power of approximately 3 MW with 3% maximum duty cycle. Due to a recent upgrade, the radar

can operate on two independent frequency channels, and has greatly improved data handling capabilities.

The first of the experiments discussed here attempts to determine the electric field from F-region data and the densities and temperatures in the E region. The two experiments are carried out within the same inter-pulse-period (IPP) by transmitting different pulse patterns on the two separate frequency channels.

The electric field measurement uses three antenna positions to obtain the vector electric field. A $320\mu s$ pulse is transmitted and the return is sampled at $14\mu s$ intervals starting at 60 km range, 600 samples are taken so the samples cover the range from 60 to 1260 km. At the end of each interpulse period a calibration pulse of known temperature is injected and samples are taken, also samples of the noise are taken at a time when no return signal is expected. The receiver filter has a 33kHz bandwidth, and the sample rate gives a Nyquist frequency of 35.7kHz. The power spectra of the return is obtained for each range gate and the first moments of the spectra give an estimate of the line-of-sight plasma velocity at each range:

$$V_1 = \frac{f_d \lambda_r}{2}, \tag{5.1}$$

where λ_r is the radar wavelength, at Sondrestrom 23.3 cm, and f_d is the first moment estimate. The antenna is sequentially positioned in three directions to obtain the line-of-sight velocities in each direction and a velocity vector is obtained. If the region sampled is high enough in altitude, i.e. above roughly 200 km, then collisions with the neutral gas may be ignored and the velocity is simply the E×B velocity and the electric field may be determined. For the data discussed here the three antenna azimuth positions were 21°, 141°, and 261°, with a constant elevation of 75°. The actual regions of the ionosphere sampled by the different antenna directions are separated in space horizontally by over 100 km, and the antenna remains in each position for five minutes to allow sufficient data integration time. Thus the field vector obtained must be considered to be an average for the time and space increments.

The 300m E-region information is obtained from a five-pulse multi-pulse technique (Farley, 1972), where the sub-pulses of the multi-pulse are coded with a 13 baud, $2\mu s$ baud, Barker code. This pulse pattern gives a lag time (τ_l) of $26\mu s$,

with lags out to 286 μs, which corresponds to 3.5kHz resolution with a Nyquist frequency of 38.5 kHz. Pulses are transmitted at time 0, 3, 4, 9, and 11 τ. The sample frequency is 2μs to match the baud rate which requires a receiver filter bandwidth of 250 kHz. This wide bandwidth leads to high noise power on this channel. The calibration and noise sampling is also carried out for this channel. By using the multi-pulse technique densities and spectral information are obtained in the E-region with high range resolution, however, due to the high noise power, the signal-to-noise ratio is often not sufficient to obtain useful spectral information within a reasonable integration time.

The first experiments were run in August of 1990. It was found that most of the time when thin layers were observed the densities outside of the layer altitude were too low to obtain spectral information within a reasonable integration time. To solve this problem the experimental technique was modified, and the experiments were run earlier in the summer (July 1991) with the expectation that there would be higher background densities due to higher photo-ionization.

The second experiment attempted to decrease the integration time required to obtain spectral information in the E-region by transmitting the Barker coded multi-pulse on both frequency channels. On one channel the range resolution is 600m while 300m is maintained on the second channel. With 600m resolution, a narrower receiver filter is used yielding better signal-to-noise ratio, further improving integration time. On the 300m channel the pulse pattern is the same as in the previous experiment. The 600m channel is also a five pulse multi-pulse, but the sub-pulses are coded with a 7 baud, 4μs baud, Barker code. This gives a lag time of 28μs with lags out to 308μs, or 3.25 kHz resolution with a Nyquist frequency of 35.7 kHz.

The third experiment obtained densities only in the range from 90 to 210km with 600m resolution with antenna elevation scans along the magnetic meridian. The pulse pattern used was a single Barker coded pulse with a high pulse repetition frequency. The antenna scanned $\pm 60°$ from the vertical with a scanning rate of 0.4° per second. This yielded north-south coverage of 360km for E-region altitudes, with a complete scan every five minutes. The integration time was 5 seconds giving a density profile every 2°, or 60 profiles per scan.

The experiments were carried out on several nights for a period of four hours near magnetic midnight. This period was chosen because the electric field is often directed in the north-west or south-west quadrants during this time. Thin layers were observed for some portion of the majority of the nights. Figure 5.1 from July 27, 1991, is a good example of the electron density contours showing the presence of a thin layer at approximately 110 km altitude from 2000 to 2200 UT. The layer remains near 110 km for the entire period, though it drifts both up and down at times. There is an oscillation of the layer altitude from approximately 2040 to 2130 UT, showing the possible evidence of a gravity wave propagating through the field of view. It appears that the layer density increases with downward propagation of the wave. The density changes markedly over the period, ranging from slightly above the background density of 10^5 to nearly 10^6 after the wave feature passes. The layer thickness, full width at half maximum, varies in the range of 1.5 to 2.5 km.

5.3 Determination of Ion Composition

The metallic ions most often found in mid-latitude thin ionization layers are Fe^+(56 amu), Ca^+(40 amu), and Mg^+(24 amu) (eg. Zbindin *et al.*). To determine the presence of the metallic ions we examine the ion temperature profile. The incoherent scatter spectrum is expressible in terms of various plasma parameters including the ion-neutral collision frequency, the ion mass to temperature ratio, and the electron temperature (Dougherty and Farley, 1960, 1961, and 1963). By measuring the spectrum and fitting an analytic expression to the measurement we can estimate these parameters. By determining the ion mass we can demonstrate the presence of metallic ions. The mean ion mass in the E region under normal conditions (a mixture of NO^+ and O_2^+ ions) is near 30.5 amu. If there is a significant fraction of heavy metallic ions, such as Fe^+ mass 56 amu, then the mean mass is higher than normal. The ion mass only appears in ratio with the temperature in the expression for the incoherent-scatter spectrum so it is not possible to unambiguously determine both parameters simultaneously. The usual procedure for determining the ion mass is to assume an ion mass for all altitudes, here 30.5 amu, and fit for the temperature profile. If the layer has a significant proportion of heavy ions, ie. Fe^+,

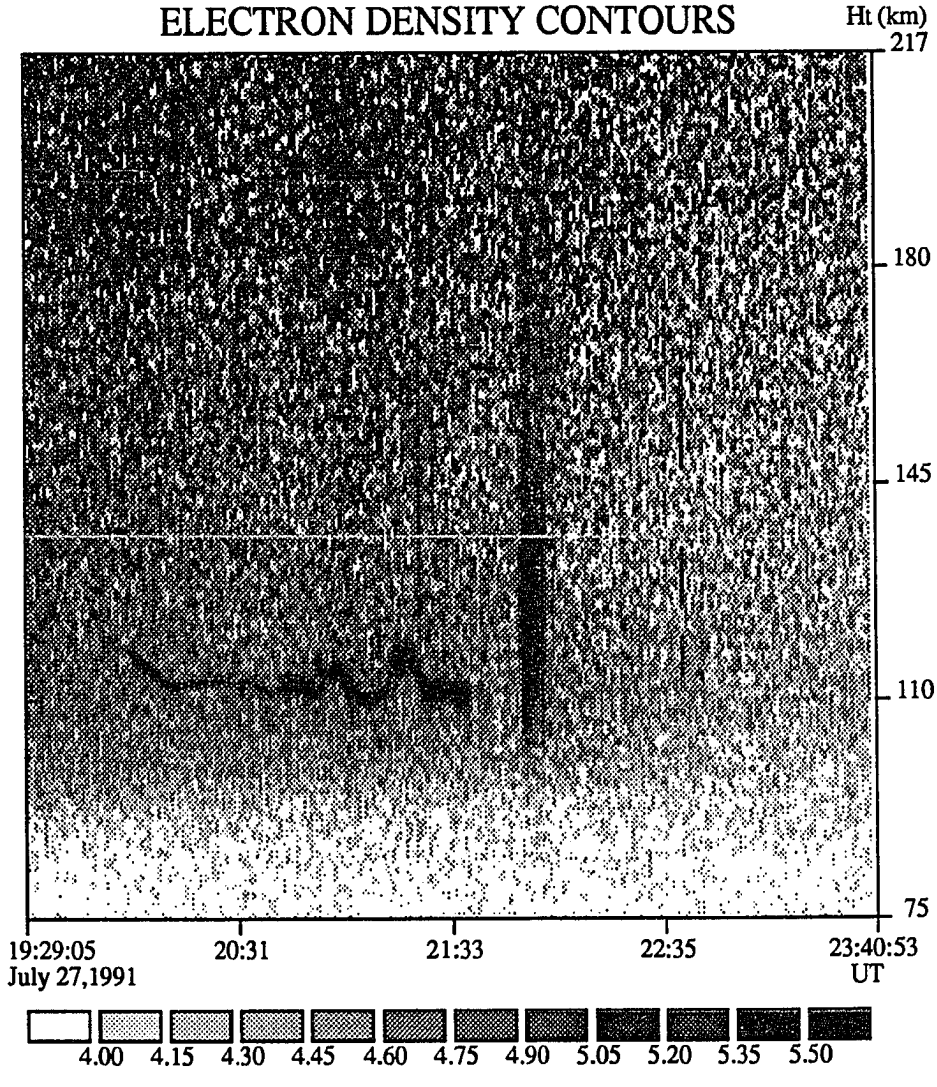

Fig. 5.1. Electron density contours with 600m range resolution in the range from 75 to 21 km altitude. A thin ionization layer is present from 2000 to 2130 UT. The area of high density at about 2200 UT is auroral ionization.

the temperature profile will show a decrease at the layer altitude. By adjusting the ion mass in the analysis routine the temperature at the layer altitude is adjusted to match the temperature outside the layer. Thus the average ion mass within the layer is determined.

Figures 5.2(a,b) show the temperature and density profiles obtained for the layer shown in figure 5.1, with the original assumption of a 30.5 amu ion mass. At the altitude of the layer peak the temperature shows a significant decrease. The signal-to-noise ratio is such that for altitudes outside of the layer the integration time is one hour, while five minutes is sufficient within the layer when it is the most intense. The period of 2020 to 2120 UT is used to determine the background profile. During this period the condition of the ionosphere appears to remain fairly constant. Since a weak layer is present during this interval, data for the layer altitude can not be used to determine the temperature, rather the ion mass is adjusted in the analysis routine until the profile appears smooth. Figure 5.2c shows the temperature profile obtained when the ion mass is adjusted in the analysis routine. This gives a mean ion mass of 44 amu in the lowest gate and 42 amu for the other two gates. Due to the high density it is likely that the actual composition is almost entirely metallic ions, a mixture of the species mentioned above. As was discussed in chapter 2, the short recombination times for the normal molecular ions do not allow accumulation to high densities in the absence of a local source.

5.4 Electric Field Data

The experiment to examine the relationship between the electric field and thin ionization layers was run on 11 nights during the period from August 1990 to August 1991. In the discussion that follows the angles of the electric fields are measured with respect to magnetic north, a positive angle counter-clockwise from north. Figure 5.3 is a good example of a layer and the measured field from the experiment of August 22,1990. A layer was present for the interval from 2150 to 2330 UT, initially the layer moved downward rapidly, then slowly drifted upwards. The electric field during this time was changing in direction with small change magnitude. When the layer initially came into the radar beam the field was pointing to 80° west of magnetic north. When the layer was at its lowest altitude the field

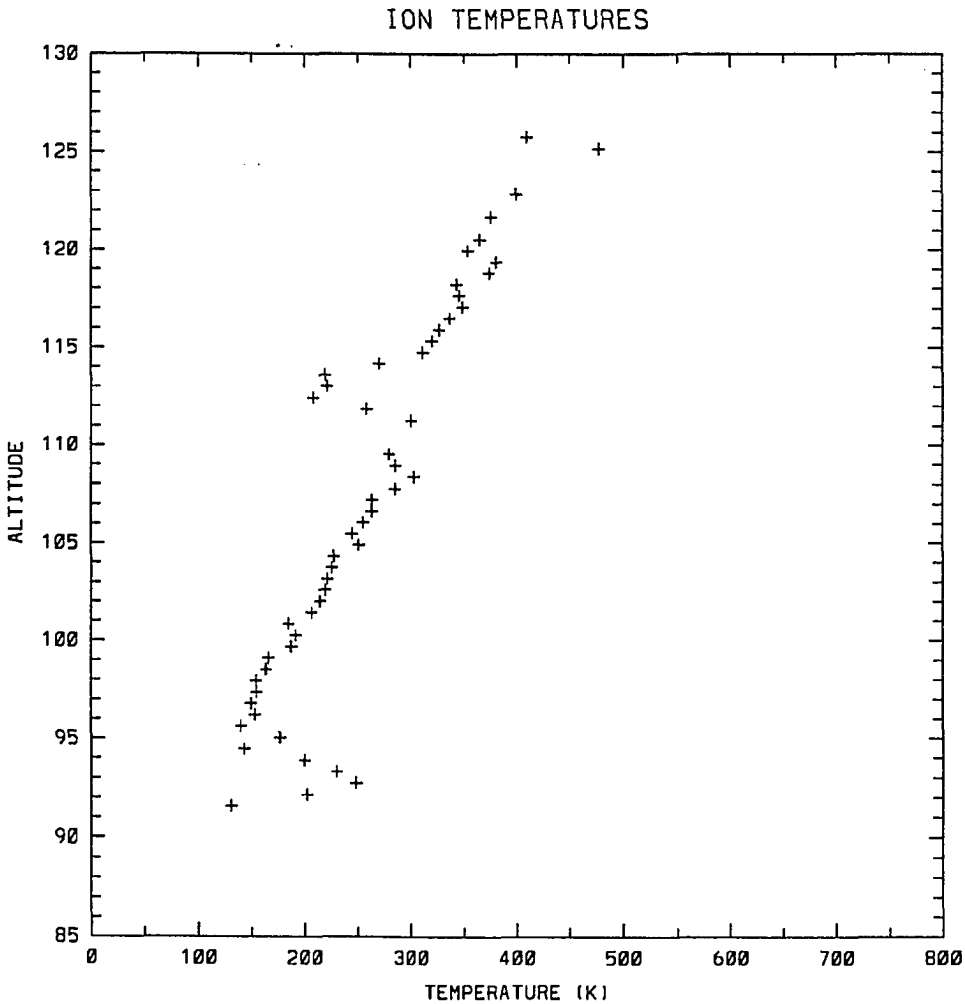

Fig. 5.2a. Ion temperature profile obtained for the layer shown in figure 5.1 with the assumed ion mass of 30.5 amu. The profile shows a significant decrease at the layer altitude.

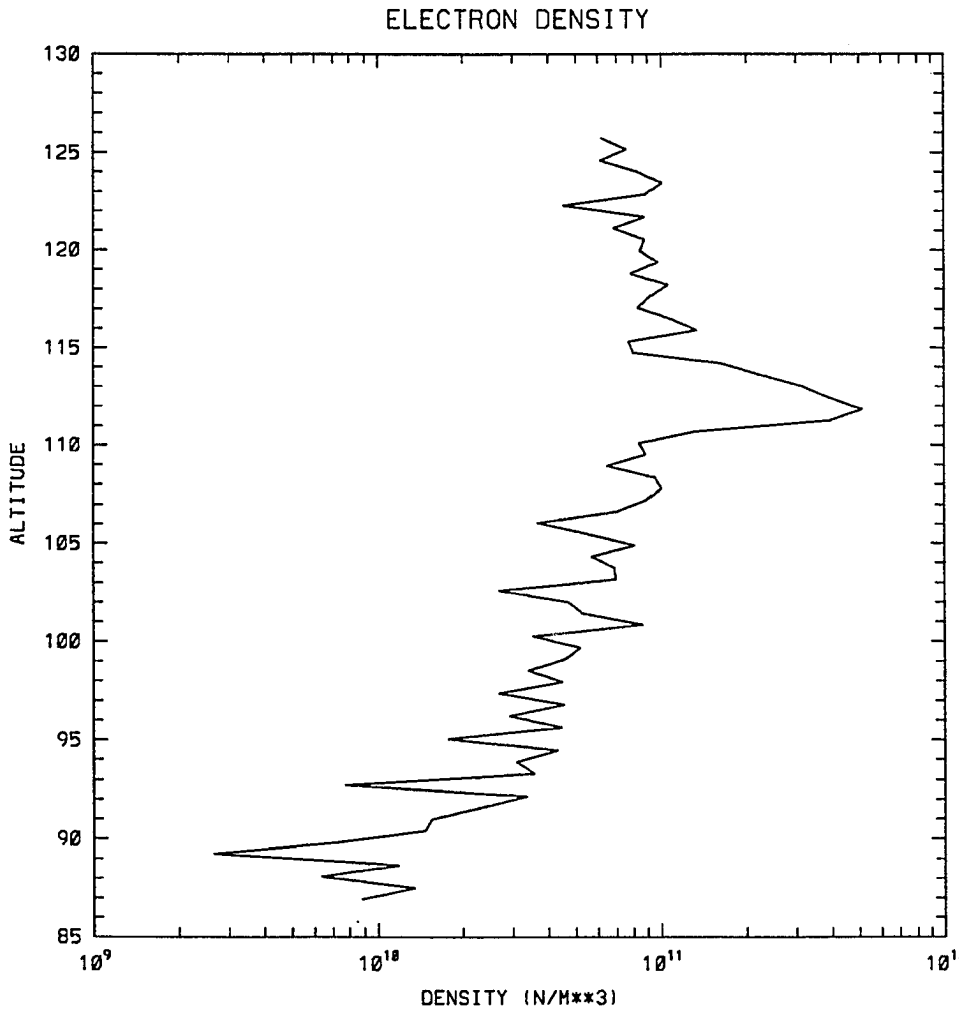

Fig. 5.2b. Density profile obtained for the layer shown in figure 5.1

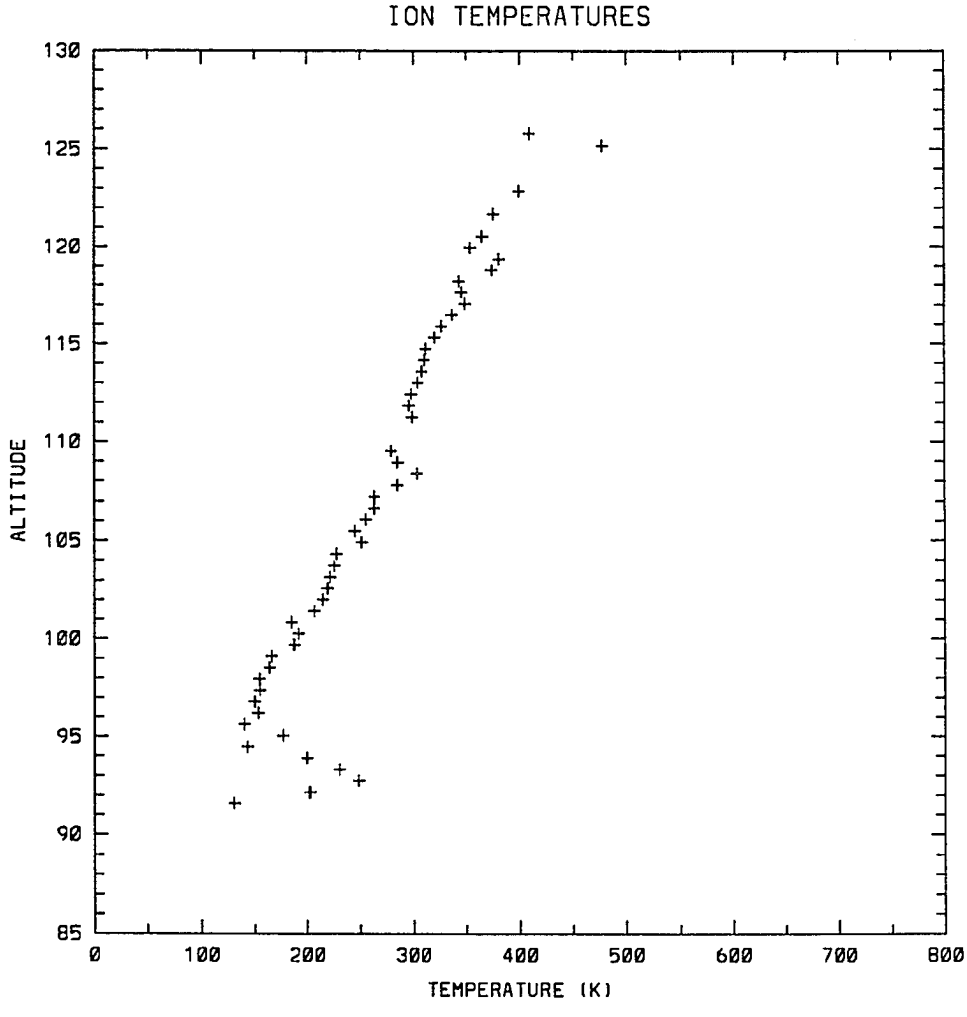

Fig. 5.2c. Ion temperature profile obtained for the layer shown in figure 5.1 when the ion mass at the layer altitude is adjusted.

was pointed to 100°. After the layer reached its lowest altitude it slowly rose until it left the field of view. During the time that the layer was rising the field was rotating northwards. At the time the layer moved out of the radar beam the field was pointing 40° west of north. During the period the field magnitude ranged between 12 and 19 mV/m.

Figure 5.4 shows the data from March 13, 1991, A layer was present for period of about an hour, 0015-0115 UT. The layer remained at about 100 km for the entire period, without any significant drift. The field remained nearly constant in direction (110°-140°), and the amplitude varied in the range of 5 to 15 mV/m.

The following is a summary of the data from the remaining nights, for which the data is not shown:

Aug. 17, 1990: A layer was in the beam for two different periods. During the First period near 2200 UT, the layer was in beam for two of the beam directions but not in third. The layer was near 103 km altitude, the field direction was changing, between roughly 70° and 100°. The second period the layer was in the beam for 25 minutes, 2320-2340 UT, at approximately 115 km altitude. During this time the field ranged between 80° and 130°. Field direction was near -40° for an extended time without layer, same true for extended period of field directed to 40°-60°.

Aug. 18, 1990: A layer was in the beam for 30 minutes with short interval not in beam. The layer altitude was near 105 km. The field direction was changing rapidly from north to south and then back. During the periods when layers were not observed the field was directed to $-20°$, or between 0° and 60°.

Aug. 19, 1990: No layers were observed on this night. The field was directed between -20° and 60° for most of the night, but was directed to 90° for a short time. During the time that the field was directed to 90°there was significant particle precipitation which would have masked any layer if it were present.

Mar. 10, 1991: No layers were observed on this night. The field was directed between 40° and 180° for the majority of the night. Field magnitude ranged between 4 and 34 mV/m. There was no observed particle precipitation.

Mar. 12, 1991: A Layer was in the beam for 1 hour, 2300 to 2400 UT. Initially the layer was at 110 km altitude, then sudden change to 103 km. The field was

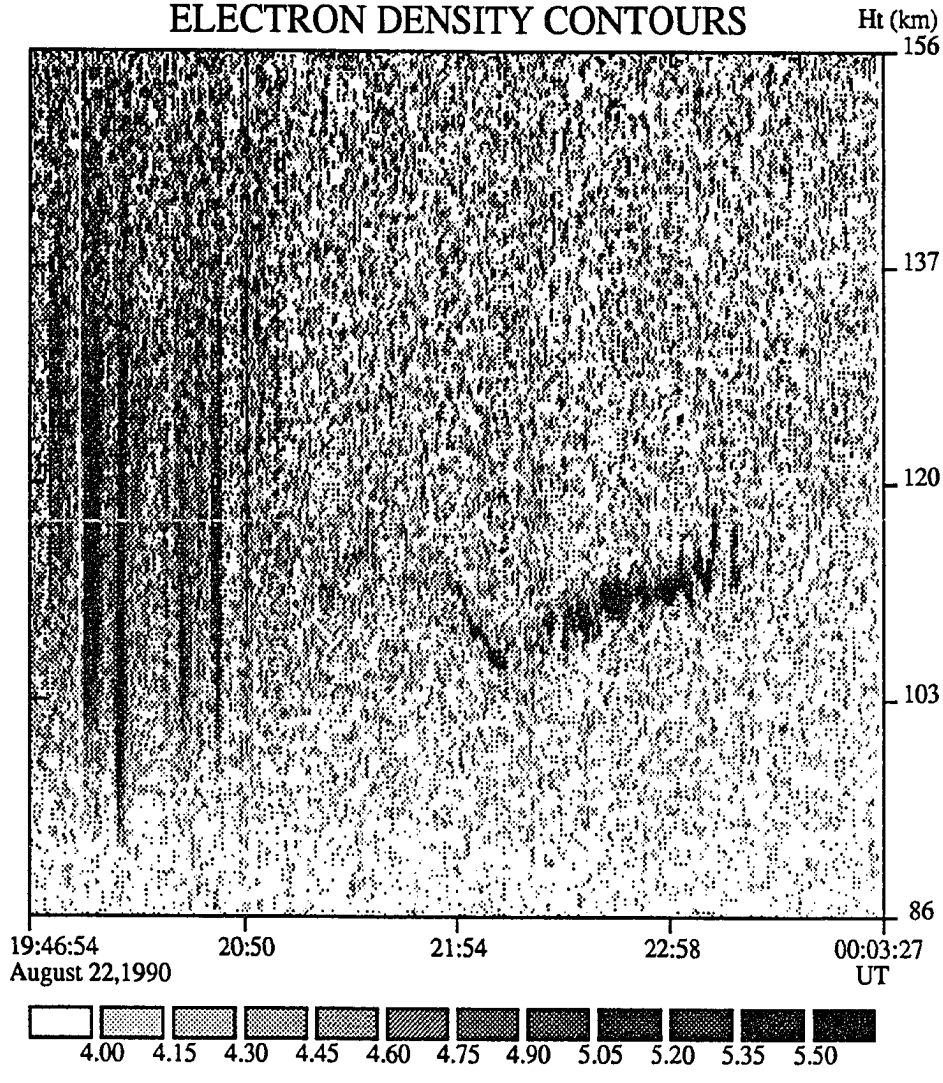

Fig. 5.3a. Electron density contours with 300m resolution for the night of August 22, 1990. A layer is present during the period from 2150 to 0000 UT, with varying altitude.

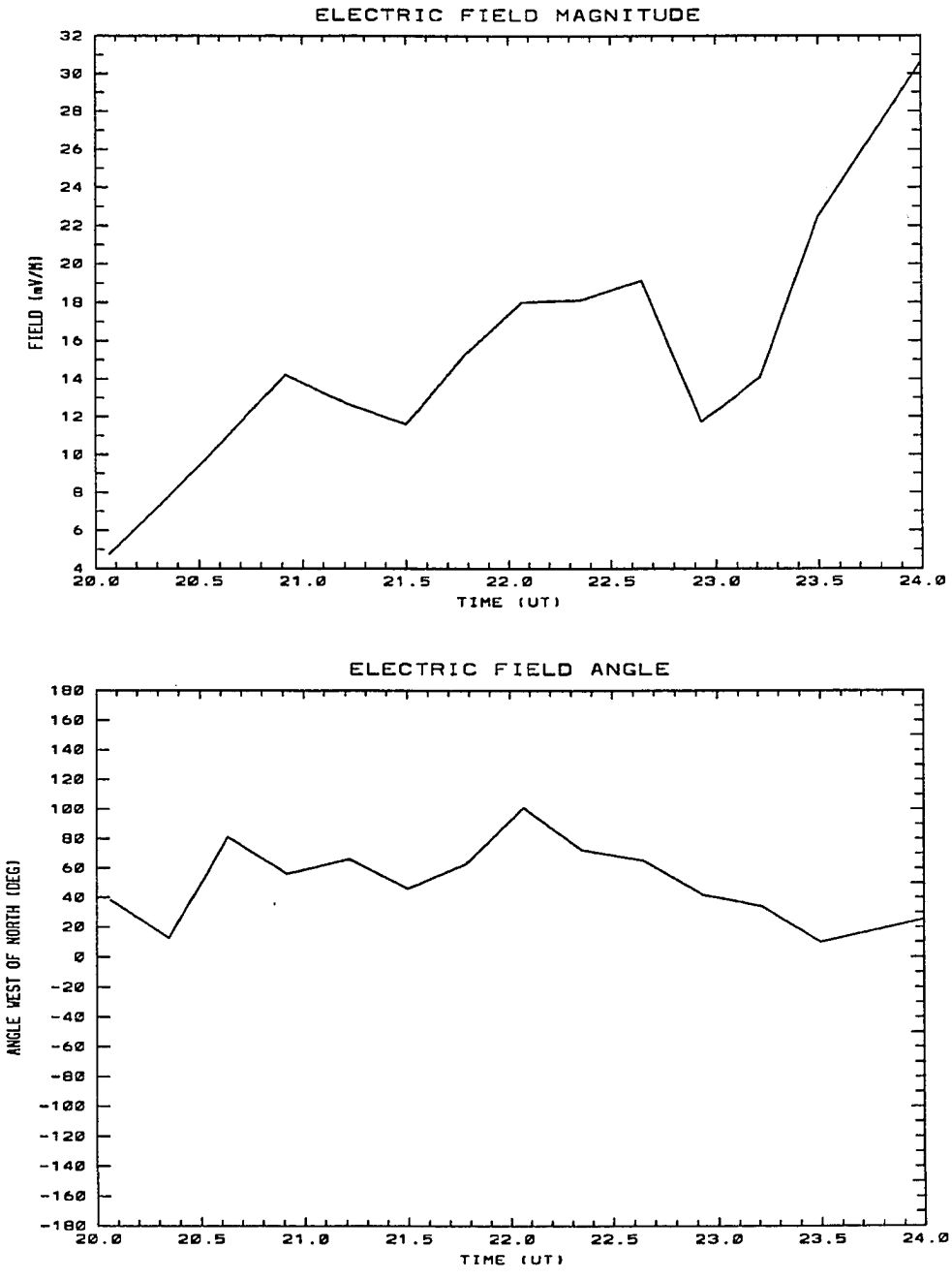

Fig. 5.3b. Electric field magnitude and angle for the night of August 22, 1990.

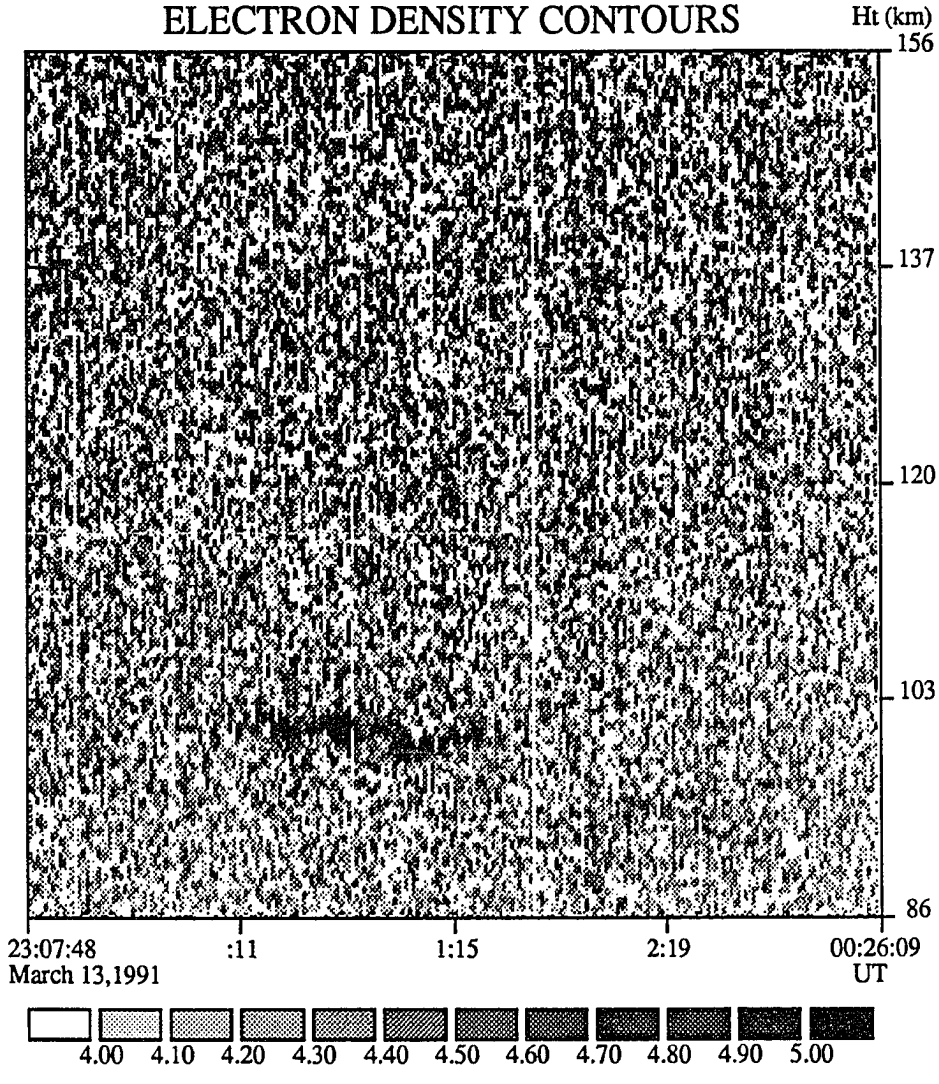

Fig. 5.4a. Electron density contours for the night of March 13, 1991. A layer is present at 103 km for period between 0000 and 0130 UT.

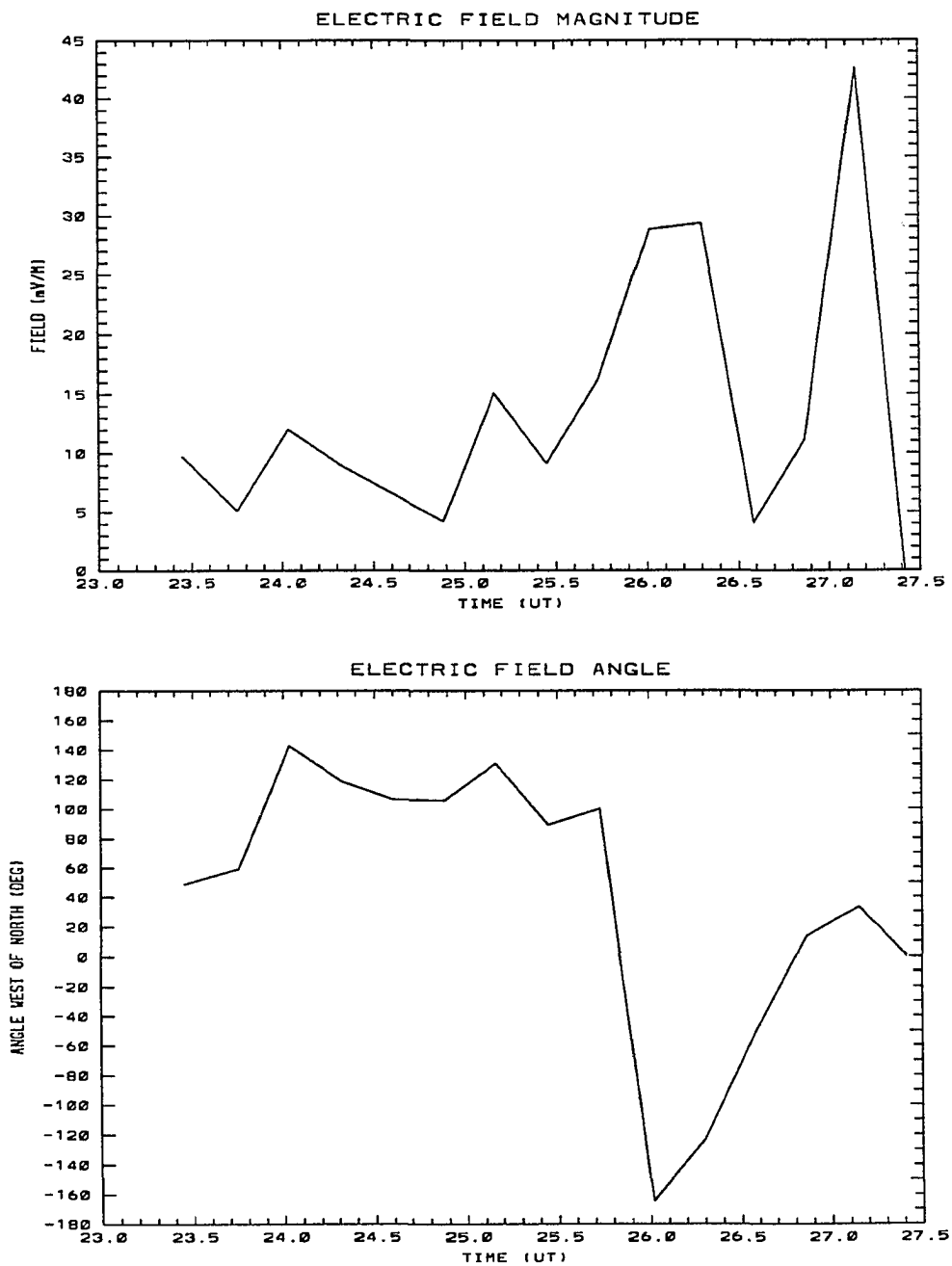

Fig. 5.4b. Electric field magnitude and angle for the night of March 13, 1991.

directed to 85° at start, then changed to approximately 110° at about time of altitude change. The layer left view at about the time that the field changed to pointing to south, and then to south-east. The field magnitude was in the range of 18-20mV/m while the layer was within the beam.

Mar. 14, 1991: No layers were observed on this night. The field was directed between -120° and 0° for the majority of the night with two short intervals when the field pointed to roughly 160°. Field magnitude ranged between 1 and 48 mV/m. There was no observed particle precipitation.

Jul. 26, 1991: A layer was present for period of 15 minutes, 2115 to 2130 UT. The layer was at approximately 115 km altitude. During the first two hours of observation the field was directed roughly to magnetic north, then rotated to the south over a period of an hour and a half. The layer was present during a portion of the transition from north to south, when the field was in the range of 75° to 120°.

Aug. 3, 1991: A layer was present for period of 15 minutes, 2400 to 0015 UT. The layer was at 100 km altitude. During the first two hours of observation the field was directed between -30° and -20°, then rotated to the west for the remainder of the observation. The layer was observed when the field was in the range of 80° to 100°.

Aug. 6, 1991: No layers were observed on this night. The field was directed between -10° and 20° for the majority of the night with a half hour interval when the field pointed to roughly 90°. Field magnitude ranged between 10 and 38 mV/m. There was observed particle precipitation at times.

Table 1 is a summary of the data for the nights when layers were observed. Layers are clearly present for varying periods on seven of the eleven nights, and were all in the altitude range of 100 to 120 km. During the time when layers are present the electric field was almost always pointed between 40° and 180° west of magnetic north. Most often the field was in the range of 80° to 100°. The field magnitude ranged in value from 2 mV to 34 mV during the times layers were

observed. Further layers were present the majority of the time when the field was directed in the south-west quadrant.

On the nights when no layers were observed, the field was most often directed to the north or north-west, although on one of the nights the field was directed between 160° and 180° for an extended period. On one night the field was directed 90° for a period of approximately 30 min, with no layers observed, however it must be noted that there was significant auroral activity during the time which may have produced sufficient ionization to mask a thin layer.

5.5 Scanning Experiment

The antenna scanning experiment was run on three nights in late July and early August, 1991. Figure 5.5 shows the data from a single north-south scan from the night of July 29, 1991. The data show the presence of a layer extending from roughly 90 Km south of the station to as much as 100 km north. The layer was more intense to the south and a well defined southern boundary, while to the north the layer is less dense, and does not have a well defined northern boundary. The layer appears to be thinner to the north, and thickest near the southern edge. The altitude of the layer is approximately constant over the whole width. It is interesting to note that directly over the station the layer shows two maxima separated by about 5kmin altitude; figure 5.6 shows the density profile at this time.

Figure 5.7 shows three successive scans from later in the same night to illustrate the motion of the layer. The layer has moved to the south and has a north south extent of less than 100 km and the double peak observed earlier has disappeared. This was a general trend on the three nights of observation; layers appeared north of the station and moved to the south.

Figure 5.8 shows the peak electron density below 130 km for several scans on two successive nights. The scan shown in figure 5.5 corresponds to the second column of figure 5.8(a). The vertical axis shows distance north and south from the station, the horizontal axis shows time. The high density areas shown correspond to areas of thin layers. The total area of layers is larger than shown since in some areas the layer density is not significantly above the background. The figures show

Table 1

Date	Layer Time (UT)	Altitude (km)	E-Field Angle	E-Field Magnitude (mV/m)
August 17, 1990	22:00	105	70°-100°	4
	23:20-23:40	115	80°-130°	4-6
August 18, 1990	22:00-22:30	105	60°-140°	2
August 22, 1990	21:50-23:15	105-115	40°-100°	14-18
March 12, 1991	23:00-23:15	110	80°	24-34
	23:15-00:10	100	100°	20
March 13, 1991	00:15-01:20	100	100°-120°	5-15
July 26, 1991	21:05-21:20	115	80°-100°	4-6
August 3, 1991	23:40-00:15	100	80°-100°	24-26

Table 1 Summary of data for nights when thin ionization layers were present.

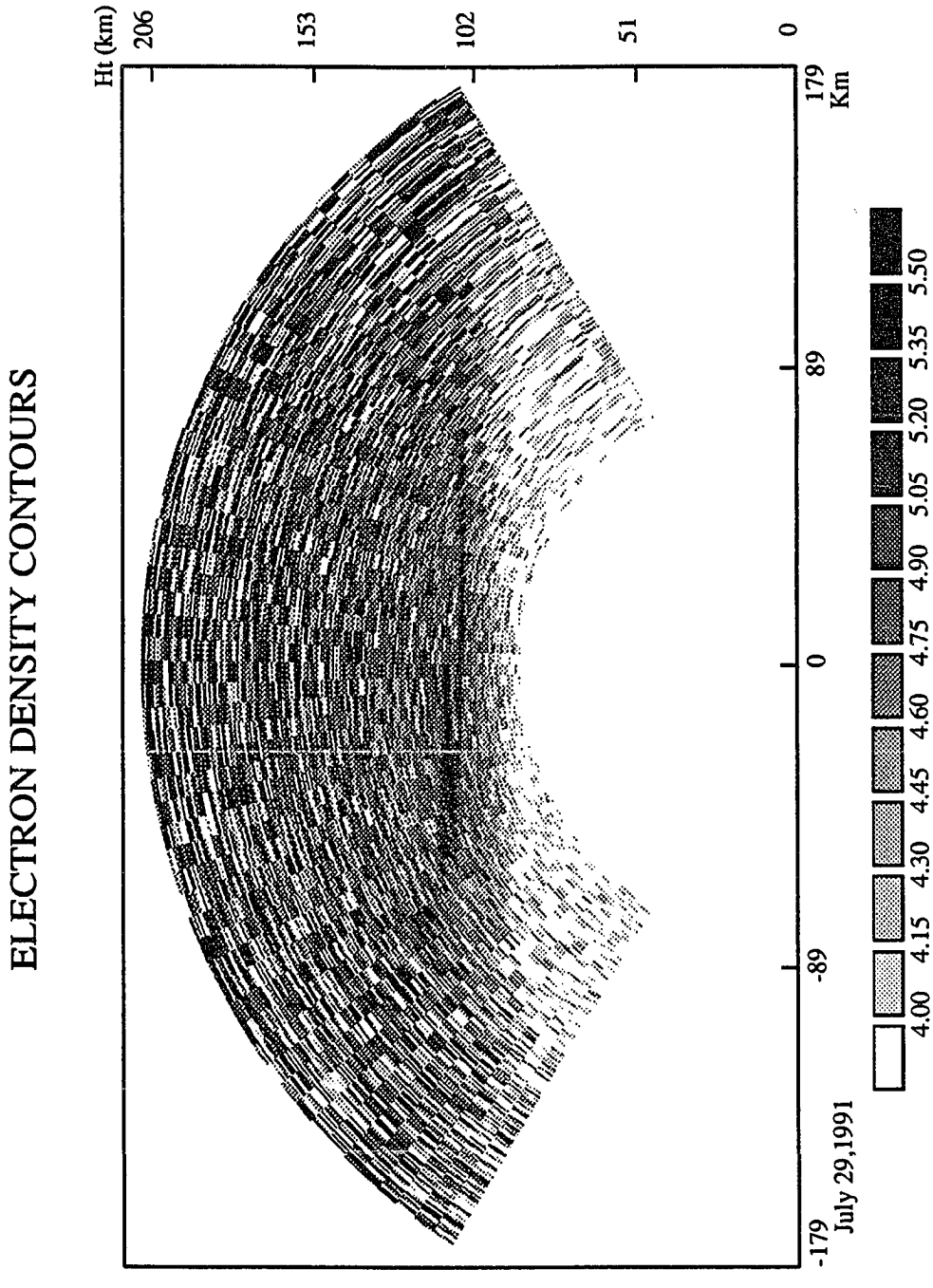

Fig. 5.5. A single antenna scan from the night of July 29, 1991. The data show a layer present for about 100 km north and south of the station, with two density peaks visible directly above the station.

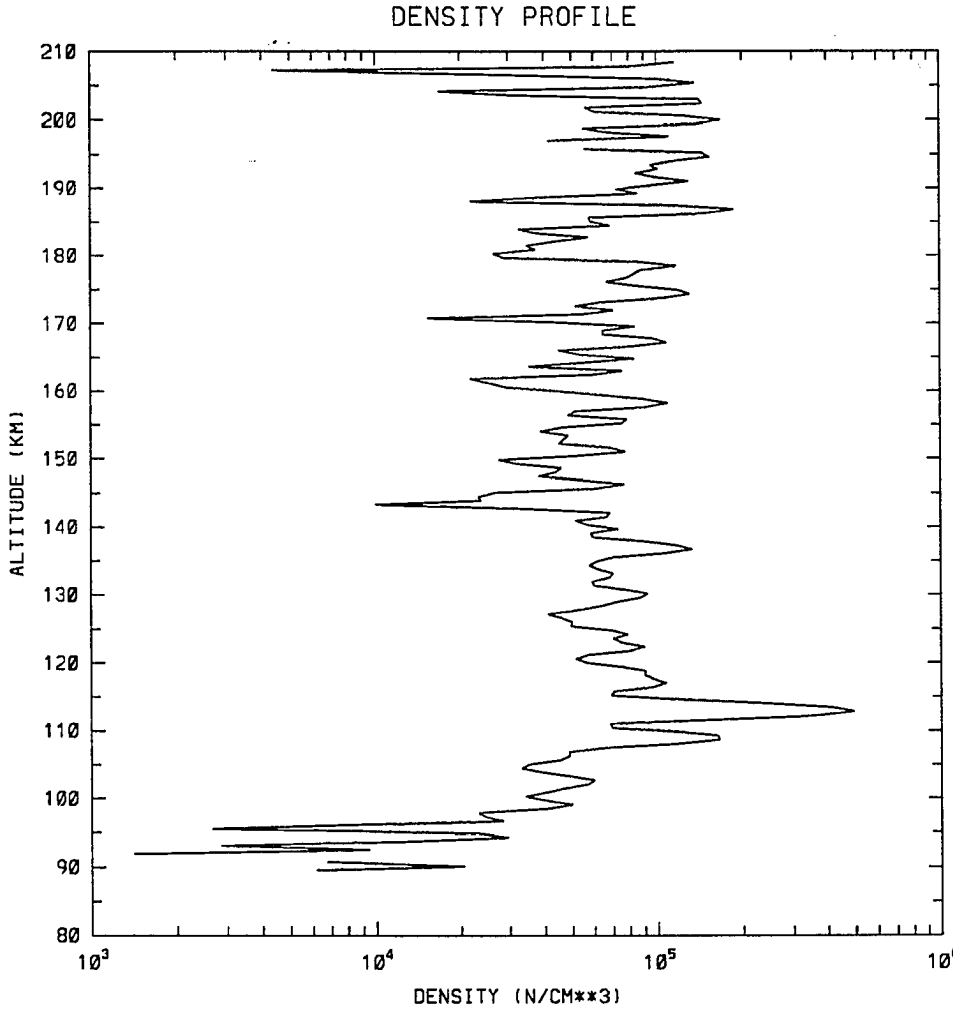

Fig. 5.6. The density profile from directly over the station illustrating the two distinct density peaks.

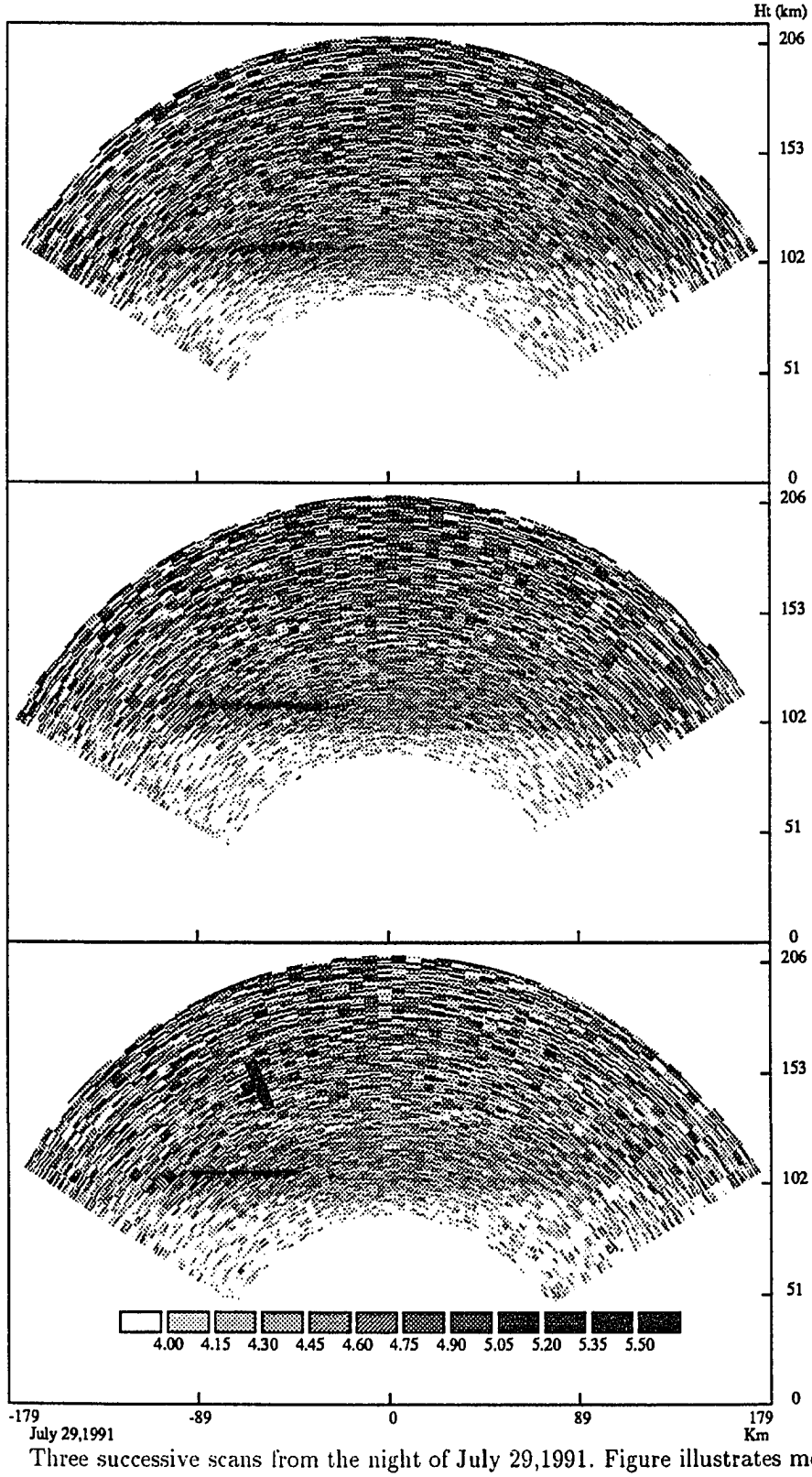

Fig. 5.7. Three successive scans from the night of July 29,1991. Figure illustrates motion of the layer.

that the layers are of a limited extent in latitude, however cover a large range in longitude.

5.6 Discussion

As a first point of interest it must be pointed out that observations were carried out on sixteen different nights for four-hour periods near magnetic midnight on each night. Thin ionization layers were observed during twelve of the sixteen experiments. The earliest observation was near 1900 UT on July 30, 1991, the latest just after 100 UT on March 14, 1991. The period of observation ranged from roughly 5 minutes to 2.5 hours.

The relatively heavy ion mass determination of 44 amu suggests that the layers are composed of metallic ions, primarily Fe^+. Mass spectrometer measurements of a mid-latitude thin ionization layer by Zbindin *et al.* show a layer almost entirely composed of metallic ions, with approximately equal concentrations of Fe^+ and Mg^+, along with much smaller concentrations of Na^+ and Ca^+. Further at the layer altitude they show a depletion of both NO^+ and O_2^+. Satellite data has shown that Fe^+ and Mg^+ are usually the two most abundant metallic ion species (Kumar and Hanson, 1980). If the layer observed here is assumed to be composed of only these two species then it would be approximately 63% Fe^+ and 37% Mg^+.

The scanning experiment showed several interesting features. First the layers were of a limited latitudinal extent, the largest extent from a single scan was roughly 200 km. This indicates that the conditions for forming the layer occur only in that limited region. The region did however move to cover a much larger latitude range beyond the field of view of the station. If the layers are formed by the action of the electric field, then the field is only appropriately directed in the limited area. This indicates that the field has significant variation over distances of less than 200 km, even in fairly quiet times. The antenna scans showing a sharp southern boundary further demonstrate the rapid change in conditions responsible for layer formation.

The limited latitudinal extent may also help to explain ionosonde observations of sporadic-E. When an ionosonde record shows the typical sporadic-E layer the traces frequently show lower frequency echos at higher altitudes. This is compatible with the limited latitudinal extent of the thin layers, which would result in the broad

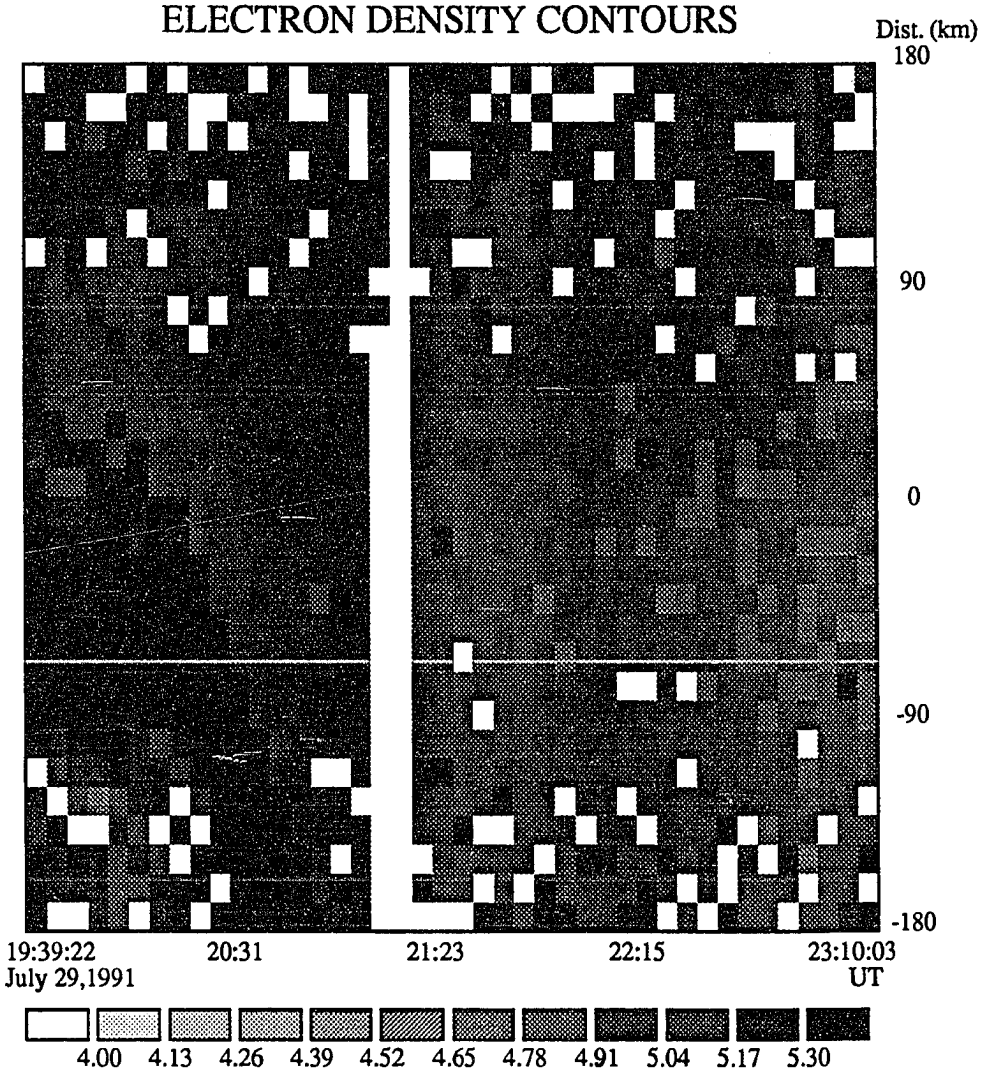

Fig. 5.8a. Peak electron density below 130km altitude plotted as a function of time and distance north and south of the station. Data is from July 29, 1991.

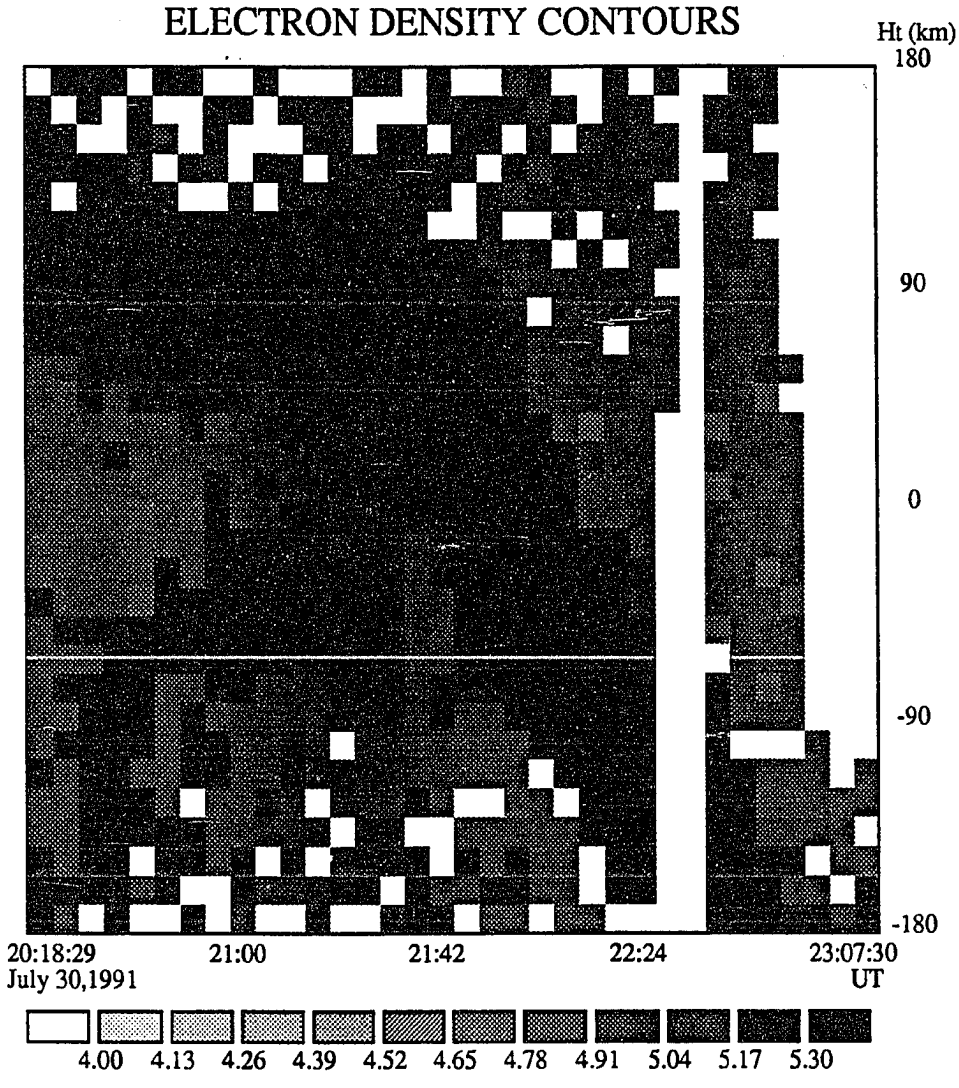

Fig. 5.8b. Peak electron density below 130km altitude plotted as a function of time and distance north and south of the station. Data is from July 30, 1991.

ionosonde beam being only partially filled by the thin layer. When the layer covers a larger area the ionosonde would be "Blanketed".

The other interesting feature of the scanning experiment is the observation of two distinct density peaks separated by nearly 5 km. This is a possible indication of the presence of two different ion species. Nygren *et al.*, 1984, discussed the density profiles expected for thin layers with two metallic ion species. They showed two distinct peaks were possible. Their results did however predict smaller separations, on the order of 1-2 km.

The electric field data showed thin layers present for field directions in both the north-west and south-west quadrants. For the majority of layer observations the field was directed between 80° and 100° west of magnetic north. This is consistent with the results of simulations, as discussed in the previous chapter. Figure 4.4 shows the results of the simulation for an electric field of 50mv/m directed to magnetic west, 2000 seconds after the application of the field. The simulation produced a thin layer of ionization at approximately 108 km altitude. This is in fairly good agreement with the data presented here. The simulation results predict that for field directions of less than 90° the layer should be higher, and lower for angles greater than 90°. This may be illustrated in the data from March 12, 1991,(data not shown) when the layer altitude changes abruptly as the field rotates from 80° the field of view as the field rotates back to 60°. The two layers shown in figures 5.3 and 5.4, both show qualitative agreement with the simulation. The layer of August 22,1990 (figure 5.3), initially forms near 115 km with the field directed to roughly 80°. As the field rotates to just over 100°the layer comes down in altitude. As the field rotates back to the north the layer rises. The agreement is only qualitative since the field rotates back to roughly 40°while the maximum layer altitude is roughly 115 km. The simulation results for a field directed to 45°showed a layer forming at 125 km. The layer observed on March 13, 1991 (figure 5.4), is in good agreement with simulation; the layer altitude remains fairly constant while the field direction also remains constant. Much of the other data is not in so close agreement. For example the data from August 17, 1990, showed layers for two different periods when the field directions were similar, however the altitudes of the two layers were quite different.

The effects of the neutral wind acting in conjunction with the electric field were examined in the simulation and results show that the neutral wind may effect both the altitude and thinness of the layers. Figure 4.10 shows the layer produced in the simulation with an electric field directed to magnetic west with a strong neutral wind directed to magnetic east. the result is a very thin layer near 110 km. The wind used was uniform in altitude, and probably stronger than would actually occur in the lower altitude ranges. The VSH neutral wind model predicts winds in the range of 50 m/s directed between north and east for the time near magnetic midnight at the location of Sondrestrom. Figure 5.9 shows the results of the simulation for conditions similar to those measured on March 13, 1991 (figure 5.8). The electric field was 15 mV/m directed 100°west of magnetic north. The neutral wind profile comes from the VSH model. The figure shows a fairly thin layer forming at just below 105 km altitude. This is in good agreement with the data.

There were often times when the electric field was pointed in the north-west quadrant when no layer was observed. As discussed in the introduction, such a field would be expected to produce an ion vertical velocity profile with a convergent null above 120 km altitude where metallic ions, if present, would accumulate. At no time were any layers observed above 120 km. A possible reason for this is the absence of sufficient metallic ions. Metallic ions are deposited in the upper atmosphere by meteor ablation, which takes place mainly between 70 and 120 km altitude with a peak near 100km.

5.7 Error Analysis

Errors in incoherent scatter measurements come from two main sources: the random fluctuations of the signal, and the random fluctuations of the noise. The received signal is a combination of the scattered signal and noise, both of which may be represented as Gaussian random variables. From a knowledge of the fluctuations of the signal and noise the uncertainties of the derived plasma parameters may be determined.

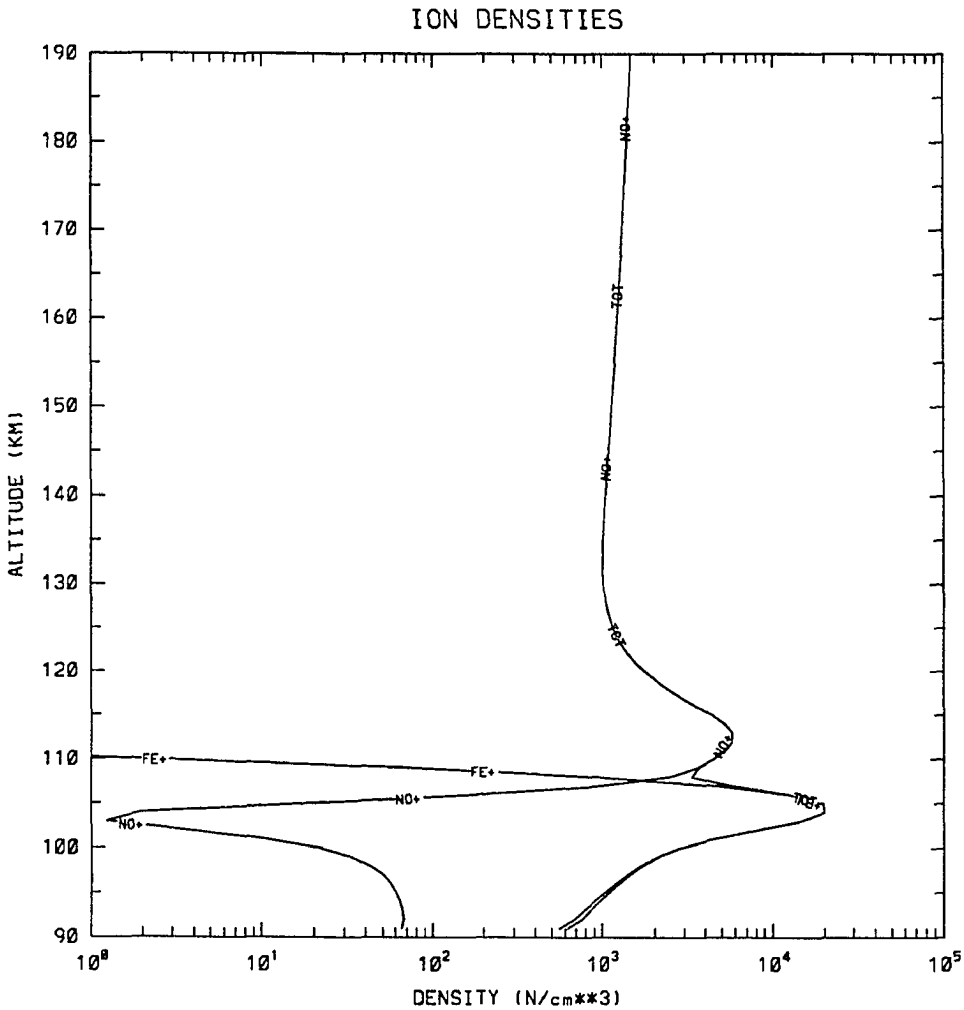

Fig. 5.9. Electron density profile from simulation results using input conditions similar to those measured on March 13, 1991.

The central idea of error analysis is contained in Chebychev's inequality (eg. Davenport and Root, pg 63):

$$P(|y - m_y| \geq \epsilon) \leq \frac{\sigma^2}{\epsilon^2}. \tag{5.2}$$

Simply stated: the probability of making a measurement of a random variable y greater than some value ϵ away from the mean value, m_y, is less than the variance over epsilon squared; the probability of measuring y greater than σ away from the mean is less than one, greater than 2σ away is less than $1/4$.

Another important idea is that the estimate of the mean value of a random variable follows a probability distribution, and thus has a variance. The variance of the mean can be determined from the variance of the data, and is:

$$\sigma_m^2 = \frac{1}{N}\sigma_x^2, \tag{5.3}$$

where N is the number of data points used in the estimate of the mean.

To estimate the plasma parameters the incoherent scatter spectrum is measured and theoretical spectrum is fit to the data. The fitting procedure is a multi-parameter non-linear least squares fit (Bevington, ch 11). The parameter χ^2 is defined as a measure of the goodness of the fit:

$$\chi^2 = \sum \left\{ \frac{1}{\sigma_i^2} [y_i - y_0(x_i)]^2 \right\}. \tag{5.4}$$

In the fitting procedure the value of χ^2 is minimized with respect to the plasma parameters. The search for the minimum is accomplished by taking the gradient of χ^2 and changing the parameters along the path of steepest decrease. At the minimum of χ^2 we get an estimate of the spectrum, and of each of the plasma parameters. χ^2 gives an estimate of the variance of the fit:

$$s^2 = \frac{\chi^2 \sigma^2}{N - n - 1}, \tag{5.5}$$

where N is the number of data points, and n is the number of parameters.

To find the uncertainties in the parameters we must examine the fitting procedure more carefully, and use statistical inversion as discussed in the chapter on radar techniques. The following is a condensation of the approach presented in that

section and some example calculations of the uncertainties in the data presented here.

The measured spectrum can be described by the theoretical spectrum plus some fluctuation:

$$y = y_0(x) + \epsilon, \tag{5.6}$$

where y is the measurement vector, $y_0(x)$ is the theoretical spectrum vector, x is the parameter vector, and ϵ is the fluctuation vector. The estimates of the parameters can be shown to follow a probability density function, $D(x)$:

$$D(x) = C\,D_{pr}(x)\exp\{-\frac{1}{2}[y_0(x) - y]^T\Sigma^{-1}[y_0(x) - y]\}, \tag{5.7}$$

where C is a constant, $D_{pr}(x)$ is any a priori probability density information, and Σ is the error covariance matrix ($\Sigma = \epsilon\epsilon^T$). The a priori probability density may be written as:

$$D_{pr}(x) = C\exp[-\frac{1}{2}(x - x_0)^T\Sigma_0^{-1}(x - x_0)]. \tag{5.8}$$

x_0 are the values of the parameters x determined by some other method, ie. the density as determined from power measurements, Σ_0 is a matrix with the associated a priori variances. Least squares fitting corresponds to maximizing the probability density, ie. minimizing the exponent when the error covariance matrix is diagonal.

To find the uncertainties of the parameters we examine the exponent at the minimum. We expand y in a Taylor series retaining only the first term:

$$y = Ax + \epsilon, \tag{5.9}$$

where the columns of A are:

$$A_i = \frac{\partial y_0}{\partial x_i}. \tag{5.10}$$

Now the probability density may be written as:

$$D(x) = C\exp[-\frac{1}{2}(x - x_0)^T Q(x - x_0)], \tag{5.11}$$

where the matrix Q is:

$$Q = \Sigma_0^{-1} + A^T\Sigma^{-1}A. \tag{5.12}$$

The variances of the parameter vector are found to be the diagonal elements of the inverse of Q.

5.8 Examples

First we examine the uncertainties in the density profiles. Figure 5.10 is a plot of the densities and the standard deviation for an interval of 5 minutes. As the figure shows, the uncertainties may be quite large in some regions. In most of the data the standard deviations of the density are on the order of 1 to 2 times the density. Thus for five minutes of data with four measurements per minute, the uncertainty in the mean value is on the order of 20% to 50%. In altitudes where the density is very high, ie. within a layer, the uncertainty is significantly less, on the order of 5% to 10%. The uncertainties here are larger than those often encountered in incoherent scatter experiments. There are several reasons for this, the main one being the range resolution of 300m. As discussed in the chapter on radar techniques uncertainty increases as the square of the range resolution. Also the inter-pulse-period used here is rather long, leading to longer integration time.

It is interesting to compare the measured uncertainties with those predicted, as discussed in the chapter on radar techniques. The predicted uncertainty in the densities is expressed as:

$$\frac{\delta n}{n} = \frac{C}{\sqrt{N}}\left(1 + \frac{1}{SNR}\right), \tag{5.13}$$

where N is the number of samples, and C is a constant on the order of 1. This was calculated and compared with the actual uncertainties, and was found to be very accurate. For example at one point near 140 km altitude, the uncertainty is 28%, the signal to noise ratio is 0.0323, the inter-pulse-period is roughly 22 ms, so there are roughly 13600 pulses in five minutes, which leads to the predicted uncertainty of 27.2%. Similar results were obtained at all altitudes.

Figure 5.11 is a plot of the percentage uncertainty as a function of altitude for temperatures for one hours data. The uncertainties are calculated as described above. Here the actual error covariance matrix was not calculated. The matrix was assumed to be diagonal with the elements being the variance of the fit for each point of the spectrum. As the figure shows at the lowest altitudes, below 100 km, the uncertainties are very large. The densities in this range are low, and thus there is very little signal. In the altitude range from 100 to 115 km the uncertainties are small, less than 5%. Above 115 km range squared losses cause the signal to

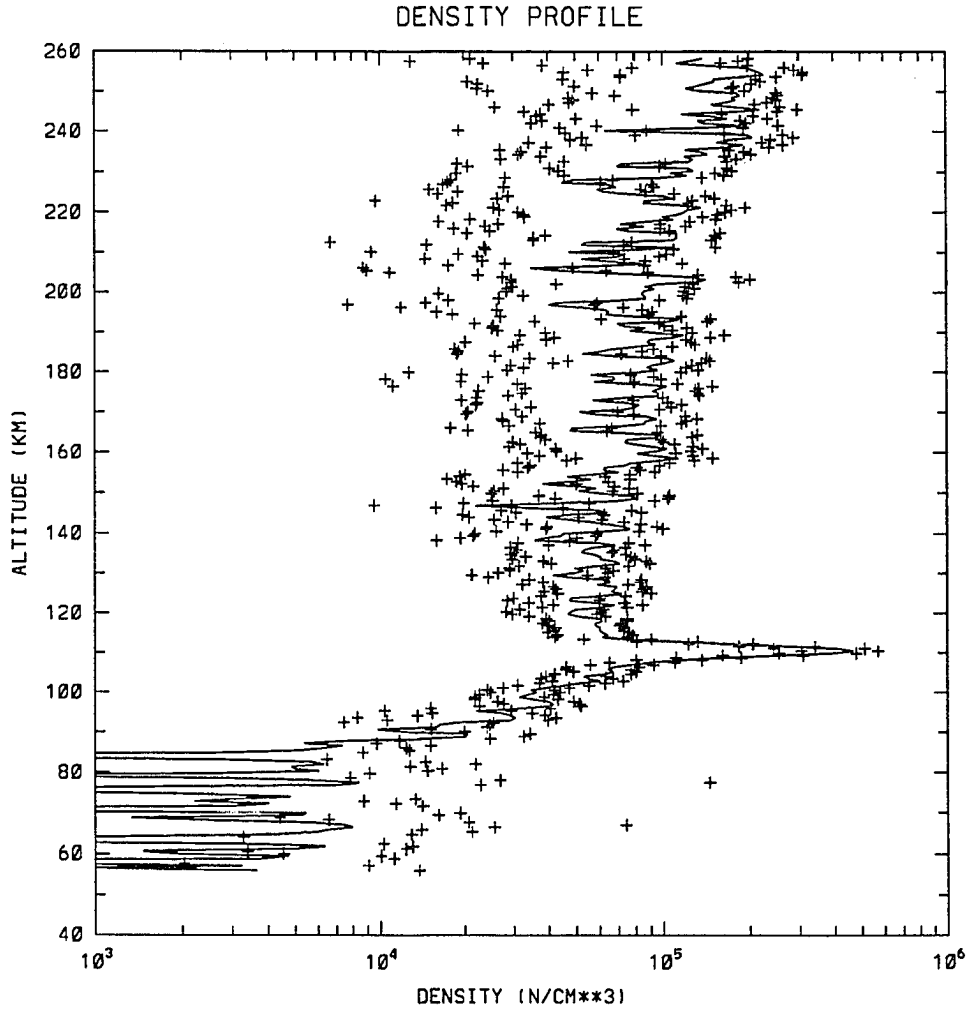

Fig. 5.10. Electron density profile and the standard deviation of the electron density at each altitude.

decrease and the uncertainties grow but remain below 30%. The low uncertainty in the region of 100 to 115 km is important since this is the altitude of the thin ionization layers. The temperature difference due to the ion mass difference is on the order of 10% to 15% which exceeds the uncertainty.

5.9 Conclusions

Thin ionization layers were present in the majority of the nights of observation. This is not a large statistical base but it does indicate that the conditions for layer formation do occur on most nights, within the same time window.

The electric field data are for the most part consistent with theory and simulation for layer formation by the action of the electric field. Layers were observed for a variety of field directions in the north-west and south-west quadrants, most often for directions close to magnetic west. Data showed a good correlation between layer altitude and field direction, although this was not always the case. The data indicate that the electric field plays a significant role in the formation of high latitude thin ionization layers, however other factors may also play an important role, neutral wind direction and magnitude for example. The lack of layers above 120 km, even though the field was directed such that layers should have formed, indicates that metallic ions may not be present in sufficient amounts above 120 km. Metallic ions have been observed as high as 1000 km, and are quite often observed at F-region altitudes at high latitudes with the highest number of observations on the day side between 70°and 80°(Grebowsky and Pharo, 1984), however altitude distributions of metallic ions are not well known.

Layers were not observed at times when the field was directed to magnetic south, for fields in the north-west quadrant with angles less than 40°, and one night for the field directed to magnetic west. Simulation predicted layers would form for each of these conditions, however there are possible explanations for the lack of layers. As discussed above, it is possible that there are not sufficient metallic ions present above 120km altitude, which would explain why no layers were observed for field angles less than 40°. For the 90°field, there was auroral ionization present which may have masked any layer if present. To understand the layer formation it will

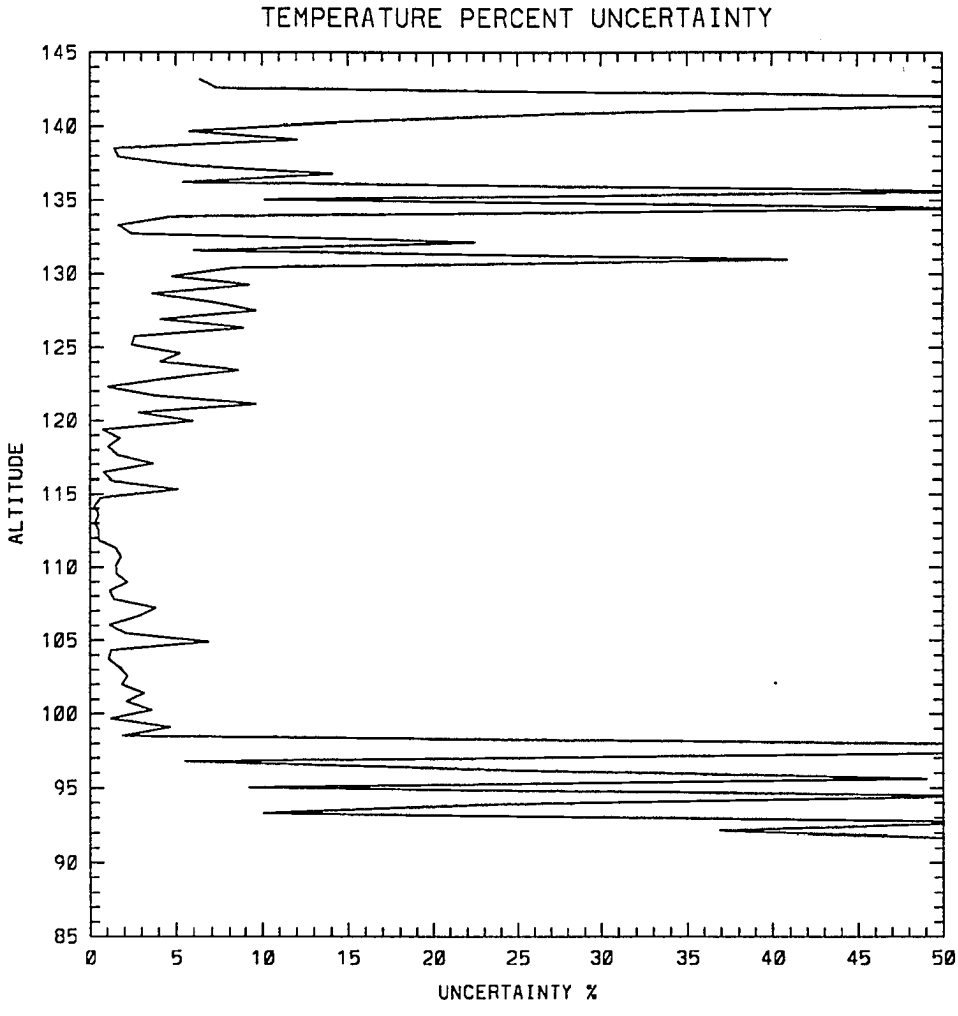

Fig. 5.11. Altitude profile of the uncertainty in the temperatures shown in figure 5.2.

be necessary to know simultaneously the neutral wind vector, electric field vector, and the metallic ion altitude distribution.

CHAPTER 6
CONCLUSIONS AND FUTURE WORK

6.1 Conclusions

In this thesis there have been two main parts to the work. The first part was a simulation which examined the effects of the convection electric field, in particular the effect its direction had on the formation of thin ionization layers. In the one dimensional simulation it was found that electric fields directed in the north-west or south-west quadrants are capable of producing thin ionization layers. The three dimensional simulation showed large areas of thin layers forming on the night-side at high-latitudes for a wide range of geophysical conditions. Finally thin layers were observed with the Sondrestrom incoherent-scatter radar at various times during a year. Layers were present on the majority of nights of observation. In this section the findings of the work will be discussed further and some comparison will be made between the observations and the predictions of the simulation.

The main finding of the one dimensional simulation was that electric fields directed in the north-west and south-west quadrants are capable of producing thin ionization layers. Fields in the north-west quadrant resulted in ion vertical velocity profiles with convergent nulls above 120 km altitude which, in the simulation, resulted in the formation of thin ionization layers at the altitude of the null. Electric fields in the south-west quadrant resulted in ion vertical velocity profiles without convergent nulls however there were gradients in the velocity directed such that there was accumulation of ionization. These velocity profiles produced thin layers in the altitude region between 100 and 110km which agrees well with observations. The altitude of the layer was dependent on the field angle; a field directed to 180°produced a layer at 100 km, a field directed to 100° produced a layer at about 108 km. The layers formed for electric field angles in the southwest quadrant were 3 to 5 km in thickness, which is thicker than layers that have been observed in this altitude range. When the action of the neutral wind was included thinner layers were produced for some electric field and wind directions.

The three dimensional simulation showed large regions of thin ionization layers on the night side forming for a wide range of conditions. The results for convection

patterns with southward IMF B_z showed layers forming on the night side in a band north of about 70°magnetic latitude in the evening sector, and between 60°and 70°in the morning sector. Results for various convection patterns with different IMF B_y were similar with small differences in the latitudes of the boundaries. Northward IMF B_z conditions also resulted in large areas of thin ionization layers. In general the layers were confined to the evening sector and were in the latitude range from 60°to 75°.

High range resolution measurements of thin ionization layers were successful in determining the average ion mass within the layers. The temperature profile obtained with an assumed ion mass of 30.5 amu showed a significant decrease in the temperature at the altitude of the layer. When the ion mass for the layer altitude was adjusted a smooth temperature profile was obtained. The experiment demonstrated the presence of heavy metallic ions within the thin ionization layer. On one occasion during the scanning experiment two distinct layers were observed separated by about 5km. This is a possible indication of the presence of two different metallic ion species.

Concurrent observations of E-region thin ionization layers and F-region electric fields showed thin layers in the altitude region between 100 and 115 km for electric field directions between 40°and 140°. The most common direction of the field was between 80°and 100°, with the corresponding layer altitudes between 100 and 105 km. Layers were not observed above 115 km or for field directions less than 40°, or for times when the electric field was directed to magnetic south. There were some cases of electric fields directed in the north-west quadrant with angles greater than 40°when no layers were observed. The simulation predicted that layers would form for each of these sets of conditions.

In general the observations showed correspondence between field direction and layer altitude and there was qualitative agreement between observation and simulation. In the simulation, fields directed near magnetic west produced layers in the range from 100 to 110km; the altitude and thinness were dependent on field direction and the neutral wind. In the observations, layers occurred at altitudes near 100 km for fields near magnetic west and usually at higher altitudes for smaller electric field angles; neutral wind information was not available. On nights when the layers

were observed over long periods and the field direction changed, the altitude of the layer changed in a manner as expected from the simulation results. On one occasion, August 22, 1990, as the field rotated from 100°to 40°, the layer altitude changed from 105 to 115 km. In the simulation a field directed to 45°resulted in a layer at an altitude of 124 km. Thus, although the observed layer altitude increased for decreasing field angle, there is some discrepancy between the observation and simulation results for the field of 40°. It is not possible to discern the source of the difference from the observations. It is possible that the difference is due to the error in the electric field measurement. As discussed in the chapter on radar techniques the electric field measurement is an average over space and time; the line-of-sight velocities are separated in space by more than 100 km and it takes fifteen minutes to make one vector measurement. To obtain a convergent null at 115 km altitude an electric field of approximately 70°is required, this corresponds to an error of 30°; it is not likely that the error in the field is this large. It is also possible that the neutral wind may cause the altitude of the convergent null to be different than that produced by the electric field alone. For example, an electric field of 20 mV/m directed to 50°, and a neutral wind of 200 m/s directed to magnetic east result in a convergent null at approximately 117 km altitude. In the absence of the neutral wind this field direction leads to a convergent null at approximately 122 km altitude; the action of the wind lowers the null by about 5 km.

For fields in the north-west quadrant it is possible that the absence of thin layers is due to a lack of metallic ions in the altitude range of the convergent nulls. The convergent nulls generally occur at altitudes above 120 km. In the simulation the initial metallic ion profile was peaked at 120 km altitude and decreased gradually above and below. The actual peak of the meteor ablation region is probably near 100 to 105 km and the majority of meteors ablate at altitudes below 120 km. It is likely that there is not a sufficient amount of metallic ions transported from the ablation region to the region of the convergent nulls.

The lack of layers for times when the electric field was observed to be directed to magnetic south is also in disagreement with the simulation. The simulation produced ionization layers near and below 100 km altitude for a field directed to magnetic south. The layers were about 5 km thick, and the peak densities were

about $2 \times 10^4 cm^{-3}$. It is possible that layers were present in the observations but were not detectable due to the low density. There are times in the data where there are not clearly detectable layers, however possible enhancements are observed. The data from the night of March 10, 1991, show a possible layer near 100 km altitude at a time when the field is directed between 120°and 180°for a period of about one hour. Again, the layer is not clearly visible. It is also possible that ionization is not accumulating due to recombination. In the simulation recombination was not considered since the recombination times for the metallic ions are so long. However below 100 km three body recombination may become important and should be included.

It is difficult to make direct comparisons between the three dimensional simulation and the observations. The inputs to the simulation are average convection patterns, and average neutral wind patterns. The actual conditions of the ionosphere at any given time may have little or no resemblance to the averages. However some qualitative comparisons may be made. Thin ionization layers were observed on 12 of the 16 nights of observation which indicates that the conditions for layer formation occur on a regular basis which agrees with the results of the simulation. The simulation showed large areas of thin layers occurring for each of the cases examined. The plots of electron density contours for Sondrestrom's latitude (figures 3.18, 3.20c, 3.21c, 3.22c, 3.23c, 3.24c) can be compared with the observations. Figure 3.18 shows the simulation results for southward B_z conditions, Hepner-Maynard 'pattern A'. A thin ionization layer is present which forms at an altitude of about 120 km, descends to about 105 km, then slowly rises back to 120 km. The layer is present from about 1900 to 0300 MLT. Other runs of the simulation show similar behavior some with the layers present for a shorter period. For Sondrestrom latitude the simulation produced layers mainly in the pre-midnight sector. Observations showed thin layers present on the various days at times ranging from 2105 to 0120 UT. At Sondrestrom, 0000 UT is 2200 MLT, this makes the observation times 1805 to 2320 MLT, ie. in the premidnight sector. The layer observed on August 22, 1990, was similar to the simulation result of figure 3.18. The layer was observed to form, then descend, then slowly rise. The layer was present for the

period from 2150 to 2315 UT, which is a shorter time than that of the simulation result.

The scanning experiment showed layers forming in a confined latitudinal region; the largest latitudinal extent observed was about 200km. This indicates that the conditions for forming the layer only occurred in that limited region. The areas where layers were observed were within the areas predicted by the simulation, however they were much smaller. The areas of thin layers produced in the simulation were on the order of 10°in latitude or larger where 200km is approximately 2°latitude. As discussed above the simulation uses average convection patterns which may smear out the actual electric field pattern.

In summary, it may be concluded that the thin ionization layers at high latitudes are composed of metallic ions. A significant fraction of the ionization is probably Fe^+ with another lighter metallic ion also present. Also it may be concluded that the perpendicular electric field plays a significant role in the formation of the layers. Simulation showed that layers may form for electric fields directed in the north-west and south-west quadrants, while observations showed layers present for a more limited range of field directions. It may be concluded that a field directed near magnetic west will most likely result in the formation of a thin ionization layer. In the experiments at almost all times that the electric field was directed to magnetic west there were layers present. There was only one time the field was directed to 90°when no layer was observed and there was particle precipitation at that time which may have masked any layer. It also may be concluded that the conditions for layer formation occur quite often. Observations distributed through a year showed layers present on 12 of 16 nights within the experiment window.

6.2 Future Work

Much work remains to be done in this area. Some discrepancies remain between the theory and observations. Thin ionization layers below 110km are often thinner than predicted by the simulation. Layers are not observed for some conditions even though the simulation predicts that layers should be present. Layer altitudes do not always agree with the simulation. It is likely that many of these discrepancies would be resolved by a knowledge of the metallic ion altitude profile and the neutral

winds. The lack of metallic ions above a certain altitude may be responsible for the absence of thin layers in some cases. Knowledge of the metallic ion altitude profile would answer this question. The direction and magnitude of the neutral winds may affect the altitude and thinness of thin layers. To make accurate predictions about the thin layers the neutral wind must be known.

Observations should be carried out on a regular basis to develop a larger statistical base. The observations presented here occurred in limited intervals; two periods in the summer months and one in March. To make general statments about the occurrence of layers more data is required. Observations should be carried out throughout the year. The number of meteors which come into the earth's atmosphere varies over a year and thus it is expected that the amount of metallic ions in the atmosphere would also vary. It would be expected that the occurrence of thin ionization layers would also vary. It would be interesting to make observations for a period of several days during one of the major meteor showers to examine any increase in the densities of the layers. Also with a larger base of observations it would be possible to make correlations with the IMF conditions and compare with the results of the three dimensional simulation. The simulation predicted variation in the time of occurrence of the layers depending on the IMF conditions.

Before making any comparisons between the data and the three dimensional simulation, the simulation should be improved to better reflect reality. The coordinate systems should be changed so that the magnetic and geographic poles do not coincide. It might also be better to include the metallic ions as a continuous deposition rather than an initial profile. Some loss mechanism for the metallic ions should also be included.

An improvement to the experiments would be to decrease the time required to make the electric field measurements. The current experiment obtains a new electric field vector every fifteen minutes. Often layers are observed for less than this time. Improvements in the noise temperature of the radar system would decrease the time required to make measurements. A lower noise temperature would also allow the detection of lower density layers.

Other experiments that could be performed include concurrent optical and radar measurements to examine any connection between enhanced aurora and thin ionization layers, and concurrent coherent-scatter and incoherent-scatter radar observations to examine any relationship between the presence of thin layers and plasma waves.

References

Axford, W.I., The formation and vertical movement of dense ionized layers in the ionosphere due to neutral wind shear. *J. Geophys. Res.* 68, 3, 769-779, 1963.

Axford, W.I., D.M. Cunnold, The wind-shear theory of temporate zone sporadic E. *Radio Sci.*, 1, 2, 191-198, 1966.

Bates, Howard F., Some effects of dense $E_s$clouds on high-latitude HF backscatter observations. *J. Geophys. Res.* 70, 23, 5895-5905, 1965.

Beaty, T.J., R.L. Collins, C.S. Gardner, C.A. Hostetler, C.F. Sechrist, Jr., Simultaneous radar and lidar observations of sporadic E and Na layers at Arecibo. *Geoph. Res. Lett.* 16, 9, 1019-1022, 1989.

Behnke, R.A., J.F.Vickery, Radar Evidence for Fe^+ in a Sproadic-E layer. *Radio Sci*, 10, 325-327, 1975.

Bevington, P.R., *Data Reduction and Error Analysis for the Physical Sciences,* McGraw-Hill, 1966.

Bills, R.E., C.S. Gardner, Lidar observations of Mesopheric Fe and sporadic Fe layers ar Urbana, Illinois. *Geoph. Res. Lett.* 17, 2, 143-146, 1990.

Bristow, W.A., B.J.Watkins, Numerical simulation of the formation of thin ionization layers at high latitudes. *Geoph. Res. Lett.* 18, 3, 404-407, 1991.

Constantinides, E., J.F. Bedinger, Observed redistribution of E-region Ionization by neutral winds. *J. Atmosph. Terr. Phys.* 33, 461-472, 1971.

Davenport, W.B., W.L. Root, *Random Signals and Noise.* McGraw-Hill, 1958.

Dougherty, J.P., D.T.Farley, A theory of incoherent scattering of radio waves by a plasma (1), *Proc. Roy. Soc. London* A, 259, 79-99, 1960.

Dougherty, J.P., D.T. Farley, A theory of incoherent scattering of radio waves by a plasma (3), Scattering in a partly ionized gas. *J. Geophys. Res.* 68, 5473-5486, 1963.

Dungey, J,W., Effect of a magnetic field on turbulence in an ionized gas. *J.Geophys.Res.* 64, 12, 2188-2191, 1959.

Farley D.T., A theory of incoherent scattering of radio waves by a plasma (4), The effect of unequal ion and electron temperatures. *J. Geophys. Res.* 17, 4091-4098, 1966.

Farley, D.T., Multiple-pulse incoherent-scatter correlation function measurements. *Radio Sci.* 7, 661-666, 1972.

Fedder, J.A., P.M.Banks, Convection electric fields and polar thermospheric winds. *J. Geophys. Res.* 77, 13, 2328-2340, 1972.

Fejer, J.A., Scattering of radio waves by an ionized gas in thermal equilibrium. *Can. J. Phys.*, 38, 1114-1133, 1960.

Forbes, J.M., Atmospheric tides 2. the solar and lunar semidiurinal components. *J. Geophys. Res.* 87, A7, 5241-5252, 1982.

Granier, C., J.P. Jegou, G. Megie, Iron atoms and metallic species in the earth's upper atmosphere. *Gephys. Res. Lett.*, 16, 3, 243-246, 1989.

Grebowsky, J.M., M.W. Pharo III, The source of midlatitude metallic ions at F-region altitudes. *Planet. Space Sci.* 33, 807-815, 1985.

Hagfors, T., Density fluctuations in a plasma in a magnetic field with applications to the ionosphere. *J. Geophys. Res.*, 66, 6, 1699-1712, 1961.

Hallinan, T.J., H.C. Stenbaek-Nielsen, C.S. Deehr, Enhanced aurora. *J. Geophys. Res.* 90, A9, 8461-8475, 1985.

Hargraves, J.K., *The Upper Atmosphere and Solar-Terrestrial Relations.*, Van Nostrand Reinhold, 1979.

Heppner, J.P., N.C. Maynard, Emperical high-latitude electric field models. *J. Geophys. Res.* 92, A5, 4467-4489, 1987.

Hoppe, U.P., T.L. Hansen, Studies of vertical motions in the upper mesosphere using the EISCAT UHF radar. *Ann. Geophys.* 6, 181-186, 1988.

Horwitz, J.L., J.R.Doupnik, P.M.Banks, Chatanika radar observations of latitudinal distributions of auroral zone electric fields, Conductivities, and Currents. *J. Geophys. Res.* 83, 1463-1481, 1978.

Hughes, D.W., "Meteors", in *Cosmic Dust*, John Wiley & Sons, pg. 123, 1978.

Hunsucker, R.D., L.Owren, Auroral sporadic-E ionization. *Journal of Research of NBS* Standards–D Radio Propagation, Vol 66D, No. 5, pp 581-592, 1962.

Hunsucker, R.D., Chatanika radar investigation of high latitude E-region ionization structure and dynamics. *Radio Sci.* 10, 277-288, 1975.

Hunsucker, R.D., *Radio Techniques for Probing the Terrestrial Ionosphere.* Springer-Verlag, 1991.

Jackson, J.D. *Classical Electrodynamics.* John Wiley and Sons, 1975.

Killeen, T.L., R.G. Roble, N.W. Spencer, A computer model of global thermospheric winds and temperatures. *Adv. Space Res.* 7, 207-215,1987.

Kirkwood, S., U. von Żahn, On the role of auroral electric fields in the formation of low altitude sporadic-E and sudden sodium layers. *J. Atmosph. Terr. Phys.* 53, 389-407, 1991.

Kirkwood,S., P.N.Collis, Gravity wave generation of simultaneous an auroral sporadic-E layer and sudden neutral sodium layers. *J.Atmos.Terr.Phys.* 51, 259-269, 1989

Kockarts, G., Nitric oxide cooling in the terrestrial thermosphere. *Geoph. Res. Lett.* 7,2,137-140,1980.

Kumar, S., W.B. Hanson, The morphology of metallic ions in the upper atomosphere. *J. Geophys. Res.* 85, 6783-6801, 1980.

Layzer, D., Theory of Midlatitude Sporadic E. *Radio Sci.*, 7, 385-395, 1972.

MacLeod,M.A.,T.J.Kenshea,R.S.Narcisi, Numerical modelling of metallic ion sporadic-E layer. *Radio Sci.* 10, 3, 371-388, 1975

Maynard, Nelson C., Electric field measurements across the Harang Discontinuity.*J.Geophys. Res.*, 79, 31, 4620-4631, 1974.

Narcisi, R.S., A.D.Bailey, L.Della Lucca, Composition measurements of a sporadic-E in the night time lower ionosphere. *Space Res.* 7, 123, 1968.

Nicholson, D.R., *Introduction to Plasma Theory.*, John Wiley and Sons, 1983.

Nygren, T., L.Jalonen, J.Oksman, T.Turunen, The role of electric field and neutral wind direction in the formation of sporadic E-layers. *J. Atmosph. Terr. Phys.* 46, 373-381, 1984.

Nygren, T., L.Jalonen, A.Huuskonen, T.Turunen, Density profile of sporadic E-layers containing two metal ion species. *J. Atmosph. Terr. Phys.* 46, 885-893, 1984.

Potter, D., *Computational Physics.* John Wiley and Sons, 1973.

Rees, M.H., J.C.G.Walker, Ion and electron heating by auroral electric fields. *Ann. De Geophys.* 24, 193-199, 1968.

Rees,M.H, *Physics and Chemistry of the Upper Atmosphere.* Cambridge University Press, 1989.

Roble, R.G., J.T.Hastings, Thermal response properties of the earth's ionospheric plasma. *Planetary Space Sci.* 25, 217-231, 1977.

Rosenbluth, M.N., N. Rostoker, Scattering of electromagnetic waves by a nonequilibrium plasma. *Phys. Fluids*, 5, 7, 776-788, 1962.

Salpeter, E.E., Plasma density fluctuations in a magnetic field. *Phys. Rev.*, 122, 6, 1663-1674, 1961.

Schunk, R.W., Transport equations for aeronomy. *Planet. Space Sci.* 23, 437-485, 1975.

Smith, L.G., E.A. Mechtly, Rocket observation of sporadic-E layers. *Radio Sci.* 7, 3, 367-376, 1972.

Solomon, S., E.E. Ferguson, D.W. Fahey, On the chemistry of H_2O, H_2 and meteoric ions in the mesophere and lower thermosphere. *Planet. Space Sci.* 30, 11, 1117-1126, 1982.

Sulzer, M.P., A radar technique for high range resolution incoherent scatter autocorrelation function measurements utilizing the full average power of klystron radars. *Radio Sci.* 21, 6, 1033-1040, 1986.

Thomas, J.A., E.K. Smith, A survey of the present knowledge of sporadic-E ionization. *J. Atmosph. Terr. Phys.* 13,295-314, 1959.

Turunen, T., J. Silen, T. Nygren, L. Jalonen, Observation ot a thin E_s-Layer by the EISCAT radar. *Planet. Space Sci.,* 33, 12, 1407-1416, 1985.

Turunen, T., T. Nygren, A. Huskonen, L. Jalonen, Incoherent scatter studies of sporadic-E using 300 m resolution. *J. Atmosph. Terr. Phys.* 50, 277-287, 1988.

Vallinkoski, Matti, Statistics of incoherent scatter multiparameter fits. *J. Atmosph. Terr. Phys.* 50, 839-851, 1988.

von Zahn, U., T.L. Hansen, Sudden neutral sodium layers: a strong link to sporadic E layers. *J. Atmosph. Terr. Phys.* 50, 2, 93-104, 1988.

Whitehead, J.D., The formation of the sporadic E-layer in the temperate zones. *J. Atmos. Terr. Phys.* 20, 49-58, 1960.

Whitehead, J.D., Mixtures of ions in the wind-shear theory of sporadic E. *Radio Sci.* 1, 2, 198-203, 1966.

Zbinden, P.A., M.A.Hidalgo, P.Eberhardt, J.Geiss, Mass spectrometer measurements of the positive ion composition in the D- and E-regions of the ionosphere. *Planetary Space Sci.* 23, 1621-1642, 1975.